

**NUMERICAL STUDY OF LARGE DEFORMATION RETROGRESSIVE LANDSLIDES
IN SENSITIVE CLAY TRIGGERED BY TOE EROSION AND EARTHQUAKE**

By

© Chen Wang

A Thesis Submitted to the

School of Graduate Studies

in partial fulfillment of the requirements for the degree of

Doctor of Philosophy

Faculty of Engineering and Applied Science

Memorial University of Newfoundland

February 2020

St. John's

Newfoundland

Canada

ABSTRACT

Landslides in sensitive clays represent a severe geohazard in eastern Canada and Scandinavia. Triggered by various factors, such as toe erosion, earthquake, and human activities, a sensitive clay landslide can affect a large area and cause damage to infrastructure. The evaluation of risk associated with sensitive clay landslides is an important but challenging task because the failure mechanisms are not well understood. Different types of landslide (e.g. flowslide, monolithic slide, and spread) occur through significantly different failure processes that affect both retrogression and run-out. Full-scale modeling of such large-scale landslides is not practically feasible. On the other hand, real-time monitoring of the failure in the field is not possible. Therefore, the characteristics of the landslides are generally evaluated by comparing post-slide field investigations with available information on the site before the landslide. Numerical modeling could be an alternative tool to obtain further insights into the failure mechanisms. The failure occurs by progressive formation of shear bands where extremely large plastic shear strain generates, and the failed soil displaces over a large distance. Consequently, the methods commonly used for slope stability analysis, such as limit equilibrium (LE) methods and Lagrangian-based finite element (FE) methods, cannot be used to model the whole process of a sensitive clay landslide.

The main objective of the present study is to analyze the factors affecting the failure pattern and extent of sensitive clay landslides triggered by toe erosion and seismic loading. A large deformation finite element (LDFE) method based on Eulerian approach is used to simulate the triggering of the landslide, subsequent failure of soil blocks and run-out of the debris. The landslide generally occurs rapidly in a matter of few minutes; therefore, the simulation is performed for the undrained condition. The strain-softening behavior of sensitive clay is defined as a function of plastic shear displacement that reduces the undrained shear strength to a very low value at a large strain. A strain-rate dependent

undrained shear strength model is used, which can model the behavior of soil and remolded clay that flows at a high speed as a fluid-like material.

The formation of a slope generally occurs due to the removal of the materials in drained condition. Moreover, groundwater seepage might dominate the failure of a slope. Numerical simulation techniques for the Eulerian based LDFE method are developed to simulate in-situ effective stresses, which can be used for the cases of widely varying earth pressure coefficient at rest, even greater than unity. Based on the thermal-hydraulic analogy, a numerical modeling technique is developed for seepage analysis. The above-mentioned methods can successfully simulate the initial stress condition in the soil that affects the failure mechanisms significantly.

Many failures of sensitive clay slope are initiated by toe erosion. Conducting LDFE simulations, the potential conditions required for a flowslide and a spread are identified. The type and extent (retrogression and run-out) of a landslide depend on a combination of several factors related to geometry and soil properties. A single parameter, such as stability number, remolded shear strength, liquidity index or remolded energy, may not always be suitable to categorize failure type. Increasing lateral earth pressure coefficient at-rest shows a trend of occurring spreads, while a low remolded shear strength and favorable conditions for rapid displacement of debris result in flowslides. The comparison of LDFE simulations and post-slide investigations of the 2010 Saint-Jude landslide show that the present numerical simulations can explain several features of the landslide, including the effects of seepage and an opposite riverbank on progressive failure.

Finally, pseudostatic and dynamic analyses are performed using the developed LDFE method to study the progressive formation of failure planes in clay slopes subjected to earthquake loading. The LDFE modeling in Eulerian approach can simulate the large displacement of the failed soil blocks, considering the reduction of shear strength due to strain-softening.

ACKNOWLEDGMENTS

I would like to express my deepest gratitude to my supervisor Dr. Bipul Hawlader, Professor of Memorial University of Newfoundland, for his continuous guidance, keen supervision, encouragement, patience and invaluable suggestions throughout my time as his student. I have been extremely lucky to have a supervisor who cared so much about my work, and who responded to my questions and queries so promptly. I would also like to thank my supervisory committee members Dr. Didier Perret, Natural Resources Canada, and Dr. Kenichi Soga, Professor of University of California, Berkeley. It was a great privilege and honor to work and study under their guidance. I have learned so much through their valuable suggestions, insightful guidance and continuous encouragement. I also benefited a lot from their life philosophy and their serious attitude towards research.

Special thanks to Dr. Rajib Dey, Dr. Sujan Dutta, Dr. Kshama Roy and Mr. Naveel Islam for their unceasing advice, suggestions, assistance and invaluable time spent throughout the work. Besides, I really cherish the strong friendship established through time with all of you.

I am truly grateful to my parents for their immeasurable love and care. They have always encouraged me to explore my potential and pursue my dreams.

At last, I would like to thank my lovely wife Jie. We came to Canada together for our Ph.D. studies. You did a really good job and became a Doctor before me. I am so proud of you, and I also really appreciate that we have similar life experiences and we share thoughts and support each other completely selflessly. I could not finish my Ph.D. without your understanding and endless support.

TABLE OF CONTENTS

ABSTRACT	II
ACKNOWLEDGMENTS.....	IV
LIST OF FIGURES.....	IX
LIST OF TABLES.....	XII
LIST OF SYMBOLS	XIII
CHAPTER 1.....	1
INTRODUCTION	1
1.1 GENERAL.....	1
1.2 RESEARCH FOCUS	4
1.3 OBJECTIVES.....	6
1.4 THESIS ORGANIZATION.....	7
CHAPTER 2.....	9
LITERATURE REVIEW	9
2.1 GENERAL.....	9
2.2 BEHAVIOR OF SENSITIVE CLAY IN UNDRAINED CONDITION.....	10
2.2.1 Strain-softening behavior of sensitive clay	10
2.2.2 Strain-rate effects of sensitive clays.....	14
2.3 SHEAR BAND PROPAGATION IN BRITTLE MATERIALS.....	18
2.4 FAILURE MECHANISMS OF SENSITIVE CLAY LANDSLIDES	22
2.4.1 Failure mechanism of flowslide.....	22
2.4.2 Failure mechanism of spread	25
2.4.3 Retrogression and run-out distance of landslides in sensitive clays	26
2.5 SLOPE FAILURE SUBJECT TO DYNAMIC LOADING	29
2.6 NUMERICAL MODELING OF LANDSLIDES	32
2.7 SUMMARY	35

CHAPTER 3.....	37
EFFECTS OF GEOMETRY AND SOIL PROPERTIES ON TYPE AND RETROGRESSION OF LANDSLIDES IN SENSITIVE CLAYS	37
3.1 ABSTRACT.....	37
3.2 INTRODUCTION.....	38
3.3 PROBLEM DEFINITION.....	41
3.4 NUMERICAL MODELING.....	43
3.5 MODELING OF SENSITIVE CLAY.....	45
3.5.1 Strain softening	45
3.5.2 Strain-rate effects on undrained shear strength	46
3.6 GEOMETRY AND SOIL PARAMETERS.....	48
3.7 FAILURE MECHANISMS	51
3.7.1 Flowslide.....	52
3.7.2 Spread	54
3.8 FACTORS AFFECTING FLOWSLIDES.....	56
3.8.1 Stability number.....	56
3.8.2 Shear strength gradient in sensitive clays	58
3.8.3 Undrained shear strength at large deformation	58
3.8.4 Remolded energy	59
3.9 FACTORS AFFECTING SPREADS.....	61
3.9.1 In-situ stress condition	61
3.9.2 Brittleness	64
3.9.3 Slope angle.....	66
3.9.4 Opposite riverbank.....	67
3.10 PRACTICAL IMPLICATIONS	67
3.11 CONCLUSIONS	69

CHAPTER 4.....	80
MODELING OF INITIAL STRESSES AND SEEPAGE IN LARGE DEFORMATION FINITE ELEMENT SIMULATION OF SENSITIVE CLAY LANDSLIDES	
	81
4.1 ABSTRACT.....	81
4.2 INTRODUCTION.....	81
4.3 NUMERICAL MODELING.....	84
4.3.1 Steps in Eulerian FE modeling.....	86
4.3.2 Validation of Eulerian FE modeling of seepage and in-situ stress.....	90
4.4 MODELING OF SENSITIVE CLAY.....	93
4.4.1 Strain softening	93
4.4.2 Strain-Rate effects on undrained shear strength.....	94
4.5 MODELING OF RETROGRESSIVE LANDSLIDE	95
4.5.1 Effects of K_0	96
4.5.2 Effects of strain-rate on undrained shear strength.....	98
4.6 SIMULATION OF THE 2010 SAINT-JUDE LANDSLIDE.....	100
4.6.1 Seepage analysis	101
4.6.2 Failure process	104
4.5.3 Comparison with field investigation	107
4.7 CONCLUSIONS	108
CHAPTER 5.....	116
IMPLEMENTATION OF A LARGE DEFORMATION FINITE ELEMENT MODELLING TECHNIQUE FOR SEISMIC SLOPE STABILITY ANALYSES.....	
	116
5.1 ABSTRACT.....	116
5.2 INTRODUCTION.....	117
5.3 PROBLEM STATEMENT	119
5.4 FINITE ELEMENT MODELLING	120

5.5	FINITE ELEMENT MODEL DEVELOPMENT.....	121
5.5.1	Eulerian analysis.....	121
5.5.2	Implicit and explicit approaches.....	122
5.5.3	FE modelling steps.....	122
5.6	MODELLING OF SOIL.....	124
5.6.1	Undrained shear strength.....	124
5.6.2	Kinematic hardening for dynamic loading.....	125
5.6.3	Elastic properties.....	126
5.6.4	Numerical implementation of shear strength.....	126
5.7	NUMERICAL SIMULATION RESULTS.....	127
5.7.1	Pseudostatic FE analyses results.....	127
5.7.2	Dynamic FE analyses.....	132
5.7.3	Dynamic FE results.....	136
5.8	COMPARISON OF TOE DISPLACEMENT.....	142
5.9	CONCLUSIONS.....	145
	CHAPTER 6.....	155
	CONCLUSIONS AND FUTURE WORK.....	155
6.1	CONCLUSIONS.....	155
6.2	RECOMMENDATIONS FOR FUTURE RESEARCH.....	156
	REFERENCES.....	158
	APPENDIX-I.....	170
	FINITE ELEMENT SIMULATION OF THE 2010 SAINT-JUDE LANDSLIDE IN QUÉBEC.....	170
	APPENDIX-II.....	180
	NUMERICAL MODELING OF THREE TYPES OF SENSITIVE CLAY SLOPE FAILURES.....	180

LIST OF FIGURES

Fig.1.1. Landslides in sensitive clays triggered by toe erosion and earthquake: (a) Saint-Jude landslide (after Locat et al. 2017); (b) Notre-Dame-de-la-Salette landslide (after Perret et al. 2013); (c) Mulgrave & Derry landslide (after Perret et al. 2013).	2
Fig. 2.1. Idealized undrained strain-softening of soft sensitive clays at laboratory strain level (after Thakur et al. 2014).	12
Fig. 2.2. Stress–strain behavior and stress paths in DSS tests (after Locat et al. 2014).	13
Fig. 2.3. Normalized stress versus displacement for Champlain clay samples (after Quinn et al. 2011)... ..	14
Fig. 2.4. Change in undrained shear strength ratio with strain rate (after Lefebvre and LeBoeuf 1987). ..	15
Fig. 2.5. Integration path for the <i>J</i> -integral (after Palmer and Rice 1973).	19
Fig. 2.6. Schematic of the shear band formation in typical submarine slope with a strain-softening clay layer (after Dey et al. 2016).	21
Fig. 2.7. Design chart for normalized length of shear band and end zone for different stress ratios (after Dey et al. 2016).	22
Fig. 2.8. Failure process of a typical flowslide (after Locat et al. 2011).	23
Fig. 2.9. Factor of safety of each soil block of the cross-section of Beaver Creek flowslide (after Huag et al. 1977).	24
Fig. 2.10. Failure process of a typical spread (after Locat et al. 2011).	25
Fig. 2.11. Schematic representation of progressive failure through time: (a) geometry and failure surface; (b) soil behavior; (c) shear stress along failure surface; (d) total stress parallel to the failure surface (after Locat et al. 2011).	26
Fig. 2.12. The relations of available kinetic energy versus (a) retrogression and (b) run-out distances (after Thakur and Degago 2014).	29
Fig. 2.13. Typical failure in model test slopes for Turnagain Heights landslide (after Abbott 1996).	32
Fig. 2.14. Simulation of an idealized spread in a sensitive clay slope using CEL approach (after Dey et al. 2015).	35
Fig. 3.1. Geometry of the slope used in finite element modeling.	42
Fig. 3.2. Progressive failure in a typical flowslide (Case-5).	54

Fig. 3.3. Progressive failure in a typical spread (Case-20).	56
Fig. 3.4. Failure process in Cases 2 and 3: (a) 3 rd block failure in Case 2 (left) and Case 3 (right); (b) typical instantaneous velocity and shear band formation.	57
Fig. 3.5. Failure in Cases 4–6: (a) retrogression; (b) 3 rd soil block failure for $k = 0$ and 3.....	58
Fig. 3.6. Effects of large strain shear strength: (a) post-slide debris in Case 7; (b) instantaneous velocity of 5 th soil block failure for Case 5 (left) and Case 7 (right).	59
Fig. 3.7. Post-slide debris in the crater of Case 8.	61
Fig. 3.8. Development of failure planes up to 200 m from crest: (a) Case 10; (b) post-slide debris in the crater of Case 10; (c) Case 12; (d) Case 13.	63
Fig. 3.9. Development of failure planes up to 120 m from crest: (a) compound failure in Case 14; (b) spread in Case 15; (c) spread in Case 16; (d) no global failure in Case 17.....	65
Fig. 3.10. Failure in Case 18.....	66
Fig. 3.11. Formation of failure planes in Case 19.....	67
Fig. 4.1. Geometry of the slope used for seepage and in-situ stress analysis.	85
Fig. 4.2. Flowchart for seepage and in-situ stress simulation using Eulerian method.....	87
Fig. 4.3. Comparison of pore water pressure and shear stress obtained from Eulerian and Implicit analyses ($K_0 = 1.5$): (a) pore water pressure (kPa); (b) deviatoric stress (kPa).....	91
Fig. 4.4. Comparison of deviatoric stress between effective and total stress analyses for in-situ stress ($K_0 = 1.5$).....	92
Fig. 4.5. Shear band formation for varying K_0	97
Fig. 4.6. Instantaneous velocity of soil debris at 5 th rotational failure: (a) Case-1, considering strain-rate effects; (b) Case-5, without strain-rate effects.....	99
Fig. 4.7. Topography at the end of landslide: (a) Case-3, considering strain-rate effects; (b) Case-7, without strain-rate effects.	100
Fig. 4.8. Cross-section B-B' of Saint-Jude landslide: (a) Geometry and hydraulic conditions; (b) undrained shear strength profile (data from CPTU 32100 of Locat et al. 2017).....	101
Fig. 4.9. Seepage simulation of the cross-section B-B' of the Saint-Jude landslide: (a) pore water pressure (kPa); (b) Hydraulic gradient.....	102

Fig. 4.10. Comparison of FE simulated pore water pressure with field data.....	103
Fig. 4.11. Failure process of cross-section B-B'.....	105
Fig. 4.12. Failure process of cross-section C-C'.....	107
Fig. 4.13. Comparison of the topography after landslide: (a) cross-section B-B'; (b) cross-section C-C'.	108
Fig. 5.1. Geometry of the slopes used in finite element modelling.....	119
Fig. 5.2. Pseudostatic analyses of Slope-I using three FE modeling approaches.....	128
Fig. 5.3. Comparison of plastic shear strain at point A in Fig. 5.2(a).....	130
Fig. 5.4. Pseudostatic analyses of Slope-II using three FE modeling approaches.....	131
Fig. 5.5. Mesh size effects on FE results based on pseudostatic analyses of Slope-II.....	132
Fig. 5.6. Stress–strain behaviour used in FE modeling.....	133
Fig. 5.7. Acceleration–time histories of earthquake input motions used in numerical simulations.....	134
Fig. 5.8. Effects of non-reflecting outflow Eulerian boundary condition on FE results for the Parkfield earthquake.....	136
Fig. 5.9. Dynamic analysis using three FE modeling approaches for non-softening soil.....	138
Fig. 5.10. Dynamic analysis using three FE modeling approaches for strain-softening soil.....	141
Fig. 5.11. Horizontal toe displacement for Chi-Chi earthquake.....	143

LIST OF TABLES

Table 2.1. Summary of the geometric properties of the historical cases (after Demers et al. 2014).....	27
Table 3.1. Geometry and soil properties used for different cases.	49
Table 3.2. Soil parameters used in FE modeling.....	51
Table 4.1. Soil parameters used in FE modeling.....	96
Table 5.1. Geotechnical parameters used in finite element analyses.	123
Table 5.2. Calculated maximum toe displacement.....	144

LIST OF SYMBOLS

As the thesis is written in manuscript format, symbols used in this study are listed at the end of each chapter (Chapters 3–5).

Chapter 1

Introduction

1.1 General

Landslides in sensitive clays represent a major hazard in eastern Canada and Scandinavia. Such landslides could be catastrophic because they usually occur in a very short period and affect a large area, causing damage to the infrastructures and even sometimes affecting the local populations. Some notable landslides are the Saint-Jean-Vianney landslide in 1971 (Tavenas et al. 1971), Rissa landslide in 1978 (Gregersen 1981; L'Heureux et al. 2012), and Saint-Jude landslide in 2010 (Locat et al. 2017). In eastern Canada, large-scale landslides occur in clayey soils deposited in the postglacial seas of Québec and Ontario. The marine limits of the ancient Champlain, Laflamme, and Goldthwait seas represent a total land area of approximately 76,000 km² and inhabited by 89 % of the population of the province of Québec (Demers et al. 2014). A total of 108 historical retrogressive landslides were recorded from 1840 to 2012, where the affected area of a landslide varied from 0.3 to 447 ha, with 19 cases exceeding 10 ha (Demers et al. 2014).

According to the classification of Tavenas (1984) and Karlsrud et al. (1984), there are four main types of landslides in sensitive clays in eastern Canada and Scandinavia: 1) single rotational slide, 2) flowslide (sometimes described as earthflow), 3) translational progressive landslide, and 4) spread. In flowslides and spreads, the failure initiates from slope toe and develop into the intact slope, which are classified as retrogressive landslides. On the other hand, in a translational landslide the failure occurs in upslope area and develops towards the slope toe, which is commonly classified as a progressive failure. Flowslide, spread and a combination of both are the most common types of large retrogressive landslides in eastern Canada (Fortin et al. 2008), while translational progressive landslides are often observed in Scandinavia (Bernander 1978, 2000,

2008). There are also large landslides described as flake-type landslide (e.g. the Rissa landslide in Norway (Gregersen 1981)). In the Province of Québec, Canada, 57 % of the large landslides are classified as flowslide, 38 % are classified as spread, and the remaining 5 % are a combination of both or unidentified types (Demers et al. 2014). Such landslides could be triggered by a variety of factors such as natural causes (e.g. river erosion, rainfall and earthquake) and human activities (e.g. placement of fill and blasting). Figure 1.1 shows the 2010 Saint-Jude landslide (spread) triggered by the combined effect of river erosion and high artesian pressure close to the river channel (Locat et al. 2017), and the Notre-Dame-de-la-Salette (flowslide) and Mulgrave & Derry (spread) slides triggered by the 2010 Val-des-Bois earthquake (Perret et al. 2013).

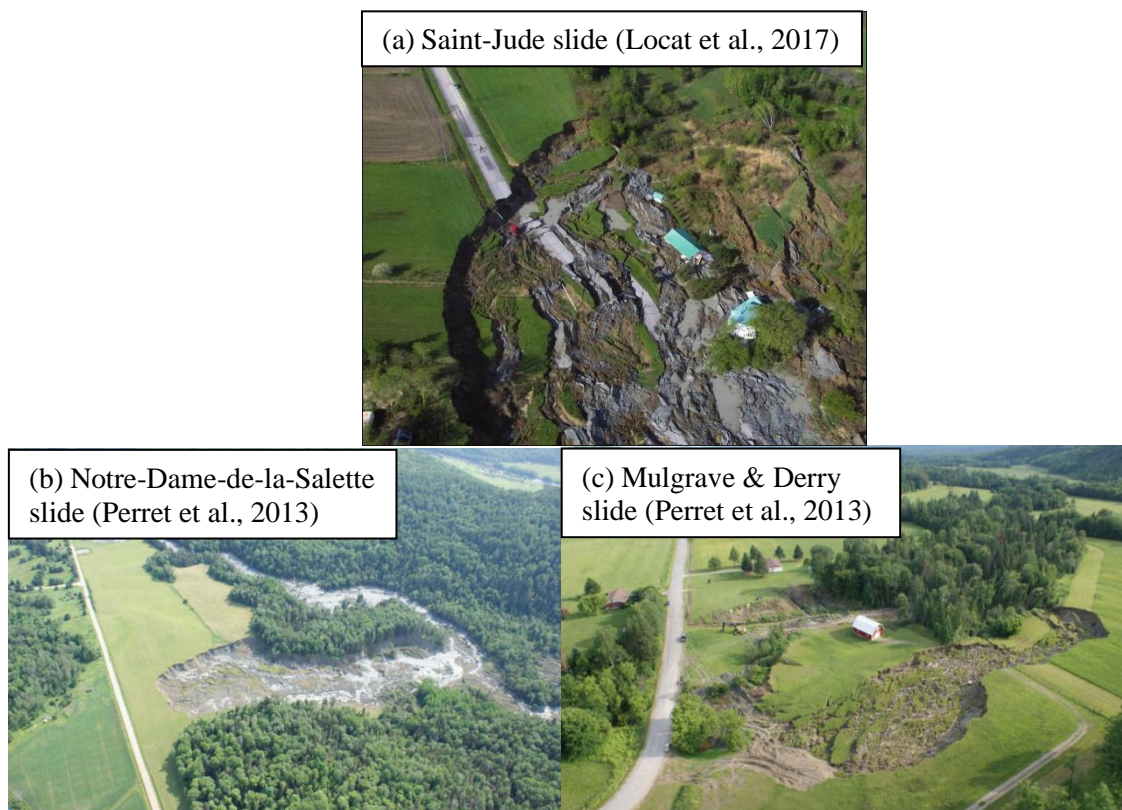


Fig.1.1. Landslides in sensitive clays triggered by toe erosion and earthquake: (a) Saint-Jude landslide (after Locat et al. 2017); (b) Notre-Dame-de-la-Salette landslide (after Perret et al. 2013); (c) Mulgrave & Derry landslide (after Perret et al. 2013).

In the past few decades, considerable progress has been made on understanding the potential causes and failure mechanisms of landslides in sensitive clays. The strain-softening behavior of the soil is one of the main causes of large-scale landslides in sensitive clays. The sensitive clays in eastern Canada and the quick clays in Scandinavia usually have a very high sensitivity (intact to residual shear strength ratio). This kind of soil tends to lose strength rapidly when subjected to excessive shear strains. Once the failure occurs, the sensitive clay liquefies and causes the adjacent intact soil to fail successively.

The shear band propagation is a unique characteristic of landslides in sensitive clays. The mechanisms of shear band propagation in sensitive clay slopes have been investigated in previous studies. Skempton (1964) and Bjerrum (1967) studied the progressive failure of overconsolidated clays, which can be adopted to explain the retrogressive/progressive failure in sensitive clay landslides. The criteria for shear band propagation in brittle materials have been analytically studied using the concept of fracture mechanics (Palmer and Rice 1973; Quinn et al. 2012) and energy balance approach (Puzrin and Germanovich 2005). Moreover, the failure mechanisms of different types of landslides have been explained conceptually or analytically. For example, Tavenas (1984) discussed the characteristics of the slopes susceptible to successive rotational slide; Bernander and his co-workers (Bernander et al. 1988) interpreted the mechanism of translational slides; and the failure mechanism and features of spreads were conceptually introduced by Cruden and Varnes (1996) and analytically analyzed by Locat et al. (2011).

Numerical simulation techniques have also been utilized to study landslides in sensitive clays. Quinn et al. (2012) studied the length and the shear stress distribution along the shear band caused by toe erosion using a finite element program. Locat et al. (2013) performed numerical modeling using PLAXIS 2D and BIFURC FE programs (Jostad and Andresen 2002) to study the

mechanism of quasi-horizontal shear band formation in a sensitive clay slope. The shear stress distribution on the propagating shear band and the active failures in the soil layer overlying the pre-defined failure surface were predicted. Dey et al. (2015) adopted an advanced LDFE method based on a Eulerian approach that can simulate the large strain localization on the shear band. The failure pattern of a spread was successfully simulated in terms of shear band formation and soil mass dislocation during the landslide.

1.2 Research Focus

Landslides in sensitive clays have been investigated by many geologists, geophysicists and geotechnical engineers. A number of case studies of the relic and recent landslides from Norway, Sweden and eastern Canada were identified and summarized in the literature, which provides a preliminary idea of the landslides in sensitive clays. Those studies were focused on the information relating to morphology, soil characterization, potential triggering factors and failure mechanisms. However, evaluating the stability of a sensitive clay slope and estimating the dimensions of a potential landslide is still a challenging task.

The present study is focused on understanding the failure mechanisms involved in the retrogressive landslides in sensitive clays and the factors that influence the failure pattern and dimensions of a landslide.

A Eulerian-based LDFE method is used in this work to numerically study the behavior of slopes in sensitive clays. The numerical simulation could be a strong tool for analyzing large-scale retrogressive landslides, due to the difficulty of monitoring the failure process of such landslides in real time. Most of the information on the characteristics and features of such landslides is obtained by comparing the field investigations before and after the landslide, while the numerical simulation can reveal the whole failure process of the landslides from initiation to post-failure.

However, the traditional FE methods based on Lagrangian approach can hardly be used for simulating retrogression of landslides where extremely large plastic strains localize in narrow shear bands and failed soil debris undergoes a large displacement. The Lagrangian-based FE methods may suffer mesh distortion and non-convergency when simulating large deformation problems (Griffiths 1999). In the Eulerian-based LDFE method used in the present study, the soils are modeled as Eulerian materials that can “flow” through the Eulerian meshes to avoid mesh distortion. This numerical method has been adopted in the previous studies to study retrogressive landslides, and it successfully captured the key features of onshore and offshore large retrogression/progression landslides (Dey et al. 2015, 2016; Islam et al. 2019; Wang et al. 2019).

The first task of this work is to study the factors influencing the failure pattern and dimensions of a landslide, because this is a crucial task for risk management of landslides in sensitive clays. Large uncertainties exist in the current approaches for the prediction of landslide retrogression based on empirical approaches and statistical data of historical landslides. Utilizing the LDFE method, the impact of the parameters on the failure pattern and dimensions of a landslide can be systematically studied. More importantly, the numerical results can reveal the whole failure process and the failure mechanisms of the studied slopes.

Secondly, simulating techniques for the Eulerian LDFE method are developed to overcome some of its limitations. For example, only single-phase material can be simulated in the Eulerian approach, so the seepage in the soil are difficult to be simulated. Thus, a technique is developed to simulate the effects of seepage on the in-situ stress condition of a slope and the subsequent failures.

Thirdly, efforts have been made to extend the application of the Eulerian LDFE method. In Canadian sensitive clays, most of the landslides have been triggered by toe erosion and/or human activities. However, earthquakes are the main cause of very large landslides (Desjardins 1980;

Aylsworth and Lawrence 2003; Locat et al. 2011; Brooks 2013; Perret et al. 2013; Demers et al. 2014). Therefore, understanding the mechanisms of sensitive clay landslides triggered by different factors has significant importance. Numerical modeling techniques are developed to simulate slope failures triggered by earthquakes using the LDFE method, including setting up proper boundary conditions, introducing the earthquake excitation and simulating the post-failure process of the slope.

1.3 Objectives

The main purpose of the present study is to understand the failure mechanisms involved in large-scale landslides in sensitive clays using a Eulerian-based LDFE numerical method that can rationally simulate the large deformation nature of such landslides. Utilizing the numerical tool, the factors that affect the failure pattern and the dimensions of the landslides are systematically studied. The LDFE numerical method also shows advantages over the traditional FE methods for simulating large-scale landslides triggered by earthquakes. The main objectives of this research include:

- Utilize a Eulerian-based dynamic LDFE modeling tool that can simulate the whole process of sensitive clay landslides, including soil mass displacement, shear bands propagation, and debris run-out.
- Investigate the factors that may influence the failure pattern and retrogression distance of a landslide. The factors such as stability number (N_s), undrained shear strength profile of the slope, sensitivity (S_t), remolded energy of the soil (E_R) and geometry of the slope and the opposite riverbank are studied.
- Develop a constitutive model of sensitive clay in the LDFE modeling tool. The soil model for sensitive clay reflects the strain-softening and strain-rate dependent behaviors of the soil

under monotonic loading in an undrained condition. Additionally, the material damping of the soil under cyclic loading is considered in the numerical simulation.

- Develop a modeling technique based on the LDFE method to rationally simulate the initial in-situ stress of the slope before failure, which considers the valley formation process, seepage and at-rest earth pressure coefficient (K_0) of the soil layer.
- Develop a large deformation FE modeling technique for pseudo-static and dynamic seismic stability analyses of soft clay slopes. The dynamic responses of clay slopes during earthquake and post-quake stages are studied comprehensively.
- Simulate a real case of a landslide in sensitive clay (the 2010 Saint-Jude landslide) using the developed numerical method. The numerical results are compared with the field investigation results. The simulation of the real case shows the advantages of the numerical tool used in the present study, which also verifies some findings on the mechanisms of landslides in sensitive clays as presented in this study.

1.4 Thesis Organization

This thesis is prepared in manuscript format. The outcome of the study is presented in six chapters and two appendices. This first chapter describes the background, motivations, scope, and objectives of the present study.

Chapter 2 presents a general literature review. As the thesis is prepared in manuscript format, the problem-specific literature reviews are provided in Chapters 3–5 and Appendices I–II.

Chapter 3 presents the effects of the geometric and geotechnical parameters on the failure mechanisms and retrogression distance of a sensitive clay slope. A constitutive model of the sensitive clay that considers the strain-softening and strain-rate effects on the undrained shear strength is discussed in this chapter. This chapter has been submitted as a technical paper for

publication to a journal, and a part of this study has been published earlier as a conference paper (Wang et al. 2017 in Appendix-II).

Chapter 4 presents the development of a modeling technique in the Eulerian-based LDFE method to rationally simulate the stress distribution in a natural slope near a riverbank. The modeling technique is used to study K_0 and strain-rate effects on the failure pattern of the slope. Furthermore, the failure process of the 2010 Saint-Jude landslide is simulated. This chapter has been submitted as a technical paper for publication in a journal, and a part of this study has been published earlier as a conference paper (Wang et al. 2016 in Appendix-I).

Chapter 5 presents an FE model development for pseudo-static and dynamic analyses of clay slopes. Dynamic FE analyses of sensitive clay slope failure due to earthquake loadings are discussed in this chapter. The content of this chapter is prepared as a journal paper published in *Soil Dynamics and Earthquake Engineering* (Wang et al. 2019). In addition, the author of this thesis worked together with another graduate student on earthquake-induced sensitive clay landslides. The work has been published as: Islam, N., Hawlader, B., Wang, C. and Soga, K. (2019). Large deformation finite-element modelling of earthquake-induced landslides considering strain-softening behaviour of sensitive clay. *Canadian Geotechnical Journal*, 56: 1003–1018. The author's contribution to this paper is primarily on parametric study and preparation of the manuscript; more specifically, the finite element analysis of the effects of strain-softening parameters on failure (pp. 1010–1012 of the paper).

Chapter 6 presents the general conclusions of the thesis and recommendations for future studies. However, the problem-specific conclusions are provided at the end of each chapter (Chapters 3–5) along with appendices (Appendices I–II). The references cited in Chapters 1 and 2 are listed in the “Reference” chapter at the end of the thesis.

Chapter 2

Literature Review

2.1 General

Evaluating the risk of landslides in sensitive clays involves many subjects, such as understanding the behavior of sensitive clays under different loading conditions, comprehending the mechanisms of successive failures of the soil mass, estimating the dimensions of a potential landslide and so on. A comprehensive review of the studies on landslides in sensitive clays is presented in this chapter. No attempt is made to present a complete bibliography of all research; rather a more selective overall summary of research with the greatest relevance to the current study is presented.

This chapter is organized based on different aspects of the studies on landslides in sensitive clays. Section 2.2 introduces the soil properties of sensitive clays. This type of study mainly focuses on the stress–strain behavior of sensitive clays under monotonic and cyclic loading obtained from in-situ and laboratory tests (Bjerrum and Landva 1966; Tavenas et al. 1983; Bernander 2000; Locat et al. 2015; Lefebvre and LeBoeuf 1987). Section 2.3 focuses on the mechanisms of progressive failure in brittle materials, which is one of the most fundamental mechanisms of large retrogressive landslides in sensitive clays, especially for spreads. Previous researchers developed both analytical (Palmer and Rice 1973; Puzrin and Germanovich 2005) and numerical (Quinn et al. 2012; Zhang et al. 2015, 2016) methods to explain the mechanisms of progressive failure in strain-softening materials. Section 2.4 introduces the mechanisms of different types of landslides. This topic has been well discussed by previous researchers (Bjerrum 1955; Mollard and Hughes 1973; Mitchell and Markell 1974; Carson 1977; Tavenas 1984; Cruden and Varnes 1996; Bernander 2000, 2008; Locat et al. 2011, 2013). Some of them also discussed

the triggering factors. Section 2.5 is concentrated on slope failure subjected to dynamic loading. Recent studies show that vibrations from blasting (e.g. Johansson et al. 2013) and from an earthquake (e.g. Perret et al. 2011) can trigger landslides in sensitive clays. However, the studies on dynamic load triggered landslides in sensitive clays are limited, and the studies mainly focused on field investigation of the post-failure landslides (Perret et al. 2011, 2013). Finally, Section 2.6 introduces large deformation numerical modeling (LDFE) methods. In recent years, large LDFE methods such as Arbitrary Lagrangian-Eulerian (ALE) method (Nazem et al. 2008, 2009) and Coupled Eulerian-Lagrangian (CEL) method (Benson 1992, 2004) are becoming popular in simulating large deformation geotechnical problems. Some researchers have performed comprehensive analyses on both onshore and offshore landslides in sensitive clays using LDFE methods (Dey et al. 2015, 2016a,b; Trapper et al. 2015; Wang et al. 2017).

2.2 Behavior of Sensitive Clay in Undrained Condition

2.2.1 Strain-softening behavior of sensitive clay

Both sensitive clays in eastern Canada and quick clays in Scandinavia show dramatic strain-softening behavior under the undrained loading condition, which means these types of soil tend to lose their strength rapidly when subjected to excessive shear loading. It is widely accepted that the strain-softening behavior of sensitive/quick clays is one of the main causes of retrogressive/progressive landslides. Previous researchers have performed laboratory tests (e.g. triaxial test, direct simple shear test and ring shear test) and in-situ field tests (e.g. CPTU and vane shear test) to understand the mechanism of the strain-softening behavior of sensitive/quick clays (Locat et al. 2015, 2017).

Bjerrum (1961) suggested the concept of friction softening and cohesion softening in the failure mechanism for soft sensitive clays and loose sands. He related an increase in pore pressure

to increasing strain, which may cause a decrease in the post-peak shear strength as a result of diminished effective stress in soft clays. Janbu (1985) suggested that the effective shear strength parameters, ϕ' and c' , of soft sensitive clays are unique and independent of whether the clays are loaded under drained or undrained conditions and whether the soil is at its peak or post-peak state. Recently, Bernander (2000), Thakur et al. (2005), Thakur (2007, 2011), Jostad et al. (2006) and Gylland et al. (2012) specified that the post-peak shear strength reduction in soft sensitive clays is governed by shear-induced pore pressure rather than by a reduction of the values of the strength parameters (ϕ' and c'). Based on these studies, an idealization of undrained strain softening is presented, as shown in Fig. 2.1 where the undrained effective stress path (ESP) follows a unique failure line when subjected to undrained shearing (Thakur et al. 2014). The resulting undrained strain-softening is related to the increasing shear-induced pore pressure p_w and thereby diminishing effective stress. Note that reductions in ϕ' and c' are possible when sensitive clays are subjected to very large strains, which is evidenced in constant volume ring shear test results on low sensitive Drammen plastic clay (Stark and Eid 1994). Stark and Contreas (1996) further suggested that a complete residual (remolded) state may occur when the specimen is sheared to several hundred millimeters, corresponding to several hundred percent shear strain in the soil specimen.

Locat et al. (2015) performed five triaxial undrained compression tests (CU) and three direct simple shear tests (DSS) on specimens from the 1992 Sainte-Monique landslide areas. The specimens for DSS tests were collected from the intact clay next to the landslide crater at the depths of 13.45 m, 13.48 m and 13.63 m, respectively. The specimens were consolidated to the vertical effective stress of about $0.64\sigma'_p$, and the at-rest earth pressure coefficient K_0 was maintained during consolidation. The critical state line of the sensitive clay was determined from the DSS test. The measured friction angle ϕ' and cohesion c' were 29.5° , and 4.8 kPa, respectively. The stress–strain

behavior and the stress paths from three DSS tests consolidated under 93 kPa are presented in Fig. 2.2. An average peak shear strength of 38.3 kPa was reached at 1.7 % to 4.5 % strain in the three tests. The average large-deformation strength, obtained at a strain of about 30%, was ~19.5 kPa (~50 % of the peak shear strength). The undrained effective stress paths of the three DSS tests followed a unique failure line between 7–30 % strain, which agreed with the hypothesis that the post-peak shear strength reduction in soft sensitive clays is governed by shear-induced pore pressure rather than a reduction of the values of the strength parameters (Bernander 2000; Thakur et al. 2005; Jostad et al. 2006; Thakur 2007, 2011; Gylland et al. 2012).

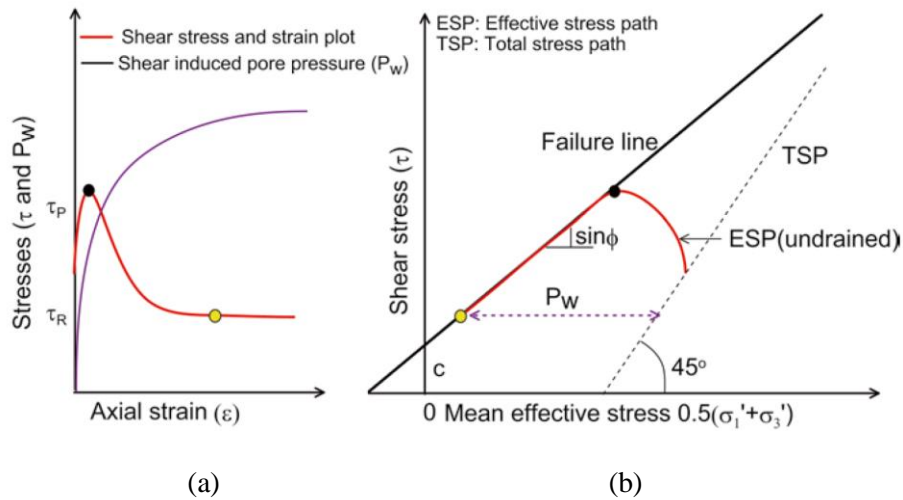


Fig. 2.1. Idealized undrained strain-softening of soft sensitive clays at laboratory strain level: (a) Stress-strain relation; and (b) Stress path (after Thakur et al. 2014).

The strain level of laboratory tests can barely be compared to the magnitude of large strains in the field. Swedish fall cone tests show that Canadian sensitive clays could have a remolded undrained shear strength s_{ur} less than 1.5 kPa (Demers et al. 2014; Locat et al. 2015, 2017). A couple of meters of shear displacement is required to remold the soil to reach such a strength level (Quinn et al. 2011). Bernander (2000) argued that post-slide investigations do not show the relevance of completely remolded shear strength s_{ur} and, therefore, recommended an undrained

shear strength s_{uR} ($> s_{ur}$) for progressive failure analysis that mobilizes in the shear band as a result of considerable shear displacement.

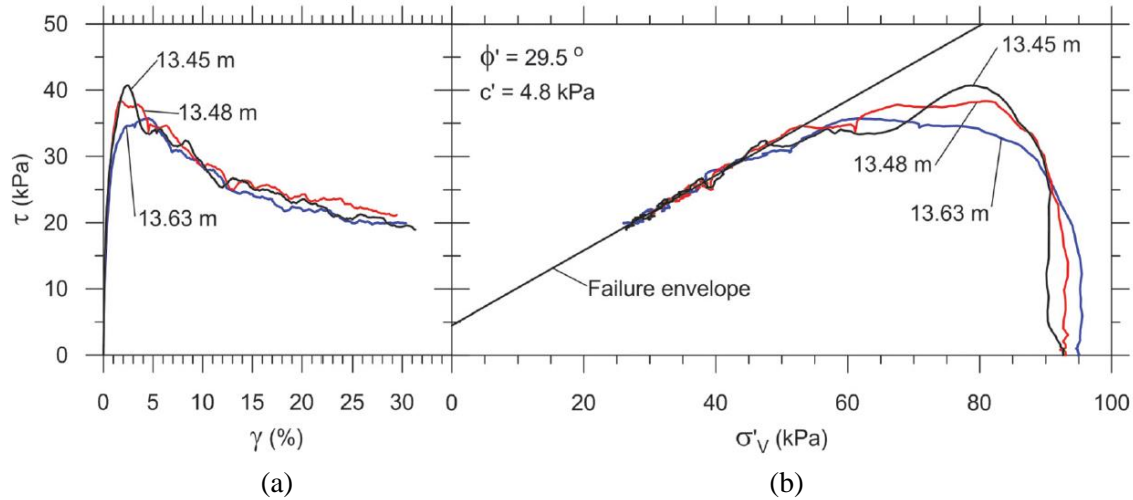


Fig. 2.2. DSS test results of sensitive clay: (a) Stress–strain behavior; and (b) Stress paths (after Locat et al. 2015).

In engineering practice, it is difficult to determine the variation of the pore pressure during a landslide. Therefore, the undrained shear strength s_u in terms of total stress is widely used to represent the strength of sensitive clays. The strain-softening behavior of sensitive clays is usually described as the undrained shear strength reduction with plastic shear strain. Lo (1972) proposed a hyperbolic relationship between post-peak shear strength and accumulated strain. Other researchers (e.g. Palmer and Rice 1973; Puzrin and Germanovich 2005; Quinn et al. 2011) used a simple linear relationship for modeling shear band formation and progressive failure for overconsolidated and sensitive clays under drained and undrained conditions. Tavenas et al. (1984) conducted undrained shear strength tests on typical eastern Canadian marine clays of various levels of sensitivity and overconsolidation ratio (OCR), which provide some basis for modeling post-peak behavior. Their study shows that the normalized shear strength (defined in term of the remolding index, I_r) decreases with strain energy w_N . Quinn et al. (2011) converted the I_{r-wN}

curves of Tavenas et al. (1984) to stress–displacement relationships, as shown in Fig. 2.3. Note that the shapes of the undrained post-peak softening behavior of sensitive clays in these cases are not linear. Therefore, it opens a scope to do further research to model the post-peak softening curve properly and incorporate that non-linear behavior in progressive failure analysis. Einav and Randolph (2005) proposed an exponential relationship between the mobilized undrained shear strength and plastic shear strain, and the relationship was adopted in other analyses (e.g. Dey et al. 2015; Zhang et al. 2015).

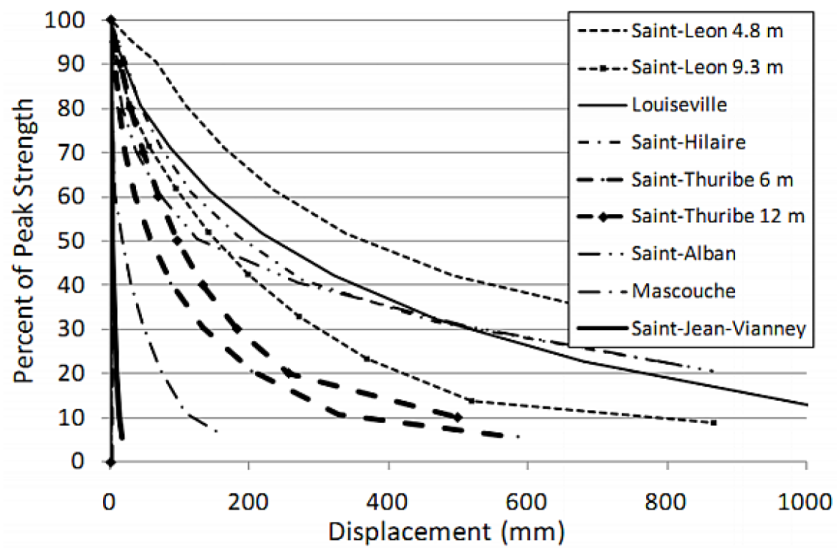


Fig. 2.3. Normalized stress versus displacement for Champlain clay samples (after Quinn et al. 2011).

2.2.2 Strain-rate effects of sensitive clays

Similar to other clayey soils, the behavior of sensitive clays is highly affected by the loading rate. Vaid et al. (1979) performed one-dimensional consolidation tests and isotropic consolidation triaxial tests on heavily consolidated Saint-Jean-Vianney (SJV) clay. The test results show that both the compressibility and the undrained shear strength of the SJV clay are profoundly influenced by the time effects. Slow rates of strain resulted in large reductions in pre-consolidation pressure and increased compressibility. The undrained shear strength is also lowered under low

strain-rate. The test results of Vaid et al. (1979) agreed with the other studies on Leda clays showing that the undrained shear strength of the soil increases about 6–12 % for a 10-fold increase in rate of strain (Crawford 1959, 1963, 1965; Coates and McRostie 1963; Conlon 1966).

Graham et al. (1983) summarized the laboratory tests on a wide variety of lightly overconsolidated natural clays (most of them eastern Canadian sensitive clays), showing that the undrained shear strength and pre-consolidation pressure are time-dependent. However, the strain-rate effect is largely independent of the overconsolidated ratio, plastic index, and the test type. They then claimed that the same magnitudes of strain-rate effect should also apply to in-situ vane shear tests.

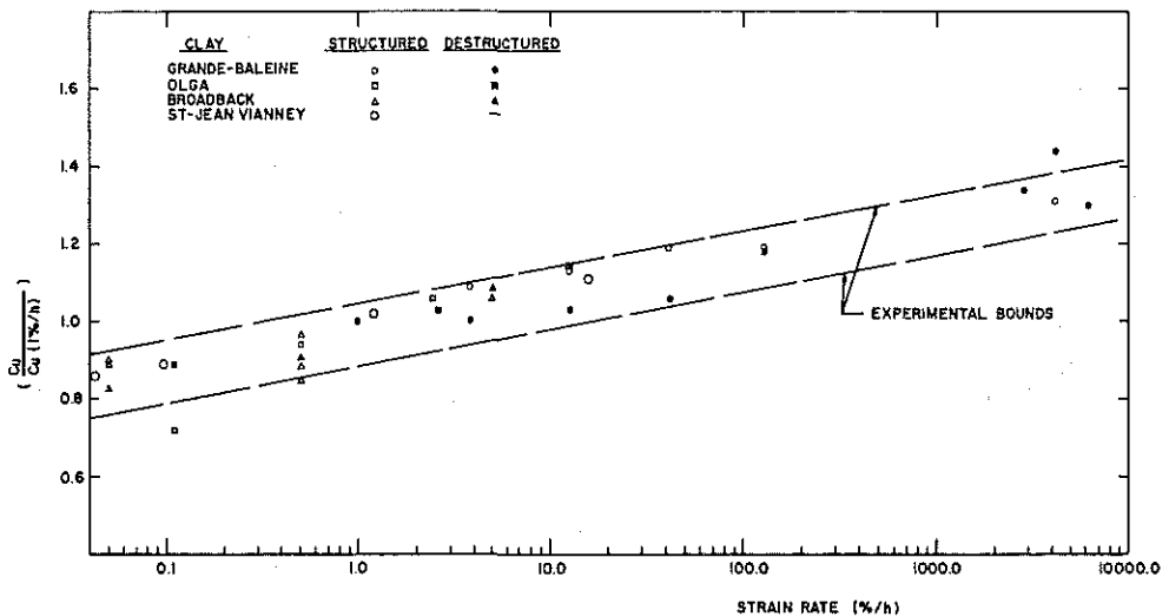


Fig. 2.4. Change in undrained shear strength ratio with strain rate (after Lefebvre and LeBoeuf 1987).

Lefebvre and LeBoeuf (1987) performed a series of monotonic and cyclic triaxial tests on three undisturbed eastern Canadian sensitive clay samples. In the monotonic strain-controlled triaxial compression tests, the strain rates varied from 0.05–132.0 %/h, while in the stress-controlled tests, strain rates of up to about 6000 %/h were used, which are equivalent to frequencies

of 1–2 Hz, typically applied in cyclic tests. They found that the effect of strain rate on the undrained shear strength of structured (overconsolidated) and destructured (normally consolidated) clays are fundamentally different. For normally consolidated clays, the effect is related to the pore pressure generation, and the failure envelope is more or less unique. For overconsolidated clays, the pore pressure generated at a given deviatoric stress is practically independent of the strain rate; however, the effective strength envelope appears to be lowered with a decreasing rate of strain as a result of fatigue. Despite the difference in the mechanics, their experimental data indicate a linear s_u/σ'_{vc} or s_u/σ'_p relationship for both normally and overconsolidated clays for five log cycles of strain rate. The gain in strength for the 1.0–10.0 %/h cycle varies from 7–14 % and is, on the average, very close to 10 %, as shown in Fig. 2.4.

Two frameworks have been developed to describe the strain rate effects: a geotechnical framework and a fluid dynamics framework. The geotechnical framework expresses the strain rate effect in terms of the soil shear strength. A semi-logarithmic relation expressed as Eq. (2.1) is commonly used in the geotechnical framework:

$$s_u = \left(1 + \mu \log \frac{\dot{\gamma}}{\dot{\gamma}_{ref}} \right) s_{u,ref} \quad (2.1)$$

where $\dot{\gamma}$ is the shear strain rate; $s_{u,ref}$ is the shear strength at the reference shear strain rate $\dot{\gamma}_{ref}$; μ is a coefficient that gives the proportional change in shear strength for each order of magnitude change in strain rate, lying in the range of 0.05–0.2 (Dayal and Allen, 1975; Graham et al. 1983; Biscontin and Pestana, 2001).

Biscontin and Pestana (2001) and Peuchen and Mayne (2007) performed vane shear tests using a wide range of rotation rates (over 9 orders of magnitude). They found that the strain rate

dependency of s_u can be better captured by a power law expressed as Eq. (2.2), with values of β in the range of 0.05–0.1.

$$s_u = \left(\frac{\dot{\gamma}}{\dot{\gamma}_{\text{ref}}} \right)^\beta s_{u,\text{ref}} \quad (2.2)$$

On the other hand, the fluid dynamics framework considers the soil as fully fluidized and applies fluid mechanics principles in modeling the soil and estimating the resulting forces. The behavior of clay debris flows can be described using the Herschel–Bulkley model, which is one of the simplest viscoplastic models and combines both plastic and shear-thinning effects (Deglo de Besses et al. 2003). The Herschel–Bulkley law can be written as follows:

$$\begin{cases} \dot{\gamma} = 0 & \text{for } |\tau| \leq \tau_0 \\ |\tau| = \tau_0 + K|\dot{\gamma}|^n & \text{for } |\tau| > \tau_0 \end{cases} \quad (2.3)$$

where τ is the shear stress; $\dot{\gamma}$ is the shear strain rate. When $n = 1$, Eq. (2.3) reduces to a Bingham fluid, giving a linear relation of the shear stress with shear strain rate, and K equals the fluid dynamic viscosity, μ .

During the process of a landslide, the sensitive clay initially fails from an intact block of material. As the soil debris displaces downslope for a long distance, the sensitive clay debris usually severely liquefies, which can be considered as Bingham or other non-Newtonian fluids. As such, two different frameworks (i.e. geotechnical and a fluid dynamics framework) are required to separately characterize the strength of debris material, as it evolves from the original soil into a viscous fluid. Zhu and Randolph (2011) proposed an additive power-law model (Eq. (2.4)):

$$s_u = \left[1 + \eta \left(\frac{\dot{\gamma}}{\dot{\gamma}_{\text{ref}}} \right)^\beta \right] s_{u0} \quad (2.4)$$

where η is a viscous property, β is the shear-thinning index and s_{u0} is the minimum undrained shear strength at a low strain rate. The reference undrained shear strength (at $\dot{\gamma}_{ref}$) is given by

$$s_{u,ref} = (1 + \eta)s_{u0} \quad (2.5)$$

Equation (2.4) originates from the power-law model but includes an additive item in a similar manner to the Herschel–Bulkley model, which can be adopted to characterize the strength behavior of both soil and fluid-like materials.

2.3 Shear Band Propagation in Brittle Materials

Due to the strain-softening behavior of sensitive clays, the plastic strain localizes in very narrow shear bands during failure. Shear band propagation is one of the fundamental mechanisms of large retrogressive landslides in sensitive clays.

Palmer and Rice (1973), hereafter designated as PR, derived the conditions for the propagation of a concentrated shear band in overconsolidated clays using fracture mechanics, namely the J -integral. An important advantage of this approach is that it treats the failure in the soil as a process of shear band propagation rather than assuming that the failure occurs instantly. Assume a shear band locates in x_1x_2 plane shown in Fig. 2.5. Let Γ be a curve which starts at a point P- on the lower surface of the shear band, goes around the tip of the band, and ends at a point P+ on the upper surface, where P+ and P- coincide in the unstrained reference state. The J -integral is defined by:

$$J_P = \int_{\Gamma} \left[(W - f_i u_i) dx_2 - T_i \frac{\partial u_i}{\partial x_i} ds \right] \quad (2.6)$$

where W is the strain energy; f_i is the components of body force per unit volume; u_i is the components of displacement; T_i is the surface tractions across Γ ; and ds is the element of arc length of Γ . This integral is useful because its value is independent of the path of integration Γ and

depends only on the points P+ and P-. Thus, one can define the path Γ following the lower surface of the band from P- to the tip of the band, and return to P+ along the upper surface (e.g. P- \rightarrow T \rightarrow P+ in Fig. 2.5). In such a particular path, Eq. (2.6) can be simplified as the following equation considering the strain-softening behavior of clay:

$$J_P - \tau_r \delta_P = \int (\tau - \tau_r) d\delta \quad (2.7)$$

where τ_r is the residual shear strength of clay; δ_P is the relative shear displacement at point P; and τ is the modified shear strength at any shear displacement δ . The $J_P - \tau_r \delta_P$ can be interpreted as the energy surplus made available per unit area of advance of the band; this surplus is the excess of the work input of the applied forces over the sum of the net energy absorbed in deforming material outside the band and the frictional dissipation against the residual part of the slip resistance τ_r within the band. Furthermore, Eq. (2.7) indicates that, for propagation to occur, the net energy surplus must just balance the additional dissipation in the end region against shear strengths in excess of the residual.

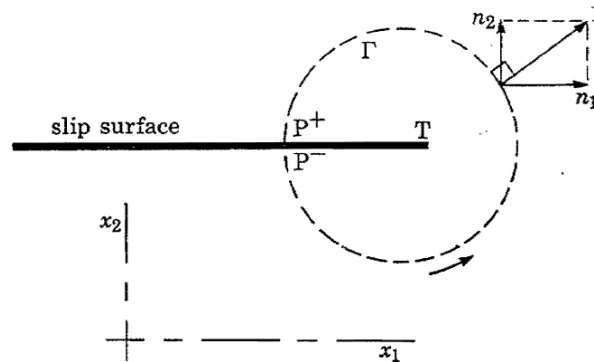


Fig. 2.5. Integration path for the J -integral (after Palmer and Rice 1973).

Puzrin and Germanovich (2005) attempted to apply the PR fracture mechanics approach to shear band propagation in sands and normally consolidated clays. To overcome the limitation of the PR approach, that the strain energy in the soil must be independent of the strain path, Puzrin

and Germanovich (2005) considered the non-elastic soil properties in their study. A simple problem of the shallow shear band propagation in an infinite slope has been studied using three approaches. In addition to the PR fracture mechanics approach, the limit equilibrium and energy balance approaches have been discussed.

In the limit equilibrium approach, the process of the shear band propagation is not considered. Instead, the forces on the potential sliding block are considered, and the factor of safety is simply calculated as the ratio between the resisting and sliding forces. The critical length of the shear band can be obtained by letting the resistance equal the sliding forces (e.g. $F_s = 1$).

In the energy balance approach, the elasto-plastic property of the soil under tension and compression conditions are considered. Puzrin and Germanovich (2005) derived the energy balance criterion for the shear band propagation. The criterion requires that the energy surplus produced in the body by incremental propagation of the shear band should exceed the work required for this incremental propagation. Mathematically, it can be expressed as the following inequality:

$$\Delta W_e - \Delta W_i - \Delta D_1 \geq \Delta D_w \quad (2.8)$$

where W_e is the external work made on the soil layer above the shear band; W_i is the internal work made by the normal stresses acting parallel to the slope surface on deformations of the layer caused by changes in these stresses; D_1 is the plastic work dissipated on the shear band, which is required to overcome the residual shear resistance along the band; and D_w is the plastic work dissipated in the shear band during its propagation, which is required to overcome the shear resistance in excess of the residual shear strength in the end zones of the band. Then, the critical length of the shear band l_{cr} can be derived.

parameters required for the analysis are slope angle, location of the weak zone and shear strength properties of the soils.

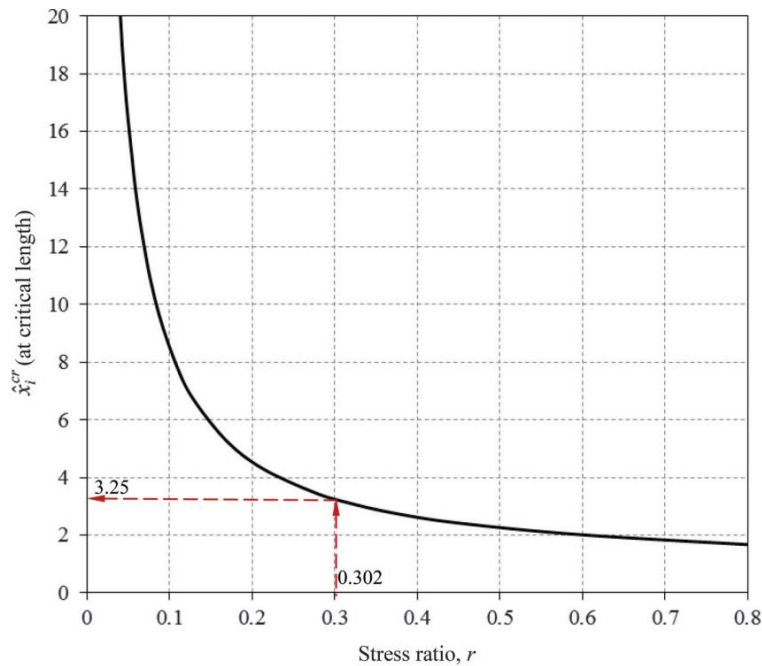


Fig. 2.7. Design chart for normalized length of shear band and end zone for different stress ratios (after Dey et al. 2016).

2.4 Failure Mechanisms of Sensitive Clay Landslides

Flowslide and spread are the two most common types of landslide in eastern Canada. This section is focused on introducing the failure mechanisms and the factors that affect the retrogression and run-out distances of these two failure types.

2.4.1 Failure mechanism of flowslide

In a typical flowslide, multiple retrogressive slides occur successively, triggered by the first local failure. The soil debris becomes highly remolded and flows out of the crater, leaving an unstable scarp. A second slide may then occur in the remaining slope behind the scarp, and the remolded clay also flows out of the crater, generating another unstable scarp. This process can continue until a final stable backscarp is formed and the retrogression stops (Fig. 2.8). This type

of landslide is characterized by an empty crater (minimal debris is left in the crater after downslope movement), and in some cases having a bottle-neck shape. Tavenas (1984) stated that this type of failure tends to occur when three conditions are met: i) an initial slide has occurred; ii) the potential energy is high enough to remold the clay effectively, which can be expressed as $\rho g H > X s_{u0}$, where ρg is the unit weight of the soil, H is the height of the slope, X varies between 3 and 8 with a tendency to increase with plasticity, and s_{u0} is the intact undrained shear strength (Leroueil et al. 1996); iii) the remolded clay has to be liquid enough to flow (i.e. liquidity index higher than 1.2 or remolded shear strength lower than 1 kPa).

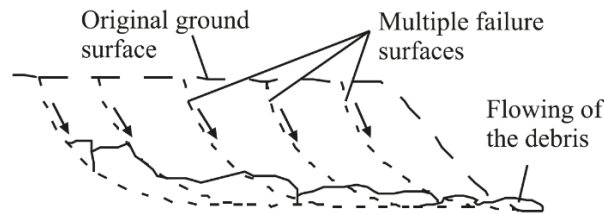


Fig. 2.8. Failure process of a typical flowslide (after Locat et al. 2011).

The mechanism of a flowslide is straightforward. A series of rotational slides occur successfully after the first local failure. Therefore, the conventional limit equilibrium method might be adopted to analyze slope stability with some additional assumptions. Huag et al. (1977) analyzed the flowslide at Beaver Creek, Saskatchewan, Canada. Their methodology of simulating the retrogressive failure was to break the slide into a series of slide blocks. The blocks can then be analyzed to determine their stability. The key to their analysis of this type of failure is to understand or simulate the relationship that exists between the sliding blocks. In their analysis, they adopted the assumption which was proposed by Thomson and Hayley (1974): the horizontal velocity of the soil mass increases with proximity to the river, which leads to slide blocks having a small restraining effect on the following blocks. The stability of each slide block was analyzed using the simplified Bishop method, by adopting the residual shear strength of the clay, since field

observations indicated very large displacement along failure surfaces. As can be seen in Fig. 2.9, a series of critical slip circles and the corresponding factors of safety were analyzed with the method described above. The authors found the factors of safety of all the slide blocks were all less than one.

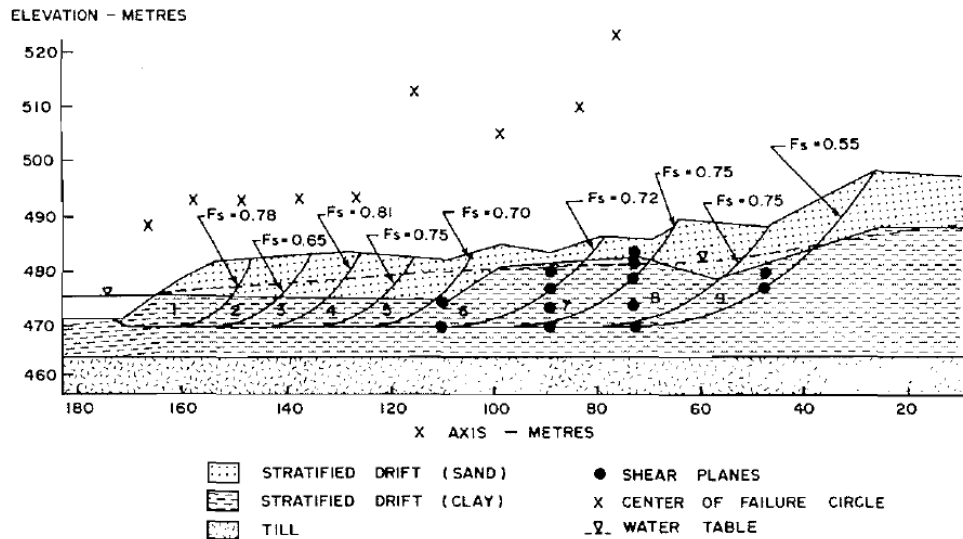


Fig. 2.9. Factor of safety of each soil block of the cross-section of Beaver Creek flowslide (after Huag et al. 1977).

In the analysis of the slides, the leading block was considered to be moving faster than the next block. Inherent in this assumption is the condition that the leading block does not provide a horizontal restraint to the movement of the following block. However, the portion of the first block which is above the slip surface of the second block must be assumed to contribute a normal force on the second block. Moreover, the analysis methodology of Huag et al. (1977) could not simulate the strain-softening behavior of sensitive clay which dramatically affects the stability of each sliding block. Thus, adopting traditional LE methods on evaluating flowslides may not be able to provide a satisfying result.

2.4.2 Failure mechanism of spread

In a typical spread, a quasi-horizontal failure plane forms from the toe of the slope, mostly due to riverbank erosion. The soil mass above this failure plane then displaces and fails successively, forming a number of horsts and grabens (Cruden and Varnes 1996). The horsts are the blocks of intact clay having a sharp wedge pointing upward, while the grabens are the blocks having a flat horizontal top surface (Fig. 2.10).

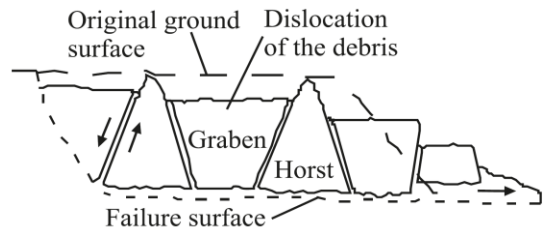


Fig. 2.10. Failure process of a typical spread (after Locat et al. 2011).

Locat et al. (2011) schematically demonstrated the mechanism of shear band propagation and soil mass dislocation during spread. They stated that active failures in sensitive clays need to be analyzed under the undrained condition since soft sensitive clays show strain-softening behavior in undrained shear bands. Figure 2.11 represents the progressive failure pattern of spread with time. An erosion or a small slide near the toe of the slope (point A in Fig. 2.11a) will increase the shear stress along the potential failure surface. Under this given disturbance at point A, the soil reaches its peak shear strength, and then the strength of the soil decreases toward its large-deformation shear strength, inducing a shear band propagating along the developing failure surface. The shear stresses along the failure surface at time i during failure progression $\tau_i(x)$ and the total horizontal stresses $\sigma_{ix}(x)$ are shown by solid lines in Figs. 2.11(c) and 2.11 (d), respectively. During failure propagation, the redistribution of shear stress with time generates changes in horizontal stress in the slope. At some time, the total horizontal stress may decrease

sufficiently to mobilize the active resistance of the soil above the failure surface ($\sigma_{Act}(x)$) (Fig. 2.11(d)) resulting in an active failure. Under this global failure process, the soil mass above the failure surface extends and dislocates into horsts and grabens that are translated downslope and they partly subside into the remolded clay of the shear zone. Grabens and horsts dislocate along the failure surface having angles close to $45 + \phi'/2$ with the horizontal, corresponding to an active Mohr-Coulomb's failure (Fig. 2.11(a)). An assumption of their conceptual model is that the failure propagates essentially independently of the dislocation of horsts and grabens.

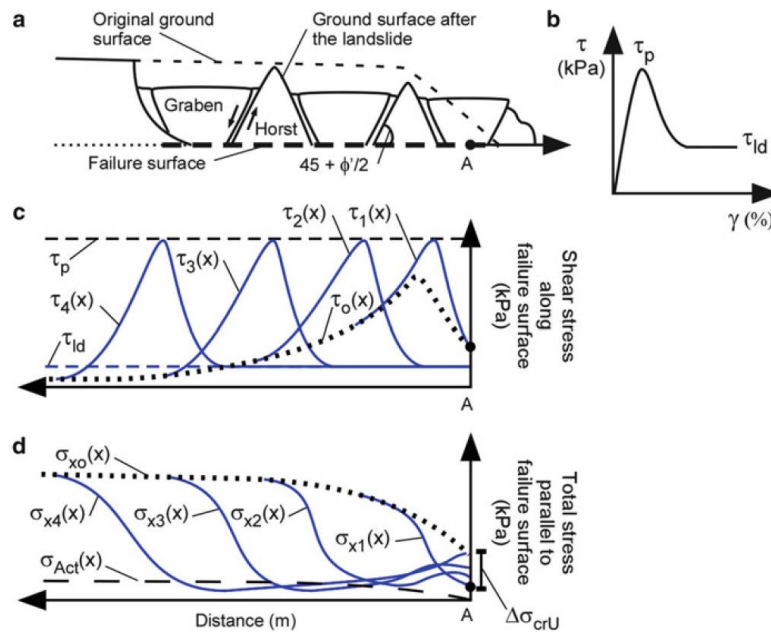


Fig. 2.11. Schematic representation of progressive failure through time: (a) geometry and failure surface; (b) soil behavior; (c) shear stress along failure surface; and (d) total stress parallel to the failure surface (after Locat et al. 2011).

2.4.3 Retrogression and run-out distance of landslides in sensitive clays

Predicting the dimension of a potential landslide is important in estimating the risk of this kind of hazard. Based on post-slide investigations, attempts have been made in the past to relate flowslide potential with topography (e.g. slope geometry, downslope gradient), geotechnical

properties (e.g. remolded shear strength s_{ur} , sensitivity S_t , liquidity index LI , stability number N_s), and percentage of sensitive clay volume in the sliding mass (Tavenas 1984; Leroueil et al. 1996; Strand et al. 2017).

Demers et al. (2014) inventoried the dimensions and the geotechnical properties of the soil involved in historical cases of landslides in eastern Canada (Table 2.1). The statistics show that the retrogression distance of flowslides ranged from 38 to 1,340 m with an average of 225 m, and the retrogression distance of spreads ranged from 30 to 560 m with an average of 145 m. The ratio between retrogression distance and slope height is 1.9 to 47.4 for flowslides and 1.9 to 46.7 for spreads.

Table 2.1. Summary of the geometric properties of the historical cases (after Demers et al. 2014).

	Flowslide		Spread	
	Range	Average	Range	Average
Retrogression (R)	38–1,340 m	225	30–560 m	145
Width (W)	50–3,500 m	250	65–1,725 m	370
Height (H)	10–73 m	27	9–35 m	18
R/H	1.9–47.4	9.5	1.9–46.7	8.0
W/H	1.4–47.9	9.1	5.3–76.2	20.7
R/W	0.3–3.1	1.2	0.1–2.5	0.5
Failure depth/H	0.3–1.0	0.7	0.8–1.3	1.0

Thakur and Degago (2014) proposed a simplified analytical method for the estimation of flowslide potential based on remolded energy E_R (Tavenas et al. 1983). The remolded energy equals the area under the stress–strain curve of the sensitive clay. They mentioned that the available kinetic energy ΔE_k during the slide should be used in the assessment of the extent of flowslides. Before the slide, some potential energy is stored in the slope due to the weight and the height of the soil. During the slide, the available potential energy is partially consumed to remold the soil and partially used to move the remolded material (Leroueil 2001). Thakur and Degago (2014) proposed an equation expressing the change in kinetic energy as:

$$\Delta E_k = \Delta E_p - \Delta E_R \quad (2.9)$$

The potential energy per unit volume is simply calculated as $2\rho gH/3$, where ρ is the mass density of sensitive clay; H is the height of the soil; and g is the gravitational acceleration.

Thakur and Degago (2014) selected five nearly similar Norwegian landslides to relate the available kinetic energy ΔE_k with the corresponding run-out distance L_u and retrogression distance L_R of the respective slides (Fig. 2.12). In these landslides, the nature of retrogression and the run-out process were similar, and the slide debris had run-out along ravines. Figure 2.12(a) shows that the available E_k is positively correlated with the resulting run-out distance. This observation from the landslide data supported the conclusion that a greater run-out distance is associated with less use of energy for the disintegration of sensitive clays, thereby making more kinetic energy available for the slide movement (Leroueil 2001). A similar correlation can also be observed between the available E_k and the retrogression distance (Fig. 2.12(b)). They also mentioned that the extent of the run-out and retrogression distances, among other factors, are dependent on secondary factors such as the topography and the stability of the area behind the initial slide zone (Mitchell and Markell 1974; Lebuis et al. 1983; Tavenas et al. 1983).

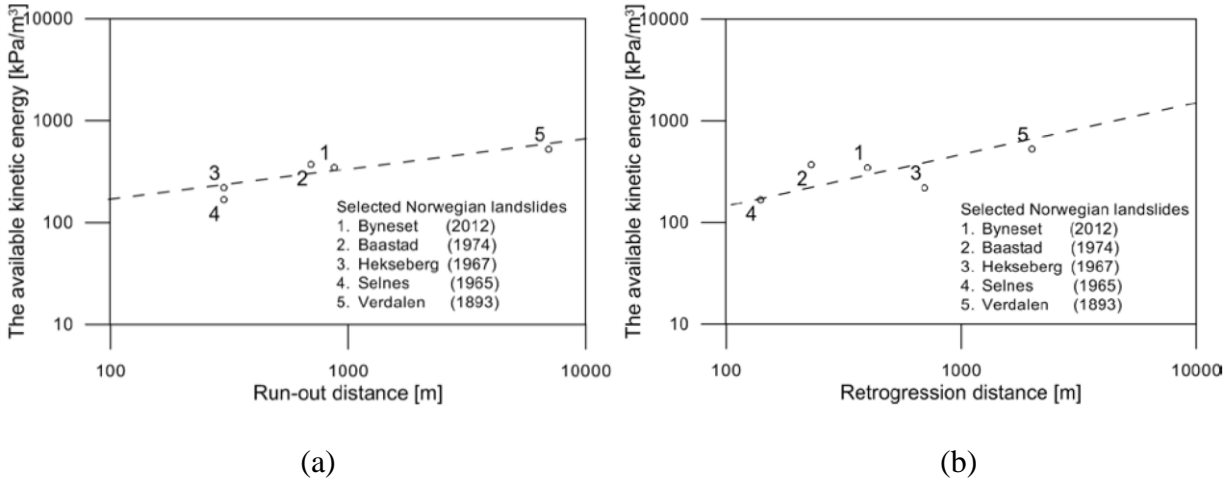


Fig. 2.12. The relations of available kinetic energy versus (a) retrogression and (b) run-out distances (after Thakur and Degago 2014).

2.5 Slope Failure Subject to Dynamic Loading

The pseudostatic approach is the most traditional and widely used method for seismic slope stability assessment. In this method, a pseudostatic force due to earthquake acceleration is added to the driving force resulting from gravitational acceleration and then solves the problem using LE method. Even though the pseudostatic method is very straightforward for practical application, many researchers criticized this approach because it is over-conservative in many situations (Jibson 1993, 2011; Bray and Travasarou 2009). Kramer (1996) mentioned that the pseudostatic approach may not be applicable if the soil undergoes post-peak shear strength degradation greater than 15% or builds up significant dynamic pore pressures. Moreover, the value of the horizontal pseudostatic coefficients k_h used in the pseudostatic analysis could vary due to case histories and the level of acceptable deformation. A comprehensive review of the pseudostatic approach is available in Jibson (2011).

Limit equilibrium analyses using the pseudostatic approach do not provide any information about the displacement of soil. Seismic displacement is normally calculated using Newmark's

Sliding Block method (Newmark 1965) in which the sliding soil mass is assumed to be a rigid body that slides over the basal plane if downslope acceleration exceeds a critical acceleration. The shear resistance along the sliding plane is assumed to be constant. However, this method has been thought to be overly simplified and may not be applicable to different types of failure and soil conditions, as it does not account for the effect of internal deformation of the failed soil mass (Seed and Martin 1966; Seed et al. 1978; Jibson 1993).

Kramer and Smith (1997) modified Newmark's method considering a discrete system of two or more blocks connected by springs and dashpots instead of one rigid block. Makdisi and Seed (1977) defined a potential failure plane in their method. Soil behaves elastically at a stress level below the yield acceleration and as perfectly plastic material above the yield acceleration. For a given potential sliding mass, in the stages at which acceleration exceeds the yield acceleration, a movement will occur along the failure plane. Ambraseys and Srbulov (1994) presented simple semi-empirical predictive relations based on their proposed sliding block model to determine earthquake-induced ground displacements as a function of the critical acceleration ratio (ratio of maximum horizontal acceleration beyond which yield will occur to the maximum predicted acceleration), earthquake magnitude and source distance. Bray and Travararou (2007) presented a simplified semi-empirical probabilistic based seismic slope displacement model based on the nonlinear coupled stick-slip deformable sliding block model originally proposed by Rathje and Bray (2000), to account for the deformability of the sliding mass as an advancement of the Newmark's model. Bray and Travararou (2009) revised their probabilistic model to develop a rational method for selecting seismic coefficient k_h depending on the expected seismic demand at the site and the desired level of seismic performance.

However, most of the analytical and empirical relationships available in the literature are for seismic stability of dams, where the acceptable seismic displacement is less than 1 m and the soil does not experience significant strength loss due to an earthquake (<15% of its initial value) (Bray and Travasarou 2009). Therefore, these approaches may not be applicable to large displacement failures that are commonly observed in landslides in soft and sensitive clays.

Very limited physical model tests on sensitive clay slope failure are available in the literature. One of the main reasons is that a large extent of failure is very difficult to accommodate in the experimental setup. Seed and Wilson (1967) presented a series of model tests to explain the failure mechanisms involved in the Turnagain Heights landslide due to the 1964 Alaska earthquake. The slopes were composed of an extremely weak layer at the level of the toe, overlain by layers of stronger clays, to understand large-scale landslides in the Turnagain Heights area. A series of retrogressive rotational slides were found in model tests (Fig. 2.13). Wartman (2005) performed four 1g shaking table tests on clay slope models to investigate the mechanisms of earthquake-induced permanent deformations. Vane shear tests were conducted to measure the undrained shear strength of the clay used in the tests. Deep rotational and translational sliding occurred in the model slopes at the interface between soft and stiff soil layers. The measured deformations in model tests have been compared with calculated deformation using Newmark's sliding block method. Park and Kutter (2015) performed a total of 4 static and 8 dynamic centrifuge experiments at 50 times gravitational acceleration for different earthquake input motions to study the effects of soil sensitivity on slope failure mechanisms. Vane shear and uniaxial compression tests were also conducted to obtain the strength and sensitivity of tested soils. Deeper failure with a diffused plastic zone was found in dynamic tests, while shallow and distinct shear bands were obtained in static tests.

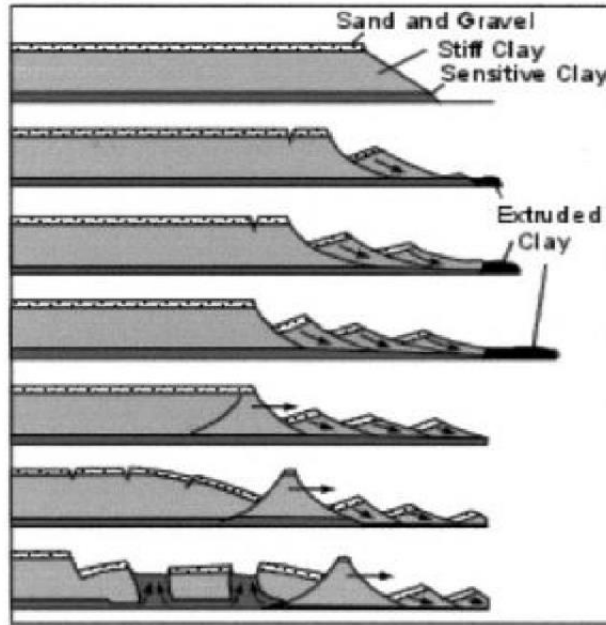


Fig. 2.13. Typical failure in model test slopes for Turnagain Heights landslide (after Abbott 1996).

2.6 Numerical Modeling of Landslides

Limit equilibrium (LE) methods have been widely used for estimating the stability of slopes. This type of analysis gives the factor of safety and the location of the critical slip surface but cannot simulate progressive failure plane development in sensitive clay slopes. The finite element method is a powerful alternative approach to slope stability analysis because fewer assumptions are required and the failure occurs through the zones where shear stress reaches the shear strength of the soil. Most of the FE models are developed based on the Lagrangian framework. One of the main disadvantages of these types of FE models is that significant mesh distortion occurs around the failure planes and the solutions generally suffer from mesh dependency, numerical instabilities and lack of convergence (Griffiths and Lane 1999). The application of FE methods becomes more complex in stability analysis of slopes in sensitive clays because such a problem is associated with very large deformation and large strain localization on narrow shear bands.

Locat et al. (2013) performed numerical modeling using PLAXIS 2D and BIFURC (Jostad and Andresen 2002) FE programs to study the mechanism of quasi-horizontal shear band formation in an infinite slope. In this decoupled modeling, the initial stress in the slope is calculated using PLAXIS 2D under drained condition. The calculated stress from PLAXIS is then transferred to BIFURC to simulate the initiation and progression of a quasi-horizontal shear band due to toe erosion. The strain-softening behavior of the predefined failure zone was modeled using a zero-thickness interface element. A linear post-peak strength degradation model was considered where failure is assumed in a simple shear condition. The limitation of their study is that the location of the failure surface is pre-defined, and the displacement and dislocation of the soil mass cannot be simulated.

Gauer et al. (2005) used the concept of computational fluid dynamics and simulated the retrogressive development of the last phase of the Storegga slide. Shear strength of the marine clay was modeled as a Bingham fluid with strain softening. Simulations were carried out for different rates of strain softening. The simulation results reproduced a retrogressive sliding process with a final deposition pattern similar to the morphology observed in the upper part of the slide scar.

Chen and Qiu (2014) presented the use of a smooth particle hydrodynamics (SPH) method to model earthquake-induced large slope deformation under undrained conditions. A constitutive model combining the isotropic strain softening, viscoplasticity and rate-dependent stiffness was implemented in the numerical model. The numerical results were compared to the shake table test result conducted by Wartman (2005). Both numerical and shake table tests showed a large displacement of a soil block.

Wang et al. (2015) studied catastrophic failure in an infinite planar slope in sensitive clay under undrained condition using a static large deformation finite element method, termed

remeshing and interpolation technique with small strain (RITSS) technique (Hu and Randolph 1998). The RITSS approach, falling in the category of ‘arbitrary Lagrangian–Eulerian’ methods, divides the whole analysis into a series of small strain analysis increments to avoid mesh distortion, followed by remeshing and interpolation of all field quantities from old to new meshes. The shear band propagation criteria were derived analytically using a process zone approach (Puzrin and Germanovich 2005) and validated numerically using the RITSS modeling technique.

Recently, the Coupled Eulerian–Lagrangian (CEL) framework available in Abaqus was used for large deformation geotechnical problems (e.g. onshore and offshore landslides, penetration of surface laid pipelines and spudcan foundations in the seabed) (Tho et al. 2011; Dey et al. 2015, 2016; Dutta et al. 2015; Hamann et al. 2015; Trapper et al. 2015). One of the main advantages of CEL is that the materials (soil) flow through the fixed mesh and therefore numerical issues related to mesh distortion are not encountered (Benson 1992, 1995; Benson and Okazawa, 2004). Adopting this simulation technique, Dey et al. (2015) simulated spread failure in sensitive clays. The soil block at the toe of the slope was moved gradually away from the slope, simulating the effect of toe erosion. The simulation was performed under a quasi-static condition. The shear band formation and soil mass dislocation were successfully simulated, as shown in Fig. 2.14. Later, Islam et al. (2019) simulated sensitive clay slope failure under seismic loading using the same numerical method.

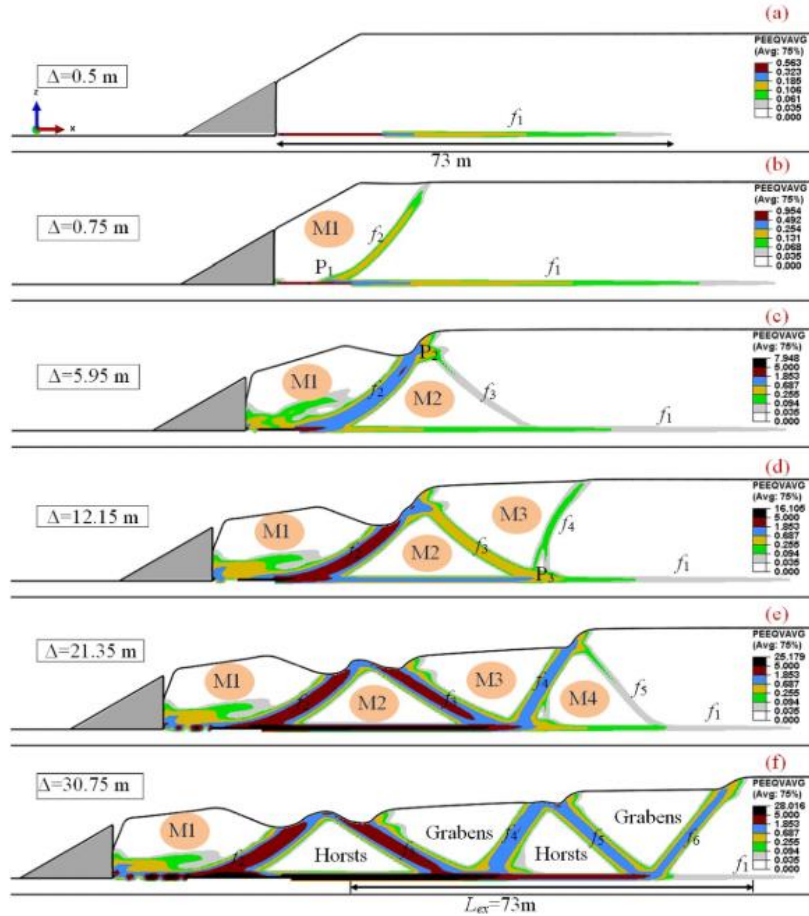


Fig. 2.14. Simulation of an idealized spread in a sensitive clay slope using CEL approach (after Dey et al. 2015).

2.7 Summary

The literature review presented in this chapter shows that the mechanism of a sensitive clay landslide is not well understood. There are many challenges in physical model tests, field investigations, and numerical modeling. In terms of physical modeling, reduced-scale tests could be conducted to understand the behavior; however, a full-scale test to model the complete process is impractical because the failure occurs over a very large area. Post-slide investigation of the failure provides some valuable information about the final stage (e.g. retrogression and run-out); however, in many cases, the initial state prior to failure, and mechanisms involved in failure (e.g.

formation of shear bands) are not known. In terms of numerical analysis, the commonly used limit equilibrium methods for slope stability analysis cannot model progressive failure of sensitive clay. Moreover, finite element methods in a Lagrangian framework cannot simulate this type of landslides because of mesh distortion. Therefore, a large deformation FE technique is used in the present study to investigate some of the key factors, including initial stresses state and seepage in the slope, and strain-rate and strain-softening effects on shear strength for the failure triggered by toe erosion near the riverbanks and earthquake loadings.

Chapter 3

Effects of Geometry and Soil Properties on Type and Retrogression of Landslides in Sensitive Clay

Co-Authorship: This chapter has been submitted as a technical paper for publication in a journal as: Wang, C., Hawlader, B., Perret, D. and Soga, K., ‘Effects of geometry and soil properties on type and retrogression of landslides in sensitive clay.’ Most of the research presented in this chapter has been conducted by the first author. He also prepared the draft manuscript. The other authors mainly supervised the research and reviewed the manuscript.

Videos s1–s20 are available in the supplementary data submitted together with this thesis.

3.1 Abstract

Flowslide and spread are two common types of landslides in sensitive clays. Empirical criteria, based on single or multiple soil properties and slope geometry, have been proposed for a rough assessment of potential landslide type and retrogression distance. A large variation has been found in the comparison of retrogression distance between empirical equations and field data. In the present study, flowslides and spreads are simulated using a Eulerian-based large deformation finite element (FE) method. In addition to strain-softening, a strain-rate-dependent undrained shear strength model that elevates the strain-rate effects on the shear strength of liquefied clay flowing at high speed is used. In flowslides, the increase in undrained shear strength gradient reduces the depth of subsequent slides, and thereby the retrogression distance. The maximum retrogression occurs for a uniform shear strength profile. The increase in horizontal to vertical stress ratio, resistance to downslope movement of the debris, and decrease in soil brittleness and slope steepness change the failure pattern from a flowslide to a spread.

3.2 Introduction

Many large-scale landslides in sensitive clays have occurred in eastern Canada and Scandinavia, where the rapid undrained failure of successive soil blocks commonly caused an upslope retrogression of several hundred meters in many cases and more than a kilometer in some events (Demers *et al.*, 2014). In Scandinavia, most of the large landslides are “flowslide” (Demers *et al.*, 2014), where the successive undrained failure of the soil blocks occurs by the formation of rotational slides (Locat *et al.*, 2011). A compilation of large landslides in Quebec shows 57% flowslides, 38% spreads and 5% undefined slides (Demers *et al.*, 2014). In a spread, a quasi-horizontal failure plane develops rapidly, and then the active failure of the soil above the horizontal shear band results in successive upslope failures, forming triangular soil blocks, commonly known as horsts and grabens (Odenstad, 1951; Carson, 1977; Locat *et al.*, 2013). As the complex mechanisms of the landslide are not well-understood and numerical modelling is challenging, the hazard assessment in sensitive clay terrains is generally performed using empirical approaches, based on statistical analysis validated using a limited number of historical landslide cases.

The following are three key questions in assessing the extent of large-scale landslides:

- i) If the initial failure of the first soil block occurs, will it cause retrogressive failure?
- ii) If retrogression occurs, will the failure be a spread or flowslide?
- iii) How do remoulding of clay and topography influence the failure pattern and retrogression distance?

These questions cannot be answered from traditionally used limit equilibrium (LE) or classical FE methods of analysis, because the former cannot model the progressive failure, and the latter cannot handle large deformation. The proposed criteria for determining the retrogression distance of large-scale landslides are defined as: stability number, $N_s > 4-8$ (Mitchell & Markell,

1974; Tavenas, 1984; Leroueil *et al.*, 1996); fully remolded undrained shear strength, $s_{ur} < 1$ kPa (Lebuis *et al.*, 1983; Demers *et al.*, 2014; Thakur *et al.*, 2014); liquidity index, $IL > 1.2$ (Tavenas, 1984); sensitivity, $S_t > 30$ (Lebuis *et al.*, 1983); and rapidity number ≥ 8 (Söderblom, 1974). When compared with historical landslide information, these approaches show limited success for estimating retrogression or runout (Thakur & Degago, 2012; Demers *et al.*, 2014). Moreover, attempts have been made to model retrogression and runout using quickness, a parameter that assesses the flow potential of remoulded clay (Thakur & Degago, 2012), and the rheological properties of sensitive clay (Norem *et al.*, 1990; Locat, 1997; Turmel *et al.*, 2019).

Retrogression and runout also depend on the type of failure. After the failure of a soil block, whether the subsequent soil failure will result in spread or flowslide depends on a complex process of clay liquefaction, downslope debris flow and propagation of shear bands. Field investigations show a trend that flowslide, spread and non-retrogressive slides occur for low, intermediate and high initial undrained shear strengths, respectively (Geertsema *et al.*, 2006). Qualitatively, flowslides always occur in very sensitive clays, while this may not be the case for spreads (Demers *et al.*, 2014). Conceptual models have been proposed for spreads to explain the dislocation of the soil mass over a predefined horizontal failure plane (Odenstad, 1951; Carson, 1977, 1979). Puzrin *et al.* (2016) derived analytical criteria for submarine spread failures. Quinn *et al.* (2011) proposed an analytical model based on fracture mechanics to estimate the development of large retrogressive landslides in sensitive clays. Locat *et al.* (2013) conducted FE modelling of the propagation of the horizontal shear band due to toe erosion but did not simulate the whole process including the formation and displacement of horsts and grabens. Dey *et al.* (2015) modelled spreads using an Eulerian-based FE approach and simulated the formation of horsts and grabens and their large displacement for a quasi-static displacement of an erosion block. However, these conceptual and

numerical models do not explain the conditions that can change the failure pattern from a flowslide to a spread.

Retrogression distance and runout are the two important parameters of concern in land-use management and landslide hazard analysis. The existing empirical relations for retrogression distance as a function of stability number or remoulded energy might provide at best a rough guideline because the calculated retrogression distance using these empirical relations varies widely from field data (Demers *et al.*, 2014; Geertsema & L'Heureux, 2014; Thakur *et al.*, 2014). The remoulding of clay and its flow governs the failure pattern. In flowslides, sensitive clay liquefies and displaces out of the crater easily, while the debris remains as more or less intact blocks in spreads. Also, the local topography, such as the presence of an opposite riverbank, could change the failure pattern by controlling the ease with which debris can move away from the landslide scar.

Although the initial shear strength could be high, the fully remoulded shear strength (s_{ur}) of highly sensitive clay could be very low (< 1 kPa) (Lebuis *et al.*, 1983; Tavenas, 1984; Demers *et al.*, 2014). The remoulded soil might flow like a fluid at a high velocity (several meters per second in some cases, Tavenas *et al.*, 1971), which represents a dominant strain-rate effect on shear strength. Previous numerical studies have not considered the strain-rate effects.

In summary, the existing empirical approaches cannot properly estimate the retrogression distance, the potential failure type, or both. The classical Lagrangian-based FE techniques cannot model the large deformation in spreads and flowslides because of mesh distortion issues. In the present study, a large deformation FE simulation is performed using a Eulerian-based FE modelling approach to identify different conditions required for the development of flowslides and spreads. The effects of strain-rate and strain-softening on undrained shear strength are considered.

The role of slope geometry and soil properties in failure patterns and retrogression distance is identified. Finally, the practical implications of the present numerical analysis for estimating the extent of sensitive clay landslides are discussed.

3.3 Problem Definition

Figure 3.1 shows the geometry of the slope model analyzed in this study. The slope has three layers: (i) a 3-m crust; (ii) a sensitive clay layer beneath the crust down to the elevation of the slope toe; and (iii) a strong underneath soil layer. The initial undrained shear strength of the sensitive clay layer (s_{u0}) (i.e. s_u before strain softening and at the reference strain rate, as discussed below) increases linearly with depth as:

$$s_{u0} = s_{ug} + kz \quad (3.1)$$

where s_{ug} is a constant in kPa; k is the strength gradient in kPa/m; and z is the depth of the soil element below the ground surface in metres. In other words, s_{u0} in the sensitive clay layer at a given depth is the same, including the soil elements below the slope. Field investigations typically show a higher undrained shear strength on average in the crust compared to the underlying clays, which is due to long-term weathering processes (Perret *et al.*, 2019). A uniform s_{u0} for the crust (= s_{u0c}) is used in this study. The strong soil layer below the toe level is modelled as an elastic non-sensitive material to save computational time.

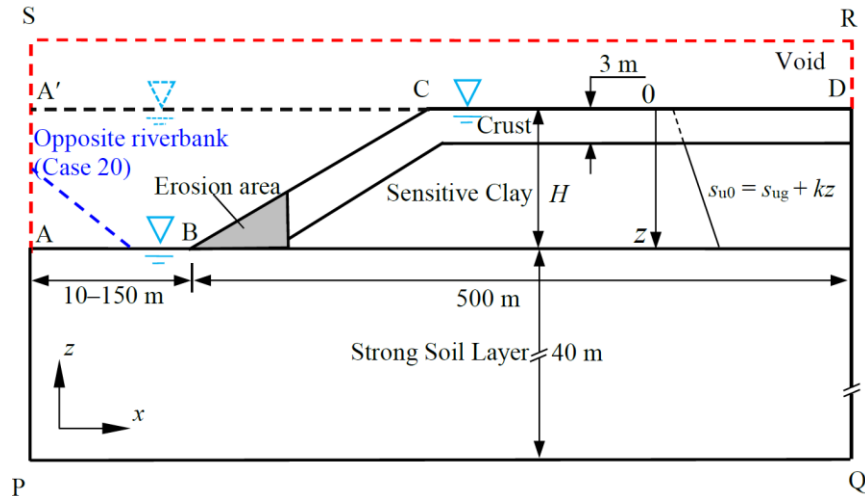


Fig. 3.1. Geometry of the slope used in finite element modeling.

Similar to many landslides along watercourses in eastern Canada, the slope failure is triggered by toe erosion by removing a 5-m-high triangular soil block near the toe (shaded triangle in Fig. 3.1). The right boundary of the model is placed at a 500 m distance from the slope toe. The distance from the toe to the left boundary is varied to simulate three different scenarios. Firstly, to simulate flowslides, the left boundary is placed at 10 m to the left of the slope toe, and no additional boundary condition is applied on the left side of the model above the level of the slope toe (i.e. above point A in Fig. 3.1). This boundary condition allows the debris to flow out of the domain without any applied restriction to simulate the flow of liquefied clay sideways, both in the upstream and downstream of the river channel, as hypothesized based on historical flowslides (Demers *et al.*, 2014; Turmel *et al.*, 2017). Secondly, the left boundary is placed 150 m from the toe to simulate the displacement of the debris over a long horizontal plane. Spreads have already occurred for this type of downslope topography—for example, in the 1980 Havre-St-Pierre landslide in Quebec, Canada, the debris traveled more than 200 m over a flat surface from the slope toe (Locat *et al.*, 2014). Finally, in one case, the opposite riverbank is modelled to examine the effects of restrictions on debris flow and failure mechanisms (e.g. the 2010 Saint-Jude landslide, Locat *et al.*, 2017). For

simplicity, the opposite riverbank is modelled as a rigid wedge inclined at the slope angle (dashed line in Fig. 3.1). Uneven ground surface, the presence or absence of water, and vegetation influence the size and shape of the area over which landslide debris accumulates (Geertsema & L'Heureux, 2014; Turmel *et al.*, 2017); however, such complex situations are not modelled here. The soil is considered fully saturated, and the seepage effect is not modelled (i.e. undrained).

3.4 Numerical Modeling

The Eulerian-based FE method available in Abaqus/Explicit FE software is used. The program uses a solid mechanics framework for Eulerian time integration based on operator splitting of the governing equations in which each time step has two phases of calculations—a conventional Lagrangian phase followed by an Eulerian phase. In the Eulerian phase, the solution obtained from the Lagrangian phase is mapped back to the spatially fixed Eulerian mesh. Therefore, the Eulerian material (soil) can flow through the fixed mesh without causing numerical issues related to mesh distortion. Thus, the large displacement of soil debris and the development of high strains in the failure planes can be simulated. Further details on the mathematical formulations of the Eulerian FE approach, mesh sensitivity analysis, and its applications to large deformation quasi-static/dynamic problems (e.g. onshore and offshore landslides, penetration of surface laid pipelines and pile jacking) are available in previous studies (Benson, 1992; Benson & Okazawa, 2004; Qiu *et al.*, 2012; Dey *et al.*, 2015, 2016; Dutta *et al.*, 2015; Trapper *et al.*, 2015; Islam *et al.*, 2019; Wang *et al.*, 2019).

In Abaqus/Explicit, the Eulerian approach has been implemented only for three-dimensional elements. Therefore, the FE analysis is performed with only one element length in the out-of-plane direction to simulate the plane strain condition. The Eulerian domain (PQRS in Fig. 3.1) is discretized into 0.25-m cubical elements using EC3D8R in the software, which is an 8-node linear

brick element of multi-materials having reduced integration and hourglass control. The Eulerian Volume Fraction (EVF) tool is used to define the material: $EVF = 1$ for the elements filled with soil, $EVF = 0$ for the void, and $0 < EVF < 1$ is for partially filled elements.

At the bottom of the domain, a zero velocity boundary conditions are applied in all three directions. Moreover, zero velocity boundary condition is applied normal to all the vertical faces of the domain, except for the left side, where $v_x = 0$ is applied only for the elements below the toe level (i.e. on surface AP in Fig. 3.1). No velocity boundary condition is given along the soil–void interface so that the soil can move into the void space when needed. In the simulation with an opposite riverbank, a rough interface condition between the Lagrangian rigid opposite riverbank and Eulerian soil is given using the general contact option in the software.

Establishing Initial Stress Condition

Most of the riverbank slopes in eastern Canada formed by gradual erosion of valleys in initially horizontal clay deposits over many centuries (Lefebvre 1986; 2017). In this study, the slope is created by soil removal assuming the soil as a one-phase undrained material. The stresses in a soil element at depth z below the horizontal ground surface (A'CD in Fig. 3.1) are: $\sigma_v = \gamma z$, $\sigma_h = K\sigma_v$; and $u = \gamma_w z$, where σ_v , σ_h and u are the total vertical, total horizontal and pore water pressure, respectively; K is the ratio between σ_h and σ_v ; γ is the total unit weight of soil; and γ_w is the unit weight of water. If the groundwater table is at the ground surface, K is related to the effective earth pressure coefficient at-rest K_0 as $K = K_0 + (1 - K_0)\gamma_w/\gamma$.

In FE modelling, the initial stress condition in three directions (σ_v , $K\sigma_v$, $K\sigma_v$) for a horizontal ground surface is defined. Then the gravitational load is applied to the soil elements ($EVF \neq 0$). As there is no soil in the zone ABCA' in Fig. 3.1, it represents the removal of soil in this zone, which is similar to the “mesh removal” in typical Lagrangian-based FE modelling of excavation (Duncan

& Dunlop, 1968; Potts *et al.*, 1997; Borges, 2008; Locat *et al.*, 2013). By defining the initial condition in this way, the simulation can be performed for $K > 1$, which is common in many sensitive clays and has a significant effect on slope failure. Previous Eulerian-based FE modelling of landslides has been performed for $K \leq 1$ (e.g. Dey *et al.*, 2015).

Initiation of Failure and Post-Failure Simulation

The failure is triggered by toe erosion by reducing the undrained shear strength of the erosion block from the intact shear strength to 0.1 kPa in 5 seconds. The downslope movement of the weak soil in the erosion block causes progressive failure of the slope. The analysis is then continued until the instantaneous velocity of the soil elements becomes negligible, or the retrogressive failure reaches the right boundary of the model.

3.5 Modeling of Sensitive Clay

The mobilized undrained shear strength (s_u) of sensitive clays is modelled using Eq. (3.2) incorporating a strain-softening factor, f_1 (≤ 1.0) and strain-rate factor, f_2 .

$$s_u = f_1 f_2 s_{uy} \quad (3.2)$$

where s_{uy} is the undrained shear strength at a very low strain rate, as will be explained.

3.5.1 Strain softening

Linear and exponential reduction of factor f_1 , as a function of accumulated plastic shear strain (ξ) or plastic shear displacement (δ), have been used in previous studies (Locat *et al.*, 2013; Dey *et al.*, 2016). The following equations are used in the present study for modelling post-peak s_u degradation.

$$f_1 = \begin{cases} \frac{s_{uR}}{s_{u0}} + \left(1 - \frac{s_{uR}}{s_{u0}}\right) e^{-3\delta/\delta_{95}} & \text{if } 0 \leq \delta < 2\delta_{95} \\ \frac{s_{uR}}{s_{u0}} - \frac{s_{uR} - s_{uld}}{s_{u0}} \frac{\delta - 2\delta_{95}}{\delta_{ld} - 2\delta_{95}} & \text{if } 2\delta_{95} \leq \delta < \delta_{ld} \\ \frac{s_{uld}}{s_{u0}} & \text{if } \delta \geq \delta_{ld} \end{cases} \quad (3.3)$$

where s_{u0} is the peak undrained shear strength at the reference shear strain rate ($\dot{\gamma}_{ref}$) before softening; s_{uR} is the value of s_u at sufficiently large δ ; δ_{95} is the value of δ at which 95% reduction of $(s_{u0} - s_{uR})$ occurs; and δ_{ld} is a very large value of δ ($> \delta_{95}$), when the soil becomes completely remoulded to $s_u = s_{uld}$. Equation (3.3) represents a quick exponential degradation of s_u at $0 \leq \delta < 2\delta_{95}$ followed by a linear degradation at $2\delta_{95} \leq \delta < \delta_{ld}$ and then a constant s_u ($= s_{uld}$) at $\delta \geq \delta_{ld}$. Before the yield, the stress–strain behaviour is modelled using undrained Young’s modulus (E_u) and Poisson’s ratio (ν_u). It is also assumed that the s_u remains constant immediately after yielding ($s_u = s_{u0}$), for a small plastic shear displacement of δ_{pc} . Further details of this strength degradation model, including the selection of model parameters and the comparison of its performance with specialized laboratory test results on sensitive clay (Tavenas *et al.*, 1983), have been presented elsewhere (Dey *et al.*, 2015, 2016).

3.5.2 Strain-rate effects on undrained shear strength

Typical large-scale landslides in sensitive clays (e.g. flowslide, spread) involve soil of widely varying undrained shear strength. The landslide initiates by the formation of failure surfaces through intact soil of high undrained shear strength; however, the failed soil mass might displace in the downslope direction at high speed, like a viscous fluid having very low s_u after remoulding ($s_u < 1$ kPa). Therefore, the modelling of this type of landslide requires a strain-rate ($\dot{\gamma}$) dependent undrained shear strength model that is suitable to simulate the behaviour of sensitive clay, from the formation of failure surfaces through intact soil that occurs at a relatively small $\dot{\gamma}$ to the flow

of low strength remoulded soil at high strain rates. The strain-rate effects on the shear resistance of soil and high solid-concentrated slurry are generally modelled differently using the geotechnical and fluid-mechanics approaches, respectively. The similarities and differences between these two approaches have been discussed in previous studies (Zhu & Randolph, 2011; Zakeri & Hawlader, 2013).

For soil, the dependency of s_u on $\dot{\gamma}$ is generally modelled using semi-logarithmic, power-law and hyperbolic-sine functions as:

$$s_u = \left[1 + \mu \log \left(\frac{\dot{\gamma}}{\dot{\gamma}_{\text{ref}}} \right) \right] s_{u,\text{ref}} \quad (3.4)$$

$$s_u = \left(\frac{\dot{\gamma}}{\dot{\gamma}_{\text{ref}}} \right)^\beta s_{u,\text{ref}} \quad (3.5)$$

$$s_u = \left[1 + \frac{\mu}{\ln(10)} \sinh^{-1} \left(\frac{\dot{\gamma}}{\dot{\gamma}_{\text{ref}}} \right) \right] s_{u,\text{ref}} \quad (3.6)$$

where $s_{u,\text{ref}}$ is the undrained shear strength at a reference rate ($\dot{\gamma}_{\text{ref}}$); μ ($= 0.05\text{--}0.2$) and β ($= 0.05\text{--}0.1$) are the model parameters (Zhu & Randolph, 2011). Note that, before softening, $s_{u,\text{ref}} = s_{u0}$ when $f_1 = 1.0$.

In semi-logarithmic and power-law models (Eqs. (3.4) & (3.5)), a significant reduction of s_u occurs with a decrease in $\dot{\gamma}$, and s_u might be unrealistically low at a very small $\dot{\gamma}$. However, in the hyperbolic-sine model (Eq. (3.6)), the reduction of s_u below $s_{u,\text{ref}}$ is very small. For example, s_u at a very low strain rate will be $\sim 4\%$ smaller than $s_{u,\text{ref}}$ with $\mu = 0.1$. For $\dot{\gamma} \geq \dot{\gamma}_{\text{ref}}$, the semi-logarithmic and hyperbolic-sine models give very similar results. Hawlader *et al.* (2016) compiled a large number of test results on soft clays and showed that the strain rate effect on s_u is more significant in tests at high strain rates on low strength materials.

In the fluid-mechanics approach, slurries are generally modelled as non-Newtonian fluids, such as using the Herschel–Bulkley model, where the rate effect is accounted for using an additive

term. Zhu & Randolph (2011) proposed the following “additive power-law model” combining the Herschel–Bulkley and power-law model (Eq. (3.5)) that can characterise the behaviour of both soil and fluid, which is used in the present study.

$$f_2 = \left[1 + \eta \left(\frac{|\dot{\gamma}_{\max}|}{\dot{\gamma}_{\text{ref}}} \right)^\beta \right] \quad (3.7)$$

where η and β are soil parameters. Based on previous studies (Jeong *et al.*, 2009; Boukpeti *et al.*, 2012; Randolph *et al.*, 2012), $\eta = 0.5$ and $\beta = 0.1$ are used in the present study.

Field vane shear and cone penetration tests are commonly performed for determining the undrained shear strength profile of sensitive clays. Einav and Randolph (2006) showed the maximum shear strain rate of $\sim 0.05 \text{ s}^{-1}$ for standard vane shear tests with a rotation rate of $0.1 \text{ }^\circ/\text{s}$. In this present study, $\dot{\gamma}_{\text{ref}} = 0.05 \text{ s}^{-1}$ is used. Finally, $s_{uy} = s_{u0}/(1 + \eta)$ can be obtained by replacing, $\dot{\gamma}_{\max} = \dot{\gamma}_{\text{ref}}$ in Eq. (3.7).

The details of the implementation of a strain-softening and strain-rate dependent soil model using a user subroutine have been presented in Dutta *et al.* (2015), although their soil model is slightly different from Eqs. (3.2), (3.3) and (3.7).

3.6 Geometry and Soil Parameters

As discussed in the introduction, post-slide investigations show that the geometry and soil properties affect not only the failure pattern but also the extent of the landslide. A total of 20 simulations are performed for varying slope angles, in-situ stresses and sensitive clay properties (Table 3.1). The additional soil properties listed in Table 3.2 remain the same for all the analyses. The selection of these parameters is discussed below.

Based on 108 historical landslides and scars in eastern Canada, Demers *et al.* (2014) showed that the average slope height is 27 m (10 m–73 m) for flowslides and 18 m (9–35 m) for spreads.

In the present study, a slope height (H) of 20 m is used. Mitchell & Markell (1974) reported the slope angle (θ) of 10° – 45° in most cases of their 41 sensitive clay landslides. A similar range was reported by Leblond *et al.* (1983) in their regional landslide hazard mapping, and by Locat *et al.* (2015) and Locat *et al.* (2017) for some well-documented landslides (e.g. $\theta = 24^\circ$ in Sainte-Monique and $\theta = 12^\circ$ – 24° in Saint-Jude). In the present study, 2:1 and 3:1 (horizontal:vertical) slopes are studied.

Field investigations show that the undrained shear strength of sensitive clays might remain almost constant or increase with depth (Lefebvre, 1992; Locat *et al.*, 2015; Geertsema *et al.*, 2006). Shear strength gradients (k in Eq. (3.1)) of ~ 1.5 – 4.5 were found from vane shear tests in sensitive clays in eastern Canada and Scandinavia (Geertsema & L'Heureux, 2014). Some other landslides also show a similar range: $k \sim 2.5$ in the Sainte-Monique and Saint-Jude landslides (Locat *et al.*, 2015; Locat *et al.*, 2017), and $k \sim 1.7$ in the Saint-Bonafice landslide (Demers *et al.*, 2000). In the present study, k equals 0 (uniform) to 3 are used.

Mitchell & Markell (1974) analysed 41 documented landslides where the stability number ($N_s = \gamma H/s_u$) varied mostly between 3 and 11 and found that undrained retrogressive failures occurred when $N_s > 6$. Demers *et al.* (2014) found large retrogression for N_s , as low as 3.3. In the present study, N_s is calculated using the uniform s_{u0} of the sensitive clay layer, while the average value of s_{ug} and s_{u0} at the toe level is used for linearly increasing shear strength cases. For the geometry and geotechnical properties used in this study, the progressive failure does not occur if $N_s < 3.1$, and the slope is unstable under the gravity load if $N_s > 6.8$; therefore, analyses are performed for $N_s = 3.1$ – 6.8 to model progressive failures. Moreover, for a given N_s , the initial shear strength gradient (k) is varied to examine its effect on failure patterns.

In addition to geometry and initial undrained shear strength, the remoulded shear strength at large displacement (s_{uld}) and the rate of strength degradation affect the failure pattern. Demers *et al.* (2014) found that $s_{uld} = 0.08\text{--}0.80$ kPa for flowslides and $s_{uld} = 0.08\text{--}1.30$ kPa for spreads, while Thakur *et al.* (2014) obtained $s_{uld} < 1$ kPa for Norwegian flowslides, In the present study, $s_{uld} = 1$ kPa is used; however, two more analyses are performed with $s_{uld} = 5$ kPa to study its effect on failure mechanisms and mobility of the debris.

The post-peak strength degradation is defined by s_{uR} , δ_{95} and δ_{ld} (Eq. 3.3). Even though the sensitive clays can have a very low remoulded undrained shear strength, it usually mobilises at very large shear strains. Dey *et al.* (2016) modelled the strength degradation using an exponential curve followed by a straight line (Eq. 3.3). A wide variation of s_{uR} , δ_{95} and δ_{ld} was found when the model was compared with test results on sensitive clays from different sites, conducted by Tavenas *et al.* (1983) and later reanalysed by Quinn *et al.* (2011). In the present study, analyses are performed for $s_{u0}/s_{uR} = 4\text{--}6$, $\delta_{95} = 0.05$ m–0.4 m, and $\delta_{ld} = 1$ m–2 m.

Table 3.1. Geometry and soil properties used for different cases.

Case	$H:V$	N_s	k	K	s_{u0} (kPa)	$s_{u(ld)}$ (kPa)	s_{u0}/s_{uR}	δ_{95} (m)	δ_{ld} (m)	E_R (kN-m/m ³)	L_R (m)	Slide type
1	2	3.8	0	1.0	90	1	6	0.05	1	39.8	15	SR
2	2	4.9	0	1.0	70	1	6	0.05	1	31.4	>500	FL
3	2	6.8	0	1.0	50	1	6	0.05	1	22.9	>500	FL
4	2	6.8	1	1.0	40-60	1	6	0.05	1	22.9	205	FL
5	2	6.8	2	1.0	30-70	1	6	0.05	1	22.9	147	FL
6	2	6.8	3	1.0	20-80	1	6	0.05	1	22.9	93	FL
7	2	6.8	2	1.0	30-70	5	6	0.05	1	30.1	96	FL
8	2	6.8	0	1.0	50	1	4	0.4	2	92.4	329	FL
9	2	6.8	1	1.2	40-60	1	6	0.05	1	22.9	>350	SP

10	2	6.8	2	1.2	30-70	1	6	0.05	1	22.9	>350	SP
11	2	6.8	3	1.2	20-80	1	6	0.05	1	22.9	>350	SP
12	2	4.9	3	1.2	40-100	1	6	0.05	1	31.4	>350	SP
13	2	3.1	3	1.4	80-140	1	6	0.05	1	48.2	>350	SP
14	2	4.9	3	1.0	40-100	1	6	0.1	1	33.4	>350	Compound
15	2	4.9	3	1.0	40-100	1	4	0.4	2	120.4	152	SP
16	2	4.9	3	1.2	40-100	1	4	0.4	2	120.4	204	SP
17	2	3.1	3	1.4	80-140	1	4	0.4	2	192.4	0	Stable
18	2	6.8	2	1.2	30-70	5	6	0.05	1	30.1	154	SP
19	3	4.9	3	1.0	40-100	1	5	0.1	1	38.7	>350	SP
*20	3	4.9	3	1.0	40-100	1	5	0.1	1	38.7	64	SP

Notes: SR: single rotational slide; SP: spread; FL: flowslide

*Case 20 is with opposite riverbank

Table 3.2. Soil parameters used in FE modeling.

Parameter	Crust	Sensitive Clay	Strong Layer
Total unit weight, γ (kN/m ³)	17	17	20
Undrained Young's modulus, E_u (MPa)	10	10	50
Undrained Poisson's ratio, ν_u	0.495	0.495	0.495
Initial undrained shear strength, s_{u0} (kPa)	60	$s_{u0} = s_{u,g} + kz$	-
Reference strain rate, $\dot{\gamma}_{ref}$ (s ⁻¹)	-	0.05	-
η	-	0.5	-
β	-	0.1	-

Note: Other soil parameters used for different cases are listed in Table 3.1

3.7 Failure Mechanisms

The progressive failure simulated in this study is a time-dependent process. Therefore, small videos are uploaded in the online supplementary data for all the analysed cases (Videos s1–s20) to provide further details of the failure mechanisms. For the analysed cases, the retrogressive failures

can be divided into three groups: flowslides (FL), spread (SP), and a combination of FL and SP (hereafter called compound slides). Note that, in addition to the major failure surfaces that define the type of failure (FL or SP), some shear bands form in the soil mass before its detachment from the intact soil and during the subsequent downslope movement. In this study, the failure types are categorised based on the formation of the major failure surfaces (e.g. successive curved failure surfaces in FL) and the shape of the failed soil blocks (e.g. horsts and grabens in SP). In the following sections, a discussion is firstly provided on a typical flowslide and a spread.

3.7.1 Flowslide

Figure 3.2 and Video s5 show the failure process in Case 5, where a typical flowslide occurs. The material of the erosion block collapses and flows downslope due to the reduction of shear strength, which results in an unloading of the remaining soil and initiation of a horizontal shear band (Fig. 3.2(a)). After propagating some distance horizontally, the shear band curves upward to the ground surface and causes the rotational failure of a soil block (R_1 in Fig. 3.2(a)). R_1 displaces downslope leaving a new scarp behind the curved failure surface. The right side of R_1 also subsides as the debris displaces further and the backscarp height (H_b) increases. When H_b is approximately 80% of the original slope height (H), the next slip surface forms and a soil block (R_2) fails with a further displacement of the debris in the front (Fig. 3.2(b)). Figure 3.2(c) shows that the third rotational slide (R_3) initiates from a shallower depth than that of R_1 and R_2 . The shape and angle of the backscarp, which is steeper than the initial slope angle (θ), together with the linearly increased shear strength profile govern the depth of retrogressive failure. After R_3 , six more rotational slides occur successively (R_4 – R_9 in Figs. 3.2(c) and 3.2(d) (also in Video s5)). The maximum depth of the failure surface reduces slightly for each rotational slide and the retrogression of the landslide eventually stops after reaching a retrogression distance (L_R) of

~147 m when $H_b/H \sim 0.65$. Note that L_R is measured from the crest in this study. In historical flowslides, the subsequent rotational failures of soil blocks during retrogression occurred either at the slope toe elevation or a higher elevation, and, in some cases, a stepped shape of the basal failure surface was observed (Demers *et al.*, 2014). Moreover, post-slide investigations of 12 flowslide scars showed $H_b/H \sim 0.28\text{--}0.85$ (Demers *et al.*, 2014). Therefore, although it is simple for practical applications, the stability number criterion should be used with caution for estimating retrogression because it is defined in terms of slope height, while the subsequent retrogressive slides might initiate from shallower backscarp depths.

Figure 3.2(d) shows that the crater can roughly be divided into two zones—a dislocation zone and a remoulded zone. In the dislocation zone, the failed soil blocks initially displace downslope, where remoulding of soil occurs through enlargement of the plastic shear zone near the failure planes and formation of additional shear bands. After significant remoulding with further displacement, the material flows like a fluid with some suspended soil blocks in the remoulded zone.

Another key observation is that, at the end of the simulation, the debris thickness is small or the crater is almost empty in the section where the depth of the failure plane is smaller than slope height (Fig. 3.2(e)). A similar observation has been made in the field. For example, Demers *et al.* (2014) found a mean debris height of ~0.18 times the slope height when the sliding occurs at multiple failure levels, and, in some cases, the crater is almost empty (Lefebvre *et al.*, 1992; Perret *et al.*, 2013). The angle of the FE simulated final backscarp is $\sim 53^\circ$, which is again similar to the typical range observed in the field (e.g. $45^\circ\text{--}55^\circ$, Mitchell & Markell, 1974).

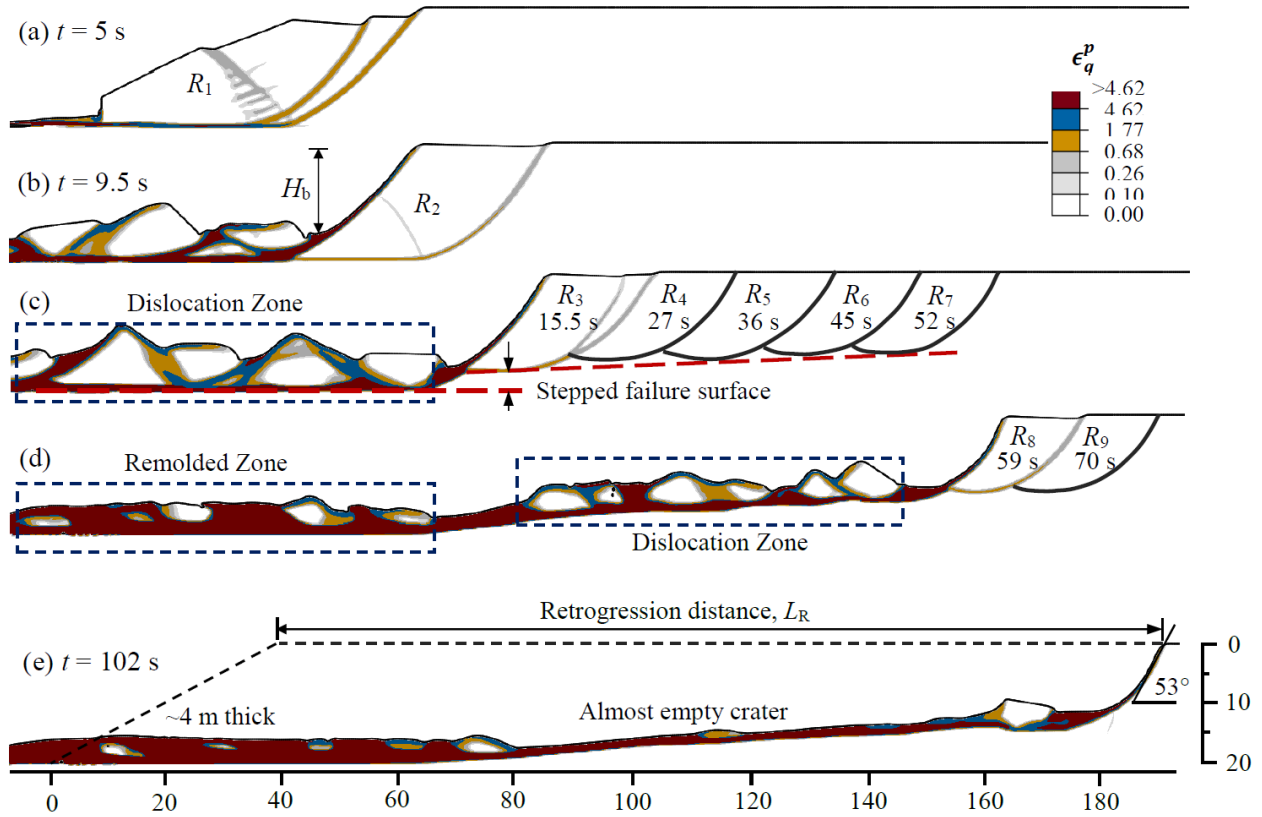


Fig. 3.2. Progressive failure in a typical flowslide (Case-5).

3.7.2 Spread

Figure 3.3 shows the failure process of Case 20, which is different from Case 5, as discussed above, in three aspects: (i) slightly stronger sensitive clay (i.e. larger s_{u0} and smaller s_{u0}/s_{uR}); (ii) milder slope; and (iii) existence of an opposite riverbank of the same slope angle at a distance of 10 m from the toe. The other parameters in Cases 5 and 20 are the same.

Figure 3.3 and Video s20 show that these three factors change the failure pattern to a spread. Similar to Fig. 3.2, the toe erosion creates a quasi-horizontal shear band (f_1), which propagates a larger distance than that in Case 5 (Fig. 3.2) before the formation of the curved upward shear bands. The extra penetration of the horizontal shear band from the failure block (e.g. P_1P_2 in Fig. 3.3(a)) is a necessary condition for a spread. The potential causes of this type of shear band formation are discussed in the following sections. Note that multiple shear bands might form above

the horizontal one when a global failure occurs (e.g. f_2 and f_3 in Fig. 3.3(a)), which cannot be modelled using LE methods.

With a further displacement of the failed soil blocks, the soil behind the backscarp fails as Δ -shaped horsts and ∇ -shaped grabens, which represents a spread. The horsts and grabens displace laterally over the horizontal shear band, during which the remoulding of the bottom of the grabens causes significant subsidence (Figs. 3.3(b) and (c)). The progressive failure in this case stops after the formation of another horst and graben because the movement of the debris has been constrained by the presence of the opposite riverbank. Figure 3.3(d) shows the final position of the debris, which completely blocks the river. Similar field observations have been reported in the literature; for example, the 1946 Sköttorp landslide (spread) in Sweden (Odenstad 1951), 1994 Sainte-Monique and 2010 Saint-Jude landslides in Quebec (Locat *et al.*, 2015; 2017). The soil blocks move over the highly remoulded shear zone at the bottom of the debris; therefore, some back-and-forth movement of the blocks occurs to reduce the kinetic energy of the system before reaching the final equilibrium position (Video s20). The other differences between a flowslide and a spread include less remoulding of the failed soil blocks and higher debris thickness at the end of a spread (Fig. 3.3(d)) than those of a flowslide (Fig. 3.2(e)). Based on historical landslides, Demers *et al.* (2014) showed that the average debris thickness is $\sim 0.6H$ for spreads and $\sim 0.18H$ for flowslides.

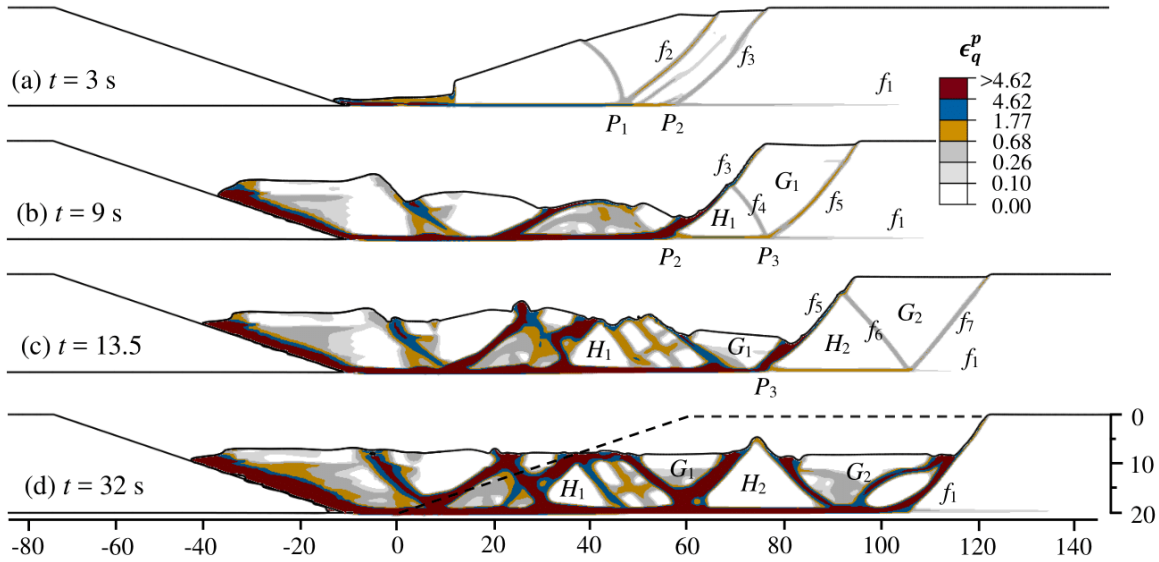


Fig. 3.3. Progressive failure in a typical spread (Case-20).

3.8 Factors Affecting Flowslides

3.8.1 Stability number

Cases 1–3 in Table 1 represent three simulations with uniform s_{u0} of 90 kPa, 70 kPa and 50 kPa, which give stability number N_s of 3.8, 4.9, and 6.8, respectively. Successive rotational slides occur in Cases 2 and 3, and the retrogressive flowslide continues until it reaches the right boundary of the domain (Videos s2 and s3). However, only one rotational slide occurs in Case 1 for a low N_s (Video s1) because the backscarp remains stable under this high s_{u0} .

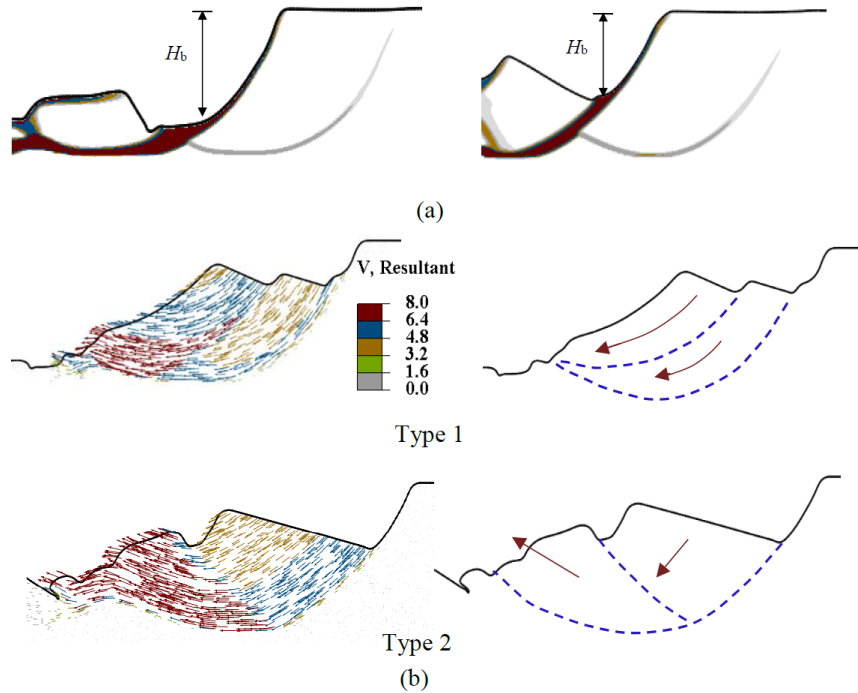


Fig. 3.4. Failure process in Cases 2 and 3: (a) 3rd block failure in Case 2 (left) and Case 3 (right); (b) typical instantaneous velocity and shear band formation.

The present FE simulations provide further insights into the retrogression. For $N_s = 4.9$, the subsequent rotational failure is initiated when the debris of the previous failure is completely detached from the backscarp (Fig. 3.4(a)). However, for $N_s = 6.8$, the subsequent failure is initiated at a backscarp height significantly smaller than slope height ($H_b < 2H/3$) because of the low s_{u0} of the sensitive clay (Fig. 3.4(a)). Two types of shear band formation occur in the failing soil blocks during the downslope movement (Fig. 3.4(b)). In type 1, the frontal part of the new soil block displaces at a faster rate, primarily in the horizontal direction, and a curved upward shear band forms. In type 2, the frontal part climbs up over the downslope moving soil and an inclined downward shear band forms in the failed soil block. These shear bands not only influence the remoulding process but also dictate the failure pattern observed after a landslide. Therefore, these flowslide simulations clearly show that the sites characterized by a low stability number are less prone to large retrogression than sites with a high stability number.

3.8.2 Shear strength gradient in sensitive clays

Cases 3–6 represent the simulations for varying shear strength gradients (k) of 0 to 3 but with the same stability number ($= 6.8$). Flowslide occurs in all four cases. Figure 3.5(a) and Videos s4–s6 show that the depth of subsequent slide decreases with an increase in shear strength gradient (Fig. 3.5(b)) because the weaker soil near the top of the sensitive clay layer cannot hold a deep backscarp stable. However, for uniform s_{u0} , as in Case 3, the depth of subsequent slide remains the same as the slope height, and the progressive flowslide continues up to the boundary of the domain. In other words, the retrogression distance increases with a decrease in k ; for example, L_R is 92.5 m and 205 m for k of 3 and 1, respectively.

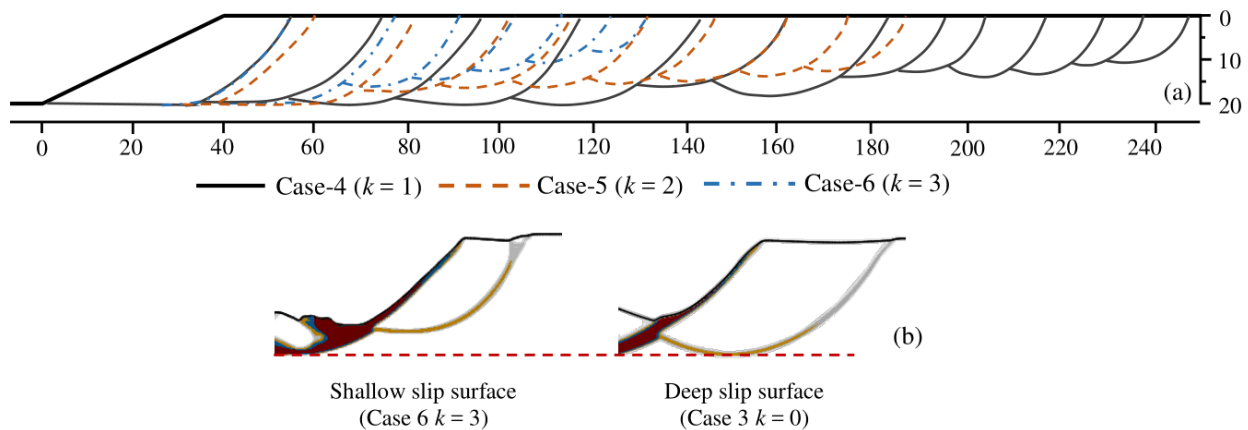


Fig. 3.5. Failure in Cases 4–6: (a) retrogression; (b) 3rd soil block failure for $k = 0$ and 3.

3.8.3 Undrained shear strength at large deformation

Previous studies show that at least 40% of the soils above the failure plane should have a very low s_u at large deformation (also known as remolded shear strength) in the range of $s_{uld} < 1.0$ kPa to cause a flowslide (Lebuis & Rissmann, 1979; Tavenas *et al.*, 1983; Strand *et al.*, 2017). The effects of s_{uld} are examined by comparing the results of Case 5 ($s_{uld} = 1$ kPa) and Case 7 ($s_{uld} = 5$ kPa). In both cases, retrogressive failure occurs by the formation of curved shear bands, which can be classified as a flowslide. For Case 5, the debris liquefies and flows out quickly by leaving

a very small amount over the basal failure surface at the end of the landslide (Fig. 3.2(e)). However, for the relatively high s_{uld} in Case 7, the remoulding occurs primarily around the shear surfaces, without significant liquefaction within the failed soil blocks, and the debris flow completely stops after several blocks in the downslope direction (Fig. 3.6(a)). The retrogression distance is ~ 147 m for $s_{uld} = 1.0$ kPa, while it is 96 m for $s_{uld} = 5.0$ kPa.

Figure 3.6(b) shows the instantaneous velocity of the soil elements after the failure of the fifth soil block in Case 5 and Case 7. As the crater is almost empty in Case 5, the failed soil block easily moves over the basal failure surface. However, in Case 7, the larger shear resistance along the failure surfaces decelerates the movement of the debris that provides additional lateral support to the backscarp. Consequently, the failed soil in Case 7 is less remoulded, and the runout and retrogression distances are reduced.

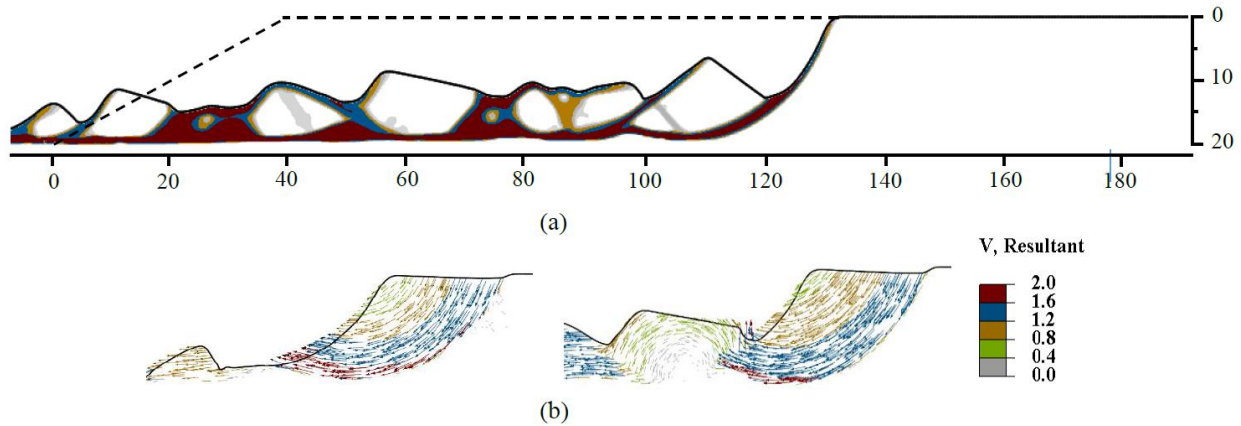


Fig. 3.6. Effects of large strain shear strength: (a) post-slide debris in Case 7; (b) instantaneous velocity of 5th soil block failure for Case 5 (left) and Case 7 (right).

3.8.4 Remolded energy

The progressive failure has also been characterized using remoulding energy E_R , which represents the area under the stress–strain curve until the soil is fully remoulded ($s_u = s_{uld}$) (Tavenas

et al., 1983; Thakur & Degago, 2012). In this study, when s_{u0} of the sensitive clay layer increases linearly with depth, the average of s_{ug} and s_{u0} at the toe level is used to calculate E_R .

The calculated E_R of all cases is listed in Table 3.1. One additional simulation is performed with a very high E_R (Case 8), compared to other flowslides analyses (Cases 2–7), by adopting high s_{uR} , δ_{95} and δ_{id} . The following are the key findings from these flowslide simulations (Cases 2–8).

i) No clear trend of increasing L_R with decreasing E_R is found. For the same E_R (= 22.9), L_R varies from 93 m to more than 500 m (Cases 3–6). Moreover, Cases 6–8 show a trend of increasing L_R with E_R . This implies that the single factor E_R is not sufficient to estimate L_R . In the attempts for a rough estimation of L_R , a large scatter has been found in L_R – E_R plots for historical landslides in Canadian and Norwegian sensitive clays, and the authors inferred that the landslide type has been a potential reason for scatteredness (Locat *et al.*, 2008; Thakur *et al.*, 2014). The present numerical simulations show that, even for the same type of landslide (flowslide), L_R cannot be estimated simply by using E_R . The other factors, as discussed above, should be considered.

ii) The simulations with high E_R produce less remoulded debris (compare Figs. 3.7 and 3.2(e)). Figure 3.7 shows that, although each soil block initially fails rotationally (flowslide), the downslope movement of the debris in this case with high E_R does not cause a significant remoulding. Therefore, ridges might be observed in a post-slide investigation, mimicking a spread-type landslide. Note that, in all the flowslide simulations, the debris moves out of the domain through the left boundary. However, in the field, the less remoulded debris (e.g. in Case 8) may not flow easily along the river channel, which might induce some resistance to the debris flow in the crater and reduce the retrogression distance.

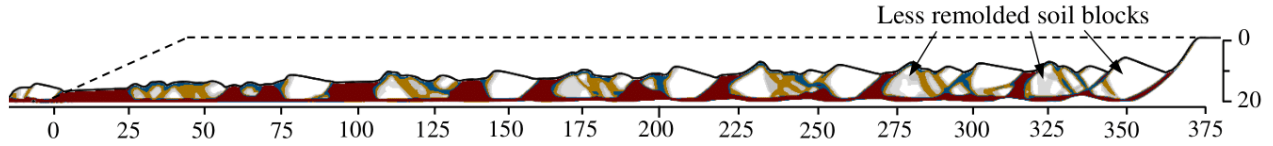


Fig. 3.7. Post-slide debris in the crater of Case 8.

3.9 Factors Affecting Spreads

3.9.1 In-situ stress condition

The three simulations in Cases 9–11 are conducted with a higher lateral earth pressure coefficient ($K = 1.2$) than that of Cases 4–6 ($K = 1.0$) while the other parameters are the same. Figure 3.8(a) shows the successive formation of shear bands (f_1 – f_{17}) for Case 10 (up to 200 m from the crest for clarity), which represents a typical spread where horsts and grabens form successively. A similar type of failure (spread) also occurs in Cases 9 and 11 (see Video s9–s11). When s_{u0} at the toe level is smaller, the tip of the quasi-horizontal shear band is further from the active failure zone in the overlying soil layer, compare Video s9 and s11. During downslope movement, the formation of additional shear bands in the graben together with significant remoulding of soil at its bottom subsides the grabens at a faster rate than horsts, which results in ridges in the debris (Fig. 3.8(b)), as observed in the field (Locat *et al.*, 2011). The retrogression continues up to the boundary of the domain ($L_R > 350$ m) for all three cases, which is significantly higher than the L_R of Cases 4–6 ($L_R = 93$ m–205 m). An increased shear strength gradient (k) changes the failure plane development and thereby reduces L_R in flowslides (Cases 4–6); however, k has less effect on retrogression in spreads simulated in Cases 9–11. In summary, comparing Cases 4–6 with Cases 9–11, it can be concluded that the earth pressure coefficient is a major factor, which affects both failure pattern and retrogression distance.

The earth pressure coefficient at-rest (K_0) and undrained shear strength ratio s_u/σ'_v of overconsolidated sensitive clay can be related to the overconsolidation ratio (OCR) as $K_0 = K_{0_NC} OCR^\alpha$

and $s_u/\sigma'_v = (s_u/\sigma'_v)_{NC}OCR^m$, respectively, where the subscript NC represents the normally consolidated stage ($OCR = 1$). Although scattered, for sensitive clays, the average values of exponents α and m are close to unity (Hamouche *et al.*, 1995), which implies that K_0 might be proportional to s_u/σ'_v . Therefore, two simulations are performed for increased K and corresponding s_{u0} (Cases 12 & 13). Note that, in Cases 9–11, s_{u0} is not increased with K because a large variation in α and m is observed; therefore, different s_u/σ'_v might also occur for a given K .

Spread occurs in both Cases 12 & 13, and the retrogressive failure continues up to the right boundary ($L_R > 350$ m) (Videos s12 & s13). In these cases, a horst forms when the previously failed graben moves a larger distance and settles more than they do in Case 9 because the higher s_{u0} in the upper part of the sensitive clay can maintain the stability of a larger unsupported soil (compare Videos s11 & s13). Moreover, the initial height of some horsts during formation is significantly smaller than slope height in Cases 12 & 13 (e.g. horsts below the shear bands f_7 & f_{15} in Fig. 3.8(c) and f_7 & f_{14} in Fig. 3.8(d)). Simulation results of Cases 9–13 show that the initial height of the horsts depends on the combined effect of s_{u0} and K , which could be one of the potential causes of varying debris thickness in the spread, as observed in the field (Demers *et al.*, 2014). An analysis has also been performed for the same geometry and soil properties as in Case 13, except for $K = 1.0$, and no retrogressive failure is found, which clearly shows the effect of K on failure.

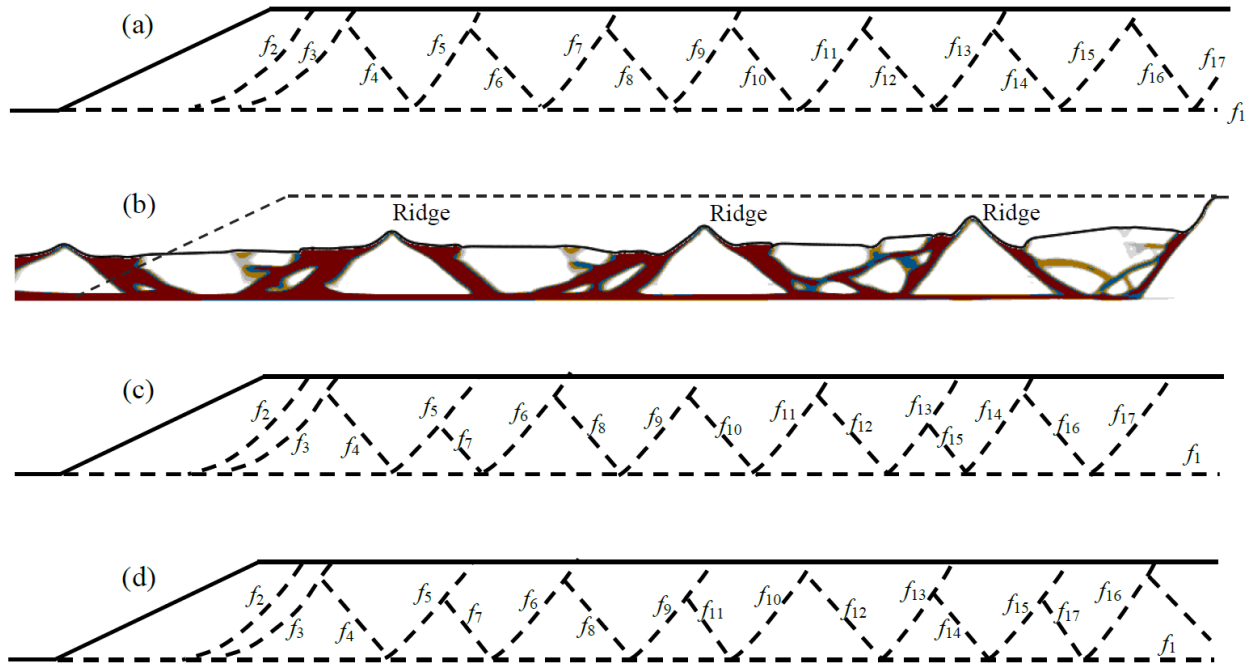


Fig. 3.8. Development of failure planes up to 200 m from crest: (a) Case 10; (b) post-slide debris in the crater of Case 10; (c) Case 12; (d) Case 13.

Previous studies show that the earth pressure coefficient K (or K_0) is an important factor that affects the failure pattern of a slope of strain-softening materials (Lo & Lee, 1973; Locat *et al.*, 2013; Potts *et al.*, 1997). A slope with high lateral stress stores more strain energy, and once it is released, for example, by the local failure triggered by toe erosion, the soil layer tends to expand laterally (Bjerrum, 1964). This explains horizontal shear band formation in Cases 9–13, rather than curving upward as in Cases 1–8. Based on several historical landslides in eastern Canada and Scandinavia, Geertsema *et al.* (2006) suggested that spreads might occur in slopes having higher s_{u0} (also higher k) than that required for a flowslide. The present FE simulation cases indicate that a higher earth pressure coefficient, which is an indicator of higher s_{u0} , might be a factor for the development of a spread. Note, however, that spread has also occurred in normally consolidated to lightly overconsolidated clays, where the earth pressure coefficient is expected to be low (Locat *et al.*, 2015), which might be due to the effects of other factors.

The retrogression distance (L_R) depends on the failure pattern. For example, in Case 1 ($N_s = 3.8$), only a rotational slide occurs, whereas, even for a lower N_s ($= 3.1$) in Case 13, the retrogression continues more than 350 m. In other words, potential retrogression and L_R may not be calculated using only N_s .

3.9.2 Brittleness

A decrease in s_{uR} and δ_{95} increases the brittleness of sensitive clays (i.e. s_u decreases rapidly with δ , see Eq. (3.3)). First, the effects of s_{uR} and δ_{95} on failure are examined through Cases 14 and 15 with a low value of K ($= 1.0$). In Case 14, the soil has higher s_{u0} and less brittleness, compare to Case 6. As discussed before, flowslide occurs in Case 6, whereas the failure pattern in Case 14 is a combination of flowslide and spread (compound failure). The first couple of soil blocks fail as rotational slides; however, horsts and grabens form in the subsequent retrogressive failure (Fig. 3.9(a) and Video s14). This type of compound failure has been observed in the field. For example, a detailed geotechnical and morphological analysis of the 2016 St-Luc-de-Vincennes bowl-shaped landslide shows that the failure occurred in two distinct phases—the landslide started as a flowslide and finished as a spread (Tremblay-Auger *et al.*, 2018). In Case 15, the soil has much lower brittleness than that in Case 14, and only spread failure is observed (Fig. 3.9(b) and Video s15).

Retrogression distance increases with brittleness: L_R is greater than 350 m in Case 14, while it is 151 m in Case 15. For less brittle soil, the driving force may not be sufficient to create a longer horizontal shear band (e.g. f_1 in Fig. 3.9(b)), and thus the retrogression stops.

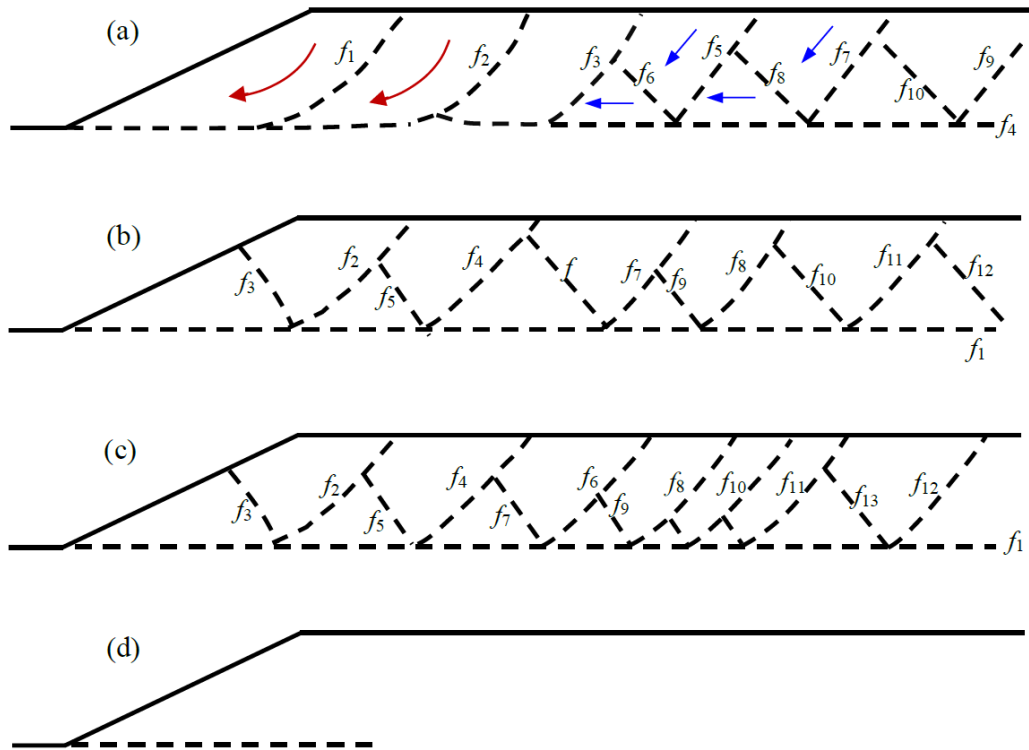


Fig. 3.9. Development of failure planes up to 120 m from crest: (a) compound failure in Case 14; (b) spread in Case 15; (c) spread in Case 16; (d) no global failure in Case 17.

Cases 16 and 17 are designed to study the effects of brittleness for higher K values ($K = 1.2$ and 1.4). Comparison of the failure pattern in Case 12 (more brittle) and Case 16 shows that spread failures occur in both cases (Figs. 3.8(c) & 3.9(c) and Videos s12 & s16), indicating that brittleness of the soil has less effect on failure patterns for these cases.

The retrogression distance in Case 16 is 204 m, which is larger than in Case 15. The only difference between Cases 15 and 16 is the stress state in the slope. With higher lateral stress (i.e. larger K value in Case 16), a higher driving force is available for the horizontal shear band propagation, and thus the landslide tends to have a larger L_R . This finding is consistent with the conclusion of Locat *et al.* (2013) based on their 1-D FE analyses on spread failure.

In Case 17, the soil has high s_{u0} ($N_s = 3.1$) and less brittleness, and a horizontal shear band forms at the bottom of the slope; however, no failure occurs in the overlying soil layer (Fig. 3.9(d))

and Video s17). Because of the high shear strength, the slope can remain stable, even with an existing basal shear band. This phenomenon might exist in the field. However, an earthquake, external loading from construction, or further riverbank erosion, could cause the global failure of a slope along an already existing basal weak layer that developed in response to a former destabilizing factor.

Finally, Case 18 is used to examine the effect of s_{uld} on the spread. The soil properties in Case 18 are the same as in Case 10, except for $s_{uld} = 5$ kPa. Figure 3.10 and Video s18 show that only a few horsts and grabens form in Case 18 and that the retrogression stops after $L_R = 154$ m. The failed soil blocks have much less downslope displacement and remoulding compared to those in Case 10 (Fig. 3.8(b)). For a spread, even though s_{uld} is increased from 1 kPa (Case 10) to 5 kPa (Case 18) only, the increased shear resistance along the failure planes significantly reduces the runout and retrogression distances.

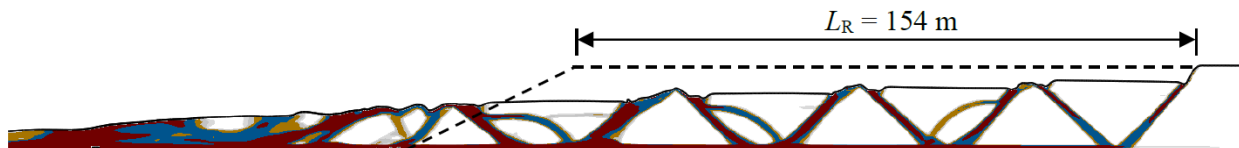


Fig. 3.10. Failure in Case 18.

3.9.3 Slope angle

A mild slope of 3:1 (Case 19) is used to study the effects of steepness on failure patterns. The s_{u0} profile of Case 19 is the same as for Case 15, but the soil is more brittle. Figure 3.11 shows that a typical spread occurs in Case 19, which indicates that a mild slope tends to have spread failure even though the soil is relatively brittle. All the FE simulations in the present study show that the first failure always occurs somewhere beneath the slope crest, whether in a flowslide or spread. In a milder slope, the horizontal shear band is longer when propagating to the same position relative to the slope crest. Consequently, the shear resistance along the failure surface is larger than

in a steeper slope. The higher shear resistance may prevent the overlying soil layer from failing, and the horizontal shear band may propagate further, inducing a spread.

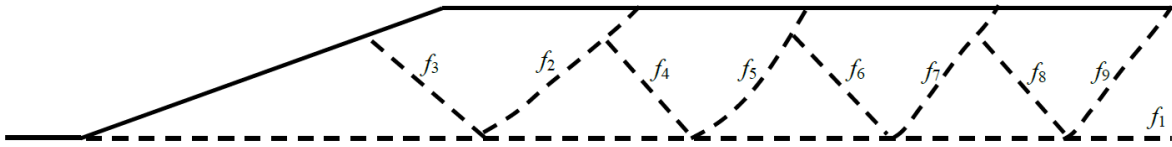


Fig. 3.11. Formation of failure planes in Case 19.

3.9.4 Opposite riverbank

The opposite riverbank is considered in Case 20, and the geometry and soil properties are the same as in Case 19. In Case 19, the debris flows freely out of the domain and the retrogression continues to the right boundary of the model ($L_R > 350$ m) (Video s19). On the contrary, in Case 20, the opposite riverbank provides enough lateral support to the almost intact soil blocks, so the debris gains equilibrium and stays inside the crater (Fig. 3.3 and Video s20). The retrogression stops after $L_R = 64$ m, even though the horizontal shear band penetrates into the slope behind the backscarp (see f_1 in Fig. 3.3(d)).

For flowslides, the restriction of the opposite riverbank is probably not a dominant factor, because the debris usually liquefies sufficiently to flow downstream and upstream. However, for spreads, because the debris is less remoulded, the topography of the opposite riverbank affects significantly the retrogression and runout distances.

3.10 Practical Implications

Until now, no widely-accepted criteria have been developed for estimating the extent of large retrogressive landslides. In Norway, three empirical approaches have been proposed to estimate the maximum retrogression distance measured from the slope toe (R) for flowslides in quick clay (Haugen *et al.*, 2017). The Norwegian Water Resources and Energy Directorate (NVE, 2014) suggested $R = 15H$. A Norwegian joint venture (NIFS, 2016) recommends that retrogression

occurs if more than 40% of the soil above the critical slip surface of the first slide is sensitive clay. In that case, R should be obtained by drawing a line from the base of the critical slip surface (as opposed to the slope toe in NVE, 2014) inclined at 1:5, 1:10 or 1:15 for three ratings of retrogression as a function of slope geometry and soil properties. The Norwegian Geotechnical Institute (NGI, 2016) also suggested using a 1:15 line from the base of the critical slip surface for a quick clay layer of $s_{\text{uid}} < 1$ kPa, and a steeper line of 1:3–1:2 for the non-sensitive soil layer. In Quebec, the Canadian province most exposed to large retrogressive landslides, a statistical method has been developed by Lebuis *et al.*, (1983) and Rissmann *et al.*, (1985) where R is estimated by applying a third-order moving average on R of the historical scars in the area of interest. Turmel *et al.* (2018) compared the performance of these approaches for historical flowslides in Quebec and showed a large variation of R from $2 H$ to $50 H$, although in many cases, $R < 15 H$. In other words, the available approaches could be significantly conservative or nonconservative.

Examining the failure mechanisms through numerical simulations in this study, the following recommendations can be made for a better assessment of failure types and estimation of retrogression distance.

- a) The landslide affected area can be divided into three zones: initiation, retrogression, and runout. A detailed geotechnical characterization, together with slope and upslope ground surface angles, is required for the former two. However, for runout, the mobility of the debris is more important, which is affected by the topography, surface roughness and debris flow along the river. Some guidelines are available for qualitative and quantitative assessment of slope stability (e.g. Lefebvre *et al.*, 2008).
- b) Retrogression or runout might occur only after the failure of the first soil block, which is currently analysed using the LE methods in effective stress (e.g. in Quebec, Canada) or total

stress (e.g. in Norway) frameworks; however, the selection of the method is still a subject of discussion, as it depends on several factors (Thakur, 2016). The soil parameters for LE analyses should be carefully selected, because the failure surfaces form progressively, as shown in the present FE analyses, which cannot be accommodated directly in the LE analysis. Calibrating against case records, the post-peak effective strength parameters (Lefebvre, 1981) and undrained shear strength are currently used in slope stability analyses. A Lagrangian-based FE software could be used to simulate progressive failure; however, it cannot model very large deformation.

- c) The following factors should be considered to estimate retrogression distance when more uncertainties are involved than in the evaluation of the first slide. In addition to peak and fully remoulded shear strength, the rate of strength degradation should be evaluated properly. For the former two, commonly used field and laboratory tests (e.g. vane shear, CPT, Swedish fall cone) could be used. For the latter one, the electric vane shear tests appear to be a promising tool. The present FE analyses show that the in-situ earth pressure coefficient could change the failure pattern. Based on typical laboratory and field tests, the OCR can be determined, which can then be used to estimate the earth pressure coefficient using empirical relations (e.g. Hamouche *et al.*, 1995) when field tests are not possible. Finally, shear strength gradient with depth should be properly evaluated because it also affects the retrogression distance. Further studies are required to develop simplified approaches for practical applications considering the factors mentioned above.

3.11 Conclusions

Post-slide investigations show that the majority of large-scale retrogressive landslides occurring in sensitive clays are flowslides and spreads. The mechanism of successive soil block

failure is very different in these two types of landslides, which affects retrogression and runout distances. In the present study, large-deformation FE analyses are performed to identify some conditions that could lead to flowslides or spreads. Strain-softening and strain-rate effects on the undrained shear strength of sensitive clay, s_u , are incorporated in the model. An increased strain-rate effect on s_u of the remoulded soil that flows at a high speed is considered. It is found that the criterion based on a single parameter or a combination of a few (e.g. remoulded shear strength, sensitivity, or stability number) cannot always characterise a flowslide or spread. The failure mechanism is rather complex, although some general agreements between empirical criteria and present FE models are found. The following conclusions are drawn from this study:

- (a) The mobility of debris can change the failure pattern. A flowslide is expected if the debris moves out of the crater easily during retrogression; however, the same slope might fail as a spread if the debris movement is reduced by other factors.
- (b) An increase in brittleness (i.e. increase in slope of the post-peak s_u degradation curve) increases the possibility of flowslide; otherwise, it would be a spread, if retrogressive failure occurs.
- (c) For an average initial undrained shear strength of sensitive clay (s_{u0}), the retrogression distance in a flowslide reduces with an increase in the gradient of s_{u0} with depth.
- (d) No clear trend of increasing retrogression distance with stability number is found for the cases analysed. Retrogression depends on a combination of several factors, including soil properties and failure type. The available empirical criteria might over- or under-estimate the retrogression distance of a flowslide.
- (e) An increase in the lateral earth pressure coefficient increases the potential of spread failures.

(f) In a spread identified as such from post-slide features, the height of the horsts during formation could be significantly smaller than slope height. Moreover, the height of the grabens reduces quickly, compared to horsts, during the downslope movement of the failed soil blocks. The combined effect of these two processes could explain the smaller debris thickness than slope height, as observed in the field.

Notations

β	parameter for strain-rate relation
θ	slope angle
δ	accumulated plastic shear displacement
δ_{95}	δ at which s_u reduced by 95% of $(s_{up}-s_{uR})$
δ_{ld}	δ at large shear displacement
γ_w	unit weight of water
$\dot{\gamma}_{ref}$	reference strain rate
ν_u	undrained Poisson's ratio
η	Parameter for strain-rate relation
σ_v	vertical total stress
σ_h	horizontal total stress
E_R	remolding energy
E_u	undrained modulus of elasticity
H	slope height
IL	liquidity index
K	earth pressure coefficient in terms of total stress

K_0	earth pressure coefficient in terms of effective stress
k	shear strength gradient
L_R	retrogression distance
N_s	stability number of the slope
R	soil rapidity
S_t	remolded sensitivity of clay, s_{u0}/s_{uR}
s_u	mobilized undrained shear strength
s_{u0}	initial (peak) undrained shear strength
s_{u0c}	initial (peak) undrained shear strength of crust
s_{uld}	undrained shear strength at large displacement
s_{ug}	undrained shear strength at ground surface
s_{uR}	remolded s_u at large plastic shear displacement
u	pore water pressure
V	horizontal dimension of the slope
z	depth below the crest of the slope

References

- Benson, D. J. (1992). Computational methods in lagrangian and eulerian hydrocodes. *Comput. Method Appl. M.* **99**, No. 2–3, 235–394.
- Benson, D. J. & Okazawa, S. (2004). Contact in a multi-material eulerian finite element formulation. *Comput. Method Appl. M.* **193**, No. 39–41, 4277–4298.
- Bjerrum, L. (1967). Progressive failure in slopes of overconsolidated plastic clay and clay shales. *Terzaghi Lecture. Journal of the Soil Mechanics and Foundations Division, ASCE.* **93**, No. 5, 3–49.

- Borges, J. L. (2008). Cut slopes in clayey soils: consolidation and overall stability by finite element method. *Geotech. Geol. Eng.* **26**, No. 5, 479–491.
- Boukpeti, N., White, D. J., Randolph, M. F. & Low, H. E. (2012). Strength of fine-grained soils at the solid–fluid transition. *Géotechnique* **62**, No. 3, 213–226.
- Carson, M. A. (1977). On the retrogression of landslides in sensitive muddy sediments. *Can. Geotech. J.* **14**, No. 4, 582–602.
- Carson, M. A. (1979). On the retrogression of landslides in sensitive muddy sediments: reply. *Can. Geotech. J.* **16**, No.2, 431–444.
- Demers, D., Robitaille, D. & Perret, D. (2000). The St. Boniface landslide of April 1996: a large retrogressive landslide in sensitive clay with little flow component. In *Landslides in Research, Theory and Practice: Proceedings of the 8th International Symposium on Landslides*, 1–447. Cardiff.
- Demers, D., Robitaille, D., Locat, P. & Potvin, J. (2014). Inventory of large landslides in sensitive clay in the province of Quebec, Canada: preliminary analysis. In *Landslides in Sensitive Clays – from geosciences to risk management* (eds J.-S. L’Heureux, A. Locat, S. Leroueil, D. Demers and J. Locat), pp. 77–89. Dordrecht, the Netherlands: Springer.
- Dey, R., Hawlader, B., Phillips, R. & Soga, K. (2015). Large deformation finite-element modeling of progressive failure leading to spread in sensitive clay slopes. *Géotechnique* **65**, No. 8, 657–668.
- Dey, R., Hawlader, B., Phillips, R. & Soga, K. (2016). Modeling of large-deformation behaviour of marine sensitive clays and its application to submarine slope stability analysis. *Can. Geotech. J.* **53**, No. 7, 1138–1155.

- Duncan, J. M. & Dunlop, P. (1968). Slopes in stiff-fissured clays and shales. California Univ Berkeley Office of Research Services. No. TE-68-6.
- Dutta, S., Hawlader, B. & Phillips, R. (2015). Finite element modeling of partially embedded pipelines in clay seabed using coupled eulerian–lagrangian method. *Can. Geotech. J.* **52**, No. 1, 58–72.
- Einav, I. & Randolph, M. (2006). Effect of strain rate on mobilised strength and thickness of curved shear bands. *Géotechnique* **56**, No. 7, 501–504.
- Geertsema, M., Clague, J. J., Schwab, J. W. & Evans, S. G. (2006). An overview of recent large catastrophic landslides in northern British Columbia, Canada. *Eng. Geol.* **83**, No. 1–3, 120–143.
- Geertsema, M. & L’Heureux, J. S. (2014). Controls on the dimensions of landslides in sensitive clays. In *Landslides in Sensitive Clays – from geosciences to risk management* (eds J.-S. L’Heureux, A. Locat, S. Leroueil, D. Demers and J. Locat), pp. 105–117. Dordrecht, the Netherlands: Springer.
- Hamouche, K. K., Leroueil, S., Roy, M. & Lutenecker, A. J. (1995). In situ evaluation of K_0 in eastern Canada clays. *Can. Geotech. J.* **32**, No. 4, 677–688.
- Haugen, E. D., Tveit, M. & Heyerdahl, H. (2017). Mapping Quick Clay Hazard Zones: Comparison of Methods for the Estimation of the Retrogression Distance. In *Landslides in sensitive clays – from research to implementation* (eds V. Thakur, J.-S. L’Heureux and A. Locat), pp. 311–321. Cham, Springer.
- Hawlader, B., Fouzder, A. & Dutta, S. (2016) Numerical modeling of suction and trench formation at the touchdown zone of steel catenary riser. *Int. J. Geomech.* **16**, No. 1, 04015033, [https://doi.org/10.1061/\(ASCE\)GM.1943-5622.0000497](https://doi.org/10.1061/(ASCE)GM.1943-5622.0000497).

- Islam, N., Hawlader, B., Wang, C. & K, Soga. (2019). Large deformation finite element modelling of earthquake-induced landslides considering strain-softening behaviour of sensitive clay. *Can. Geotech. J.* **56**, 1003–1018.
- Jeong, S. W., Leroueil, S. & Locat, J. (2009). Applicability of power law for describing the rheology of soils of different origins and characteristics. *Can. Geotech. J.* **46**, 1011–1023.
- Lebuis, J. & Rissmann, P. (1979). Les coulées argileuses dans le région de Québec et de Shawinigan. In: *Argiles sensibles, pentes instables, mesures correctives et coulées des régions de Québec et Shawinigan*, Geological Association of Canada Guidebook, pp. 19–40.
- Lebuis, J., Robert, J. M. & Rissmann, P. (1983). Regional mapping of landslide hazard in Quebec. In *Proceedings of the symposium on slopes on soft clays*. Swedish Geotechnical Institute report no. 17, 205–262. Sweden, Linköping.
- Lefebvre, G. (1981). Fourth Canadian Geotechnical Colloquium: Strength and slope stability in Canadian soft clay deposits. *Can. Geotec. J.* **18**, No. 3, 420–442.
- Lefebvre, G. (1986). Slope instability and valley formation in Canadian soft clay deposits. *Can. Geotech. J.* **23**, No. 3, 261–270.
- Lefebvre, G., Demers, D., Leroueil, S. & Robitaille, D. (2008). Slope stability evaluation: more observation and less calculation. In *Proceedings of the 4th Canadian Conference on Geohazards: From Causes to Management*, Quebec.
- Lefebvre, G., Leboeuf, D., Hornych, P. & Tanguay, L. (1992). Slope failures associated with the 1988 Saguenay earthquake, Quebec, Canada. *Can. Geotech. J.* **29**, No. 1, 117–130.
- Lefebvre, G. (2017). Sensitive clays of eastern Canada: From geology to slope stability. In *Landslides in sensitive clays – from research to implementation* (eds V. Thakur, J.-S. L’Heureux and A. Locat), pp. 15–34. Cham, Springer.

- Leroueil, S., Vaunat, J., Picarelli, L., *et al.* (1996). Geotechnical characterisation of slope movements. In *proceedings of the 7th International Symposium on Landslides*, vol. 1, pp. 53–74. Trondheim.
- Lo, K. Y. and Lee, C. F. (1973). Stress analysis and slope stability in strain-softening materials. *Géotechnique* **23**, No. 1, 1–11.
- Locat, A., Leroueil, S., Bernander, S., *et al.* (2011). Progressive failures in eastern Canadian and Scandinavian sensitive clays. *Can. Geotech. J.* **48**, No. 11, 1696–1712.
- Locat, A., Jostad, H. P. & Leroueil, S. (2013). Numerical modeling of progressive failure and its implications for spreads in sensitive clays. *Can. Geotech. J.* **50**, No. 9, 961–978.
- Locat, A., Leroueil, S., Fortin, A., Demers, D. & Jostad, H. P. (2015). The 1994 landslide at Sainte-Monique, Quebec: geotechnical investigation and application of progressive failure analysis. *Can. Geotech. J.* **52**, No. 4, 490–504.
- Locat, A., Locat, P., Demers, D., *et al.* (2017). The Saint-Jude landslide of 10 may 2010, Quebec, Canada: Investigation and characterization of the landslide and its failure mechanism. *Can. geotech. J.* **54**, No. 10, 1357–1374.
- Locat, J. (1997). Normalized rheological behaviour of fine muds and their flow properties in a pseudoplastic regime. In *Debris-flow hazards mitigation: mechanics, prediction, and assessment*. ASCE, New York, pp. 260–269.
- Locat, P., Leroueil, S. & Locat, J. (2008). Remaniement et mobilité des débris de glissements de terrain dans les argiles sensible de l’est du Canada. In *Proceedings of the 4th Canadian conference on geohazards: from causes to management*, pp. 97–106. Presse de l’Université Laval, Québec.

- Locat, P., Leroueil, S., Locat, J. & Demers, D. (2014). Characterization and post-failure analysis of the 1980 landslide in sensitive clays at Havre-St-Pierre, Québec, Canada. In *Landslides in Sensitive Clays – from geosciences to risk management* (eds J.-S. L’Heureux, A. Locat, S. Leroueil, D. Demers and J. Locat), pp. 133–144. Dordrecht, the Netherlands: Springer.
- Mitchell, R. J. & Markell, A. R. (1974). Flowsliding in sensitive soils. *Can. Geotech. J.* **11**, No. 1, 11–31.
- NGI (2016). Teknisk notat 20140848-01-TN rev.2 Beskrivelse av L/H tabellen for vurdering av løснеområdet for områdeskred, 01.02.2016.
- NIFS (2016). Metode for vurdering av løсне- og utløpsområder for områdeskred. Naturfareprosjektet: Delprosjekt 6 Kvikkleire. NVE- rapport 14/2016. ISSN: 1501-2832.
- Norem, H., Locat, J. & Schieldrop, B. (1990). An approach to the physics and the modeling of submarine flowslides. *Mar. Georesour. Geotec.* **9**, No. 2, 93–111.
- NVE (2014). Safety against quick clay landslides Guideline 7/2014.
- Odenstad, S. (1951). The landslide at Sköttorp on the Lidan River, February 2, 1946. *R. Swedish Inst. Proc.* **4**, 1–38.
- Perret, D., Mompin, R., Demers, D., Lefebvre, G. & Pugin, A. J. M. (2013). Two large sensitive clay landslides triggered by the 2010 Val-Des-Bois earthquake, Quebec (Canada)—implications for risk management. In *1st Int. Workshop on Landslides in Sensitive Clays (IWLSC)*, Poster. Quebec, Canada.
- Perret, D., Therrien, J., Locat, P. & Demers, D. (2019). Influence of surficial crusts on the development of spreads and flows in Eastern Canadian sensitive clays. In *Proceedings of the 72nd Canadian Geotechnical Conference*, St. John’s.

- Potts, D., Kovacevic, N. & Vaughan, P. (1997). Delayed collapse of cut slopes in stiff clay. *Géotechnique* **47**, No. 5, 953–982.
- Puzrin, A. M., Gray, T. E. & Hill, A. J. (2016). Retrogressive shear band propagation and spreading failure criteria for submarine landslides. *Géotechnique* **67**, No. 2, 95–105.
- Qiu, G. & Grabe, J. (2012). Numerical investigation of bearing capacity due to spudcan penetration in sand overlying clay. *Can. Geotech. J.* **49**, No. 12, 1393–1407.
- Quinn, P. E., Diederichs, M. S., Rowe, R. K. & Hutchinson, D. J. (2011). A new model for large landslides in sensitive clay using a fracture mechanics approach. *Can. Geotech. J.* **48**, No. 8, 1151–1162.
- Randolph, M. F., White, D. J. & Yan, Y. (2012) Modelling the axial soil resistance on deep-water pipelines. *Géotechnique* **62**, No. 9, 837–846.
- Rissman, P., Allard, J. D. & Lebuis, J. (1985). Zones exposées aux mouvements de terrain le long de la rivière Yamaska, entre Yamaska et Saint-Hyacinthe. Ministère de l'Énergie et des Ressources du Québec.
- Söderblom, R. (1974). A new approach to the classification of quick clays. Swedish Geotechnical Institute reprints and preliminary reports, No. 55, pp. 1–17.
- Strand, S. A., Thakur, V., L'Heureux, J. S., *et al.* (2017). Runout of landslides in sensitive clays. In *Landslides in sensitive clays – from research to implementation* (eds V. Thakur, J.-S. L'Heureux and A. Locat), pp. 289–300. Cham, Springer.
- Tavenas, F., Chagnon, J. Y. & La Rochelle, P. (1971). The Saint-Jean-Vianney landslide: observations and eyewitnesses accounts. *Can. Geotech. J.* **8**, No. 3, 463–478.

- Tavenas, F., Flon, P., Leroueil, S. & Lebus, J. (1983). Remolding energy and risk of slide retrogression in sensitive clays. In *Proceedings of the Symposium on Slopes on Soft Clays*, SGI Report, No. 17, 423–454. Linköping, Sweden.
- Tavenas, F. (1984). Landslides in Canadian sensitive clays — a state-of-the-art. In *Proceedings of the 4th International Symposium on Landslides*, Toronto, Ontario, vol. 1, pp. 141–153.
- Thakur, V. & Degago, S. A. (2012). Quickness of sensitive clays. *Géotechnique Letters*, **2**, No. 3, 87–95.
- Thakur, V., Degago, S., Oset, F., *et al.* (2014). Characterization of post-failure movements of landslides in soft sensitive clays. In *Landslides in Sensitive Clays – from geosciences to risk management* (eds J.-S. L’Heureux, A. Locat, S. Leroueil, D. Demers and J. Locat), pp. 91–103. Dordrecht, the Netherlands: Springer.
- Thakur, V. (2016). Landslide hazards in sensitive clays: Recent advances in assessment and mitigation strategies. In *Proceedings of the 17th Nordic Geotechnical Meeting, Challenges in Nordic Geotechnics*, Reykjavik, Iceland, pp. 1141–1152.
- Tremblay-Auger, F., Locat, A., Leroueil, S., *et al.* (2016). The 2016 landslide at St-Luc-de-Vincennes. In *Proceedings of the 71st Canadian Geotechnical Conference and the 13th Joint CGS/IAH-CNC Groundwater Conference*, Edmonton, Alberta.
- Turmel, D., Locat, J., Locat, P. & Demers, D. (2017). Parametric analysis of the mobility of debris from flow slides in sensitive clays. In *Landslides in sensitive clays – from research to implementation* (eds V. Thakur, J.-S. L’Heureux and A. Locat), pp. 301–310. Cham, Springer.
- Turmel, D., Potvin, J., Demers, D., (2018). Empirical estimation of the retrogression and the runout distance of sensitive clay flowslides. In *Proceedings of the 7th Canadian Geohazards Conference*, Canmore, Alberta.

- Turmel, D. Locat, P., Locat, J., Locat, A. & Leroueil, S. (2019). The energy reduction factor (F_{ER}) to model sensitive clay flowslides using in situ geotechnical and rheological data. *Landslides* 1–15, <https://doi.org/10.1007/s10346-019-01321-5>.
- Wang, C., Hawlader, B., Islam, N. & Soga, K. (2019). Implementation of a large deformation finite element modeling technique for seismic slope stability analyses. *Soil Dyn. Earthq. Eng.* **127**, 105824, <https://doi.org/10.1016/j.soildyn.2019.105824>.
- Zakeri, A. & Hawlader, B. (2013). Drag forces caused by submarine glide block or out-runner block impact on suspended (free-span) pipelines—Numerical analysis. *Ocean Eng.* **67**, 89–99.
- Zhu, H. & Randolph, M. F. (2011). Numerical analysis of a cylinder moving through rate dependent undrained soil. *Ocean Eng.* **38**, No. 7, 943–953.

Chapter 4

Modeling of Initial Stresses and Seepage in Large Deformation Finite Element Simulation of Sensitive Clay Landslides

Co-Authorship: This chapter has been submitted as a technical paper for publication in a journal as: Wang, C., Hawlader, B., Perret, D. and Soga, K., ‘Modeling of initial stresses and seepage in large deformation finite element simulation of sensitive clay landslides.’ Most of the research presented in this chapter has been conducted by the first author. He also prepared the draft manuscript. The other authors mainly supervised the research and reviewed the manuscript.

Videos s1–s9 are available in the supplementary data submitted together with this thesis.

4.1 Abstract

In-situ effective stresses and seepage forces, which are then used for modeling subsequent undrained retrogressive failure in total stress, triggered by toe erosion. A strain-softening and strain-rate dependent undrained soil strength model, which captures the behavior of soil from its intact condition to a fluid-like remolded material, is adopted in the retrogressive failure analysis. The FE simulation covers different phases of a landslide, including the initiation and retrogression of failure, and debris runout. Finally, using the developed numerical technique, the 2010 Saint-Jude landslide in Quebec, Canada, is simulated.

4.2 Introduction

Large-scale landslides in sensitive clays usually involve successive failure of soil blocks, and the impact of such failures might extend over several hundred meters (Demers et al. 2014). The whole process involves both drained and undrained loadings. Most of the slopes along watercourses are created by valley formation over thousands of years, which could be considered as a drained process (Locat et al. 2013). However, once the failure is triggered and necessary

conditions for retrogression are satisfied, the retrogressive landslide might occur rapidly, in a few minutes, under an undrained condition.

Currently, the retrogressive landslide hazard is assessed using empirical or statistical approaches. For example, in Norway, the maximum retrogression of a quick clay landslide is considered to the point where a 1:5 to 1:15 inclined line from the slope toe or the bottom of the first failure surface intersects the upslope ground surface (Haugen et al., 2017). However, in Canada, statistical approaches based on the size of historical scars are used to estimate retrogression distance (Lebuis et al. 1983; Rissmann et al. 1985). One of the main challenges involved in investigating the mechanisms of this type of large-scale landslides is that the complete process cannot be modeled using typical limit equilibrium (LE) or small-strain finite element (FE) modeling techniques.

Empirical, conceptual, analytical, and numerical modeling techniques have been proposed to explain upward progressive failure. The criteria for estimating the retrogression of large-scale landslides are defined by one or a combination of the following parameters: stability number, $N_s > 4-8$ (Mitchell and Markell 1974; Mitchell 1978; Tavenas 1984; Leroueil 2001); fully remolded undrained shear strength, $s_{ur} < 1$ kPa (Lebuis et al. 1983; Demers et al. 2014; Thakur et al. 2014); liquidity index, $IL > 1.2$ (Tavenas 1984); sensitivity, $S_t > 30$ (Lebuis et al. 1983); or rapidity number ≥ 8 (Söderblom 1974). The mechanism of spread has been explained conceptually by the formation of quasi-horizontal failure planes through a weak zone and subsequent failure of the upper soil as Δ -shaped horsts and ∇ -shaped grabens (Odenstad 1951; Carson 1977).

Locat et al. (2013) conducted numerical modeling of upward progressive failure. The in-situ stresses of soil were calculated first under a drained condition. Then, the initiation and progression of a quasi-horizontal shear band were modeled simply by introducing unloading to the soil layer

overlying the predefined shear zone. This quasi-static approach can simulate the progressive formation of a horizontal shear band due to strain-softening; however, it cannot model the failure of elastic soil above the horizontal shear band. Dey et al. (2015) showed that the Eulerian FE modeling can simulate the large deformation of soil and the complete failure process, such as formation of horsts and grabens in a spread. However, several key factors influencing the failure, as discussed below, have not been investigated.

Progressive failure is significantly influenced by in-situ stress conditions, specifically the earth pressure coefficient at-rest (K_0). The whole process in previous Eulerian FE analyses was simulated in total stress, where the in-situ stresses were given by the ratio of the lateral and vertical total stresses ($K \leq 1.0$) (Dey et al. 2015). However, field evidence suggests that K_0 of sensitive clays could be significantly higher than 1.0 (Hamouche et al. 1995).

Groundwater seepage and high artesian pressure can increase the potential for triggering a landslide (e.g., 2010 Saint-Jude landslide, Locat et al. 2017). The seepage cannot be modeled directly in the present Eulerian FE approach because it can handle only a single-phase material. Also, seepage has not been modeled in previous large deformation numerical studies of progressive landslides (Dey et al. 2015; Tran et al. 2019).

The shear strength of sensitive clay could be high when the failure initiates; however, the remolding of soil with downslope movement could reduce the shear strength to a very low value (< 1 kPa) (Lebuis et al. 1983; Tavenas 1984; Demers et al. 2014). In a spread, horsts and grabens might slide at a high speed over the remolded soil. Similarly, in a flowslide, the remolded soil might flow like a fluid at a high velocity (several meters per second in some cases) (Tavenas et al. 1971). Moreover, a retrogressive landslide is a dynamic rather than a quasi-static problem, as has been assumed in previous numerical studies (Locat et al. 2015; Dey et al. 2015). Therefore, a

model for strain-rate effects that can capture the strength behavior of both soil and fluid-like material needs to be implemented in the Eulerian FE analysis to simulate large landslides.

In the present study, the numerical approaches of modeling seepage and in-situ stresses in terms of effective stress for a Eulerian FE modeling are presented. Using the developed techniques, the retrogressive landslide is simulated where a strain-softening and a strain-rate dependent undrained shear strength model of sensitive clay is implemented. Finally, the mechanism of a large-scale landslide in Quebec, which was triggered by the combined effects of toe erosion and artesian pressure near the slope, is investigated.

4.3 Numerical Modeling

The numerical analysis is performed using the Eulerian-based FE method available in Abaqus/Explicit FE software; however, for the verification of the modeling, some analyses are performed using Abaqus/Standard, which uses an implicit time integration scheme (called “implicit FE” in the following sections). In the Eulerian approach, the material (soil) flows through the fixed mesh without causing numerical issues related to mesh distortion. Thus, the large displacement of soil debris and the development of large strains in the failure planes can be simulated. Further details on the mathematical formulations of the Eulerian FE approach, mesh sensitivity analysis, and its applications are available in previous studies (Benson 1992; Benson and Okazawa 2004; Qiu and Grabe, 2012; Dey et al. 2015, 2016; Dutta et al. 2015; Islam et al. 2019; Wang et al. 2019).

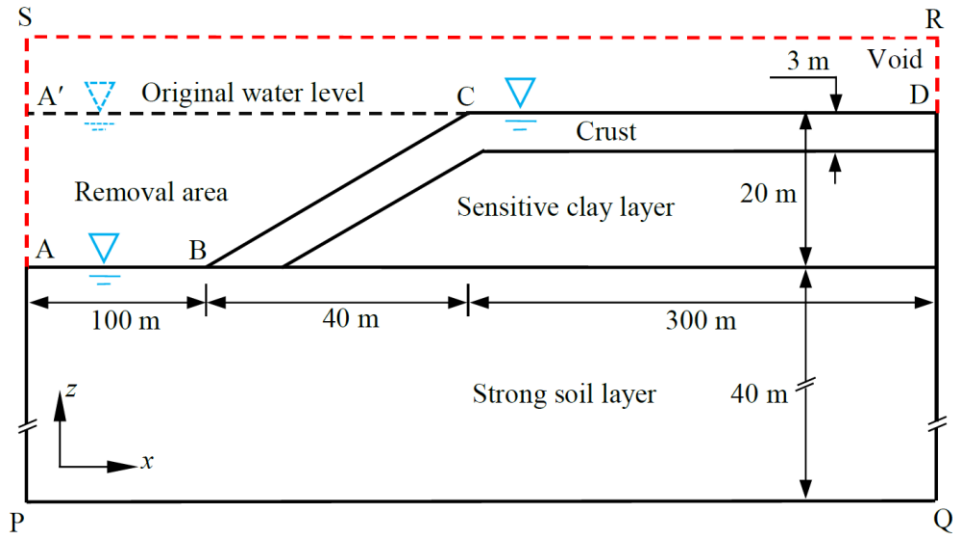


Fig. 4.1. Geometry of the slope used for seepage and in-situ stress analysis.

Two slopes are analyzed in the present study. Firstly, a typical 2:1 sensitive clay slope is modeled with a primary objective to validate the numerical approaches developed in the present study to simulate seepage and in-situ stress, and their effects on large-scale landslides (Fig. 1). Except for the validation of Eulerian FE modeling for seepage and in-situ stresses, the slope has three layers: (i) a 3-m crust; (ii) a sensitive clay layer beneath the crust down to the elevation of the slope toe; and (iii) a strong underneath soil layer. The left and right boundaries are placed at 100 m and 340 m, respectively, from the slope toe, in order to accommodate retrogression and runout when a landslide occurs. Secondly, the 2010 Saint-Jude landslide in Quebec, Canada, is simulated, as discussed in later sections.

In Abaqus/Explicit, the Eulerian approach has been implemented only for three-dimensional elements. Therefore, the FE analysis is performed with only one element length in the out-of-plane direction to simulate the plane strain condition. The Eulerian domain (PQRS in Fig. 4.1) is discretized into 0.25-m cubical elements using EC3D8RT in the software, which is an 8-node multi-material thermally coupled linear brick element having reduced integration and hourglass

control. The Eulerian Volume Fraction (EVF) tool is used to define the material: $EVF = 1$ for the elements filled with soil, $EVF = 0$ for the void, and $0 < EVF < 1$ is for partially filled elements.

4.3.1 Steps in Eulerian finite element modeling

Most of the riverbank slopes in eastern Canada formed by the gradual erosion of valleys in initially horizontal clay deposits (e.g., A'CD in Fig. 4.1) under drained condition (Lefebvre 1986, 2017). In this study, the riverbank slope is created by removing the soil in zone ABCA'. It is assumed that the valley formation lowers the water level on the left side of the slope toe to AB, while it remains at the same level (CD) on the right side of the crest. Therefore, seepage and shear stress increase will occur near the slope. In the present study, decoupled analyses are performed where the seepage analysis is conducted first for a weightless soil without considering any deformation, and the results from the seepage analysis are then used for subsequent in-situ stress and slope failure analyses.

Although the Eulerian approach of the software allows the simulation of large deformation, it does not have a direct option for proper modeling of seepage and initial effective stress considering pore water, since only single-phase material has been implemented in Abaqus/Explicit. Therefore, the effects of these factors are incorporated by conducting the analysis in three steps: (i) seepage analysis, (ii) in-situ stress modeling, and (iii) retrogressive landslide simulation (Fig. 4.2).

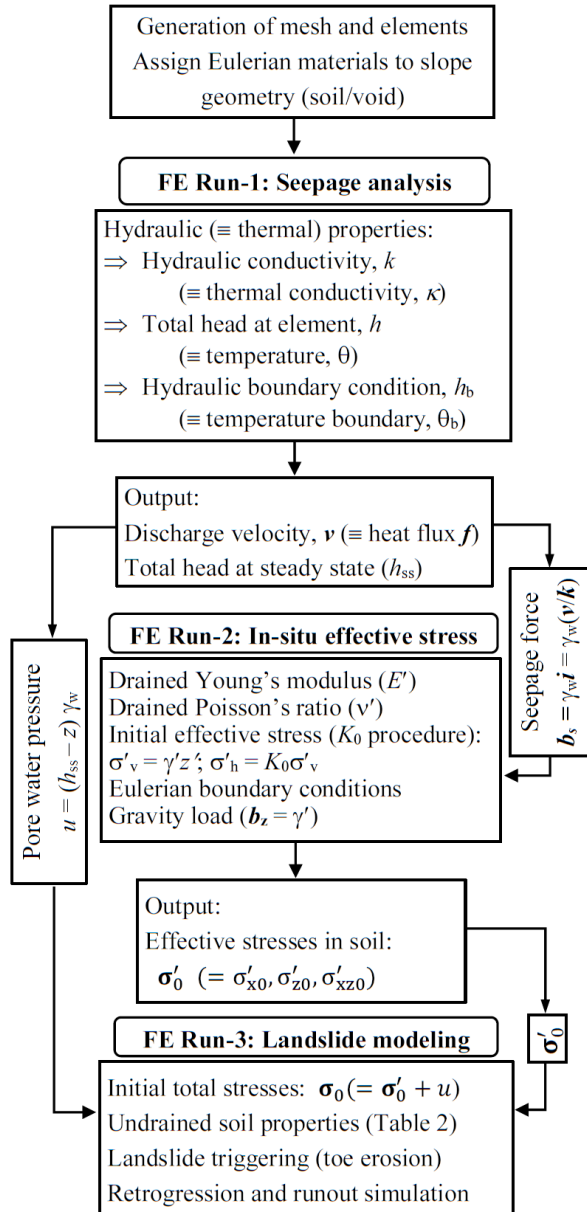


Fig. 4.2. Flowchart for seepage and in-situ stress simulation using Eulerian method.

4.3.1.1 Modeling of seepage

In the field, the seepage in a slope before the landslide can be regarded as a steady-state flow. The steady-state seepage can be modeled using Darcy's law and the fluid flow continuity equations as:

$$\mathbf{v} = -\mathbf{k} \cdot \nabla h \quad (4.1)$$

$$k_x \frac{\partial^2 h}{\partial x^2} + k_y \frac{\partial^2 h}{\partial y^2} + k_z \frac{\partial^2 h}{\partial z^2} = 0 \quad (4.2)$$

where \mathbf{v} is the Darcy velocity; k_x , k_y and k_z are the coefficients of permeability of the soil in the x , y and z directions, respectively; h is the total hydraulic head; and ∇h is the hydraulic gradient.

The steady-state groundwater flow in saturated soil and heat flow by conduction are governed by similar basic equations. Therefore, the seepage can be modeled through thermal analysis using the built-in fully coupled thermal-stress analysis available in the software (Hamann et al. 2015), where the parameters in Eqs. (4.1) and (4.2) are replaced by the following thermal variables: $\mathbf{v} = \mathbf{f}$; $h = \theta$; $\mathbf{k} = \boldsymbol{\kappa}$, where \mathbf{f} is the heat flux; θ is the temperature; and $\boldsymbol{\kappa}$ is the thermal conductivity. Although the complete process of seepage, including the transient phase, can be modeled using this approach, the main interest in this study is the final steady-state condition, which represents the typical field condition. No volume change in soil during seepage simulation is considered.

The hydraulic boundary conditions are applied in the form of temperature. The groundwater boundary condition is defined at the horizontal surfaces at the toe and crest levels (AB and CD in Fig. 4.1) ($\theta = \gamma_w z$, where γ_w is the unit weight of pore fluid and z is the elevation from the datum). The bottom of the model (PQ) is impermeable ($\mathbf{f} = 0$); however, for an artesian pressure condition, as presented in the later sections for the Saint-Jude landslide, a hydraulic head boundary condition is given. Although the hydraulic conductivity of clay is very low, a high value of $\boldsymbol{\kappa}$ is used to reduce the computational time because the value of $\boldsymbol{\kappa}$ affects only the results in the transient phase, not the final steady-state condition. The calculated temperature in each element at the final time increment of the seepage analysis represents the total head at the steady-state, which is called through a user subroutine. The hydraulic gradients i ($=\Delta h/\Delta s$) for the x and z directions are then

calculated, where Δs is the distance between two integration points of the adjacent elements. Finally, the pore water pressure (u) of each soil element is calculated as $u = (h - z) \gamma_w$. In addition, the discharge velocity (v) (heat flux in this case) of each soil element is obtained. Both u and v are used in the subsequent analyses (Fig. 4.2).

4.3.1.2 *In-situ stress*

The calculation starts with a horizontal ground surface (A'CD in Fig. 1). The in-situ effective stress condition is established by conducting an analysis under drained condition. At the bottom of the domain, zero velocity boundary conditions are applied in all three directions. Moreover, a zero velocity boundary condition is applied normal to all the vertical faces of the domain, except for the left side, where lateral restraint is applied only for the elements below the toe level (i.e., on surface AP in Fig. 4.1). No velocity boundary condition is given along the soil–void interface so that the soil can move into the void space when needed.

The stresses in a soil element at depth z' below the horizontal ground surface are given as the initial condition, as: $\sigma'_{z_ini} = \gamma' z'$ and $\sigma'_{x_ini} = \sigma'_{y_ini} = K_0 \sigma'_{z_ini}$, where σ'_{x_ini} , σ'_{y_ini} and σ'_{z_ini} are the effective stress components, and K_0 is the earth pressure coefficient at-rest. It is assumed that the slope under the in-situ stress condition is stable without any plastic strain. Therefore, for only this part of the analysis, the soil is modeled as an elastic material using a high Young's modulus and drained Poisson's ratio, which assures no significant deformation when gravitational load and seepage force are applied. Then, the gravitational load and seepage force, in the form of body forces, are applied only to the soil elements ($EVF \neq 0$) (see Fig. 4.2). As there is no soil in the zone ABCA' in Fig. 4.1 ($EVF = 0$), it represents the removal of soil in this zone, which is similar to the “mesh removal” in typical Lagrangian-based FE modeling of excavation (Potts et al. 1997; Locat et al. 2013). Defining the initial condition in this way, the simulation can be performed

for $K_0 > 1$, which is common in many sensitive clays and has a significant effect on slope failure. Previous Eulerian-based FE modeling of landslides has been performed for the earth pressure coefficient in terms of total stress ($\sigma_h/\sigma_v \leq 1$) (e.g., Dey et al. 2015).

The analysis is then continued until the equilibrium condition is reached, which gives the in-situ effective stresses in the slope (σ'_0).

4.3.1.3 *Landslide modeling*

A landslide might be triggered by drained or undrained loadings. Once triggered, the large-scale landslide occurs very quickly. In the present study, both triggering and subsequent retrogressive failure are modeled as undrained condition by conducting total stress analysis. The in-situ total stress (σ_0) is obtained by adding the effective stress (σ'_0) calculated in the in-situ stress analysis and pore water pressure (u) calculated in the seepage analysis. The same boundary conditions described in the “In-situ stress” section are applied.

The failure is triggered by toe erosion by reducing the undrained shear strength of the erosion block from 60 to 0.1 kPa in 5 seconds. The downslope movement of the weak soil in the erosion block causes the progressive failure of the slope. The analysis is then continued until the instantaneous velocity of the soil elements becomes negligible, or the retrogressive failure reaches the right boundary of the model.

4.3.2 Validation of Eulerian FE modeling of seepage and in-situ stress

Seepage and in-situ stresses in the slope (Fig. 4.1) are simulated using the Eulerian approach described above. To validate the results, the simulations are also performed using the implicit approach of the software with the built-in steady-state coupled pore fluid diffusion/stress procedure. In implicit modeling, hinges at the bottom and rollers on the vertical faces of the domain are used, which represent similar boundary conditions as in Eulerian analysis. Note that the

implicit approach cannot simulate the large deformation because of significant mesh distortion; therefore, the landslide modeling is not performed using this approach.

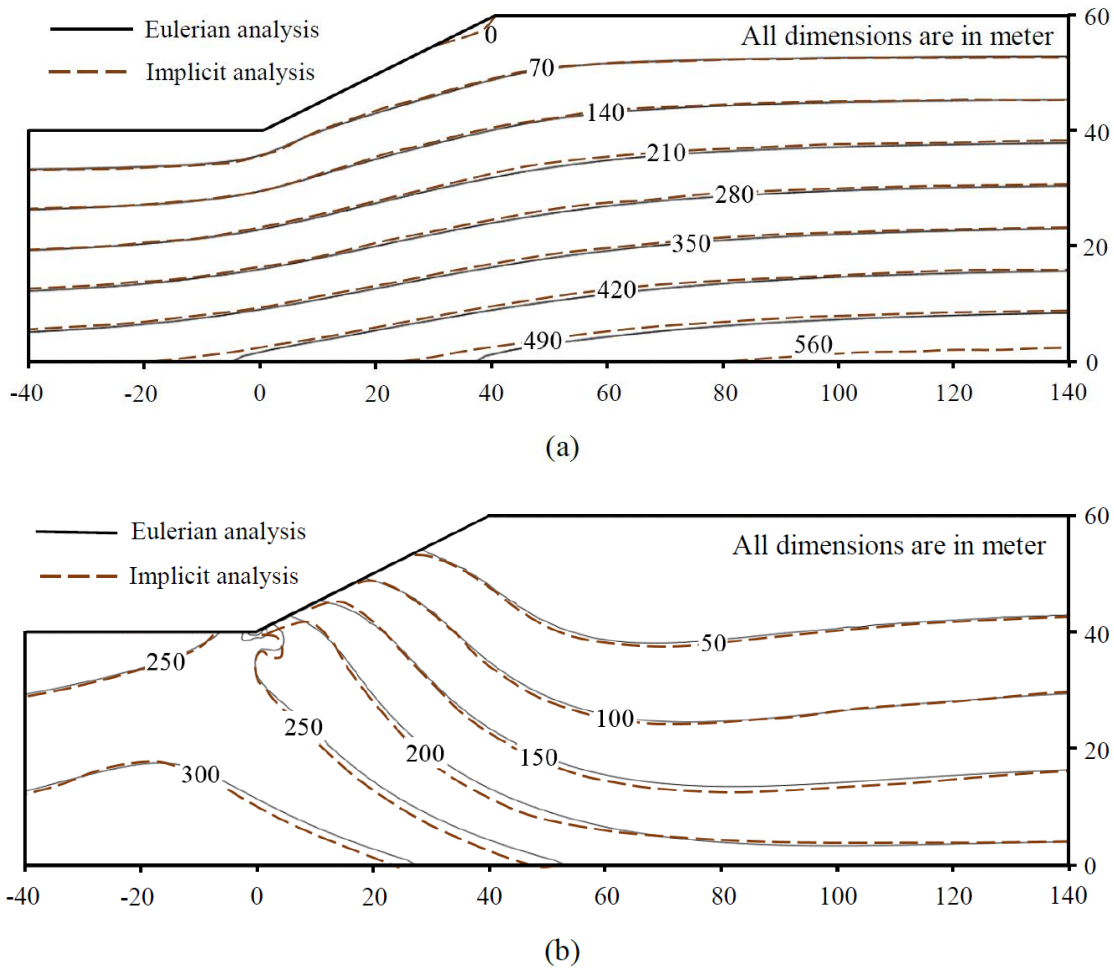


Fig. 4.3. Comparison of pore water pressure and shear stress obtained from Eulerian and Implicit analyses ($K_0 = 1.5$): (a) pore water pressure (kPa); (b) deviatoric stress (kPa).

Figures. 4.3(a) and 4.3(b), respectively, show the pore water pressure (u) at the steady-state condition and the in-situ deviatoric stress (q) in the slope induced by valley formation and seepage. Both u and q obtained from the Eulerian and implicit FE approaches match closely, which implies that the developed Eulerian approach can successfully simulate seepage and in-situ stresses.

The in-situ stress condition has been established using K (ratio between total horizontal and vertical stresses) in previous Eulerian-based and some Lagrangian-based FE simulations (Duncan and Dunlop 1968; Dey et al. 2015). If the groundwater table is at the ground surface, K is related to K_0 as $K = K_0$. Following the same procedure described in the “In-situ stress” section, a simulation is performed for the in-situ total stress in the same slope (Fig. 4.1) using K and considering the groundwater level at the ground surface (without modeling seepage force) and saturated unit weight of soil. Figure 4.4 shows that q obtained from K_0 and K are mainly different around the slope, and that the difference becomes smaller in the soil elements located further from the slope. A number of simulations for varying K and corresponding K_0 show that the difference between q with K and K_0 reduces quickly with distance from the slope when K_0 is closer to unity.

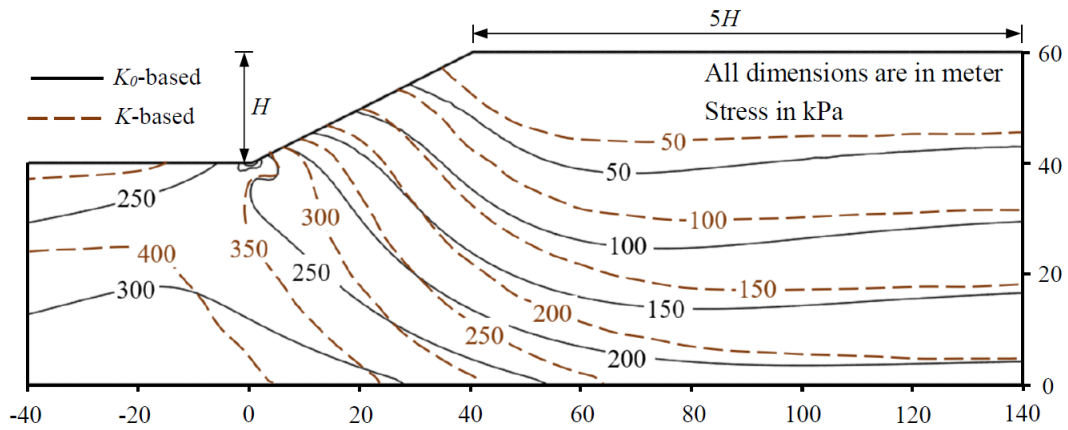


Fig. 4.4. Comparison of deviatoric stress between effective and total stress analyses for in-situ stress ($K_0 = 1.5$).

The following are the practical implications of these simulations. The landslide triggering is significantly influenced by the in-situ deviatoric stress near the slope. Therefore, K_0 -based modeling with seepage force will give more accurate results, as it represents a state closer to the field condition. However, large-scale landslides generally retrogress over a large distance from the crest. Therefore, the successive failures of the soil blocks will not be significantly affected by the

difference of in-situ stresses near the slope calculated using K_0 and K . Moreover, there are considerable uncertainties in landslide triggering factors, including the size of the toe erosion block and rate of erosion. In other words, if the interest is to model the retrogression process, both K_0 and K methods would be acceptable. However, if the focus is to model the triggering of a landslide, the K_0 method, as presented in this study, would be a better choice.

For all the analyses presented in the following sections, the in-situ total stress is obtained through the K_0 -method, together with the modeling of seepage where groundwater is at the level of crest and toe.

4.4 Modeling of Sensitive Clay

The mobilized undrained shear strength (s_u) of sensitive clays is calculated using the following equation by incorporating a strain-softening factor, f_1 (≤ 1.0) and strain-rate factor, f_2 .

$$s_u = f_1 f_2 s_{uy} \quad (4.3)$$

where s_{uy} is the undrained shear strength at a very low strain rate.

4.4.1 Strain softening

The following equations is used in the present study for modeling post-peak s_u degradation (Dey et al. 2015).

$$f_1 = \begin{cases} \frac{s_{uR}}{s_{u0}} + \left(1 - \frac{s_{uR}}{s_{u0}}\right) e^{-3\delta/\delta_{95}} & \text{if } 0 \leq \delta < 2\delta_{95} \\ \frac{s_{uR}}{s_{u0}} - \frac{s_{uR} - s_{uld}}{s_{u0}} \frac{\delta - 2\delta_{95}}{\delta_{ld} - 2\delta_{95}} & \text{if } 2\delta_{95} \leq \delta < \delta_{ld} \\ \frac{s_{uld}}{s_{u0}} & \text{if } \delta \geq \delta_{ld} \end{cases} \quad (4.4)$$

where s_{u0} is the peak undrained shear strength at the reference shear strain rate ($\dot{\gamma}_{ref}$) before softening; δ is the plastic shear displacement; s_{uR} is the value of s_u at sufficiently large δ ; δ_{95} is the value of δ at which 95% reduction of $(s_{u0} - s_{uR})$ occurs; and δ_{ld} is a very large value of δ ($> \delta_{95}$) when

the soil becomes completely remolded to $s_u = s_{uld}$. Equation (4.4) represents a quick exponential degradation of s_u at $0 \leq \delta < 2\delta_{95}$, followed by a linear degradation at $2\delta_{95} \leq \delta < \delta_{ld}$ and then a constant $s_u (= s_{uld})$ at $\delta \geq \delta_{ld}$. The stress–strain behavior before the yield is modeled using undrained Young’s modulus (E_u) and Poisson’s ratio (ν_u). Further details of this strength degradation model, including the selection of model parameters and the comparison of its performance with specialized laboratory test results on sensitive clay (Tavenas et al. 1983), have been presented elsewhere (Dey et al. 2015, 2016).

4.4.2 Strain-Rate effects on undrained shear strength

The shear strength of soil changes significantly during landslides in sensitive clays. At the beginning of the slide, the strength of the intact soil governs the behavior; however, the failed soil block might move in the downslope direction at high speed over the highly remolded sensitive clay, which could be considered as a viscous fluid. Geotechnical and fluid mechanics approaches are commonly used to model strain-rate ($\dot{\gamma}$) on s_u . To capture the behavior of both soil and fluid-like materials that might experience a low to very high shearing rate, the following “additive power-law model” proposed by Zhu and Randolph (2011) is used, which has been developed by combining the Herschel–Bulkley and power-law models.

$$f_2 = \left[1 + \eta \left(\frac{|\dot{\gamma}_{\max}|}{\dot{\gamma}_{\text{ref}}} \right)^\beta \right] \quad (4.5)$$

where η and β are soil parameters. In the present study, $\eta = 0.5$ and $\beta = 0.1$ are used (Jeong et al. 2009; Boukpeti et al. 2012; Randolph et al. 2012).

The undrained shear strength of sensitive clay is commonly estimated based on field vane shear and cone penetration tests. Einav and Randolph (2006) showed the maximum shear strain rate of $\sim 0.05 \text{ s}^{-1}$ for standard vane shear tests of a rotation rate of $0.1 \text{ }^\circ/\text{s}$. In this present study, $\dot{\gamma}_{\text{ref}}$

$= 0.05 \text{ s}^{-1}$ is used. Finally, $s_{uy} = s_{u0}/(1 + \eta)$ can be obtained by replacing, $\dot{\gamma}_{\max} = \dot{\gamma}_{\text{ref}}$ in Eq. (4.5).

The details of the implementation of a strain-softening and strain-rate dependent soil model using a user subroutine have been presented in Dutta et al. (2015), although their soil model is slightly different from Eqs. (4.3)–(4.5).

4.5 Modeling of Retrogressive Landslide

The numerical modeling presented in this section shows the importance of K_0 and the strain-rate dependent undrained shear strength model in the failure of a sensitive clay slope (Fig. 4.1). The soil parameters used in the analyses are listed in Table 4.1. The crust is modeled as an elastic-perfectly plastic material, while for sensitive clay the strain-softening and strain-rate effects on s_u are considered. Further details on the selection of model parameters have been presented in previous studies (Dey et al. 2015, 2016). The failure is triggered by toe erosion, as discussed in the “Landslide modeling” section.

In the following sections, the failure pattern is shown by the accumulated plastic shear strain ε_q^p along the shear bands. As the progressive failure is a time-dependent process, small videos are uploaded in the supplementary data to provide further details of the failure mechanisms (Videos S1–S9).

Table 4.1. Soil parameters used in FE modeling.

Parameter	Crust	Sensitive Clay	Strong Layer
Total unit weight, γ (kN/m ³)	17	17	20
Undrained Young's modulus, E_u (MPa)	10	10	50
Undrained Poisson's ratio, ν_u	0.495	0.495	0.495
Earth pressure coefficient at-rest, K_0 (kPa)	0.75–2.0	0.75–2.0 [0.7]	0.75–2.0
Initial undrained shear strength, s_{u0} (kPa)	60 [75]	30–140 [25–65 [§]]	-
Remoulded undrained shear strength, s_{uR} (kPa)	-	$s_{u0}/3.5$	-
Large displacement undrained shear strength, s_{uld} (kPa)	-	1.6	-
Plastic shear displacement for 95% degradation of soil strength, δ_{95} (m)	-	0.05*	-
Plastic shear displacement for large displacement undrained shear strength, δ_{ld} (m)	-	1*	-
Reference strain rate, $\dot{\gamma}_{ref}$ (s ⁻¹)	-	0.05	-
η	-	0.5	-
β	-	0.1	-

[§] s_{u0} of sensitive clay layer varies linearly with depth

* for FE input, the plastic shear strain is calculated using δ and element size

[] values used for Saint-Jude landslide

4.5.1 Effects of K_0

Four simulations are performed for varying K_0 ($= 0.75\text{--}2.0$) to examine its effect on failure patterns (Cases 1–4, Fig. 5.5). For sensitive clays, both K_0 and the undrained shear strength under a given effective vertical stress increase with the overconsolidation ratio (Hamouche et al. 1995). Therefore, a higher initial undrained shear strength (s_{u0}) is used for higher K_0 where s_{u0} increases

linearly from the crust to the level of slope toe as: 35–55, 30–70, 40–100 and 80–140 (in kPa) with K_0 of 0.75, 1.0, 1.5 and 2.0 for Cases 1 to 4, respectively.

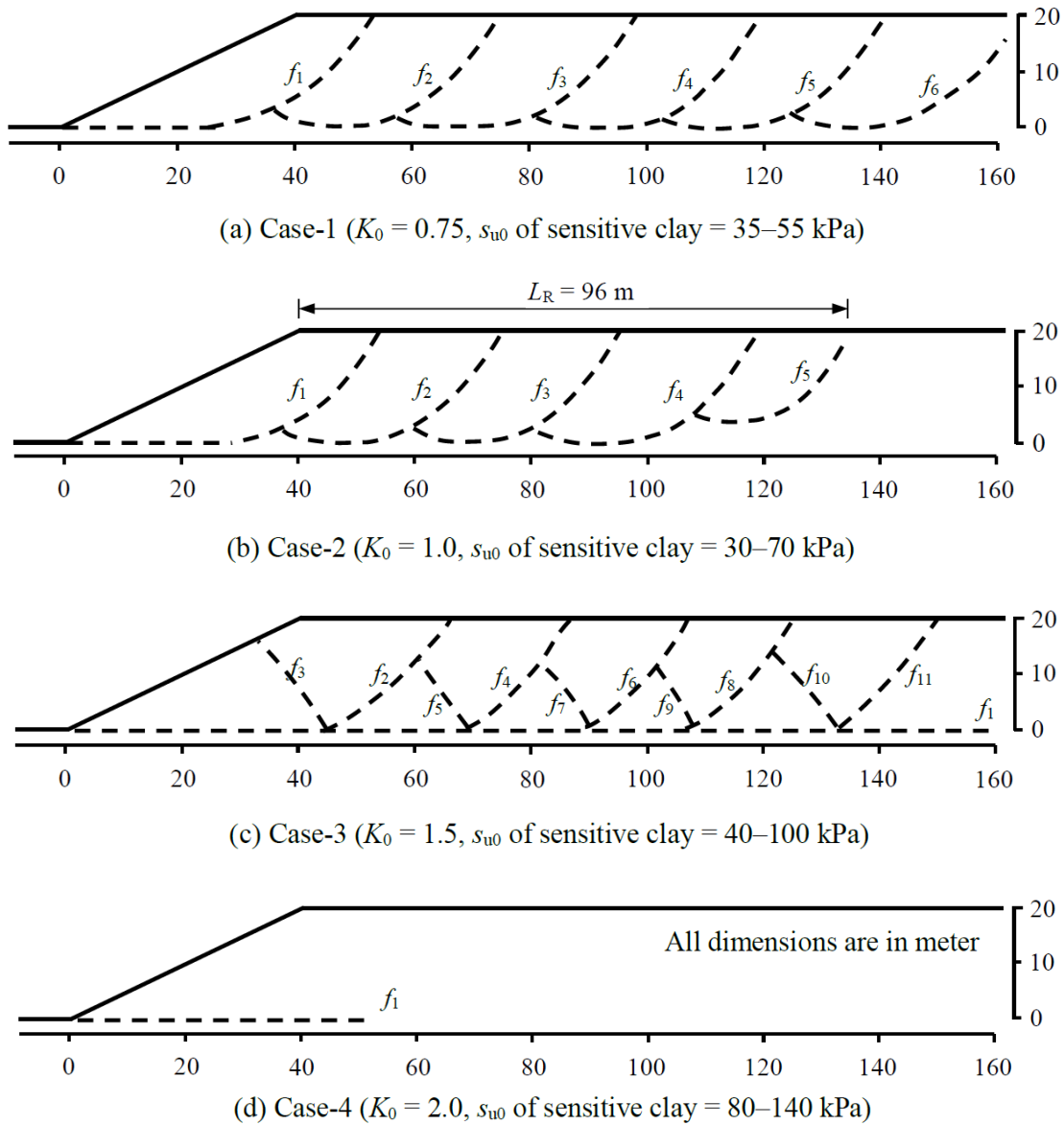


Fig. 4.5. Shear band formation for varying K_0 .

Figure 4.5 schematically shows the failure surface development and the failure pattern. To provide further details on the time-dependent retrogressive landslides in Cases 1–3, videos S1–S3 are uploaded in the supplementary data. Figures 4.5(a) and 4.5(b) show that flowslide occurs in Cases 1 and 2. The toe erosion causes the rotational failure of the first soil block. The downslope

displacement of the failed soil block results in ground surface subsidence and reduction of lateral support to the remaining soil, which causes rotational failure of subsequent soil blocks. In Case 2, the subsequent soil blocks fail at shallower elevations and retrogression stops after a retrogression distance (L_R) of 96 m (Fig. 4.5b); however, in Case 1, the retrogressive failure continues without a reduction of depth of slide of the subsequent soil block. These two simulations show that an increase of shear strength gradient and K_0 can reduce the depth of failure of subsequent soil blocks.

Figure 4.5(c) shows a typical spread failure in Case 3, which is different from Cases 1 and 2 (flowslides). Toe erosion creates a shear band at the level of the toe that propagates horizontally (f_1 in Fig. 4.5(c)). When f_1 is sufficiently long, active failure occurs in the soil layer over f_1 , due to the formation of inclined shear bands that dislocate Δ -shaped horsts and ∇ -shaped grabens (see Video S3 in the Supplemental data). The failure process continues with downslope displacement of the debris. The failure mechanism of Case 3 agrees well with the conceptual model of spreads (Odenstad, 1951; Carson, 1977; Cruden and Varnes 1996; Locat et al. 2011).

Finally, in Case 4, toe erosion creates only a horizontal shear band from the toe without causing global failure (see Video S4 in the Supplemental data). In other words, a slope with high shear strength might be weakened by this shear band, although global failure may not occur because the overlying soil is strong enough to prevent active failure.

4.5.2 Effects of strain-rate on undrained shear strength

Three additional simulations (Cases 5–7) are performed in which all the conditions are the same as in Cases 1–3, respectively, except that the strain-rate effects on s_u are not considered (i.e., $f_2 = 1.0$ in Eq. 4.3). Figure 4.6 shows the instantaneous velocity vectors of the debris when the fifth soil block fails from the intact soil. The overall velocity of the debris is lower in the simulation with a strain-rate effect, because it increases the mobilized s_u of remolded soil.

Consideration of strain-rate might also give a mobilized s_u smaller than s_u at the reference strain rate when $|\dot{\gamma}_{\max}| < \dot{\gamma}_{\text{ref}}$, which might have a profound influence on the failure pattern of a slope that is on the verge of failure. For example, in Case 2, a flowslide occurs with five successive failures (Fig. 4.5(b) and Video S2); however, a single rotational failure occurs in Case 6 when the strain-rate effect is not considered (Video S6). The stability of the scarp is overestimated in Case 6 because s_u at $\dot{\gamma}_{\text{ref}} (= 0.05 \text{ s}^{-1})$ is used, although this soil has a very low shear strain-rate before the failure, which gives lower s_u in Case 2 and results in progressive failure of the scarp.

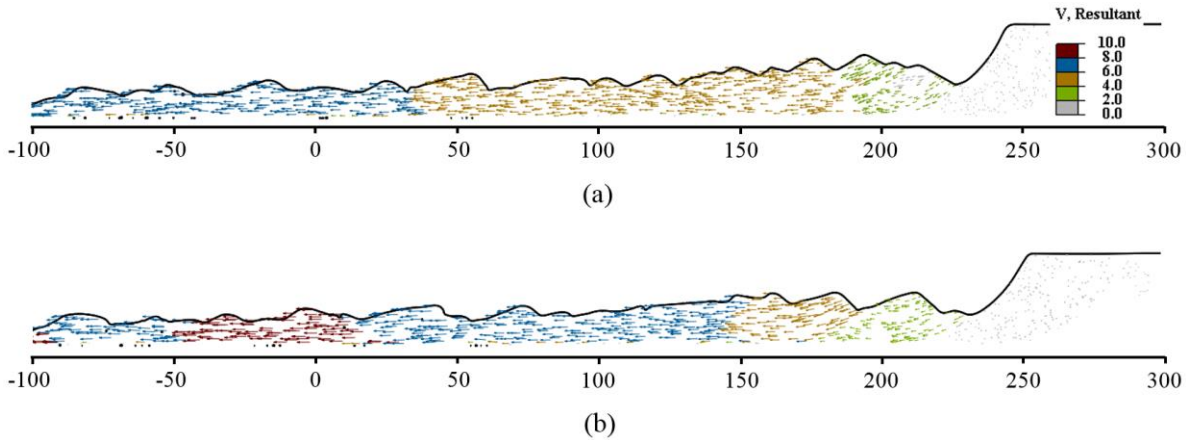


Fig. 4.6. Instantaneous velocity of soil debris at 5th rotational failure: (a) Case-1, considering strain-rate effects; (b) Case-5, without strain-rate effects.

Strain-rate also affects the retrogression and downslope debris displacement in a spread. Figure 4.7 shows the retrogression distance of 222 m and 197 m for Cases 3 and 7, respectively, although the failure type is a spread in both cases. As explained earlier for Cases 2 and 6 comparisons, low mobilized s_u of the soil behind the scarp at low strain rates ($|\dot{\gamma}_{\max}| < \dot{\gamma}_{\text{ref}}$) facilitates the retrogression process in Case 3. However, if the strain-rate effect is not considered, the mobility of the debris increases because of low mobilized s_u of highly remolded soil; for example, the distances between adjacent horsts in Case 7 are much longer than those in Case 3.

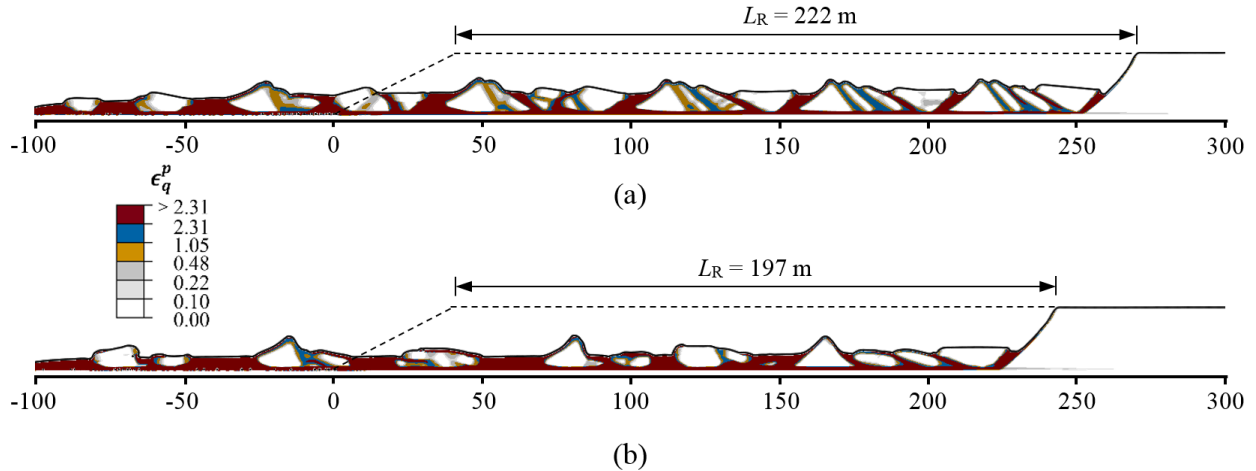


Fig. 4.7. Topography at the end of landslide: (a) Case-3, considering strain-rate effects; (b) Case-7, without strain-rate effects.

4.6 Simulation of the 2010 Saint-Jude Landslide

On May 10, 2010, a large retrogressive landslide occurred along the Salvail River, in the municipality of Saint-Jude, Quebec, Canada. Post-slide field investigations show that the failure occurred through highly sensitive clay, and horsts and grabens were observed in the crater of the landslide, indicating a spread. A detailed report, including field investigations and limitations of the limit equilibrium modeling, is available in Locat et al. (2017). However, they did not model the entire failure process, retrogression and runout are not included.

Two cross-sections of the slope are simulated in this study (B-B' and C-C' in Locat et al. 2017). Figure 8 shows schematically shows the geometry of slope. In the FE analysis, the ground surface profile is obtained from Locat et al. (2017). As for previous analyses, the soil is modeled as a Eulerian material, which can displace in the void space above the ground surface during the landslide process. The opposite riverbank is also modeled in this study.

Based on the work of Locat et al. (2017), five soil layers are considered, which have different hydraulic conductivity (Fig. 4.8(a)). Field tests show high, although erratic, s_{u0} in the crust

followed by a linearly increasing s_{u0} with depth in the thick sensitive clay layer (Fig. 4.8(b)). The shear strength of soil of the underlying layers (Layer C–Layer E) is very high. Moreover, the failure did not extend to this layer. Therefore, for numerical analysis, these layers are simply defined as a strong layer and modeled as an elastic material. Table 1 shows the soil parameters used in the FE simulations. Site-specific strain-softening and strain-rate parameters are not available; therefore, typical values of sensitive clays are used (Dey et al. 2015; Quinn et al. 2011). The soil is lightly overconsolidated (OCR \sim 1.4, Locat et al. 2017); therefore, $K_0 = 0.7$ is used.

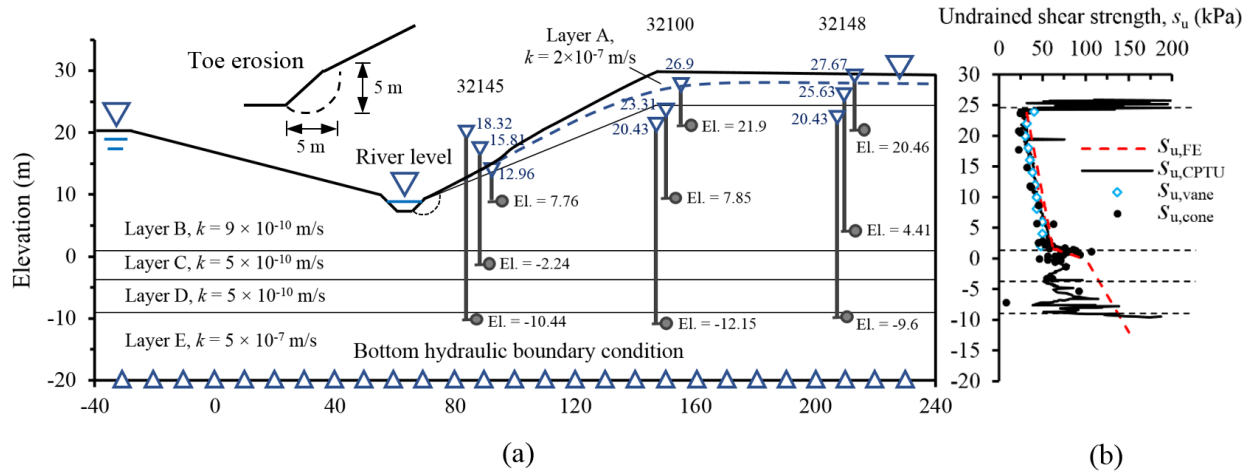


Fig. 4.8. Cross-section B-B' of Saint-Jude landslide: (a) Geometry and hydraulic conditions; (b) undrained shear strength profile (data from CPTU 32100 of Locat et al. 2017).

4.6.1 Seepage analysis

The numerical simulation started with seepage analyses as described in previous sections. The hydraulic boundary conditions for this case are not known. Therefore, in SEEP/W analysis, Locat et al. (2017) imposed an infiltration rate on the upslope area to model pore water pressure (u) similar to the measured values using nine piezometers (Fig. 4.8). In the present study, to define the hydraulic boundary conditions, the total head (h) measured by the piezometers is plotted with depth (almost linear) for three locations (32145, 32100, 32148 in Fig 4.8), which are then

extrapolated to obtain hydraulic boundary conditions (i.e., total head) at the ground surface (h_g) and bottom of the domain (El. -20) (h_b) for these three locations. The water level in the river is assumed to be at an elevation of 7.0 m (Locat et al. 2017). A linear variation of h_g and h_b is assumed between the locations of known h_g and h_b to defined hydraulic boundaries on the right side of the river. No piezometer reading is available below the opposite riverbank; therefore, the groundwater table is assumed at the ground surface. Moreover, h_b on the left side of the river is assumed as the mirror image of h_b on the right side. As described before, h_g and h_b are given as temperature boundary conditions in FE simulations.

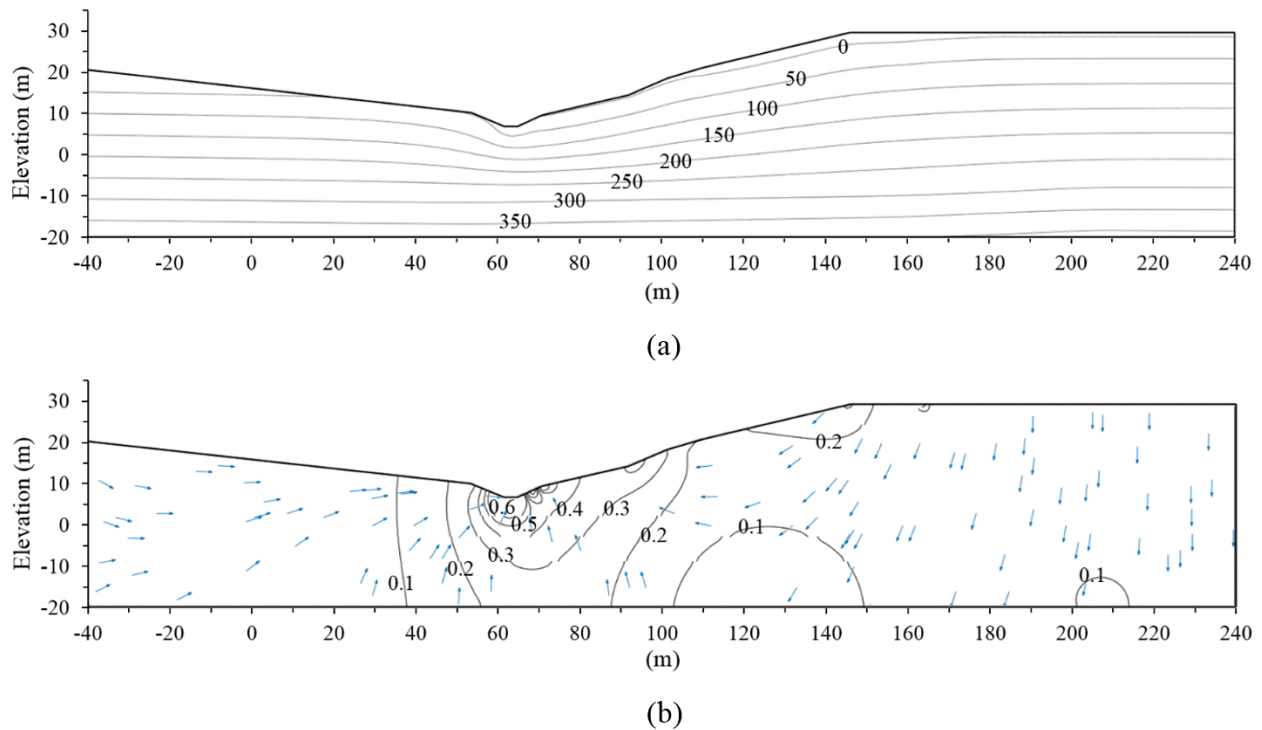


Fig. 4.9. Seepage simulation of the cross-section B-B' of the Saint-Jude landslide: (a) pore water pressure (kPa); (b) Hydraulic gradient.

Figure 4.9(a) shows the FE simulated pore pressure (u) distribution in cross-section B-B'. Figure 4.9(b) shows the contour lines of the hydraulic gradient (i) and the directions of the water flow (arrows). In the upslope area, the pore water flows downward with $i \sim 0.1-0.2$. A large upward

hydraulic gradient near the river ($i \sim 0.4\text{--}0.6$) could reduce the effective stress significantly and create a favorable condition for the failure of a soil block near the toe to trigger the landslide.

Seepage analysis is also performed for cross-section C-C'. Figure 4.10 shows that the FE calculated u matches well with the piezometer readings at three locations (32145, 32100 and 32148, Fig. 4.8(a)), which implies that the seepage is properly modeled. For locations 32100 and 32148, u is lower than the hydrostatic pressure (u_0), indicating downward flow in the upslope area. In location 32145, $u > u_0$ at elevations below ~ 4 m, indicating upward seepage caused by the artesian pressure.

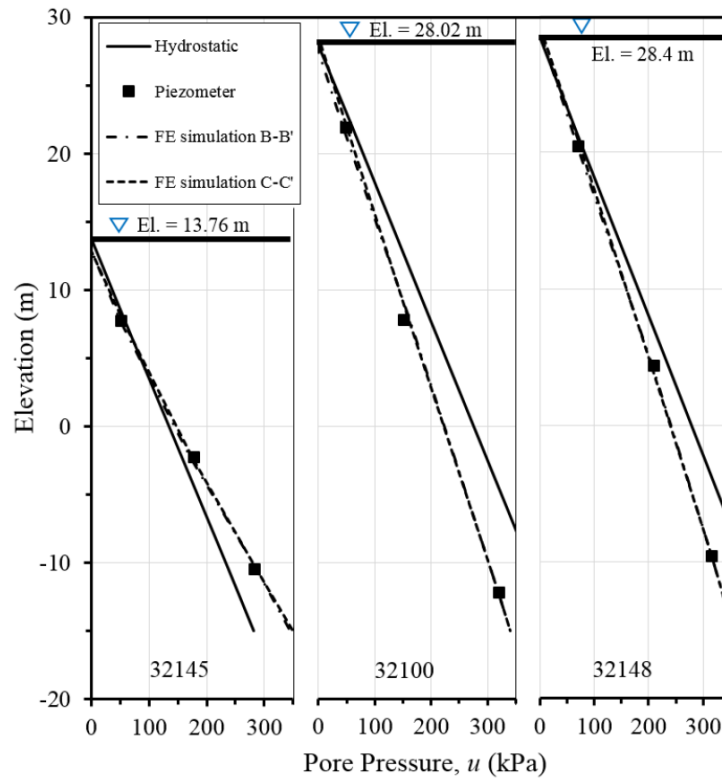


Fig. 4.10. Comparison of FE simulated pore water pressure with field data.

4.6.2 Failure process

Following the procedure discussed in previous sections, the in-situ stress is then established based on the K_0 -method, incorporating seepage effects. Finally, the failure is triggered by toe erosion, by reducing the shear strength of a small soil block, shown in the inset of Fig. 4.8(a).

Cross-section B-B'

Figure 4.11(a) shows that toe erosion initiates a shear band (f_1) that propagates horizontally through the sensitive clay layer ~1 m below the toe and ~2 m above the interface between the sensitive clay and the strong soil layer. This implies that the quasi-horizontal shear band might form anywhere in the sensitive clay layer. The horizontal shear band propagates a long distance beneath the mild slope and then curves upward to the ground surface (f_2). Figure 4.11(b) shows that the failed soil block has disintegrated into smaller pieces during its downslope movement. After sufficient displacement of the failed soil, another shear band (f_3) initiates from the toe of the scarp (point P), propagates for a short distance and then curves upward to the ground surface (f_4). The horizontal shear bands f_1 and f_3 locate at almost the same elevation. Furthermore, as the failed soil displaces downslope, inclined shear bands generate inside the soil chunks, forming horst shaped soil blocks (e.g., Fig. 4.11(c)). The debris flow stops because of the restriction from the opposite riverbank. Small strain generates inside the failed soil blocks, and the remolding primarily occurs near the shear bands. Even though the simulated failure mechanism of the cross-section B-B' does not perfectly match the conceptual model of spreads (Odenstad, 1951; Carson, 1977; Cruden and Varnes 1996; Locat et al. 2011), it is similar to the more complex succession of intact soil blocks, ridges and flat ground surfaces, as observed in the landslide crater (Fig. 4.11(d) and 4.11 (e)).

Some shallow rotational slides occur after the failure through f_4 (e.g., f_6 in Fig. 4.11(d)). The debris remains inside the crater and gains equilibrium due to the topography, so no further deep-seated failure occurs after f_4 . However, f_4 has a steep angle and the height of the backscarp increases as the failed soil subsides. Consequently, the failure of additional soil blocks occurs at shallower depth, forming a stepped basal failure plane (Fig. 4.11(e)). The numerical results explain similar observations made in the field (Locat et al. 2017), although the FE simulated stepped failure surface is inclined and shallower than that in the field. The difference might be due to the selection of soil properties, as simplified shear strength profiles are used for the simulations.

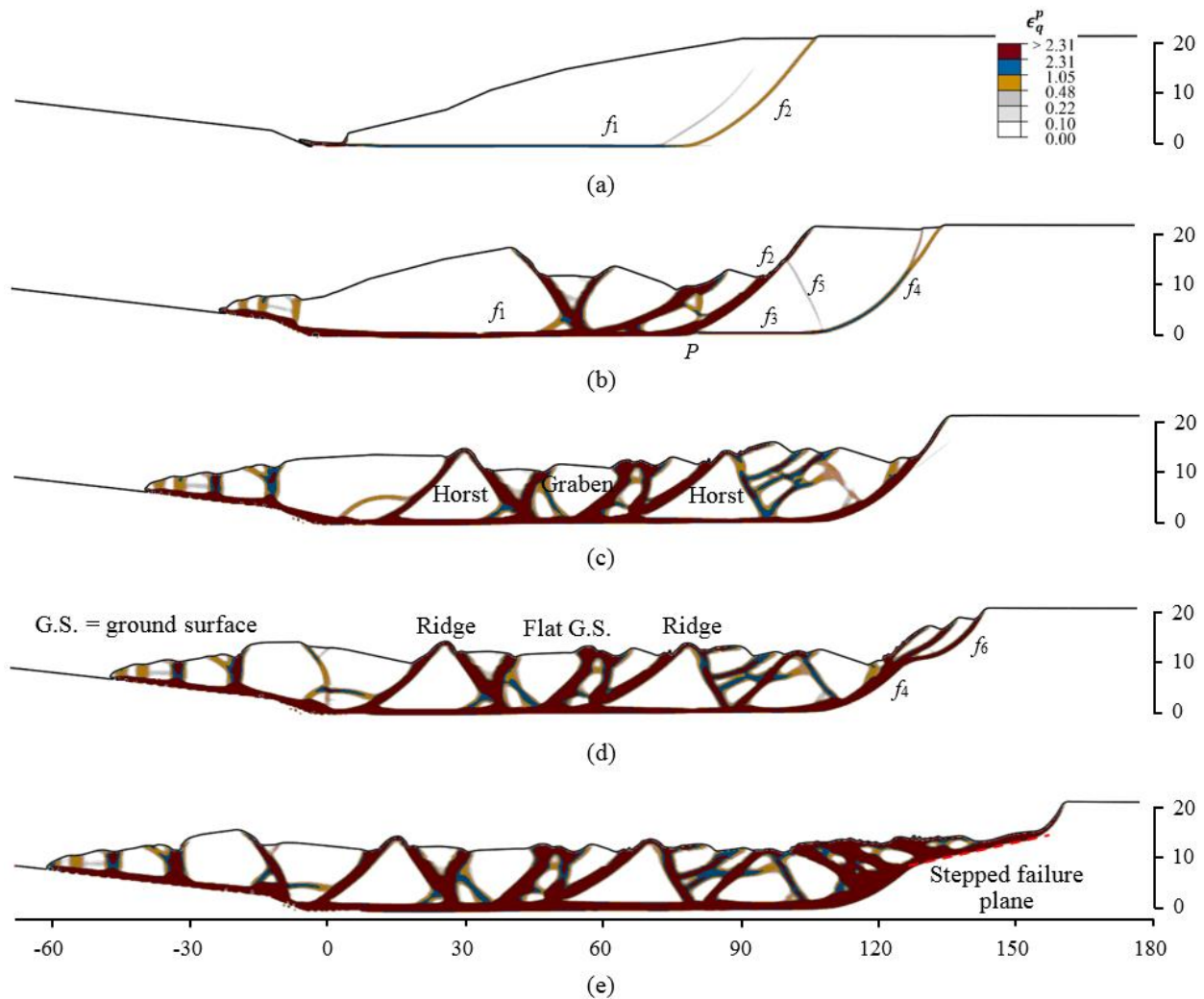
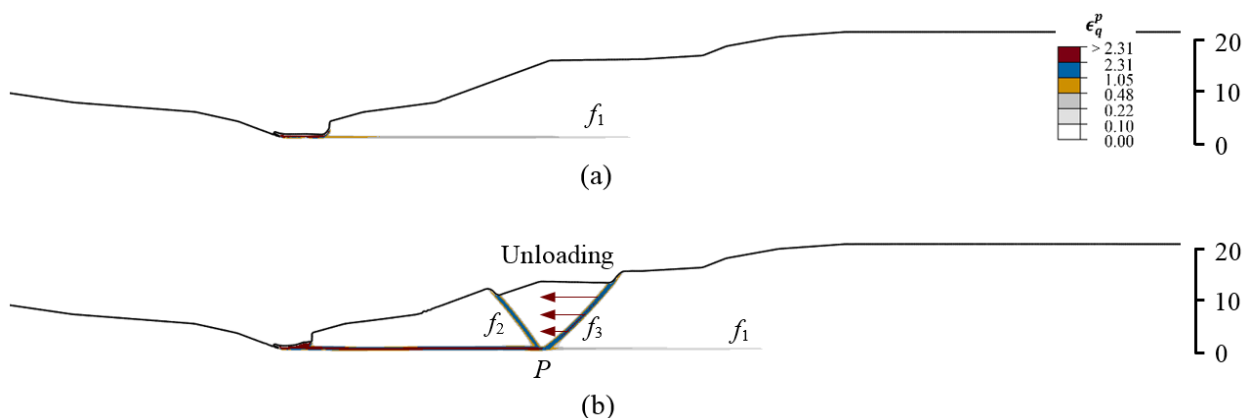


Fig. 4.11. Failure process of cross-section B-B'.

Cross-section C-C'

Similar to the cross-section B-B', the toe erosion causes local failure near the riverbank, and a shear band f_1 propagates horizontally through the sensitive clay layer (Fig. 4.12(a)). Unlike in the B-B' simulation (Fig. 4.11(b)), the shear band f_1 does not curve upward but keeps propagating horizontally. The existence of a flat platform on the slope in C-C' might be the reason for different failure mechanisms in these two cross-sections. Active failure occurs in the soil layer above f_1 by the formation of two inclined shear bands f_2 and f_3 forms from point P (Fig. 4.12(b)). The failed soil displaces horizontally towards the river channel over f_1 , meanwhile the soil mass bounded by f_2 and f_3 subsides. The downslope displacement and the settlement of the failed soil reduce the support to the soil behind the backscarp, which results in further propagation of f_1 and formation of a series of inclined shear bands (f_4 - f_6), and failure of additional soil blocks in the forms of horst and graben. Comparison of Figs. 4.10 and 4.11 shows that a small variation in slope geometry changes the failure pattern significantly, although other conditions, including soil properties, are the same. This might be one of the causes of different types of landslides that have occurred in almost similar slopes. The failure mechanism of the cross-section C-C' matches better the conceptual models of spread.



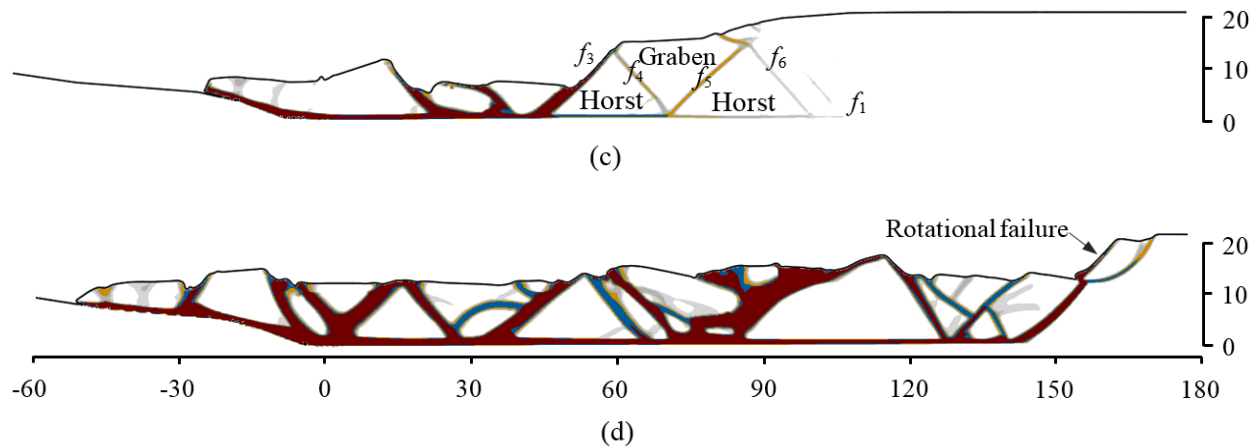


Fig. 4.12. Failure process of cross-section C-C'.

4.5.3 Comparison with field investigation

Figure 4.13 shows the failure pattern and the topography after the landslide. Based on field investigation, Locat et al. (2017) presented the final position of the horsts, location of the failure planes and debris profiles, which are also shown in Fig. 4.13. The probable basal failure plane inferred by Locat et al. (2017) from CPTU is ~ 1 m below the FE simulated location. An interesting result is that the simulated failure initiates below the slope toe, in agreement with field investigations. The top surface of the failed soil is almost flat, and the FE results match the field observations. The retrogression and runout distances are reasonably simulated. However, the final positions of the FE simulated horsts do not match the field observations very well, which is potentially due to the selection of strain-softening and strain-rate model parameters, as they are estimated from typical sensitive clay behavior. Since a $\phi = 0^\circ$ model is used in FE analysis, the tip angle of the horsts is $\sim 90^\circ$, which is larger than that observed in the field (50° – 70° , Locat et al. 2011); therefore, the width of the horsts is larger in FE simulations. In addition, while some shallow failures of the right scarp are modeled, the failure pattern reconstituted by Locat et al.

(2017) could not be simulated properly. In summary, while there are some discrepancies, the present numerical technique can simulate the process reasonably well.

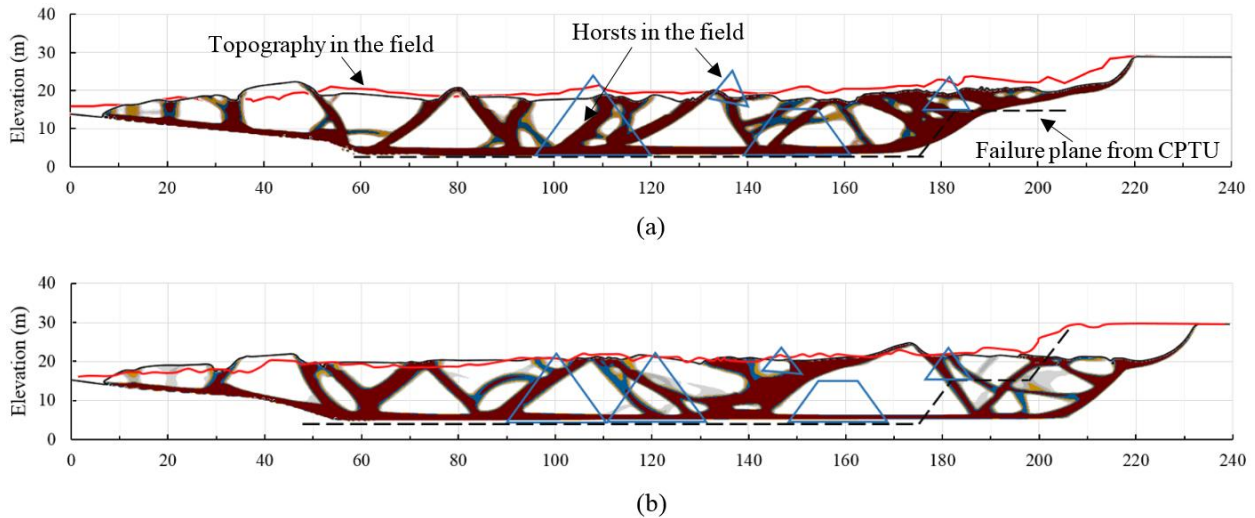


Fig. 4.13. Comparison of the topography after landslide: (a) cross-section B-B'; (b) cross-section C-C'.

4.7 Conclusions

The process of large-scale landslides cannot be modeled using the limit equilibrium or typical FE analysis, because the former one fails to model the progressive failure and the latter one suffers from significant mesh distortion at large displacements. The Eulerian-based FE approach can simulate large deformation. In the present study, the techniques for Eulerian FE modeling of seepage, in-situ stresses, and retrogressive failure of soil blocks, considering strain-softening and strain-rate effects on undrained shear strength, are presented. The steady-state seepage condition is simulated using a thermal-hydraulic analogy available in the software that gives pore water pressure and seepage forces, which are then used to model the in-situ stress condition for a varying earth pressure coefficient at-rest (K_0) and subsequent landslide. The methods presented in this study can simulate the long-term drained in-situ stress development and rapid undrained landslide, which represent the complete process, including the static condition, landslide triggering,

retrogression and runout. In addition, the landslide modeling is performed for an in-situ condition established by the ratio of total stresses in the lateral and vertical directions (K). The following conclusions can be drawn from this study.

- Seepage might increase the potential for triggering a landslide. A high artesian pore pressure in the soil near the toe could be a major factor for the initiation of failure, as occurred in the Saint-Jude landslide.
- In-situ total stresses calculated using K_0 together with seepage and K with groundwater table at the ground surface are different close to the slope, which can significantly influence the initiation of failure.
- A higher earth pressure coefficient together with higher shear strength, as it occurs with an increase in the overconsolidation ratio, could change the failure pattern from flowslide to spread, and thereby the retrogression distance.
- An increase in strain-rate reduces the mobility of the debris, which reduces the retrogression and runout distances and can even change the failure pattern from flowslide to spread.
- In a spread, the quasi-horizontal failure plane does not always form at the toe level. If the sensitive clay layer extends below the toe, the shear band might propagate horizontally below the level of the toe, depending on the shear strength gradient and size/shape of the toe erosion block.
- The FE simulations reasonably explain the mechanisms of the 2010 Saint-Jude landslide, although the location of the horsts and step change of the quasi-horizontal planes observed in the field could not be modeled accurately. The spatial variability of soil properties in the field might explain this discrepancy.

Notations

β	parameter for strain-rate relation
θ	temperature
δ	accumulated plastic shear displacement
δ_{95}	δ at which s_u reduced by 95% of $(s_{up}-s_{uR})$
δ_{ld}	δ at large shear displacement
γ_w	unit weight of water
$\dot{\gamma}_{ref}$	reference strain rate
κ	thermal conductivity
ν'/ν_u	drained/undrained Poisson's ratio
η	Parameter for strain-rate relation
σ'_0/σ_0	effective/total initial stress matrix
σ'_h/σ_v	vertical effective/total stress
σ'_h/σ_h	horizontal effective/total stress
E'/E_u	drained/undrained Young's modulus
f	heat flux
H	slope height
h	total hydraulic head
i	hydraulic gradient
K/K_0	earth pressure coefficient in terms of total/effective stress
k	coefficient of permeability
L_R	retrogression distance

q	deviatoric stress
S_t	remolded sensitivity of clay, s_{u0}/s_{uR}
s_u	mobilized undrained shear strength
s_{uld}	undrained shear strength at large displacement
s_{ug}	undrained shear strength at ground surface
s_{uR}	remolded s_u at large plastic shear displacement
u	pore water pressure
v	Darcy velocity
z	elevation above the datum
z'	depth beneath the ground surface

References

- Benson, D. J. 1992. "Computational methods in lagrangian and eulerian hydrocodes." 99 (2–3): 235–394. [https://doi.org/10.1016/0045-7825\(92\)90042-I](https://doi.org/10.1016/0045-7825(92)90042-I).
- Benson, D. J. and S. Okazawa. 2004. "Contact in a multi-material eulerian finite element formulation." 193 (39–41), 4277–4298. <https://doi.org/10.1016/j.cma.2003.12.061>.
- Boukpeti, N., D. J. White, M. F. Randolph, and H.Low. 2012. "Strength of fine-grained soils at the solid–fluid transition." *Géotechnique* 62 (3): 213–226. <https://doi.org/10.1680/geot.9.P.069.1977>. "On the retrogression of landslides in sensitive muddy sediments." 14 (4): 582–602. <https://doi.org/10.1139/t77-059>.
- Cruden, D. M. and Varnes, D. J. (1996). "Landslides: investigation and mitigation. Chapter 3 – landslide types and processes." *Transportation research board special report*, (247).
- Demers, D., D. Robitaille, P. Locat, and J. Potvin. 2014. "Inventory of large landslides in sensitive clay in the province of Quebec, Canada: preliminary analysis." In *Landslides in Sensitive Clays*

– *from geosciences to risk management*, edited by JDemers, and J. Locat, 77–89. Dordrecht, the Netherlands: Springer.

Dey, R., B. Hawlader, R. Phillips, and K. Soga. 2015. “Large deformation finite-element modeling of progressive failure leading to spread in sensitive clay slopes.” *Géotechnique*, 65 (8): 657–668. <https://doi.org/10.1680/geot.14.P.193>.

Dey, R., B. Hawlader, R. Phillips, and K. Soga. 2016. “Modeling of large-deformation behaviour of marine sensitive clays and its application to submarine slope stability analysis.” 53 (7): 1138–1155. <https://doi.org/10.1139/cgj-2015-0176>.

Duncan, J. and P. Dunlop. 1968. “Slopes in stiff-fissured clays and shales.” Dutta, S., B. Hawlader, and R. Phillips. 2015. “Finite element modeling of partially embedded pipelines in clay seabed using coupled eulerian–lagrangian method.” 52 (1): 58–72. <https://doi.org/10.1139/cgj-2014-0045>.

Einav, I., and M. F. Randolph. 2006. “Effect of strain rate on mobilised strength and thickness of curved shear bands.” *Géotechnique* 56 (7): 501–504. <https://doi.org/10.1680/geot.2006.56.7.501>.

Hamann, T., G. Qiu, and J. Grabe. 2015. “Application of a coupled eulerian–lagrangian approach on pile installation problems under partially drained conditions.” *Comput. Geotech.* 63: 279–290. <https://doi.org/10.1016/j.compgeo.2014.10.006>.

Hamouche, K., S. Leroueil, M. Roy, and A. Lutenegeger. 1995. “In situ evaluation of K_0 in eastern Canada clays.” 32 (4): 677–688. <https://doi.org/10.1139/t95-067>.

Haugen, E. D., M. Tveit, and H. Heyerdahl. 2017. “Mapping quick clay hazard zones: Comparison of methods for estimation of the retrogression distance.” In *Landslides in sensitive clays – from research to implementation*, edited by V. Thakur, J.-S. L’Heureux, and A. Locat, Islam, N., B.

- Hawlder, C. Wang, and K. Soga. 2019. "Large deformation finite element modelling of earthquake-induced landslides considering strain-softening behaviour of sensitive clay." 56 (7): 1003–1018. <https://doi.org/10.1139/cgj-2018-0250>.
- Jeong, S. W., S. Leroueil, and J. Locat. 2009. "Applicability of power law for describing the rheology of soils of different origins and characteristics." 46 (9): 1011–1023. <https://doi.org/10.1139/T09-031>.
- Lebuis, J., M. Robert, and P. Rissmann. 1983. "Regional mapping of landslide hazard in Quebec." *Rapport-Statens geotekniska institut*, No.1986. "Slope instability and valley formation in Canadian soft clay deposits." 23 (3): 261–270. <https://doi.org/10.1139/t86-039>.
- Lefebvre, G. 2017. "Sensitive clays of eastern Canada: From geology to slope stability." In *Landslides in sensitive clays – from research to implementation*, edited by V. Thakur, J.-S. L'Heureux, and A. Locat, 15–34. Cham, Springer.
- Leroueil, S. 2001. "Natural slopes and cuts: movement and failure mechanisms." *Géotechnique*, 51 (3): 197–243. <https://doi.org/10.1680/geot.2001.51.3.197>.
- Locat, A., S. Leroueil, S. Bernander, et al. 2011. "Progressive failures in eastern Canadian and Scandinavian sensitive clays." 48 (11): 1696–1712. <https://doi.org/10.1139/t11-059>.
- Locat, A., H. P. Jostad, and S. Leroueil. 2013. "Numerical modeling of progressive failure and its implications for spreads in sensitive clays." 50 (9), 961–978. <https://doi.org/10.1139/cgj-2012-0390>.
- Locat, A., S. Leroueil, A. Fortin, D. Demers, and H. P. Jostad. 2015. "The 1994 landslide at Sainte-Monique, Quebec: geotechnical investigation and application of progressive failure analysis." 52 (4): 490–504. <https://doi.org/10.1139/cgj-2013-0344>.

Locat, A., P. Locat, D. Demers, et al. 2017. “The Saint-Jude landslide of 10 May 2010, Quebec, Canada: Investigation and characterization of the landslide and its failure mechanism.” 54 (10): 1357–1374. <https://doi.org/10.1139/cgj-2017-0085>.

Mitchell, R. and A. Markell. 1974. “Flowsliding in sensitive soils.” 11 (1): 11–31. <https://doi.org/10.1139/t74-002>.

Mitchell, R. 1978. “Earthflow terrain evaluation in Ontario.” Min. of Transportation and Communications of Ontario, Research and Development Division, Report RR213, 29 p.

Odenstad, S. 1951. “The landslide at Sköttorp on the Lidan River, February 2, 1946.” In *Royal Swedish Institute proceedings*, vol. 4, 1–40.

Potts, D., N. Kovacevic, and P. Vaughan. 1997. “Delayed collapse of cut slopes in stiff clay.” *Géotechnique*, 47 (5): 953–982. <https://doi.org/10.1680/geot.1997.47.5.953>.

Qiu, G. and J. Grabe. 2012. “Numerical investigation of bearing capacity due to spudcan penetration in sand overlying clay.” 49 (12): 1393–1407. <https://doi.org/10.1139/t2012-085>.

Quinn, P. E., S. Diederichs, R. K. Rowe, and D. J. Hutchinson. 2011. “A new model for large landslides in sensitive clay using a fracture mechanics approach.” 48 (8): 1151–1162. <https://doi.org/10.1139/t11-025>.

White, and Y. Yan. 2012. “Modelling the axial soil resistance on deep-water pipelines.” *Géotechnique* 62 (9): 837–846. <https://doi.org/10.1680/geot.12.OG.010>.

J. D. Allard, and J. Lebuis. 1985. “Zones exposées aux mouvements de terrain le long de la rivière Yamaska, entre Yamaska et Saint-Hyacinthe. [In French] Ministère de l’Énergie et des Ressources du Québec.

Söderblom, R. 1974. “A new approach to the classification of quick clays.”

Tavenas, F., J. Chagnon, and P. La Rochelle. 1971. “The Saint-Jean-Vianney landslide: observations and eyewitnesses accounts.” 8 (3): 463–478. <https://doi.org/10.1139/t71-048>.

- Tavenas, F. 1984. "Landslides in Canadian sensitive clays – a state-of-the-art." In *Proc., 4th International Symposium on Landslides*, vol. 1, 16–21. Toronto, Ontario. University of Toronto Press.
- Tavenas, F., P. Flon, S. Leroueil, and J. Lebuis. 1983. "Remolding energy and risk of slide retrogression in sensitive clays." In *Proc., Symposium on Slopes on Soft Clays*, SGI Report, No. 17, 423–454. Linköping, Sweden.
- Thakur, V., S. Degago, F. Oset, et al. 2014. "Characterization of post-failure movements of landslides in soft sensitive clays." In *Landslides in Sensitive Clays – from geosciences to risk management*, edited by J.-S. L'Heureux, A. Locat, S. Leroueil, D. Demers, and J. Locat, 91–103. Dordrecht, the Netherlands: Springer.
- Tran, Q. A. and W. Sołowski. 2019. "Generalized interpolation material point method modelling of large deformation problems including strain-rate effects–application to penetration and progressive failure problems." *Comput. Geotech.* 106, 249–265.
<https://doi.org/10.1016/j.compgeo.2018.10.020>.

Chapter 5

Implementation of a Large Deformation Finite Element Modelling Technique for Seismic Slope Stability Analyses

Co-Authorship: This chapter has been published in the Soil Dynamics and Earthquake Engineering as: Wang, C., Hawlader, B., Islam, N. and Soga, K. (2019), ‘Implementation of a large deformation finite element modelling technique for seismic slope stability analyses.’ Most of the research presented in this chapter has been conducted by the first author. He also prepared the draft manuscript. The other authors mainly supervised the research and reviewed the manuscript.

5.1 Abstract

Post-slide investigations show large displacement of failed soil mass in many earthquake-triggered landslides. An Eulerian-based finite-element modelling (FEM) of large deformation of soil, for pseudostatic and dynamic loadings, is presented in this study. The Eulerian FEM is compared with Lagrangian-based explicit and implicit finite-element (FE) modeling approaches. The dynamic FE modelling of two hypothetical slopes for eight earthquake acceleration–time histories show that the failure surfaces develop progressively, which cannot be modelled using the traditional limit equilibrium method (LEM). A large plastic shear strain concentration (i.e. shear band formation) occurs when the strain-softening behaviour of soil is considered. The similarities and differences between the results of dynamic and pseudostatic FE analyses based on estimated pseudostatic coefficient from acceleration–time records are presented. The duration of an earthquake influences the failure process and displacement of the failed soil mass. The displacement of the toe obtained from FEM is compared with Newmark's simplified approach. The developed Eulerian-based FE modelling technique has been used to simulate large-scale landslides in sensitive clays due to earthquake loading [1].

5.2 Introduction

The pseudostatic approach is commonly used in geotechnical engineering practice to evaluate the stability of slopes in which a destabilizing horizontal body force representing the earthquake-induced force is included in the conventional static limit equilibrium method (LEM). The factor of safety (F_s) can be calculated from pseudostatic analysis; however, it does not provide the information about displacement. Depending upon the severity of an earthquake and peak ground acceleration and site characteristics, a wide range of horizontal pseudostatic coefficients (k_h) has been recommended. In some cases, the k_h is recommended by calibrating against acceptable displacement, for example, for less than 1 m in earth dams [2]. However, considering the uncertainties in evaluating geotechnical properties, earthquake loading and geological settings, this method has been widely used in standard engineering practice.

The permanent deformation of the slope is generally calculated using the Newmark sliding block method [3], assuming the failed soil mass as a rigid block that slides downslope on a basal shear surface when its acceleration exceeds the critical acceleration. A number of studies also attempted to improve this method and proposed empirical relations calibrating against post-slide field data [4–6]. Post-slide investigations show that earthquake-induced landslides involve the failure of a number of soil blocks. The failure planes may not develop at the same time; instead, the failure occurs progressively, which could be captured in finite-element modelling.

The FEM developed in the Lagrangian framework has been used in the past to model slope failure. Implicit and explicit time integration schemes are commonly used in FE programs, where the former one requires iteration in each step while, in the latter one, the analysis progresses without any iteration and therefore requires small time increments for a stable solution. Explicit methods use the large-deformation theory and generally perform better in high-speed dynamic

problems and are computationally efficient for large models, compared to implicit analyses. Loukidis et al. [7] conducted FE analysis using an implicit approach to calculate the limiting k_h that required to fail a homogeneous slope. Tan and Sarma [8] conducted pseudostatic FE analyses using the ICFEP FE program [9], where k_h is gradually increased until the failure of the slope. Kourkoulis et al. [10] conducted dynamic FE analysis using an implicit approach, where the earthquake excitation is applied at the base of the model. They also considered the post-peak degradation of shear strength parameters with accumulated plastic shear strain. However, these studies did not investigate the large deformation behavior of failed soil mass as occurred in earthquake-triggered landslides.

Typical Lagrangian-based FE modelling suffers from numerical issues related to convergence and mesh distortion at large strains [11]. In recent years, advanced FE modelling techniques have been developed to accommodate large strains, which have been used for static and quasi-static geotechnical problems [12,13]. Adaptive mesh refinement algorithms using the updated Lagrangian formulation show a better performance for large deformation modelling than purely Lagrangian formulations [14,15]. In addition, the explicit finite difference methods based on Lagrangian and updated Lagrangian procedure have been used in some computer programs to cope with some level of large deformation, such as FLAC [16]. For a very large deformation, the soil has been modelled as an Eulerian material [12]; however, it has not been used in dynamic slope stability analyses, except for some preliminary studies [17,18].

The aim of this research is to simulate large-scale landslides, triggered by an earthquake, using an Eulerian-based FE modelling technique. To this end, the Eulerian FE modelling technique is validated and its advantages are shown in this paper by comparing the results with Lagrangian-based FE analyses, which can accommodate limited deformation. The Eulerian FE modelling

technique, including some input parameters, is calibrated against the simulations with the commercial software and simplified approaches used in the industry. Conducting simulations for eight earthquake acceleration–time histories, the key factors that influence the failure of a slope are identified. Finally, using this FEM technique, large-scale landslides in sensitive clays have been simulated, which has been presented elsewhere [1].

5.3 Problem Statement

Figure 5.1 shows the geometry of the slopes considered in the present study. A 15m high 2H:1V clay slope, stable under gravity load, is subjected to earthquake loading. A large soil domain of 400 m long (200 m on each side from the toe of the slope) is modelled in order to avoid boundary effects on slope failure. Analyses are performed for two slopes (Fig. 5.1(a) and 5.1(b)). In Slope-I, the soil profile consists of a 25 m thick upper clay layer of uniform undrained shear strength (s_{u0}) underlain by a 10 m thick strong base layer (Fig. 5.1(a)). The soil profile in Slope-II consists of two clay layers and a strong base layer (Fig. 5.1(b)). In the upper clay layer, s_{u0} increases linearly with depth, while it is constant in the bottom stiff clay layer. As will be shown later, the failure of the slope mainly occurs through the upper clay layers. The groundwater table is located at the ground surface.

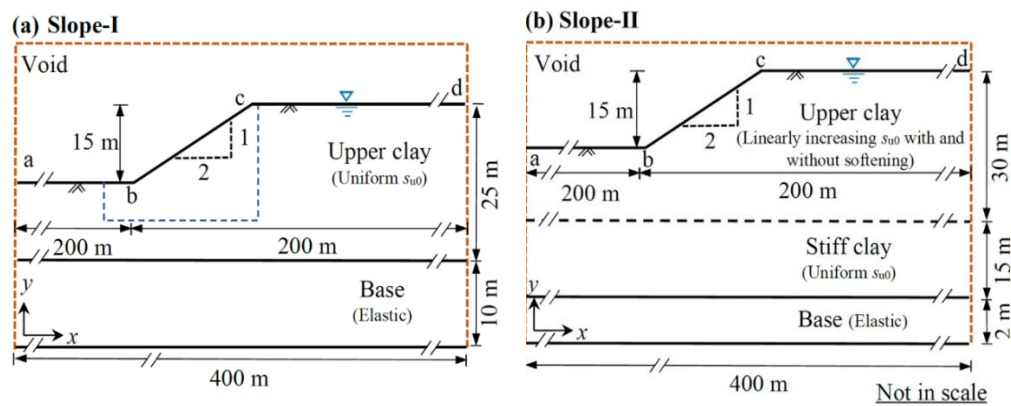


Fig. 5.1. Geometry of the slopes used in finite element modelling.

5.4 Finite Element Modelling

A number of studies show the advantages of FEM over traditional LEM for slope stability analysis [11,19]. The main advantages of FEM are: (i) a priori definition of the failure plane is not required as with LEM; instead, the failure occurs through the locations where shear stress reaches the shear strength, (ii) progressive formation of failure plane can be simulated, and (iii) the deformation of the failed soil mass can be calculated.

Many slope stability problems involve large deformation of the failed soil mass. Most of the FEM used in previous studies have been developed in purely Lagrangian frameworks [20,21] and therefore cannot simulate very large deformation because of significant mesh distortion around the failure planes that causes numerical instabilities and non-convergences of the solutions [11]. Recognizing the limitations of Lagrangian FEM, large deformation FEM techniques have been used for modelling slope failures [14,15,22].

The FE modelling becomes more complex if the soil has strain-softening behaviour because large strain concentrations occur in narrow zones in the form of shear bands, which is one of the key factors in modelling progressive failure of slopes [23–27]. The strain localization has been modelled using other approaches such as the Cosserat model [28,29], gradient or nonlocal theories [30], computational fluid dynamics [23], extended finite element [31], material point method [32] and smoothed particle hydrodynamics (SPH) [33]. The authors and their co-workers provided a review of the currently available large deformation FE modelling techniques for static and quasi-static problems elsewhere [12,34]. The application of these large deformation FEM techniques for earthquake-triggered landslides is very limited. A summary of finite element analysis of earthquake-induced slope failure has been presented in Ref. [17].

5.5 Finite Element Model Development

Numerical simulation is performed using Abaqus 6.14.2 FE software [35]. The software adopted implicit and explicit schemes for dynamic time integration for modelling Lagrangian materials. The explicit scheme has also been used for Eulerian formulations. In this paper, these numerical techniques are simply called *Implicit*, *Explicit*, and *Eulerian* analysis.

5.5.1 Eulerian analysis

One of the main advantages of the Eulerian approach is that the material (soil) flows through the fixed mesh and therefore numerical issues related to mesh distortion are not encountered. Further details of mathematical formulations, its application to large deformation static and quasi-static geotechnical problems and the advantages are available in previous studies [12,13,36,37].

In Abaqus/Explicit, the Eulerian approach is implemented only for three-dimensional elements. Therefore, the analysis is performed with only one element length in the out-of-plane direction in order to simulate plane strain condition. The domain is discretized using 0.25 m cubical elements, except for the mesh sensitivity analysis. The soil is modelled as an Eulerian material using EC3D8R, which is 8-node linear brick elements of multi-materials having reduced integration with hourglass control. A void space above the ground surface is created in order to accommodate the displaced soil mass during the failure of the slope. The Eulerian volume fraction (EVF) tool in the software is used to create the initial void and soil domains. For an element, $EVF = 1$ means that the element is filled with soil and $EVF = 0$ means the element is void. A fractional value of EVF means that the element is partially filled with soil.

Zero velocity boundary conditions are applied normal to the bottom and all the vertical faces in pseudostatic analysis. In other words, the bottom of the model is restrained from any vertical movement while the vertical faces are restrained from any lateral movement. For dynamic analysis,

non-reflecting boundary conditions are applied to the left and right vertical faces, as discussed in Section 5.7.2.2. No boundary condition is applied along the soil–void interface to allow the displaced soil to move in the void space when needed.

5.5.2 Implicit and explicit approaches

Using the “sizing controls” option in the software, a mesh of ~ 0.25 m is created in a zone near the slope, as shown by thin dashed lines in Fig. 5.1(a). Outside this zone, the mesh size is 0.25 m. The analysis is performed using 4-node bilinear plane strain quadrilateral elements with reduced integration and hourglass control (CPE4R). The bottom of the domain is restrained from vertical movements. In the pseudostatic analysis, the two vertical faces are restrained from any lateral movement using roller supports. However, in the dynamic FE analysis, infinite elements are used to avoid wave reflection from lateral boundaries, as discussed in Section 5.7.2.2.

5.5.3 FE modelling steps

FE modelling consists of following three consecutive steps:

- i. Gravity loading: The geostatic load is applied to establish the in-situ stress condition. The slope is stable at the end of this loading step.
- ii. Earthquake loading: Two approaches are used for seismic loading. In the pseudostatic analysis, the horizontal component of body force is increased gradually with time. In the dynamic analysis, a horizontal excitation (acceleration–time history) is applied at the base of the model. The only pseudostatic analysis is performed for Slope-I (Fig. 5.1(a)).
- iii. Post-quake simulation: In the dynamic analysis, the analysis is continued for a period of time after the earthquake loading, to investigate post-quake behaviour. The purpose of the step is to examine the continuation of displacement of the failed soil mass until it comes to a new equilibrium.

The automatic time increments calculated by the software is used, which ensures that the distance travelled by the fastest wave in the model in each time increment is smaller than the smallest characteristic element size. For further verification, analysis is conducted by reducing the software-calculated automatic time increment by 50 %, and no significant change in the results is found. Moreover, for the soil parameters used in this study, the shear wave velocity, $V_s (= \sqrt{G/\rho})$ is ~ 40 m/s. For a maximum frequency (f_0) of 5–20 Hz, the wavelength of the shear wave $\lambda (= V_s/f_0)$ is 8.2–2.05 m, which represents 8–33 elements for the FE mesh size of 0.25 m. Therefore, the spurious oscillation is not expected.

Table 5.1. Geotechnical parameters used in finite element analyses.

Parameters	Values		
	Upper Clay	Stiff Clay	Base
Undrained Young's modulus, E_u (MPa)	10	10	100
Poisson's ratio, ν_u	0.495	0.495	0.495
Saturated unit weight, γ_{sat} (kN/m ³)	20	20	20
Undrained shear strength for slope-I, s_{u0} (kPa)	60	—	—
Peak undrained shear strength for slope-II, s_{u0} (kPa)	15+2.67z*	150	—
Rayleigh damping parameter, β	0.000375 [§]	0.000375 [§]	—
Remoulded sensitivity, S_t	1.5**	—	—
Plastic shear displacement for 95% degradation of soil strength, δ_{95} (m)	0.25**	—	—

* z is the depth below the crest of the slope in meter

§ used in dynamic analysis

** used in dynamic analysis for strain-softening clay

5.6 Modelling of Soil

The analyses are performed for an undrained loading condition because the earthquake loading and failure occur in a short period of time. For dynamic analysis, a kinematic hardening model (see Section 5.6.2) is used for clay. In pseudostatic analysis, the clay layers are modelled as an elastic-perfectly plastic material. The yield strength (σ_y) is related to undrained shear strength s_{u0} as $\sigma_y = \sqrt{3}s_{u0}$. The soil parameters used in the analysis are shown in Table 5.1.

5.6.1 Undrained shear strength

For Slope-I, uniform $s_{u0} = 60$ kPa is used for the upper clay layer. For Slope-II, analyses are performed for two types of stress–strain behavior of the upper clay layer. Firstly, in the non-softening case, s_{u0} of the upper clay layer is increased linearly with depth from 15 kPa at the ground surface (level of the crest) to 95 kPa at 30 m depth. For the stiff clay layer, a uniform undrained shear strength of 150 kPa is used. The base layer is modelled as an elastic material. Secondly, in the strain-softening case, in addition to the linear increase of s_{u0} , a post-peak degradation of mobilized undrained shear strength (s_u) is incorporated, using Eq. (5.1).

$$s_u = \left[\frac{1}{S_t} + \left(1 - \frac{1}{S_t} \right) e^{-\frac{3\delta}{\delta_{95}}} \right] s_{u0} \quad (5.1)$$

where δ is the accumulated plastic shear displacements from loading and unloading; S_t is the remoulded sensitivity ($= s_{u0}/s_{uR}$) in which s_{uR} is the remoulded s_u at a large plastic shear displacement; and δ_{95} is the value of δ at which 95% reduction of $(s_{u0} - s_{uR})$ occurs. Note that a linear degradation of post-peak shear strength with accumulated plastic shear strain during cyclic loading has been used in previous studies [38][39].

The pseudostatic slope stability analysis generally provides reasonable results if the strength degradation due to earthquake loading is not very significant [4,5]. For example, Kramer [40]

recommended that this procedure could be used if strength degradation is less than 15% of the peak shear strength. Therefore, in the present study, the post-peak strength degradation model is not used in pseudostatic analysis.

5.6.2 Kinematic hardening for dynamic loading

A simple kinematic hardening model is used for the upper clay layer for dynamic analyses. A detailed discussion on the use of this model for undrained cyclic behaviour of clay, including the selection of model parameters, is available in previous studies [41]. According to this model, the yield surface (F) is defined as

$$F = f(\boldsymbol{\sigma} - \boldsymbol{\alpha}) - \sigma_0 \quad (5.2)$$

where $\boldsymbol{\alpha}$ is the backstress, and σ_0 is the yield stress at which plastic shear strain is zero. Typically, σ_0 is a fraction (0.1–0.3) of the yield strength σ_y [41]. In this study, $\sigma_0 = 0.3\sigma_y$ is used.

The evolution of stress composed of both kinematic and isotropic hardening components. The kinematic component hardening is evaluated through $\boldsymbol{\alpha}$, using the following nonlinear function.

$$\dot{\boldsymbol{\alpha}} = C \frac{1}{\sigma_0} (\boldsymbol{\sigma} - \boldsymbol{\alpha}) \dot{\epsilon}^p - \bar{\gamma} \boldsymbol{\alpha} \dot{\epsilon}^p \quad (5.3)$$

where $\dot{\epsilon}^p$ = equivalent plastic shear strain rate; C = initial hardening modulus; and $\bar{\gamma}$ = a parameter that determines the rate of decrease of kinematic hardening with an increase in plastic strain. For the undrained behaviour of clay, Anastasopoulos et al. [41] showed that $C = E_u$ (Young's modulus) and $\bar{\gamma} = C/(\sigma_y - \sigma_0)$. The above formulation ensures that, at a large plastic strain, $\boldsymbol{\sigma} = \sigma_y$ and $\dot{\boldsymbol{\alpha}} = 0$.

The isotropic component of hardening defines the evolution of the size of the yield surface. For the non-softening soil model, the yield surface remains constant. However, for the strain-

softening model, the size of the yield surface decreases as a function of mobilized s_u , as defined by Eq. (5.1).

5.6.3 Elastic properties

The undrained Young's modulus (E_u) depends on a number of factors including the undrained shear strength, plasticity index and overconsolidation ratio [42]. In addition, shear modulus degradation due to cyclic loading, even at shear stresses smaller than yield strength, has been reported from laboratory tests [43,44]. In this present study, the effects of these factors are not explicitly considered. A constant value of E_u (= 10 MPa) has been used. For the upper clay layer, through which failure occurs, E_u/s_{u0} is 167 for the Slope-I, and 182 for the average value of s_{u0} in Slope-II.

5.6.4 Numerical implementation of shear strength

Uniform s_{u0} for the upper clay layer in Slope-I and stiff layer in Slope-II is given as the yield strength. However, the linear variation of s_{u0} in the upper clay layer in Slope-II cannot be given directly as an input, and therefore it is defined using the temperature as a dummy variable. For the strain-softening cases, the yield strength is given as a function of equivalent plastic shear strain ϵ_q^p , which is related to engineering plastic shear strain (γ^p) as $\epsilon_q^p = \gamma^p/\sqrt{3}$, where $\gamma^p = \delta/t_{FE}$ for simple shear condition and t_{FE} is the size of the elements used in this study. Note that ϵ_q^p is a scalar variable that represents the integration of plastic deviatoric strain rate tensor ($\dot{\epsilon}_{ij}^p$) over the period of analysis (t).

$$\epsilon_q^p = \int_0^t \sqrt{\frac{2}{3} \dot{\epsilon}_{ij}^p : \dot{\epsilon}_{ij}^p} dt \quad (5.4)$$

Note that FE results are highly mesh dependent when the strain-softening behaviour of soil is considered. In that case, defining shear strength degradation as a function of γ^p , which is related to plastic shear displacement (Eq. 5.1) and finite element size (i.e. mesh-size regularization), can reduce the mesh dependency of the solution [1][12].

5.7 Numerical Simulation Results

In the following sections, the development of failure planes is explained by the formation of shear bands, where the concentration of ϵ_q^p occurs due to earthquake loading.

5.7.1 Pseudostatic FE analyses results

Similar to previous studies [7,8], the pseudostatic load is gradually applied in FE modelling by increasing the horizontal body force $F_b (= k_h \gamma)$ per unit volume of soil, where γ is the bulk unit weight of soil. Except for some implicit analyses, where the solution stops because of numerical issues due to mesh distortion, k_h is increased to a maximum value of 0.1, which represents a severe earthquake, as per Rossi-Forel IX [45]. To maintain a quasi-static condition, k_h is increased slowly.

5.7.1.1 Pseudostatic simulation results for slope-I

The left column of Fig. 5.2 shows the Eulerian simulation results for Slope-I (Fig. 5.1(a)). At the end of the geostatic step ($k_h = 0$), very small plastic shear strains develop at the interface between the upper clay and base layer below the middle of the slope (Fig. 5.2(a–c)). However, the slope is globally stable under this load. A limit equilibrium analysis (Spencer's method) is also performed using the Slope/W software [46], which gives $F_s = 1.24$ for the geostatic loading condition. The circular dashed line in the first column of Fig. 5.2 shows the critical circle (minimum F_s) obtained from Slope/W. The critical circle also passes through the interface between clay and base layer. For clarity, the critical circles are shown only on Eulerian simulation results.

With an increase in k_h , the shear band propagation occurs mainly on the left side of point A and reaches the downslope ground surface (Fig. 5.2(d)). The equivalent plastic shear strain distribution for $k_h = 0.03$ shows that a triangular wedge develops by the formation of another shear band from the toe of the slope (Fig. 5.2(g-i)).

From FE results, the failure of a slope can be defined based on several criteria, such as bulging of slope profile, limiting shear stress on the failure plane, non-convergence of the solution and formation of a complete shear band for the global failure of a soil block [7,11]. In the present study, the last criterion is used to define failure.

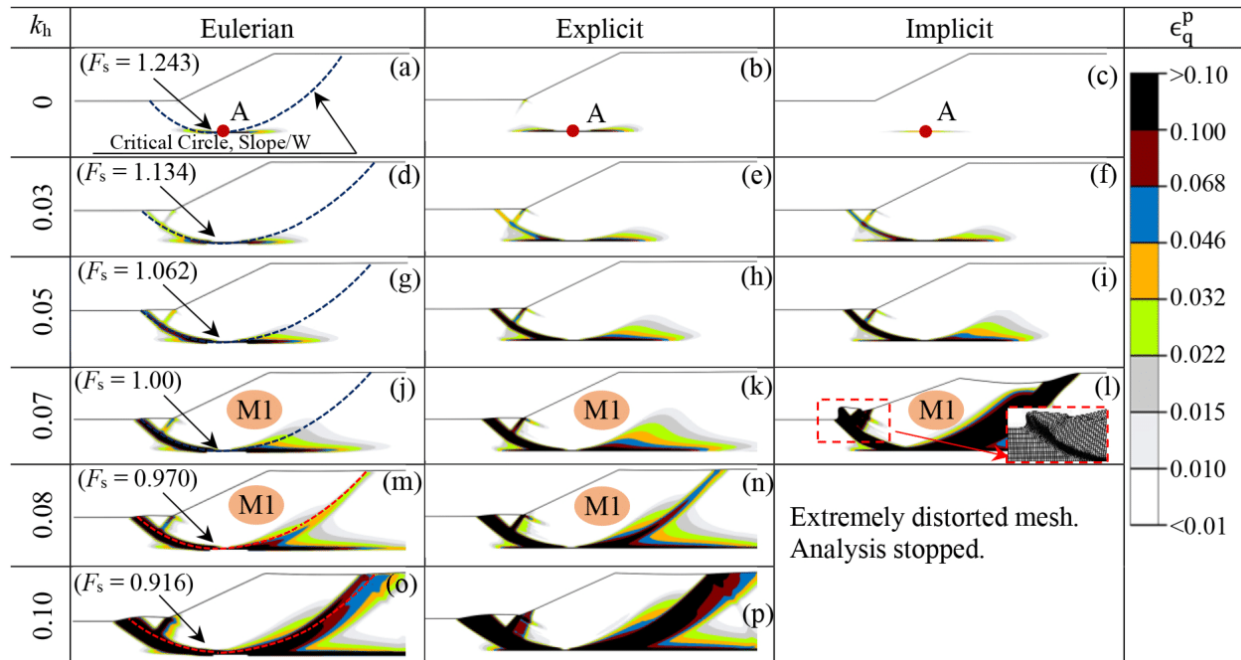


Fig. 5.2. Pseudostatic analyses of Slope-I using three FE modeling approaches.

The accumulation of plastic strains in the shear band and its propagation on the right side of point A continues with an increase in k_h (Figs. 5.2(g and j)). A curved shear band forms from the horizontal shear band and reaches the ground surface (Fig. 5.2(m)). Figures 5.2(j and m) show that the global failure of the soil mass M1 occurs at $k_h = 0.07$ – 0.08 . The LEM gives $F_s = 1.0$ at this level of k_h . The value of k_h that gives $F_s = 1.0$ is known as the yield coefficient (k_y) [47]. In other

words, k_y obtained from the Eulerian analysis and LEM are comparable. For $k_h > k_y$, the magnitude of ϵ_q^p increases in the shear bands and also the length of the horizontal shear band increases.

In order to compare the performance of Eulerian approach for large deformation modelling of slopes, analyses are also performed with explicit and implicit schemes. The first three rows of Fig. 5.2 show that simulation results are very comparable for these three types of FE analysis for $k_h < 0.05$, where ϵ_q^p is not significantly high. However, at $k_h = 0.05-0.07$, a complete sliding surface develops, causing a global failure of soil mass M1 in the implicit analysis. Considerable heave near the toe and settlement in the upslope area occur at this stage. The FE mesh along the failure planes becomes extremely distorted (inset of Fig. 5.2(l)). Figures 5.2(k and n) show that the failure pattern in explicit is similar to Eulerian modelling, although ϵ_q^p in explicit is higher than Eulerian. At a large $k_h (= 0.1)$, the zone of accumulated ϵ_q^p widens in Explicit (Fig. 5.2(p)) while ϵ_q^p mainly concentrates in a relatively narrow band in the Eulerian analysis (Fig. 5.2(o)). At this level of large displacements, significant mesh distortion also occurs in explicit, which is discussed further in the following sections.

The FEM provides information about deformations/strains in soil elements. Figure 5.3 shows the increase in ϵ_q^p with k_h at point A in Figs. 5.2(a-c). The calculated ϵ_q^p using all three approaches are comparable for low $k_h (\leq 0.05)$. From $k_h \sim 0.07$, ϵ_q^p increases abruptly in the implicit approach when a significant mesh distortion occurs. However, in the Explicit and Eulerian FEM, ϵ_q^p increases gradually and, at $k_h \sim 0.1$, the rate of increase of ϵ_q^p becomes high. In summary, the present Eulerian FEM can successfully simulate the failure of a clay slope, even at large deformation.

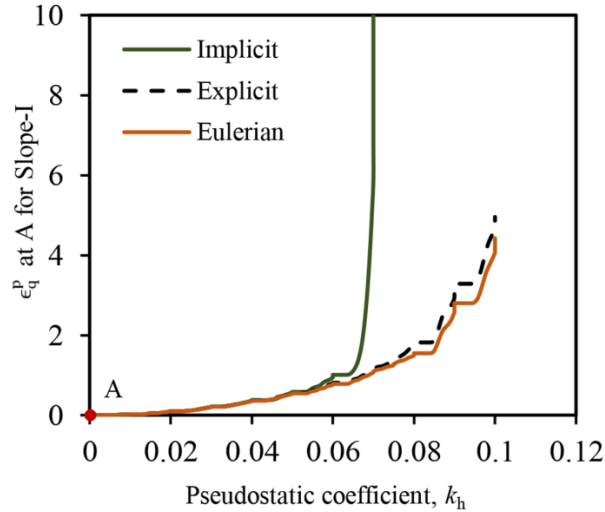


Fig. 5.3. Comparison of plastic shear strain at point A in Fig. 5.2(a).

5.7.1.2 Pseudostatic simulation results for slope-II

In Slope-I, because of uniform s_{u0} in the upper clay layer, failure initiates from the interface between the clay and base layers (Fig. 5.2(a–c)). In order to investigate the effects of the shear strength of the upper clay layer on failure patterns, pseudostatic FE and LE analyses are performed for Slope-II. Fig. 5.4 shows the progressive development of failure planes with k_h using three FE modelling approaches. As the linearly increasing s_{u0} profile is used, the failure plane does not reach the bottom of the upper clay layer. Only the curved failure planes develop without formation of any horizontal shear band as in Fig. 5.2. The critical circles obtained from LE analysis using Slope/W are comparable to FE analysis as shown in the first column of Fig. 5.4. The maximum depth of the failure plane from the toe is $\sim 3\text{--}4$ m. Similar to Slope-I, the yield coefficient k_y (i.e. value of k_h when ϵ_q^p generates along a complete failure plane) is lower in the implicit analysis than with the other two FE methods: $k_y \sim 0.04$ in Implicit, while $k_y \sim 0.06$ in Explicit and Eulerian FEM. Figure 5.4(l) shows that extremely large mesh distortion occurs after k_y , which implies that the

solution obtained from the Lagrangian-based implicit FE approach is not acceptable at large deformations. However, the mesh distortion issue is completely avoided in the Eulerian approach.

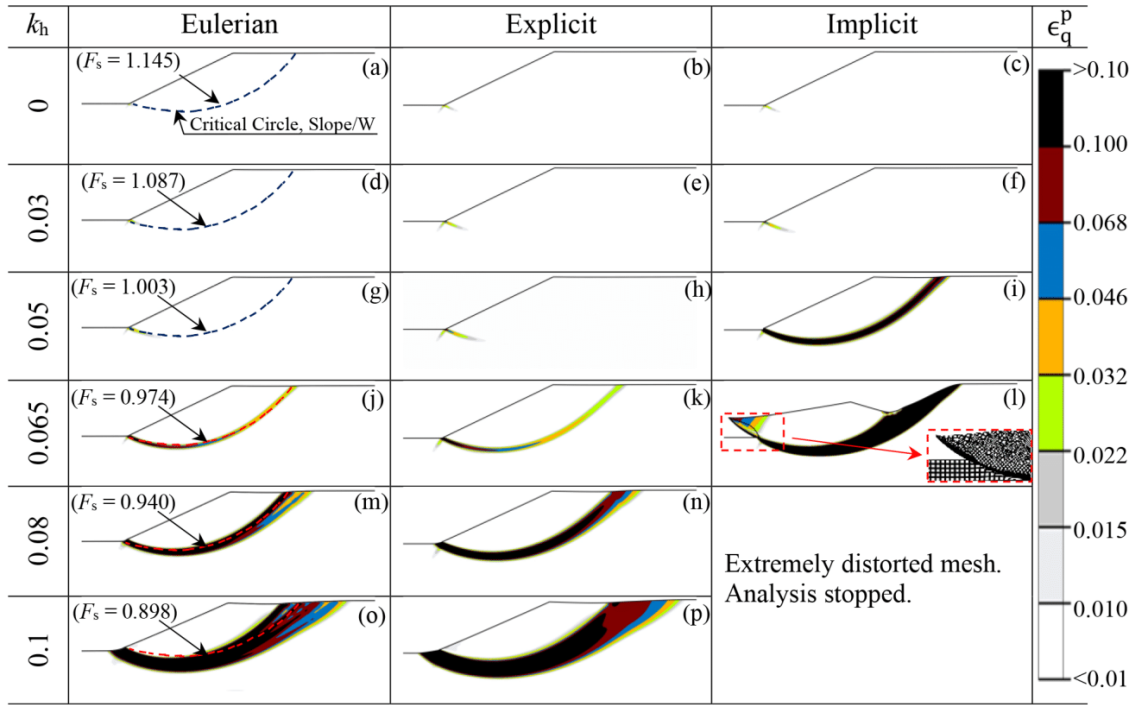


Fig. 5.4. Pseudostatic analyses of Slope-II using three FE modeling approaches.

5.7.1.3 Effect of FE mesh size

Figure 5.5 shows the formation of failure planes with k_h for four mesh sizes. The width of the ϵ_q^p accumulation zone increases with an increase in mesh size. At large k_h , a number of distinct shear bands form in the upslope area near the ground surface for small meshes (e.g. 0.125 m, Fig. 5.5(c)). However, ϵ_q^p accumulates in a thick zone in the large mesh model (e.g. 1.0 m, Fig. 5.5(l)). Overall, the failure pattern is very similar for these mesh sizes; however, the computational cost increases significantly for the small mesh. Therefore, in the present study, all the other analyses are performed using 0.25 m cubical elements.

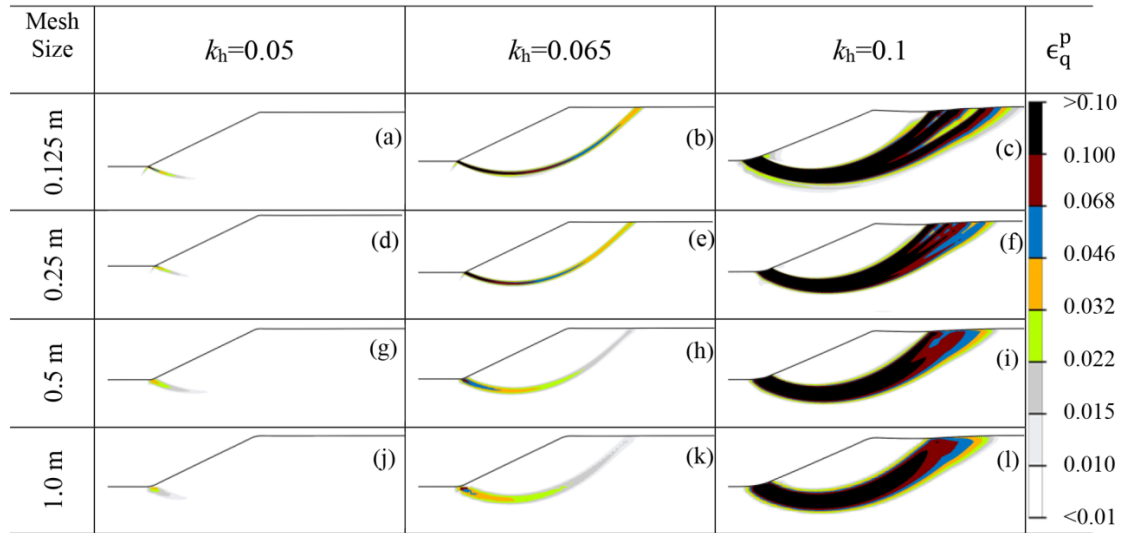


Fig. 5.5. Mesh size effects on FE results based on pseudostatic analyses of Slope-II.

5.7.2 Dynamic FE analyses

The pseudostatic analysis may not provide the actual response of the slope in many cases [5,47,48]. In addition to the uncertainty in the selection of an appropriate value of k_h , generally it tends to provide an over-conservative solution, while in some cases it is less conservative [48]. Dynamic analysis is presented in this section, aiming to show the similarities and differences between the results of pseudostatic and dynamic FE models. The dynamic analysis is also performed considering the strain-softening behaviour of the soil.

The following are some of the challenging issues in dynamic FE modeling: (i) modeling of stress–strain behaviour of soil including the degradation of shear strength due to earthquake loading; (ii) modeling of large deformation without numerical issues; (iii) selection of input ground motion; and (iv) modelling of boundary conditions. The advantages of the Eulerian approach for modelling large deformation are discussed in previous sections. The dynamic analyses are performed for the Slope-II (Fig. 5.1(b)) with and without strain-softening (ab and ace in Fig. 5.6).

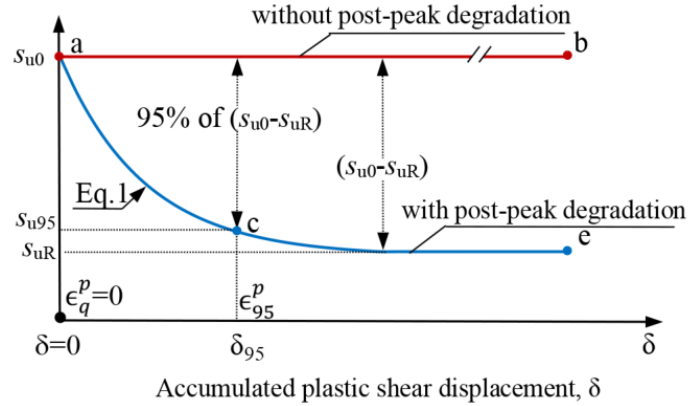


Fig. 5.6. Stress–strain behaviour used in FE modeling.

5.7.2.1 Input motions

The intensity of earthquake excitation could significantly affect slope failure mechanisms. Fig. 5.7 shows the horizontal acceleration–time histories of eight reference earthquake input motions used in the present numerical simulations, which are obtained from the Pacific Earthquake Engineering Research Center (PEER) ground motion database [49]. These earthquakes are considered because they cover a wide range of peak ground accelerations ($a_{\text{peak}} = 0.183 \text{ g}–0.434 \text{ g}$) and significant durations ($t_{\text{sig}} = 4.34 \text{ s}–24.91 \text{ s}$). The moment magnitude (M_M) varies between 6.0 and 7.6, which can cause widespread landslides [50]. All these motions are baseline corrected, which is verified using DEEPSOIL software [51], to avoid unexpected velocity and displacement. The input earthquake excitation is applied as an acceleration–time history at the base of the model.

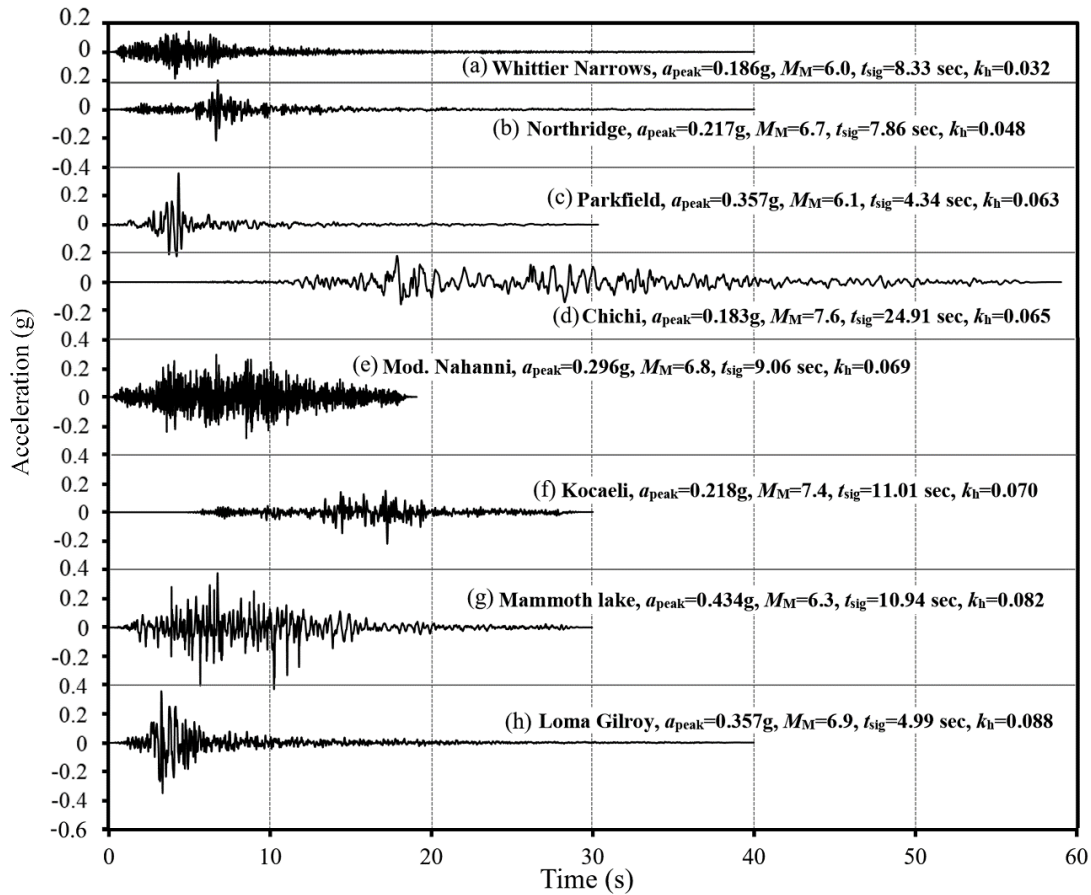


Fig. 5.7. Acceleration–time histories of earthquake input motions used in numerical simulations.

5.7.2.2 Boundary conditions

The selection of appropriate boundary conditions is a challenging task in dynamic FE modelling. In pseudostatic FE analysis, fixed boundary conditions at a sufficiently large distance from the slope, defined by velocity or fixity, do not affect the simulation results. However, in a dynamic FE analysis, the energy radiation and wave reflection from the boundary plays a major role. Different approaches have been used in the past, which include the placement of the lateral boundary very far from the slope, infinite elements at the end, and the use of absorbent, transmitting or non-reflecting lateral boundaries to minimize the undesirable parasitic boundary effect due to the seismic reflection to the zone of concern [10,52–54].

In the present analysis, the lateral boundary effects are minimized by placing them at a large distance from the slope together with appropriate boundary conditions. For implicit and explicit analyses, infinite elements are used at the two lateral ends of the model. However, infinite elements cannot be used in the Eulerian analysis. Hence, a non-reflecting Eulerian outflow boundary condition is used in the Eulerian modelling. The mathematical formulations of inflow/outflow Eulerian boundaries for modelling non-reflecting boundary conditions can be found in previous studies [55,56]. The effects of the lateral boundary condition on slope failure are discussed later.

5.7.2.3 *Material damping*

The energy dissipation primarily occurs due to frequency-independent hysteretic behaviour of soil, which can be incorporated in a dynamic FE analysis using a nonlinear stress–strain relationship [57–59]. As a nonlinear elasto-plastic soil model with kinematic hardening is used in the present study, the plastic flow can simulate hysteretic damping when loading/unloading occurs after the yield stress (σ_0) (see Section 5.6.2). For a cyclic loading below the yield stress, the energy dissipation can be achieved by a nonlinear variation of stiffness with Masing's rule [60,61] and viscous damping. The pre-yield stiffness variation is not considered in the present study. Mánica et al. [58] compared the damping models available in FLAC software [16] and showed the best performance with the Rayleigh damping method for their problems. In the present study, the viscous damping is incorporated using the Rayleigh damping. The default bulk viscosity is used to control high-frequency oscillations. The Eulerian approach neglects the mass proportional damping. The stiffness proportional damping $\beta = 0.000375$ is used, which represents an approximately 2–3 % damping ratio (frequency 17–25 Hz) for the problems analyzed in this study. This is verified by comparing the acceleration of the soil elements in the slope using Quake/W

with the damping ratio [46] and FE analyses with the Rayleigh damping, assuming elastic soil behaviour.

5.7.3 Dynamic FE results

5.7.3.1 Effects of lateral boundary conditions

Figure 5.8 shows the simulation results with and without the Eulerian non-reflecting lateral boundary conditions for Slope-II (Fig. 5.1(b)) subjected to the Parkfield earthquake (Fig. 5.7(c)), at $t = 30$ s. In both cases, the lateral boundaries are placed at 200 m from the toe of the slope. The analysis with the non-reflecting boundary condition shows the development of small plastic shear strain only near the toe (Fig. 5.8(a)). However, the analysis without the non-reflecting boundary condition shows the development of a complete failure plane (Fig. 5.8(b)). This is because of considerable wave reflection from the lateral boundaries, even though they are placed sufficiently far from the slope. As mentioned before, infinite elements have been successfully used in Lagrangian FE methods to avoid boundary effects. A dynamic explicit analysis is also performed with infinite elements at the lateral boundaries. The acceleration–time history in soil elements and the development of ϵ_q^p are in good agreement with the Eulerian FEM having Eulerian non-reflecting boundary conditions.

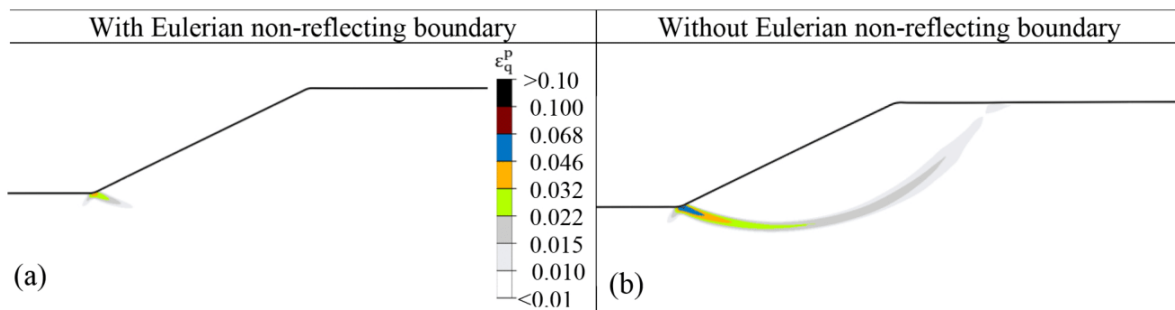


Fig. 5.8. Effects of non-reflecting outflow Eulerian boundary condition on FE results for the Parkfield earthquake.

5.7.3.2 Dynamic FE results for non-softening upper clay layers

The soil parameters used in dynamic FE modelling are shown in Table 5.1. Figure 5.9 shows the development of failure planes in Slope-II using three FE approaches for the eight earthquakes shown in Fig. 5.7. For brevity, ϵ_q^p only at the end of the simulation is shown in Fig. 5.9.

In order to compare the results of dynamic FE analysis (Fig. 5.9) with pseudostatic FE analysis (Fig. 5.4), the pseudostatic horizontal coefficient k_h for the earthquakes shown in Fig. 5.7 is estimated. As mentioned in the introduction, the estimation of k_h is a challenging task. Terzaghi [62] recommended k_h based simply on the severity of the earthquake. Considering a tolerable seismic displacement of 1 m for earth dams, k_h between 0.05 and 0.15 has been recommended [63]. Some studies suggested k_h as a percentage of the peak ground acceleration (a_{peak}) [64][65]. Pyke [66] proposed a chart for k_h/a_{peak} as a function of the earthquake magnitude M_M (reproduced in [67]). Note that improved methods for estimation of k_h , incorporating other factors, have also been proposed. For example, Bray and Travararou [5] considered the fundamental period of the potential sliding mass and the site-dependent seismic demand. In the present study, for modelling of the hypothetical slopes, k_h is estimated from Pyke's chart because the parameters required to obtain k_h (i.e. a_{peak} and M_M) are known for the earthquakes considered. The estimated values of k_h are shown in Fig. 5.7 and in the first column of Fig. 5.9. Using this value of k_h , limit equilibrium analysis is performed using Slope/W. The location of the critical circle (dashed line) and corresponding F_s are shown in the second (Eulerian) column of Fig. 5.9.

Figures 5.9(a–f) show the development of very small ϵ_q^p only near the toe for the Whitter Narrows and Northridge earthquakes. The LE analyses with corresponding k_h ($= 0.032$ and 0.048) give F_s greater than 1.0. Compared with pseudostatic FE analysis for this range of k_h in Fig. 5.4 (3rd and 4th rows), similar ϵ_q^p is shown in the Eulerian and Explicit analyses. However, the implicit

analysis gives higher ϵ_q^p in pseudostatic analysis (Fig. 5.4(i)) than with dynamic FE analysis (Fig. 5.9(f)) for the Northridge earthquake.

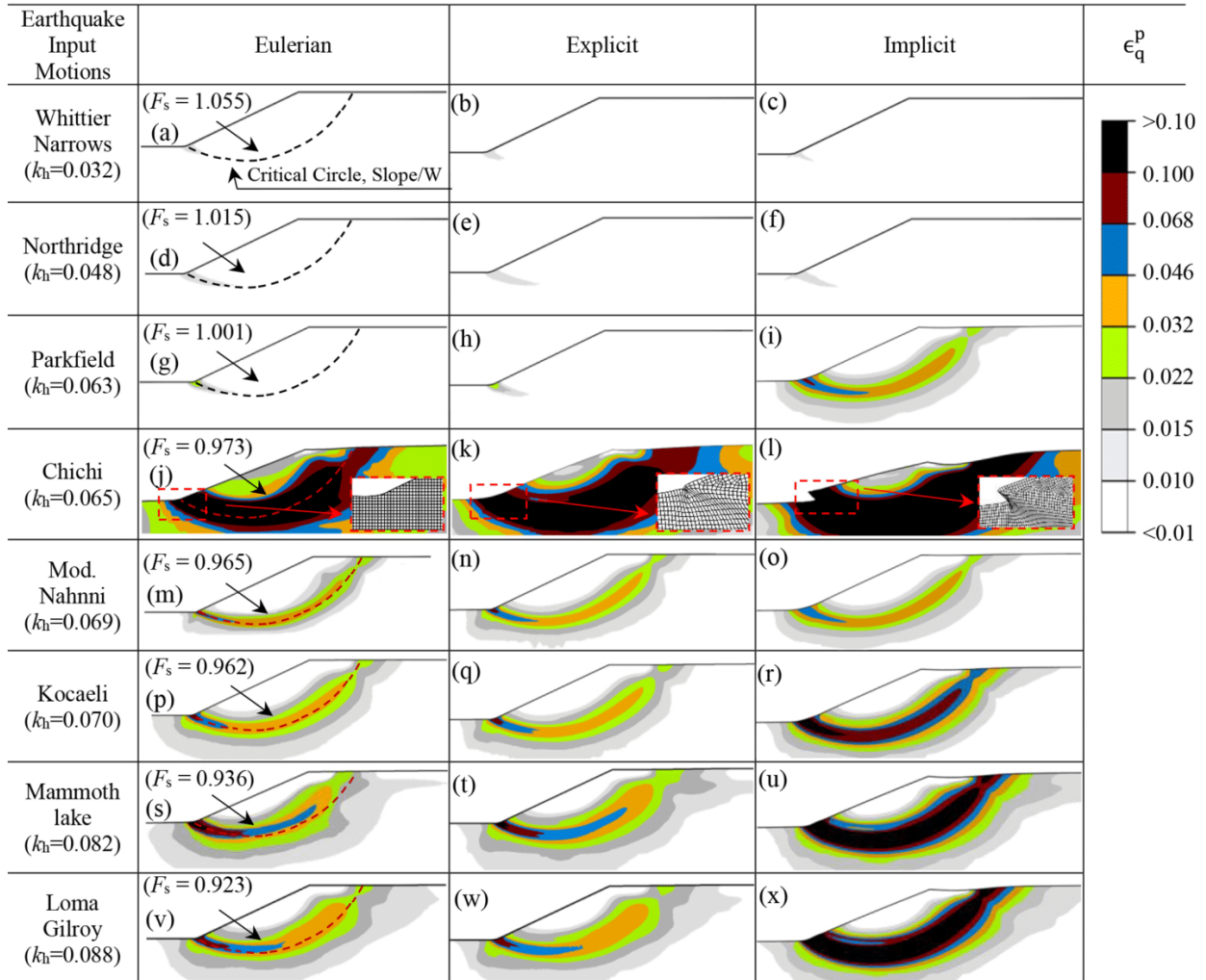


Fig. 5.9. Dynamic analysis using three FE modeling approaches for non-softening soil.

The Parkfield earthquake was of short duration ($t_{sig} = 4.34$ s). The Eulerian and Explicit dynamic analyses do not show global failure (Figs. 5.9(g and h)) while the pseudostatic analysis with corresponding k_h ($= 0.065$) shows the formation of a complete failure plane (Figs. 5.4(j and k)). Calculated toe displacement for implicit analysis is less in the dynamic FE modelling (Fig.

5.9(i)) than that in pseudostatic modelling (Fig. 5.4(l)). This simulation shows that the duration of an earthquake influences the failure and displacement of the slope [6][60],[68][69].

Global failure occurs for the other five earthquakes (see the last 5 rows of Fig. 5.9). The calculated F_s using Slope/W with k_h obtained from Pyke's chart is less than 1.0. The critical circle obtained from Slope/W is located along the shear band obtained from the Eulerian dynamic FE analysis.

In the implicit and explicit FE simulations of the Chi-Chi earthquake, significantly high ϵ_q^p generates in a wide shear band in the dynamic analysis (Figs. 5.9(k and l)) as compared to pseudostatic analysis with estimated $k_h = 0.065$ (Figs. 5.4(k and l)). A potential reason for this difference is the long duration of the earthquake ($t_{sig} = 24.91$ s). Once the failure is initiated, the displacement of the failed soil mass over a long period of cyclic loading widens the zone of plastic shear strain. However, in pseudostatic analysis, the earthquake-induced body force simply acts as a permanent force where the loading period does not have any effect.

In the cases of the Kocaeli, Mammoth Lake, and Loma Gilroy earthquakes, the dynamic analysis gives a lower ϵ_q^p than the pseudostatic analysis. A significantly large distortion of mesh occurs in the pseudostatic implicit analyses for the estimated range of $k_h = 0.070$ – 0.088 , and therefore it is not shown in Fig. 5.4. However, in the dynamic analysis, the mesh distortion is relatively small (Figs. 5.9(r, u and x)).

In summary, the comparison between Figs. 5.4 and 5.9 reveals the following: (i) the Eulerian approach can successfully simulate the failure of the slope, including the large deformation of the failed soil mass, (ii) the pseudostatic FE modeling results may not be always consistent with dynamic FE analysis results, and (iii) the duration of earthquake loading also influences the failure process.

5.7.3.3 Dynamic FE results with strain-softening behaviour of upper clay

In addition to the geotechnical parameters required for non-softening soil model, two additional parameters (S_t and δ_{95} in Eq. 5.1) are required for modelling the post-peak degradation of s_u of the upper clay layer (Fig 5.1(b)). In this study, $S_t = 1.5$ and $\delta_{95} = 0.25$ m are used. Note that S_t in this paper is used to represent the reduction of s_u of typical clay due to cyclic loading, which is very similar to “remoulded sensitivity” used by Randolph and his co-workers [70][71]. The remoulded sensitivity of typical clay, such as kaolin or glacial clay, is in the range of 1.5–3.0 [12], while the sensitivity of sensitive clay could be significantly higher than these values. A large amount of accumulated plastic shear strain is required to reach s_{uR} [70][71]. For the value of δ_{95} and element size used in this study, the 95% reduction in s_u will occur at $\gamma^p = 100\%$ (i.e. δ_{95}/t_{FE}).

Figures 5.10(a–c) show that the slope is globally stable for the Whittier Narrows earthquake. As shown in Eq. (5.1), the s_u degradation occurs only if plastic shear strains develop. For this earthquake, very small plastic shear strain generates, which is not sufficient to reduce s_u significantly. Therefore, the post-peak degradation of s_u does not have a significant effect on failure patterns.

Similarly, Figs. 5.10(d and e) show that the slope is globally stable in the Eulerian and Explicit dynamic FE analyses for the Northridge earthquake. However, the implicit analysis shows the formation of a complete failure plane (Fig. 5.10(f)). As mentioned before, the implicit analysis calculates higher ϵ_q^p than Explicit and Eulerian analyses, especially around and after global failure (cf. Figs. 5.4(g–l)). The reduction of s_u at these ϵ_q^p causes redistribution of load and therefore a complete failure plane develops. A very similar response is found for the Parkfield earthquake in the Eulerian and Explicit simulations (Figs. 5.10(g and h)). However, a very significant mesh

distortion occurs in the implicit analysis and therefore the results are not presented. Note that global failure is calculated from implicit analysis even without softening (Fig. 5.9(i)).

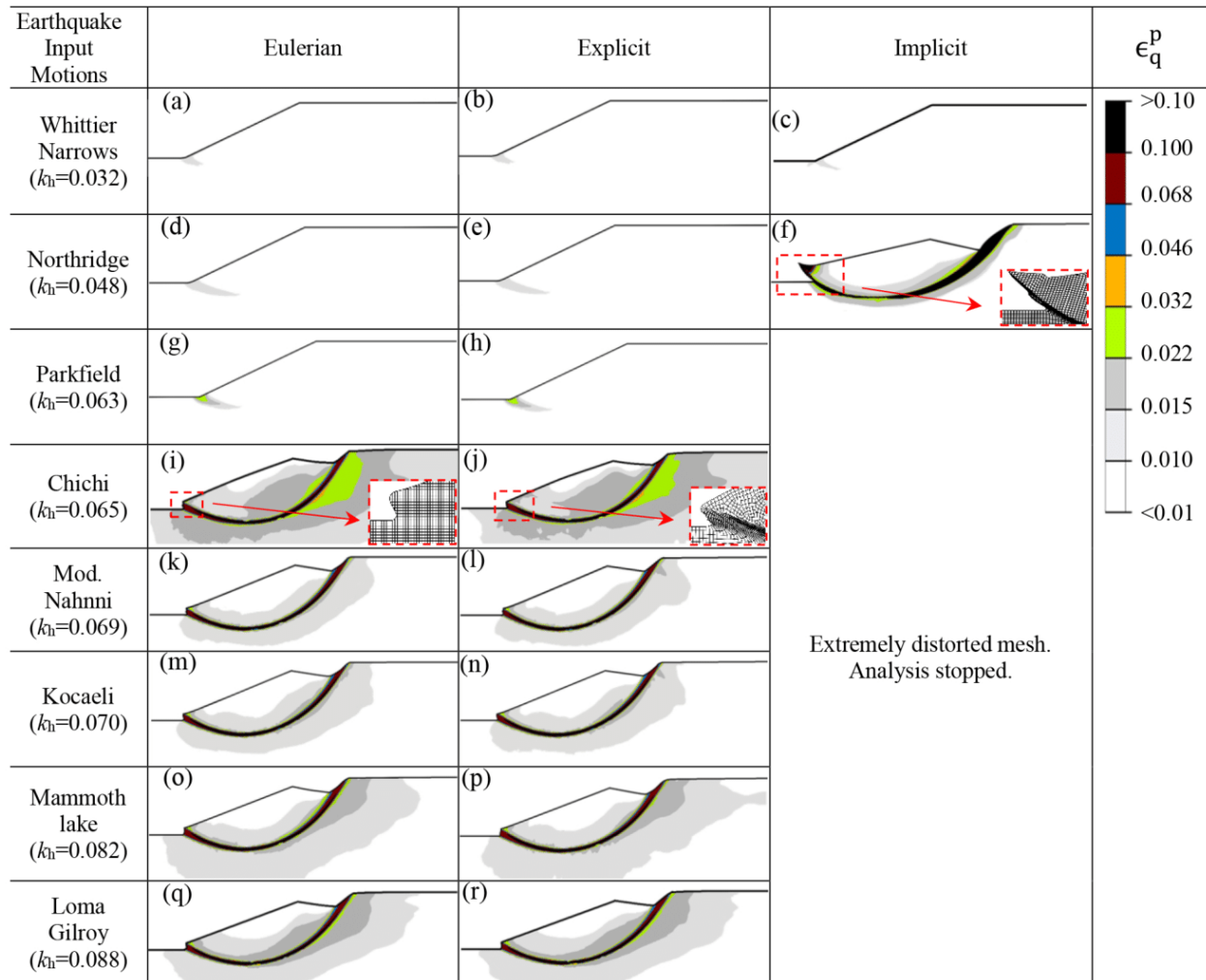


Fig. 5.10. Dynamic analysis using three FE modeling approaches for strain-softening soil.

For the non-softening cases (Fig. 5.9), the last five rows show the development of ϵ_q^p along the complete failures planes. As softening is considered in the simulations presented in Fig. 5.10, ϵ_q^p reduces s_u which generates additional ϵ_q^p along the failure planes. The following are the key observations from the last five rows of Figs. 5.9 and 5.10:

- Strain-softening increases ϵ_q^p along the failure planes. Clear shear bands form in a narrow zone, as compared to the non-softening case because of the concentration of ϵ_q^p due to softening.
- The failed soil mass displaces significantly, as observed from the upslope ground settlement near the failure plane and heave at the toe (e.g. Fig. 5.10(i)).
- Extremely distorted mesh at large deformation is observed in the implicit and explicit analyses. Therefore, in the modelling of large deformation slope failure, the implicit analysis may not be suitable and explicit analysis is questionable. The Eulerian FEM does not have any mesh distortion issue.

5.8 Comparison of Toe Displacement

The lateral displacement of the toe of Slope-II for the Chi-Chi earthquake is shown in Fig. 5.11. As the soil flows through the fixed mesh, the toe displacement in the Eulerian FE analysis is obtained from the deformed shape of the slope, and shown by discrete points. For the implicit and explicit analyses, the deformation of the node at the toe is shown in this figure.

For the non-softening soil model, the explicit and Eulerian FEM gives comparable displacements with a maximum value of ~ 2.0 m. The implicit analysis also gives similar toe displacement until $t \sim 27$ s; thereafter the FE mesh along the failure plane becomes highly distorted, although the solution did not stop, and calculates excessively high toe displacement.

The displacement is also calculated using Newmark's sliding-block method [3], which is widely used in standard engineering practice. This method calculates the displacement based on: (i) a critical acceleration (a_c) above which permanent deformation occurs, and (ii) a representative earthquake acceleration–time for the sliding block. The critical acceleration is calculated as $a_c = (F_s - 1)g \sin\theta$, where F_s is the static factor of safety under gravity, g is the gravitational

acceleration, and θ is the slope angle. For the Slope-II, $F_s = 1.15$ is obtained from the limit equilibrium analysis. The selection of appropriate ground motion is a challenging task. Following the work of Taiebat et al. [53], the calculated acceleration–time from the Explicit FE analysis in a soil element near the toe is used for Newmark’s analysis. Figure 5.11 shows that Newmark’s method gives a slightly lower maximum toe displacement (~ 1.7 m) than that obtained from the Eulerian and Explicit FE analyses.

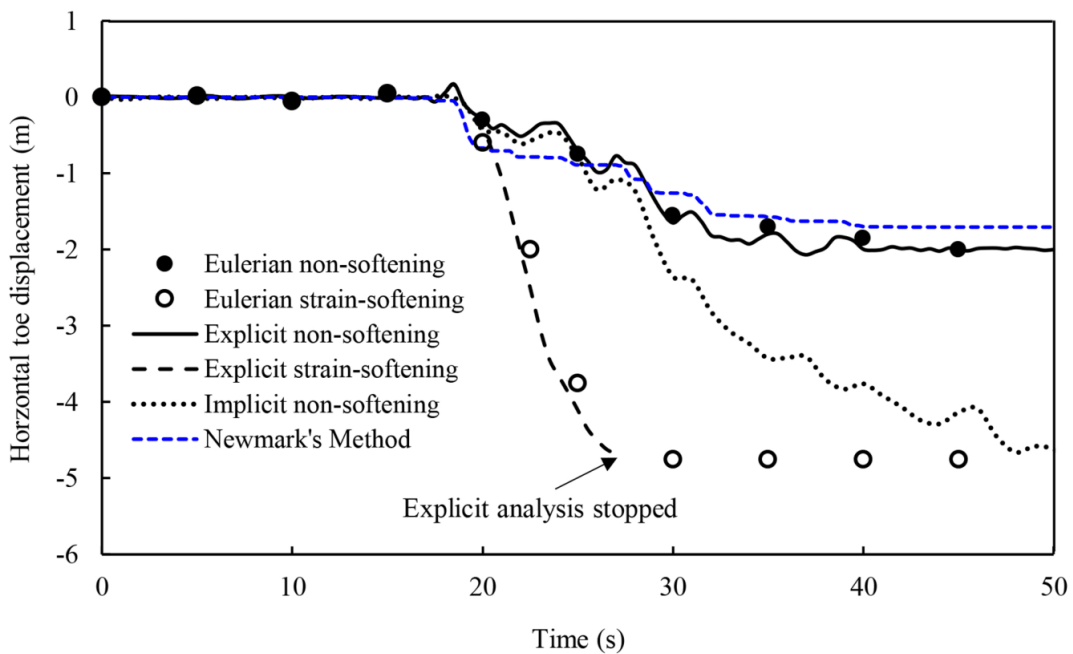


Fig. 5.11. Horizontal toe displacement for Chi-Chi earthquake.

The lateral displacement of the toe for the strain-softening soil model is significantly higher than that of the non-softening model (Fig. 5.11). As shown in Fig. 5.10, due to mesh distortion issues, the implicit analyses could not be completed for this case. The explicit analysis also stopped at $t \sim 27$ s but the Eulerian analysis continued and gives a maximum lateral toe displacement of ~ 4.75 m. Note that, while a small toe displacement is calculated at $t > 30$ s in the non-softening

case, it is almost zero during this period in the softening case, which is due to the highly deformed shape of the slope in the latter case.

The maximum toe displacements of Slope-II for all eight earthquakes (Fig. 5.7) are shown in Table 5.2. For the non-softening case, the Eulerian and Explicit FE analyses give toe displacements that are comparable to the values obtained from Newmark's method. For the softening case, the maximum toe displacements in Eulerian and Explicit analyses are similar; however, in some cases, the Explicit analysis stopped after a considerable displacement. The Implicit analysis could not be completed in most of the cases with strain-softening soil model. Therefore, the Eulerian approach is a better choice for large deformation, especially for sensitive clay slope failure, as presented in Ref. [1].

Table 5.2. Calculated maximum toe displacement.

Earthquake	Maximum toe displacement (m)						
	Non-softening				Softening		
	Eulerian	Explicit	Implicit	Newmark	Eulerian	Explicit	Implicit
Whittier Narrows	-0.02	-0.02	-0.02	-0.04	-0.02	-0.02	-0.02
Northridge	-0.03	-0.03	-0.03	0.00	-0.03	-0.03	-5.20
Parkfield	-0.06	-0.06	-0.14	-0.08	-0.06	-0.06	**
Chi-Chi	-1.95	-2.00	-4.62 [§]	-1.70	-4.75	-4.68	**
Mod. Nahanni	-0.15	-0.15	-0.12	-0.20	-3.75	-4.05	**
Kocaeli	-0.20	-0.21	-0.47	-0.32	-4.30	-4.50	**
Mammoth lake	-0.38	-0.36	-0.80	-0.47	-4.25	-4.60	**
Loma Gilroy	-0.25	-0.22	-0.84	-0.30	-4.50	-4.59	**

Notes: **Analysis stopped because of numerical issues
[§] Significant mesh distortion occurred

5.9 Conclusions

Large deformation FE modelling of clay slope failure due to earthquake loading is presented in this study. The numerical simulations are performed using an Eulerian approach through a systematic calibration of results against implicit and explicit simulations, which have been used in previous studies for slope stability analysis. Two approaches are used to incorporate earthquake effects in FE simulations: (i) in the pseudostatic method, the earthquake-induced force is applied by a pseudostatic horizontal coefficient k_h ; and (ii) in the dynamic analysis, the acceleration–time history is applied at the base of the model. The performance of Eulerian FEM, in terms of the location of the global failure plane and earthquake load required to cause slope failure, is compared with the traditional limit equilibrium method. The following conclusions are drawn from this study:

- a) The Eulerian approach can be used for modelling clay slope failure. The results are comparable to implicit and explicit FE analyses at small deformation levels. However, the latter two approaches cannot be used for a very large deformation because of significant mesh distortion.
- b) The location of the global failure planes obtained from the pseudostatic FE modelling is consistent with the critical circle in the pseudostatic limit equilibrium analysis. However, FE modelling with uniform s_{u0} in the upper clay layer shows horizontal (local) shear bands.
- c) The dynamic FE simulation results do not always match the pseudostatic FE results based on estimated k_h using Pyke's chart. The duration of an earthquake influences the deformation behaviour and thereby failure process.

- d) The post-peak degradation of shear strength increases the propensity of failure initiation if the slope is on the verge of failure. The deformation of the failed soil and plastic shear strain accumulation along the failure planes increase with degradation of strength.

Finally, one of the limitations of the present study is the modelling of soil. Further studies are required for stress–strain behaviour of clays, especially at large strains under dynamic loading.

Notations

α	backstress
β	stiffness proportional damping
δ	accumulated plastic shear displacement
δ_{95}	δ at which s_u reduced by 95% of $(s_{up}-s_{uR})$
$\dot{\epsilon}_{ij}^p$	plastic deviatoric strain rate tensor
ϵ_q^p	generalized plastic shear strain
γ^p	engineering plastic shear strain
$\bar{\gamma}$	a parameter for kinematic hardening model
ν_u	undrained Poisson's ratio
σ	stress
σ_0	stress at zero plastic strain in kinematic hardening model
σ_y	yield strength
a_{peak}	peak acceleration
C	initial hardening modulus
E_u	undrained modulus of elasticity
F	yield surface

F_b	horizontal body force per unit volume
F_s	factor of safety
k_h	horizontal pseudostatic coefficient
k_y	yield pseudostatic coefficient
M_M	moment magnitude of earthquake
PI	plasticity index
S_t	remoulded sensitivity of clay, s_{u0}/s_{uR}
s_u	mobilized undrained shear strength
s_{u0}	initial (peak) undrained shear strength
s_{uR}	remolded s_u at large plastic shear displacement
t_{FE}	length of cubical elements (FE mesh size)
t_{sig}	significant duration of earthquake ground motion
z	depth below the crest of the slope

References

- [1] Islam N, Hawlader B, Wang C, Soga K. Large deformation finite-element modelling of earthquake-induced landslides considering strain-softening behaviour of sensitive clay. *Can Geotec J* 2018.
- [2] Hynes-Griffin ME, Franklin AG. Rationalizing the seismic coefficient method [Report GI-84-13]. Vicksburg, Mississippi: Department of the Army Waterways Experiment Station; 1984. 21p.
- [3] Newmark NM. Effects of earthquakes on dams and embankments. *Géotechnique* 1965; 15(2):139–160.

- [4] Bray JD, Travasarou T. Simplified procedure for estimating earthquake-induced deviatoric slope displacements. *J Geotech Geoenviron Eng, ASCE* 2007;133(4):381–392.
- [5] Bray JD, Travasarou T. Pseudostatic coefficient for use in simplified seismic slope stability evaluation. *J Geotech Geoenviron Eng, ASCE* 2009;35(9):1336–1340.
- [6] Kramer SL, Smith MW. Modified Newmark model for seismic displacements of compliant slopes. *J Geotech Geoenviron Eng, ASCE* 1997;123(7):635–644.
- [7] Loukidis D, Bandini P, Salgado R. Stability of seismically loaded slopes using limit analysis. *Géotechnique* 2003;53(5):463–479.
- [8] Tan D, Sarma SK. Finite element verification of an enhanced limit equilibrium method for slope analysis. *Géotechnique* 2008;58(6):481–487.
- [9] Potts DM, Zdravkovic L. *Finite element analysis in geotechnical engineering: Theory*. London: Thomas Telford; 1999.
- [10] Kourkoulis R, Anastasopoulos I, Gelagoti F, Gazetas, G. Interaction of foundation–structure systems with seismically precarious slopes: Numerical analysis with strain softening constitutive model. *Soil Dyn Earthq Eng* Zhu, H. 2010;30(12):1430–1445.
- [11] Griffiths DV, Lane PA. Slope stability analysis by finite elements. *Géotechnique* 1999;49(3):387–403.
- [12] Dey R, Hawlader B, Phillips R, Soga K. Large deformation finite element modeling of progressive failure leading to spread in sensitive clay slopes. *Géotechnique* 2015;65(8):657–668.
- [13] Qiu G, Henke S, Grabe J. Application of a Coupled Eulerian–Lagrangian approach on geomechanical problems involving large deformations. *Comput Geotech* 2011;38(1):30–39.

- [14] Mohammadi S, Taiebat HA. A large deformation analysis for the assessment of failure induced deformations of slopes in strain softening materials. *Comput Geotech* 2013;49:279–288.
- [15] Mohammadi S, Taiebat HA. *H*-adaptive updated Lagrangian approach for large-deformation analysis of slope failure. *Int J Geomech* 2015;15(6):04014092.
- [16] Itasca. FLAC3D. Fast Lagrangian analysis of continua in 3-dimensions, version 5.0, manual. Itasca, Minnesota; 2012.
- [17] Islam N, Hawlader B. Pseudostatic seismic slope stability analyses using a large deformation finite element modeling technique. In: *Proceedings of the 69th Canadian Geotechnical Conference*, Vancouver, 2016.
- [18] Moormann C, Hamad F. MPM dynamic simulation of a seismically induced sliding mass. *IOP Conference Series: Earth and Environmental Science*, Stuttgart, Germany, 2015;26(1): p.1–6.
- [19] Duncan JM. State of the art: limit equilibrium and finite-element analysis of slopes. *J Geotech Eng* 1996;122(7):577–596.
- [20] Dawson EM, Roth WH, Drescher A. Slope stability analysis by strength reduction. *Géotechnique* 1999;49(6):835–840.
- [21] Zheng H, Liu DF, Li CG. Slope stability analysis based on elasto-plastic finite element method. *Int J Numer Meth Eng* 2005;64(14):1871–1888.
- [22] Wang D, Randolph “Numerical analysis of a cylinder moving through rate dependent undrained soil.” MF, White DJ. A dynamic large deformation finite element method based on mesh regeneration. *Comput Geotech* 2013;54:192–201.

- [23] Gauer P, Kvalstad J, Forsberg CF, Bryn P, Berg K. The last phase of the Storegga Slide: simulation of retrogressive slide dynamics and comparison with slide-scar morphology. *Mar Petrol Geol* 2005;22(1–2):171–178.
- [24] Kvalstad TJ, Nadim F, Kaynia AM, Mokkelbost KH, Bryn P. Soil conditions and slope stability in the Ormen Lange area. *Mar Petrol Geol* 2005;22(1–2):299–310.
- [25] Potts DM, Dounias GT, Vaughan PR. Finite element analysis of progressive failure of Carsington embankment. *Géotechnique* 1990,40(1):79–101.
- [26] Puzrin AM, Germanovich LN, Kim S. Catastrophic failure of submerged slopes in normally consolidated sediments. *Géotechnique* 2004,54(10):631–643.
- [27] Puzrin AM, Gray TE, Hill AJ. Significance of the actual nonlinear slope geometry for catastrophic failure in submarine landslides. In: *Proceedings of the Royal Society A, The Royal Society*, 2015;471(2175):20140772.
- [28] De Borst R. Simulation of strain localization: a reappraisal of the Cosserat continuum. *Eng Computation* 1991;8(4):317–332.
- [29] De Borst R, Sluys LJ, Muhlhaus HB, Pamin J. Fundamental issues in finite element analyses of localization of deformation. *Eng Computation* 1993;10(2):99–121.
- [30] Troncone A. Numerical analysis of a landslide in soils with strain-softening behaviour. *Géotechnique* 2005;55(8):585–596.
- [31] Thakur V. Strain localization in sensitive soft clays. PhD thesis, Norwegian University of Science and Technology, Norway, 2007.
- [32] Zabala F, Alonso EE. Progressive failure of Aznalcóllar dam using the material point method. *Géotechnique* 2011;61(9):795–808.

- [33] Bui HH, Fukagawa R, Sako K, Wells JC. Slope stability analysis and discontinuous slope failure simulation by elasto-plastic smoothed particle hydrodynamics (SPH). *Géotechnique* 2011;61(7):565–574.
- [34] Soga K, Alonso E, Yerro A, Kumar K, Bandara S. Trends in large-deformation analysis of landslide mass movements with particular emphasis on the material point method. *Géotechnique* 2016;66(3):248–273.
- [35] Dassault Systèmes. Abaqus user manual, version 6.14-EF2. Waltham, MA, USA, 2013.
- [36] Benson DJ, Okazawa S. Contact in a multi-material Eulerian finite element formulation. *Comput Methods Appl Mech Eng* 2004;193(39):4277–4298.
- [37] Henke S, Hamann T, Grabe J. Coupled Eulerian-Lagrangian simulation of the deep vibration compaction process as a plastodynamic problem. In: Proceedings of the 8th international conference on structural dynamics EUROLYN, Leuven, Belgium, 2011, p.482–489.
- [38] Nadim F. Slope stability under earthquake loading. Appendix F in Seabead project [Report 982512-2]. Norway, NGI; 1998.
- [39] Pestana JM, Nadim F. Nonlinear site response analysis of submerged slopes [Report UCB/GT/2000-04]. University of California, Berkeley; 2000, 51p.
- [40] Kramer SL. Geotechnical earthquake engineering. New Jersey, USA: Pearson Education; 1996.
- [41] Anastasopoulos I, Gelagoti F, Kourkoulis R, Gazetas G. Simplified constitutive model for simulation of cyclic response of shallow foundations: validation against laboratory tests. *J Geotech Geoenviron* 2011;137(12):1154–1168.
- [42] Duncan JM, Buchignani AL. An engineering manual for settlement studies [Report UCB/GT-76-01]. University of California, Berkeley; 1976.

- [43] Dobry R, Vucetic M. Dynamic properties and seismic response of soft clay deposits. In: Proceedings of the International symposium on geotechnical engineering of soft soils, Ciudad, Mexico, 1987; p. 51–86.
- [44] Okur DV, Ansal A. Stiffness degradation of natural fine grained soils during cyclic loading. *Soil Dyn Earthq Eng* 2007;27:843–854.
- [45] Corps of Engineers. Stability of earth and rock-fill dams, Engineer Manual 1110-2-1902, U.S. Army Corps of Engineers, Washington D.C., USA; 1970.
- [46] GeoStudio, GEOSLOPE International Ltd. Calgary, AB, Canada; 2016.
- [47] Jibson RW. Methods for assessing the stability of slopes during earthquakes—A retrospective. *Eng Geol* 2011;122(1–2):43–50.
- [48] Jibson RW. Predicting earthquake-induced landslide displacements using Newmark's sliding block analysis. *Transportation Research Record*, 1993, p. 9–17.
- [49] PEER (Pacific Earthquake Engineering Research Center). Ground motion database, 2010. (<http://peer.berkeley.edu/smcat/>)
- [50] Keefer DK. Landslides caused by earthquakes. *Geol Soc Am Bull* 1984;95(4):406–421.
- [51] Hashash YMA, Musgrove MI, Harmon JA, Groholski DR, Phillips CA, Park D. DEEPSOIL 6.1, User manual. Board of Trustees of University of Illinois at Urbana-Champaign, Urbana; 2015.
- [52] Nielsen AH. Towards a complete framework for seismic analysis in Abaqus. In: Proceedings of the Institution of Civil Engineers—Engineering and Computational Mechanics, 2014;167(1):3–12.

- [53] Taiebat M, Kaynia AM, Dafalias YF. Application of an anisotropic constitutive model for structured clay to seismic slope stability. *J Geotech Geoenviron Eng, ASCE* 2011;137(5):492–504.
- [54] Wakai A, Ugai K, Onoue A, Kuroda S, Higuchi K. Numerical modeling of an earthquake-induced landslide considering the strain-softening characteristics at the bedding plane. *Soils Found* 2010;50(4):533–545.
- [55] Atassi OV, Galán JM. Implementation of nonreflecting boundary conditions for the nonlinear Euler equations. *J Comput Phys* 2008;227(3):1643–1662.
- [56] Cerjan C, Kosloff D, Kosloff R, Reshef M. A nonreflecting boundary condition for discrete acoustic and elastic wave equations. *Geophysics*, 1985;50(4):705–708.
- [57] Kwok AO, Stewart JP, Hashash YMA, Matasovic N, Pyke R, Wang Z, Yang Z. Use of exact solutions of wave propagation problems to guide implementation of nonlinear seismic ground response analysis procedures. *J Geotech Geoenviron Eng, ASCE* 2007;133(11):1385–1398.
- [58] Mánica M, Ovando E, Botero E. Assessment of damping models in FLAC. *Comput Geotech* 2014;59:12–20.
- [59] Tsai CC, Park D, Chen CW. Selection of the optimal frequencies of viscous damping formulation in nonlinear time-domain site response analysis. *Soil Dyn Earthq Eng* 2014;67:353–358.
- [60] Chen W, Qiu T. Simulation of earthquake-induced slope deformation using SPH method. *Int J Numer Anal Met*, 2014;38(3):297–330.

- [61] Masing G. Eigenspannungen and verfertigung beim messing [Fundamental stresses and strengthening with brass]. In: Proceeding of the 2nd International Congress on Applied Mechanics, Zurich, 1926, p.332–335.
- [62] Terzaghi K. Mechanisms of landslides, Eng Geol, 1950;83–123.
- [63] Abramson LW, Lee TS, Sharma S, Boyce GM. Slope stability and stabilization methods, 2nd ed., New York: Wiley; 2002.
- [64] Matsuo M, Itabashi K, Sasaki Y. Study on a seismicity of earth structures by inverse analyses of actual cases. In: Proceedings of the Japan Society of Civil, Japan Society of Civil Engineers, 1984, 343:25–33.
- [65] Seed HB. Considerations in the earthquake-resistant design of earth and rockfill dams. Géotechnique 1979;29(3):215–263.
- [66] Pyke R. Selection of seismic coefficients for use in pseudo-static slope stability analyses. Consulting Engineer, Lafayette CA; 1991.
- [67] Baker R, Shukha R, Operstein V, Frydman S. Stability charts for pseudo-static slope stability analysis. Soil Dyn Earthq Eng 2006;26(9):813–823.
- [68] Bray JD, Rathje EM. Earthquake-induced displacements of solid-waste landfills. J Geotech Geoenviron Eng, ASCE 1998;124(3):242–253.
- [69] Park DS, Kutter BL. Static and seismic stability of sensitive clay slopes. Soil Dyn Earthq Eng 2015;79:118–129.
- [70] Einav I, Randolph MF. Combining upper bound and strain path methods for evaluating penetration resistance. Int J Numer Meth Eng 2005;63(14):1991–2016.
- [71] Randolph MF. Characterisation of soft sediments for offshore applications. In: Proceedings of the 2nd International Conference on Site Characterisation, Porto, 2004, p. 209–231.

Chapter 6

Conclusions and Future Work

6.1 Conclusions

This thesis is focused on studying the failure mechanisms of sensitive clay slopes. Numerical analysis is performed to identify the factors affecting the failure pattern and retrogression of large-scale landslides, triggered by toe erosion and seismic loading. A Eulerian-based large deformation finite element (LDFE) modeling technique is used for numerical analysis. The Eulerian-based LDFE can overcome one of the major limitations of traditional Lagrangian-based FE analysis related to mesh distortion. A soil constitutive model that considers the strain-softening and strain-rate effects on the undrained shear strength of sensitive clay is used. A unified strain-rate dependent model is incorporated to better model both solid (intact) and fluid-like (remolded) sensitive clay; strain-rate effects on the undrained shear strength are higher in the latter one.

The following sections provide a general overview of the entire thesis. Problem specific conclusions and practical implications are presented at the end of each chapter (Chapters 3–5) and appendices.

The criterion based on a single parameter or a combination of a few (e.g. remolded shear strength s_{ur} , sensitivity S_t or stability number N_s) cannot always characterize the flowslide or spread, neither the retrogression of the landslide. Numerical simulations show that the mobility of debris can change the failure pattern. A flowslide is expected if the debris moves out of the crater easily during retrogression. On the other hand, the increase in horizontal to vertical stress ratio, resistance to downslope movement of the debris, and decrease in soil brittleness and slope steepness changes the failure pattern from a flowslide to a spread.

Simulation techniques are developed for modeling seepage, in-situ stresses, and the subsequent failure of soil blocks for the LDFE analysis. The steady-state seepage condition is simulated using a thermal-hydraulic analogy available in the software that gives pore water pressure and seepage forces which are used to model the in-situ stress condition under varying earth pressure coefficient at-rest (K_0), and subsequent landslide modeling. The methods presented in this study can successfully simulate the long-term drained in-situ stress development and rapid undrained landslides, which represent the complete process, including the static condition, landslide triggering, retrogression, and run-out. The developed modeling technique could also simulate the 2010 Saint-Jude landslide reasonably.

Another simulation technique is developed to extend the usage of the LDFE method for simulating clay slopes under earthquake loading. Techniques for modeling acceleration-time history and minimizing undesirable boundary effects due to the seismic reflection in Eulerian LDFE method are presented. In this analysis, kinematic hardening and strain-softening behavior of soil are considered.

6.2 Recommendations for Future Research

The present study has some limitations, although many features and characteristics of large-scale landslides in sensitive clays are successfully simulated. Some of the limitations are discussed at the end of Chapters 3–5. In addition, the following issues could be addressed in future research:

- i) Finite element simulations are performed in total stress analysis, using the undrained shear strength of the soil. Total stress analysis may not perfectly reflect the behavior of soil during failure. For example, field investigations in eastern Canada show that the angle of the tips of the horst in a spread is 50° – 70° while it is 90° in the present numerical simulations, because of the use of an undrained $\phi = 0^\circ$ condition in the total stress analysis.

- ii) The present study mainly focuses on landslide retrogression and the run-out of the debris. However, the landslide triggering is equally important. The failure of a sensitive clay slope near a riverbank could be initiated by several factors (e.g. toe erosion, effective stress reduction due to artesian pressure, seasonal variation of the groundwater, and earthquake). The failure could initiate both in drained and undrained conditions. In the present study, the failure is triggered by toe erosion and earthquake loading in the undrained condition.
- iii) When strain-softening behavior of soil is considered, the numerical results are very sensitive to mesh size. The element size scaling rule is used in this study to reduce mesh dependency. Several mesh regulation techniques have been proposed in the past. The effectiveness of these techniques for large deformation finite element analysis needs to be studied.
- iv) In the present study, the modeling has been performed in the plane-strain condition. However, the landslide in the field is a three-dimensional problem. Field observations also show that three-dimensional effects could influence the failure pattern and the affected area of a landslide. For example, the 2016 Saint-Luc-de-Vincennes landslide had a pear-shaped scar with a small bottleneck close to the watercourse. More importantly, both the characteristics of flowslide and spread were observed in this landslide. Three-dimensional modeling might reveal the mechanisms behind such a unique failure; however, it would be computationally very expensive.

REFERENCES

- Abbott, P. L. (1996). *Natural Disasters*. Wm. C. Brown Publishing Co., pp 438.
- Ambraseys, N. N., & Srbulov, M. (1994). Attenuation of earthquake-induced ground displacements. *Earthquake engineering and structural dynamics*, 23(5), 467–487.
- Aylsworth, J.M., & Lawrence, D.E. (2003). Earthquake-induced landslide east of Ottawa; a contribution to the Ottawa Valley Landslide Project. In *Proceedings of the 3rd Canadian Conference on Geotechnique and Natural Hazards*, Edmonton, Alberta, pp. 77–84.
- Benson, D. J. (1992). Computational methods in lagrangian and eulerian hydrocodes. *Computer Methods in Applied Mechanics and Engineering*, 99(2-3), 235–394.
- Benson, D. J. (1995). A multi-material Eulerian formulation for the efficient solution of impact and penetration problems. *Computational Mechanics*, 15(6), 558–571.
- Benson, D. J. & Okazawa, S. (2004). Contact in a multi-material eulerian finite element formulation. *Computer Methods in Applied Mechanics and Engineering*, 193(39-41), 4277–4298.
- Bernander, S. (1978). Brittle failures in normally consolidated soils. *Väg-och Vattenbyggaren*, 1978(8–9), 49.
- Bernander, S., Gustås, H., & Olofsson, J. (1988). Improved model for progressive failure analysis of slope stability. In *Proceedings of the Nordic Geotechnical Conference*, NGM 88, Oslo, Norway.
- Bernander, S. (2000). Progressive landslides in long natural slopes, formation, potential extension and configuration of finished slides in strain-softening soils. Licentiate thesis, Department of Civil and Mining Engineering, Luleå University of Technology, Luleå, Sweden.

- Bernander, S. (2008). Down-hill progressive landslides in soft clays, triggering disturbance agents, slide propagation over horizontal or gently sloping ground, sensitivity related to geometry. Department of Civil and Mining Engineering, Luleå University of Technology, Luleå, Sweden. Research Report.
- Biscontin, G., & Pestana, J. M. (2001). Influence of peripheral velocity on vane shear strength of an artificial clay. *Geotechnical Testing Journal*, 24(4), 423–429.
- Bjerrum, L. (1955). Stability of natural slopes in quick clay. *Géotechnique*, 5(1), 101–119.
- Bjerrum, L. (1961). The effective shear strength parameters of sensitive clays. In *Proceedings of the 5th international conference soil mechanics foundation engineering*, Paris, pp 23–28.
- Bjerrum, L., & Landva, A. (1966). Direct simple-shear tests on a Norwegian quick clay. *Géotechnique*, 16(1), 1–20.
- Bjerrum, L. (1967). Progressive failure in slopes of overconsolidated plastic clay and clay shales. *Journal of Soil Mechanics & Foundations Div.*
- Bray, J. D., & Travasarou, T. (2007). Simplified procedure for estimating earthquake-induced deviatoric slope displacements. *Journal of Geotechnical and Geoenvironmental Engineering*, 133(4), 381–392.
- Bray, J. D., & Travasarou, T. (2009). Pseudostatic coefficient for use in simplified seismic slope stability evaluation. *Journal of Geotechnical and Geoenvironmental Engineering*, 135(9), 1336–1340.
- Brooks, G.R. (2013). A massive sensitive clay landslide, Quyon Valley, southwestern Québec, Canada, and evidence for a paleoearthquake triggering mechanism. *Quaternary Research*, 80(3): 425–434.

- Carson, M. A. (1977). On the retrogression of landslides in sensitive muddy sediments. *Canadian Geotechnical Journal*, 14(4), 582–602.
- Chen, W., & Qiu, T. (2014). Simulation of earthquake-induced slope deformation using SPH method. *International Journal for Numerical and Analytical Methods in Geomechanics*, 38(3), 297–330.
- Coates, D. F., & McRostie, G. C. (1963). Some deficiencies in testing Leda clay. *American Society for Testing and Materials*, Special Technical Publication 361, pp. 459–470.
- Conlon, R. J. (1966). Landslide on the Toulmoustouc River, Québec. *Canadian Geotechnical Journal*, 3(3), 113–144.
- Crawford, C. B. (1959). The influence of rate of strain on effective stresses in sensitive clay. In *Papers on Soils 1959 Meetings*. ASTM International.
- Crawford, C. B. (1963). Cohesion in an undisturbed sensitive clay. *Géotechnique*, 13(2), 132–146.
- Crawford, C. B. (1965). The resistance of soil structure to consolidation. *Canadian Geotechnical Journal*, 2(2), 90–97.
- Cruden, D. M., & Varnes, D. J. (1996). Landslides: investigation and mitigation. Chapter 3- Landslide types and processes. *Transportation research board special report*, (247).
- Dayal, U., & Allen, J. H. (1975). The effect of penetration rate on the strength of remolded clay and sand samples. *Canadian Geotechnical Journal*, 12(3), 336–348.
- De Besses, B. D., Magnin, A., & Jay, P. (2003). Viscoplastic flow around a cylinder in an infinite medium. *Journal of Non-newtonian Fluid Mechanics*, 115(1), 27–49.
- Demers, D., Robitaille, D., Locat, P., & Potvin, J. (2014). Inventory of large landslides in sensitive clay in the province of Québec, Canada: preliminary analysis. In *Landslides in Sensitive Clays* (pp. 77–89). Springer, Dordrecht.

- Desjardins, R. (1980). Tremblements de terre et glissements de terrain: Corrélation entre des datations au 14C et des données historiques à Shawinigan, Québec. *Géographie Physique et Quaternaire*, 34(3), 359–362.
- Dey, R., Hawlader, B., Phillips, R., & Soga, K. (2015). Large deformation finite-element modeling of progressive failure leading to spread in sensitive clay slopes. *Géotechnique*, 65(8), 657–668.
- Dey, R., Hawlader, B. C., Phillips, R., & Soga, K. (2016a). Numerical modelling of submarine landslides with sensitive clay layers. *Géotechnique*, 66(6), 454–468.
- Dey, R., Hawlader, B., Phillips, R., & Soga, K. (2016b). Numerical modeling of combined effects of upward and downward propagation of shear bands on stability of slopes with sensitive clay. *International Journal for Numerical and Analytical Methods in Geomechanics*, 40(15), 2076–2099.
- Dutta, S., Hawlader, B., & Phillips, R. (2014). Finite element modeling of partially embedded pipelines in clay seabed using Coupled Eulerian–Lagrangian method. *Canadian Geotechnical Journal*, 52(1), 58–72.
- Einav, I., & Randolph, M. (2006). Effect of strain rate on mobilised strength and thickness of curved shear bands. *Géotechnique*, 56(7), 501–504.
- Fortin, A., Ouellet, D., Paradis, S. & Demers, D. (2008). Développement au Ministère des Transports du Québec d'un portail informatique pour l'accès à des bases de données géotechnique. In *Proceedings of the 4th Canadian Conference on Geohazards: From Causes to Management*, Québec, Que., 20–24 May 2008. Edited by J. Locat, D. Perret, D. Turmel, D. Demers, and S. Leroueil. Presses de l'Université Laval, Québec, Que. pp. 169–174.

- Gauer, P., Kvalstad, T. J., Forsberg, C. F., Bryn, P., & Berg, K. (2005). The last phase of the Storegga Slide: simulation of retrogressive slide dynamics and comparison with slide-scar morphology. *Marine and Petroleum Geology*, 22(1–2), 171–178.
- Graham, J., Crooks, J. H., & Bell, A. L. (1983). Time effects on the stress-strain behaviour of natural soft clays. *Géotechnique*, 33(3), 327–40.
- Gregersen, O. (1981). The quick clay landslide in Rissa, Norway. *Norwegian Geotechnical Institute Publication*, 135, 1–6.
- Griffiths, D. V., & Lane, P. A. (1999). Slope stability analysis by finite elements. *Géotechnique*, 49(3), 387–403.
- Gylland, A., Jostad, H. P., & Nordal, S. (2012). Failure geometry around a shear vane in sensitive clays. In *Proceedings of the 16th Nordic geotechnical meeting*, vol. 1, Copenhagen, pp 103–110.
- Hamann, T., Qiu, G., & Grabe, J. (2015). Application of a Coupled Eulerian–Lagrangian approach on pile installation problems under partially drained conditions. *Computers and Geotechnics*, 63, 279–290.
- Haug, M., Sauer, E. K., & Fredlund, D. (1977). Retrogressive slope failures at beaver creek, south of Saskatoon, Saskatchewan, Canada. *Canadian Geotechnical Journal*, 14(3), 288–301.
- Hu, Y., & Randolph, M. F. (1998). A practical numerical approach for large deformation problems in soil. *International Journal for Numerical and Analytical Methods in Geomechanics*, 22(5), 327–350.
- Islam, N., Hawlader, B., Wang, C., & Soga, K. (2018). Large-deformation finite-element modelling of earthquake-induced landslides considering strain-softening behaviour of sensitive clay. *Canadian Geotechnical Journal*, 56(7), 1003–1018.

- Janbu, N. (1985). Soil models in offshore engineering. *Géotechnique*, 35(3), 241–281.
- Jibson, R.W. (1993). Predicting earthquake-induced landslide displacements using Newmark's sliding block analysis. *Transportation research record*, pp 9.
- Jibson, R.W. (2011). Methods for assessing the stability of slopes during earthquakes—A retrospective. *Engineering Geology*, 122(1), 43–50.
- Jostad, H. P., Andresen, L., & Thakur, V. (2006). Calculation of shear band thickness in sensitive clays. In: *6th numerical methods in geotechnical engineering*, vol. 1, pp 27–32.
- Johansson, J., Løvolt, F., Andersen, K.H., Madshus, C., & Aabøe, R. (2013) Impact of blast vibrations on the release of quick clay slides. In *Proceedings of the 18th ICSMGE*, Paris.
- Jostad, H.P., & Andresen, L. (2002). Capacity analysis of anisotropic and strain-softening clays. In *Proceedings of NUMOG VIII*, Rome, Italy. pp. 469–474.
- Karlsrud, K., Aas, G., & Gregersen, O. (1984). Can we predict landslide hazards in soft sensitive clays? Summary of Norwegian practice and experiences. In *Proceedings of the 4th International Symposium on Landslides*, Toronto, Ont., 16–21 September 1984. University of Toronto Press, Toronto, Ont. Vol. 1, pp. 107–130.
- Kramer, S. L. (1996). *Geotechnical earthquake engineering*. Pearson Education.
- Kramer, S. L., & Smith, M. W. (1997). Modified Newmark model for seismic displacements of compliant slopes. *Journal of Geotechnical and Geoenvironmental Engineering*, 123(7), 635–644.
- L'Heureux, J. S., Eilertsen, R. S., Glimsdal, S., Issler, D., Solberg, I. L., & Harbitz, C. B. (2012). The 1978 quick clay landslide at Rissa, mid Norway: subaqueous morphology and tsunami simulations. In *Submarine mass movements and their consequences* (pp. 507–516). Springer, Dordrecht.

- Lebuis, J., Robert, J.-M., & Rissmann, P. (1983). Regional mapping of landslide hazard in Québec. Swedish Geotechnical Institute, Report No.17, Linköping, 205–262.
- Lefebvre, G., & LeBoeuf, D. (1987). Rate effects and cyclic loading of sensitive clays. *Journal of Geotechnical Engineering*, 113(5), 476–489.
- Leroueil, S., Locat, J., Lee, H., & Faure, R. (1996). Geotechnical characterization of slope movements. In *Proceedings of the 7th International Symposium on Landslides*, Trondheim, Norway, 17–21 June 1996. Edited by K. Senneset. Balkema, Rotterdam, the Netherlands. Vol. 1, pp. 53–74.
- Leroueil, S. (2001). Natural slopes and cuts: movement and failure mechanisms. *Géotechnique*, 51(3), 197–243.
- Lo, K.Y. (1972). An approach to the problem of progressive failure. *Canadian Geotechnical Journal*, 9(4), 407–429.
- Locat, A., Leroueil, S., Bernander, S., Demers, D., Jostad, H. P., & Ouehb, L. (2011). Progressive failures in eastern Canadian and Scandinavian sensitive clays. *Canadian Geotechnical Journal*, 48(11), 1696–1712.
- Locat, A., Jostad, H. P., & Leroueil, S. (2013). Numerical modeling of progressive failure and its implications for spreads in sensitive clays. *Canadian Geotechnical Journal*, 50(9), 961–978.
- Locat, A., Leroueil, S., Fortin, A., Demers, D., & Jostad, H. P. (2014). The 1994 landslide at Sainte-Monique, Québec: geotechnical investigation and application of progressive failure analysis. *Canadian Geotechnical Journal*, 52(4), 490–504.
- Locat, A., Locat, P., Demers, D., Leroueil, S., Robitaille, D., & Lefebvre, G. (2017). The Saint-Jude landslide of 10 May 2010, Québec, Canada: Investigation and characterization of the landslide and its failure mechanism. *Canadian geotechnical journal*, 54(10), 1357–1374.

- Makdisi, F. I., & Seed, H. B. (1977). Simplified procedure for estimating dam and embankment earthquake-induced deformations. In ASAE Publication No. 4-77. *Proceedings of the National Symposium on Soil Erosion and Sediment by Water*, Chicago, Illinois, December 12-13, 1977.
- Mitchell, R. J., & Markell, A. R. (1974). Flowsliding in sensitive soils. *Canadian Geotechnical Journal*, 11(1), 11–31.
- Mollard, J. D., & Hughes, G. T. (1973). Earthflows in the Grondines and Trois Rivieres areas, Québec: discussion. *Canadian Journal of Earth Sciences*, 10(2), 324–326.
- Nazem, M., Sheng, D., Carter, J. P., & Sloan, S. W. (2008). Arbitrary Lagrangian–Eulerian method for large-strain consolidation problems. *International Journal for Numerical and Analytical Methods in Geomechanics*, 32(9), 1023–1050.
- Nazem, M., Carter, J.P., & Airey, D.W. (2009). Arbitrary Lagrangian–Eulerian method for dynamic analysis of geotechnical problems. *Computers and Geotechnics*, 36, 549–557.
- Newmark, N. M. (1965). Effects of earthquakes on dams and embankments. *Géotechnique*, 15(2), 139–160.
- Palmer, A. C., & Rice, J. R. (1973). The growth of slip surfaces in the progressive failure of over-consolidated clay. *Proceedings of the Royal Society of London. A. Mathematical and Physical Sciences*, 332(1591), 527–548.
- Park, D. S., & Kutter, B. L. (2015). Static and seismic stability of sensitive clay slopes. *Soil Dynamics and Earthquake Engineering*, 79, 118–129.
- Perret, D., Mompin, R., Bossé, F. & Demers, D. (2011) Stop 2-5B: the Binette road earth flow induced by the June 23rd, 2010 Val-des-Bois earthquake. In Russell HAJ, Brooks GR, Cummins DI (eds) Deglacial history of the Champlain Sea basin and implications for urbanization. Joint

- annual meeting GAC-MAC-SEG-SGA, Ottawa, Ontario, May 25–27, 2011, Field Guide Book, pp. 72–74. Geological Survey of Canada, Open File 6947.
- Perret, D., Mompin, R., Demers, D., Lefebvre, G. & Pugin, A.J.M. (2013). Two large sensitive clay landslides triggered by the 2010 Val-Des-Bois earthquake, Québec (Canada)—implications for risk management. Poster, *First Int. In Workshop on Landslides in Sensitive Clays (IWLSC)*, Québec, Canada, 28–30.
- Peuchen, J., & Mayne, P. (2007). Rate effects in vane shear testing. In *Offshore Site Investigation and Geotechnics, Confronting New Challenges and Sharing Knowledge*. Society of Underwater Technology.
- Puzrin, A. M., & Germanovich, L. N. (2005). The growth of shear bands in the catastrophic failure of soils. *Proceedings of the Royal Society A: Mathematical, Physical and Engineering Sciences*, 461(2056), 1199–1228.
- Quinn, P. E., Diederichs, M. S., Rowe, R. K., & Hutchinson, D. J. (2011). A new model for large landslides in sensitive clay using a fracture mechanics approach. *Canadian Geotechnical Journal*, 48(8), 1151–1162.
- Quinn, P. E., Diederichs, M. S., Rowe, R. K., & Hutchinson, D. J. (2012). Development of progressive failure in sensitive clay slopes. *Canadian Geotechnical Journal*, 49(7), 782–795.
- Rathje, E. M., & Bray, J. D. (2000). Nonlinear coupled seismic sliding analysis of earth structures. *Journal of Geotechnical and Geoenvironmental Engineering*, 126(11), 1002–1014.
- Seed, H. B., & Martin, G. R. (1966). The seismic coefficient in earth dam design. *Journal of Soil Mechanics & Foundations Div*, 92(Paper 4824).
- Seed, H. B., & Wilson, S. D. (1967). The Turnagain heights landslide, Anchorage, Alaska. *Journal of Soil Mechanics & Foundations Division*.

- Seed, H. B., Makdisi, F. I. & De Alba, P. (1978). Performance of earth dams during earthquakes. *Journal of Geotechnical and Geoenvironmental Engineering*, 104(ASCE 13870 Proceeding).
- Skempton, A. W. (1964). Long-term stability of clay slopes. *Géotechnique*, 14(2), 77–102.
- Stark, T. D., & Contreas, I. A. (1996). Constant volume ring shear apparatus. *GTJ* 19(1):3–11.
- Stark, T. D., & Eid, H. T. (1994). Drained residual strength of cohesive soils. *Journal of Geological Engineering*, 120(5), 856–871.
- Lacasse, S., Karlsrud, K., Nyheim, T., Aunaas, K., Ottesen, H., Gjelsvik, V., Fauskerud, O.A., & Sandven, R. (2017). Run-out of landslide in sensitive clays. In: *Landslides in sensitive clays. From research to implementation*. Thakur, V., L'Heureux, J-S., Locat, A. (eds), Springer, Dordrecht, pp
- Tavenas, F., Chagnon, J. Y., & Rochelle, P. L. (1971). The Saint-Jean-Vianney landslide: observations and eyewitnesses accounts. *Canadian Geotechnical Journal*, 8(3), 463–478.
- Tavenas, F., Leblond, P., Jean, P., & Leroueil, S. (1983). The permeability of natural soft clays. Part I: Methods of laboratory measurement. *Canadian Geotechnical Journal*, 20(4), 629–644.
- Tavenas, F. (1984). Landslides in Canadian sensitive clays-a state-of-the-art. In *Proceedings of the 4th International Symposium on Landslides*, Toronto, Ont. (pp. 16–21).
- Thakur, V., Nordal, S., Jostad, H. P., & Andresen, L. (2005). Study on pore water pressure dissipation during shear banding in sensitive clays. In *11th international conference on computer methods and advances in geomechanics, IACMAG*, Turino, Italy, 4, pp 289–296.
- Thakur, V. (2007). Strain localization in sensitive soft clays. PhD thesis, Norwegian University of Science and Technology.
- Thakur, V. (2011). Numerically observed shear bands in soft sensitive clays. *International Journal of Geomechanics and Geoengineering*, 6(2), 131–146.

- Thakur, V., Degago, S. A., Oset, F., Aabøe, R., Dolva, B. K., Aunaas, K., & Robsrud, A. (2014). Characterization of post-failure movements of landslides in soft sensitive clays. In *Landslides in sensitive clays* (pp. 91-103). Springer, Dordrecht.
- Tho, K. K., Leung, C. F., Chow, Y. K., & Palmer, A.C. (2011). Deep cavity flow mechanism of pipe penetration in clay. *Canadian Geotechnical Journal*, 49(1): 59–69.
- Thomson, S., & Hayley, D. (1974). The little smoky landslide. *Canadian Geotechnical Journal*, 12(3), 379–392.
- Trapper, P. A., Puzrin, A. M., & Germanovich, L. N. (2015). Effects of shear band propagation on early waves generated by initial breakoff of tsunamigenic landslides. *Marine Geology*, 370, 99–112.
- Vaid, Y., Robertson, P., & Campanella, R. (1979). Strain rate behaviour of Saint-Jean-Vianney clay. *Canadian Geotechnical Journal*, 16(1), 34–42.
- Wartman, J., Seed, R. B., & Bray, J. D. (2005). Shaking table modeling of seismically induced deformations in slopes. *Journal of Geotechnical and Geoenvironmental Engineering*, 131(5), 610–622.
- Wang, C., Hawlader, B., Islam, N. & Soga, K. (2019). Implementation of a large deformation finite element modeling technique for seismic slope stability analyses. *Soil Dynamics and Earthquake Engineering* (In press).
- Zhang, W., Wang, D., Randolph, M. F., & Puzrin, A. M. (2015). Catastrophic failure in planar landslides with a fully softened weak zone. *Géotechnique*, 65(9), 755–769.
- Zhang, W., Wang, D., Randolph, M. F., & Puzrin, A. M. (2016). Dynamic propagation criteria for catastrophic failure in planar landslides. *International Journal for Numerical and Analytical Methods in Geomechanics*, 40(17), 2312–2338.

Zhu, H. & Randolph, M. F. (2011). Numerical analysis of a cylinder moving through rate dependent undrained soil. *Ocean Engineering*, 38(7), 943–953.

Appendix-I

Finite Element Simulation of the 2010 Saint-Jude Landslide in Québec

This paper has been published in the 69th Canadian Geotechnical Conference, GeoVancouver 2016. Most of the research work presented in this paper was conducted by the first author. He also prepared the draft manuscript. The other authors supervised the research and reviewed the manuscript.

Finite Element Simulation of the 2010 Saint-Jude Landslide in Quebec

Chen Wang and Bipul Hawlader

*Department of Civil Engineering, Memorial University, St. John's
NL, Canada, A1B 3X5*

Didier Perret

Natural Resources Canada, Quebec City, QC, Canada, G1K 9A9



ABSTRACT

Spread is a type of large-scale landslides that can occur in sensitive clay deposits. One of the unique features of a spread is that a long quasi-horizontal shear band first forms because of local instability such as toe erosion. The soil mass above the shear band is then displaced over a large distance and can be dislocated into a number of blocks. The mechanisms and kinematics of spread cannot be explained using limit equilibrium (LE) methods commonly used for slope stability analysis. Moreover, because of extremely large deformation of the failed soil mass, spreads cannot be simulated using the traditional finite element (FE) modeling techniques developed in Lagrangian framework. In the present study, FE simulation of spreads is performed using a large deformation FE method. Numerical analysis is performed using the Coupled Eulerian Lagrangian (CEL) approach available in Abaqus FE software. A model for post-peak degradation of undrained shear strength of sensitive clay is implemented in FE analysis. The Saint-Jude landslide, which occurred in 2010 in Quebec, Canada, is simulated. It is shown that many features reported from post-slide investigations could be explained using the present FE simulation. The initiation of failure, development of quasi-horizontal shear band, formation of a rotational slide, dislocation of failed soil blocks, retrogressive distance and the morphology of the debris after landslide are successfully simulated.

RÉSUMÉ

Un étalement est un grand glissement de terrain pouvant se produire dans des dépôts d'argiles sensibles. L'une des caractéristiques de ce type de glissement est qu'une longue bande de cisaillement quasi-horizontale peut se former suite à une instabilité locale, provoquée par exemple par de l'érosion en pied de talus. La masse de sols au-dessus de la bande de cisaillement peut se déplacer sur de grandes distances et peut se disloquer en plusieurs blocs. Les mécanismes de la rupture et la cinématique des étalements ne peuvent pas être expliqués par les méthodes d'analyse à l'équilibre limite utilisés couramment pour évaluer la stabilité d'une pente. De plus, les étalements ne peuvent pas être simulés par les méthodes classiques en éléments finis (EF) développées selon une formulation Lagrangienne, en raison des très grandes déformations impliquées. Dans cette étude, des simulations d'étalements sont effectuées en utilisant une méthode en EF à grande déformation. Les analyses numériques sont conduites en utilisant une approche couplée Eulérienne-Lagrangienne disponible dans le logiciel Abaqus. Un modèle de la dégradation post-pic de la résistance au cisaillement non drainé d'une argile sensible est implémenté dans le modèle. Nous simulons l'étalement de Saint-Jude qui s'est produit en 2010 au Québec, Canada. On montre que les simulations expliquent raisonnablement bien les principales caractéristiques de l'étalement. L'initiation de la rupture, le développement d'une bande de cisaillement quasi-horizontale, la formation d'un glissement rotationnel, la dislocation de la masse de sols, la distance de rétrogression, ainsi que la morphologie des débris, sont correctement simulés.

1 INTRODUCTION

Many large landslides along river bank slopes in sensitive clays have been reported in the literature. Among the different types of large landslides (slide area >1 ha) that occurred in the province of Quebec since 1870, spread represents more than 37% (Demers et al. 2013). Spreads have some unique failure patterns compare to other types of landslides. The traditional limit equilibrium (LE) methods commonly used for slope stability analysis cannot explain the mechanisms of this type of failure.

Based on post-slide observation, previous researchers recognized that a horizontal weak layer/surface is required for this type of large-scale landslide (Odenstad 1951; Carson 1977). The mechanisms involved in formation of this weak layer are still debated. Examining slope failures in sensitive clays, recent studies suggest that a weak layer might form due to erosion, excavation or small slides near the toe of the slope (Locat et al. 2008, 2011, 2013; Quinn

et al. 2011). This type of small local failure could create a long horizontal shear band (zone of strain concentration) where the shear strength reduces because of strain softening behaviour of sensitive clays. The soil mass above the horizontal shear band slides above this rupture surface and breaks into several blocks at large displacements.

The strain softening behaviour of sensitive clay cannot be incorporated in traditional LE methods. Griffiths and Lane (1999) suggested that finite element (FE) method is a powerful alternative approach for modeling of slopes because, unlike LE methods, fewer a priori assumptions are required and the failure occurs naturally through the zones where shear stress reaches the shear strength of the soil. However, the FE programs developed in purely Lagrangian framework cannot handle such large deformation problems because significant mesh distortion occurs around the failure planes that results in numerical instabilities and lack of convergence. A comprehensive discussion on FE modeling of large-scale failure of

sensitive clay slopes provided by the authors in Dey et al. (2015, 2016a,b).

The authors of the present study and their co-workers developed an advanced FE modeling technique to simulate sensitive clay slope failure (Dey et al. 2015, 2016b). It has been shown that modeling of large deformation, post-peak softening behaviour of undrained shear strength and kinematics of the failed soil blocks mainly control the failure process. Analyses have been performed for slope failure both in onshore and offshore environments (Dey et al. 2015, 2016a,b; Wang et al. 2015).

In the present study, FE analysis is performed to simulate the 2010 Saint-Jude landslide that occurred in Quebec, Canada. The paper has been organized in the following way. First, a brief description about the landslide is provided based on available literature. FE modeling of this landslide is presented in the second part. Finally, the FE simulation results are compared with field observation and possible mechanisms involved in this landslide is explained.

2 BRIEF REVIEW OF THE 2010 SAINT-JUDE LANDSLIDE

On May 10, 2010, a large retrogressive landslide occurred along the bank of Salvail River in Saint-Jude, Quebec (Locat et al. 2011). The width of the landslide was about 275 m and the retrogressive distance was about 150 m measured perpendicular to the watercourse, which affected an area of 42,000 m². Field investigation indicated that the slope was mainly constituted of eastern Canadian sensitive clay. The total height of the slope before landslide was 22 m. The angle of the slope was moderate ranging from 12° to 20°. The ground surface behind the crest of the slope was almost horizontal before landslide. The triggering factor of the landslide was inferred as high artesian pressure and active river erosion near the toe of the slope. Figure 1 shows a cross-section of the landslide (Locat et al. 2011, cross-section C-C'). The black dots in this figure show the location of the failure plane interpreted from CPTU tests, which indicates that a quasi-horizontal shear band propagated at about 2.5 m below the toe of the slope. After propagating about 120 m, the elevation of the shear band raised approximately by 10 m and then propagated another 40 m to the back scarp. The total retrogressive distance of the landslide was 80 m from the crest. The debris moved downward laterally and then on the opposite river bank over a distance of approximately 60 m. The post-failure topography of the landslide materials inside the scar was almost horizontal. In the post-slide

investigation reports (Locat et al. 2011, Locat et al. 2012), the debris has been divided into four zones (Fig. 1). The Zone 1 was the area of the opposite river bank covered by debris. The debris in this zone mainly comes from previous river bed and near the toe of the slope before landslide. In Zone 2, the failed soil mass formed almost a horizontal surface where the trees were standing almost vertically. This zone of debris was formed by the soil from the upper two-third of the original slope. Zone 3 was the area where soil moved laterally during the landslide. Dislocated blocks of horst and graben shapes were observed in this area, indicating a spread type landslide (Locat et al. 2011, and Demers et al 2013). Finally, in Zone 4, the failure pattern is similar to Zone 3. Horsts and grabens were also observed in this zone. However, some inclined soil slices between 25° and 50° were found which are rarely observed in spread failures.

Slope stability analysis of an idealized section similar to the one shown in Fig. 1 has been performed by previous researchers (Locat et al. 2011). The limit equilibrium method, combined with seepage analysis, was used to calculate the factor of safety of the slope both in drained and undrained conditions using SLOPE/W and SEEP/W software (GeoStudio 2007). Based on hydrogeological conditions recorded in piezometers, high artesian water pressure near the toe has been considered in seepage analysis. In the drained analysis, the minimum factor of safety (F_s) of 0.99 was found when the SLOPE/W identified the critical failure plane from the automatically generated potential circular slip surfaces. The approximate location of the critical slip surface is shown in Fig. 1. Slope stability analysis has also been performed by adopting a user specified failure plane as the one interpreted from CPTU tests in the field, which gives $F_s=3.13$ and $F_s=2.16$ in for drained and undrained conditions, respectively (Locat et al. 2011).

The above analyses clearly show that the LE methods cannot explain such large-scale landslides. Although the automatically searched critical failure plane gives $F_s < 1.0$ (i.e. failure), the extent of failure is limited to only near the toe of the slope. The critical slip circle intersects the ground surface approximately at the middle of the slope. On the other hand, user specified slip circle gives high F_s (3.13 & 2.16) which again indicates that LE cannot explain this failure. Therefore, an alternative technique for slope stability analysis is required to explain this type of landslide.

In this paper, a large deformation finite element (FE) modeling technique is used to simulate this landslide.

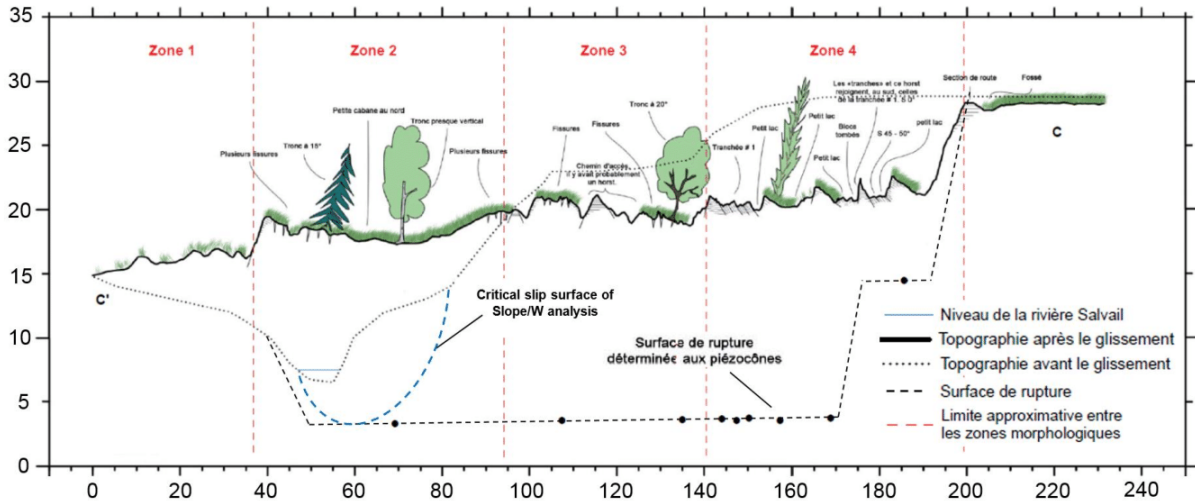


Figure 1 Failure plane and topography after the 2010 St. Jude landslide (after Locat et al. 2011, cross-section C-C')

3 FINITE ELEMENT MODELING

During landslide, large plastic shear strains localize in a narrow shear band and the soil mass moves on the shear band to very long distances. The conventional FE modeling techniques developed in Lagrangian framework cannot model such large deformation problems properly because significant mesh distortion occurs during simulation causing convergence problems. In order to overcome these issues, the Coupled Eulerian-Lagrangian (CEL) technique available in Abaqus FE software is used in this study. The performance of Abaqus CEL for modeling sensitive clay slopes have been discussed by the authors in previous studies (Dey et al. 2014, 2015, 2016b, Wang et al. 2015). In Abaqus CEL, the Eulerian material (soil) can flow through the fixed mesh. Therefore, there is no numerical issue of mesh distortion or mesh tangling even at extremely large shear strains in the zone around the failure planes.

3.1 FE Simulation of the 2010 Saint-Jude Landslide

Figure 2 shows the geometry of the model used in FE simulation of the 2010 Saint-Jude landslide. The profile of the slope is created from stereophotogrammetry and field investigation descriptions available in the report (Locat et al. 2011). The coordinate of each point is also shown in Fig. 2. Three layers of soil are considered in the present FE modeling. This idealized soil profile has been established from post-slide field investigation data (Locat et al. 2011). As shown in Fig. 2(a) that a 4 m thick crust is considered below the ground surface (El. 24–28 m). Below the crust, a 22 m thick sensitive clay layer is considered (El. 2–24 m). The elevation of the bottom of the river channel is at 6.5 m which is 4.5 m above the lower boundary of the sensitive

clay layer. The total height of the slope in the right side of the river is 22 m. The slope angle of the river bank near the toe is 40°, and becomes mild in the upper part ranging between 12° and 20°. The slope angle shown in Fig. 2 has been drawn based on Locat et al. (2011). The ground surface in the right side of the crest of the slope is horizontal.

In addition to above mentioned two soil layers, three soil layers of relatively high shear strength were found below the sensitive clay layer and above the bedrock at El. -15 m (Locat et al. 2011). The total thickness of these three layers is approximately 17 m. In FE modeling, these three layers have been modeled as one soil layer. Note that analysis has been also performed by assigning geotechnical properties to these three layers separately as reported in Locat et al. (2011); however, no significant effect on slope failure is found. Therefore, for simplicity these three layers (El.-15 to 2 m) are combined together and named as “stiff layer” in the following sections.

The profile of the slope is created from field investigation report (Locat et al. 2011). The coordinate of each point is also shown in Fig. 2.

As reported in post-slide investigations, toe erosion and/or small slides near the toe could be the main triggering factor of the landslide. In FE modeling, a circular slide of near the toe is created to trigger the failure of the slope. The dimensions of the small slide are shown in the inset of Fig. 2, which will be referred as “eroded block” in the following sections.

As mentioned above, in the 2010 Saint-Jude landslide, the movement of the debris was restricted by the opposite river bank topography. Therefore, in order to model this, the opposite river bank slope is also created as shown in Fig. 2(a).

Point	a	b	c	d	e	f	g	h
Coordinate	(0, 15)	(62, 6.5)	(67, 10)	(88, 14)	(110, 22.5)	(141, 24)	(171, 28)	(300, 28)

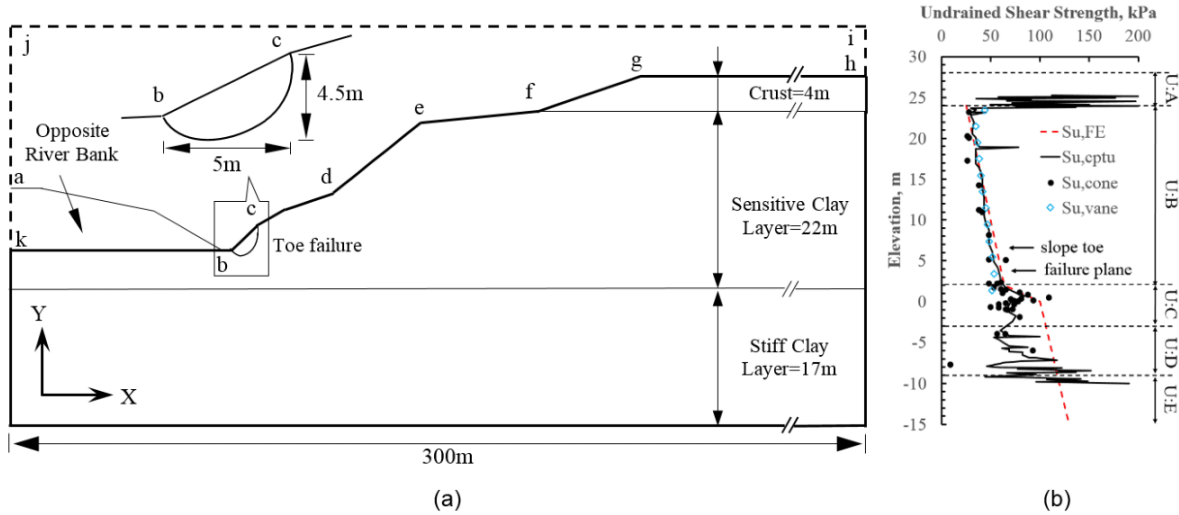


Figure 2. Geometry and shear strength profile used in FE modeling of the 2010 Saint-Jude landslide

Only three-dimensional models can be generated in Abaqus CEL. In order to avoid any boundary effect, a 300 m long soil domain is modeled. The model is only one element thick perpendicular to the x-y plane. The soil is modeled as Eulerian material using EC3D8R elements, which are 8-node linear brick elements. In this study, 0.5 m cubical EC3D8R elements are used. A void space above the ground surface (*abcdefghij* in Fig. 2(a)) is also created to accommodate the displaced soil mass. The soil in the opposite river bank (above line *kb*) is modeled as a rigid body. Soil and void spaces are created in Eulerian domain using Eulerian Volume Fraction (EVF) tool. For the void space above the ground surface, $EVF=0$ is assigned. On the other hand, $EVF=1$ is assigned for the soil elements below the ground surface and slopes, which means that these elements are filled with Eulerian materials of different types of soil.

Zero velocity boundary conditions perpendicular to the face is applied to all the vertical faces. At the bottom boundary, all three components of velocity is zero (i.e. $v_x=v_y=v_z=0$). Therefore, as no movement of soil is allowed perpendicular to the x-y plane, the simulation represents the plane strain condition. The above mentioned boundary conditions could be also viewed as rollers in the vertical faces and hinges at the bottom. No boundary condition is applied at the ground surface such that the displaced soil can move to the void space when needed. The boundaries are placed at sufficiently large distances to avoid boundary effect on slope failure.

The present FE simulation consists of three steps. In the first step, gravitational load is applied to the slope to bring the soil elements to the in-situ stress condition. In the second step, the triggering factor is activated to initiate the landslide. This is done by gradual reduction of shear

strength of the eroded block with time. As will be shown later, a global failure of the eroded block occurs (i.e. a small slide near the toe) due to reduction of shear strength. In the third step, the analysis is continued without any change in boundary or loading conditions.

3.2 Soil Properties in FE Model

Analysis is performed for undrained loading condition. The authors understand that the local slide near the toe, which triggered the landslide, might have occurred under drained or undrained condition. However, the modeling of that local slide is very difficult as many factors are unknown and is not the focus of the present study. Instead, this study evaluates how this large landslide might have occurred if there is a small local failure near the toe.

The red dashed line in Fig. 2(b) shows the undrained shear strength profile used in FE analysis. This shear strength profile is selected based on the CPTU test performed immediately outside the scar of the landslide (CPTU 32100 in Locat et al. 2011). The crust is modeled as a homogeneous layer with uniform undrained shear strength (s_u) of 45 kPa. This soil is modeled as elastic-perfectly plastic material without sensitivity. In the sensitive clay layer, the initial s_u increases linearly with depth from 25 to 65 kPa. Note that, in the sensitive clay layer, s_u decreases from the initial values with accumulated plastic strains as discussed in the following sections. In the stiff layer, s_u increases linearly from 65 to 120 kPa, which is modeled as elastic-perfectly plastic material without softening.

The strain-softening behavior of the sensitive clay layer is defined using an exponential relationship between s_u and plastic shear displacement (Eq. 1). The authors discussed

the model parameters required in this equation and its application in modeling sensitive clay slope in previous studies (Dey et al. 2012, 2013, 2015, Wang et al. 2015).

$$s_u = [1 + (S_t - 1)\exp(-3\delta/\delta_{95})]s_{uR} \quad [1]$$

where, s_u is the mobilized undrained shear strength at displacement δ ; S_t is the sensitivity of the soil; $\delta = \delta_{total} - \delta_p$; δ_p is the displacement required to attain the peak undrained shear strength s_{up} ; and δ_{95} is the value of δ at which the undrained shear strength of the soil is reduced by 95% of $(s_{up} - s_{uR})$. Eq. [1] is a modified form of strength degradation equation proposed by Einav and Randolph (2005) but in terms of displacement.

Figure 3 shows the relationship between the shear strength and shear displacement. Line oa represents a linear elastic pre-peak behavior. s_{up} is mobilized at point a and remains constant up to point b for a displacement of δ_{pc} . The curve bcd is defined by Eq. 1. After s_{uR} , the shear strength reduces slowly with shear displacement. The reduction of s_u in this zone is defined by a linear line de from s_{uR} to s_{uld} at a large displacement. After that, s_u remains constant ($s_u = s_{uld}$).

Field investigation revealed that the sensitive clay layer is highly sensitive. The ratio between the peak and remolded shear strength varies between 30 and 80. In the present FE modeling, $s_{up}/s_{uld} = 50$ and $s_{up}/s_{uR} = 6$ are used. Other parameters used in FE modeling is shown in Table

1. A detailed discussion on selection of these parameters can be found in Dey et al. (2015, 2016).

Adopting von-Mises yield criterion, the undrained shear strength is defined in Abaqus using yield strength ($=2s_u$) as a function of plastic shear strain γ_p and depth. Assuming simple shear condition, γ_p is calculated as $\gamma_p = \delta/t$, where t is the thickness of the shear band. In this study, $t = t_{FE}$ is used, where t_{FE} is the length of the cubical EC3D8R element.

The variation of s_u with depth and accumulated plastic shear strain is implemented Abaqus by writing a program in FORTRAN via user subroutine.

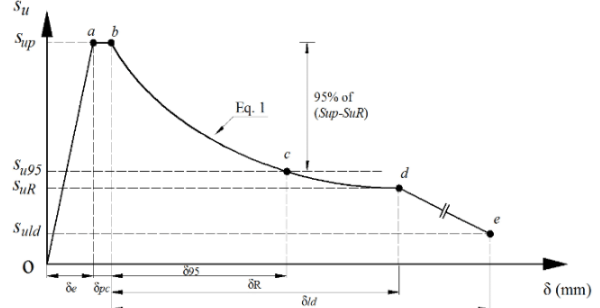


Figure 3. Stress-displacement behavior of sensitive clay used in FE modeling

Table 1: Parameters used for finite element modeling

Parameters	Values		
	Sensitive clay	Crust*	Stiff layer*
Undrained Young's modulus, E_u (MPa)	10	10	10
Poisson's ratio, ν_u	0.495	0.495	0.495
Peak undrained shear strength, s_{up} (kPa)	25-65	45	65-120
Residual undrained shear strength, s_{uR} (kPa)	$s_{up}/6$	-	-
Large displacement undrained shear strength, s_{uld} (kPa)	$s_{up}/50$	-	-
δ_{pc} (m)	0.004	-	-
δ_{95} (m)	0.025	-	-
δ_{ld} (m)	2.0	-	-
Soil unit weight, γ (kN/m ³)	16.0	18.6	16.8

*crust and stiff layer is modeled as elastic-perfectly plastic without softening

4 FINITE ELEMENT SIMULATION RESULTS

Figure 4 shows the simulation results of the 2010 Saint-Jude landslide. Equivalent plastic shear strain (PEEQVAVG) in Abaqus is used to show the shear bands formation during the landslide. Note that, PEEQVAVG is related to plastic shear strain (γ^p) as $\gamma^p = \sqrt{3}PEEQVAVG$.

4.1 Formation of failure planes

As shown in Fig. 4(a), because of reduction of shear strength in the eroded block, a circular slope failure occurs

locally near the toe of the slope. In addition, as the eroded block displaces to the left, a shear band (f_1) initiates from the bottom of the eroded block, propagates downward approximately 2 m below the bottom of the river and then propagates almost horizontally through the sensitive clay layer. The horizontal section of the shear band f_1 is located 2 m above the interface between the sensitive clay and stiff layer indicating that the propagation of the horizontal shear band is not strictly restricted by the stiff soil layer. Instead, the quasi-horizontal shear band forms in the sensitive clay layer. Note that many post-failure investigations show this type of shear band formation (Locat et al. 2008, 2015).

As the shear band propagates further, an active failure occurs in the soil layer above the shear band f_1 . A curved shear band f_2 forms from point P_1 . When f_1 propagates 97.5 m, the shear band f_2 propagates up to the ground surface (Fig. 4(b)). The instantaneous velocity in Fig. 4(c) shows a rotational movement of the failed soil mass near the shear band f_2 while the debris in the front moves almost laterally above the horizontal shear band f_1 . As the shear band f_1 propagates further through the sensitive clay layer, active failures occur in the overlying soil layer. However, as the ground surface behind the crest is horizontal, rotational slide does not occur in the right side the shear band f_2 . Instead, the failed soil mass breaks into a number of blocks forming horsts and grabens. As can be seen in Fig. 4(d), two inclined shear bands f_3 and f_4 form from the point P_2 . The shear band f_4 propagates deeper to the shear band f_1 . With further displacement of the failed soil blocks, another inclined shear band f_5 forms from the intersection of f_1 and f_4 (point P_3 in Fig. 4(e)) and propagates up to the ground surface. The soil block bounded by the shear bands f_4 and f_5 forms a graben. Once the shear band f_5 reaches the ground surface, an inclined shear band f_6 forms beneath the crust (Fig. 4(f)). The soil block bounded by f_1 , f_5 and f_6 has a tip pointing upward, which is known as a horst. Figure 4(g) shows that the failure process continues and another inclined shear band f_7 forms from the end of the shear band f_1 , which creates another graben bounded by the shear bands f_1 , f_6 and f_7 . At the same time, the shear band f_3 propagates deeper to the band f_1 forming a horst bounded by the shear bands f_1 , f_3 and f_4 .

The accumulated plastic shear strain PEEQVAVG indirectly reflects the degradation of s_u . For the soil parameters and element size listed above, PEEQVAVG ≤ 0.005 indicates no degradation of s_u (segment ab in Fig. 4). In this zone, the undrained shear strength is $s_{u,p}$. On the other hand, the soil elements with PEEQVAVG > 2.3 have been subjected to relative displacement greater than δ_{id} and therefore the shear strength of these elements are $s_{u,ld}$. Figure 4 shows that significant strain concentration occurs in the narrow shear bands. Outside these shear bands, the plastic shear strain is zero or negligible. Such extremely large strain concentration cannot be simulated using the traditional FE modeling technique developed in pure Lagrangian framework. The soil blocks, such as horsts and grabens, are almost intact during displacement and the soil at the interface between the blocks is remoulded. However, high plastic shear strains are calculated in the debris located in front part (Fig. 4(g)). The movement of the soil is opposed by the other bank in the left side. Therefore, a number of shear bands form in this soil mass during its displacement over the left side river bank. It is to be noted here that post-failure observation shows a number of cracks in this zone (Locat et al. 2011). The present numerical study could not simulate those cracks because the soil is modeled as elastic-plastic material.

The shear band f_1 does not propagate further after the formation of last graben. The reason is that the ground surface is horizontal and therefore the driving force is smaller than the resistance. The shear band f_1 propagates a maximum distance of 120 m from the toe.

Figure 4(h) shows the instantaneous velocity vectors of soil elements after the formation of horsts and grabens. The horsts and grabens displace almost laterally above the horizontal shear band f_1 except for the last graben near the back scarp where the soil elements move inclined downward direction.

In summary, the present FE simulation show that the failure is initiated by formation of horizontal shear band, followed by rotational slides and then formation of horsts and grabens mainly under the horizontal ground surface. Similar interpretation has been also provided by Local et al. (2011) from post failure observation.

4.2 Failure pattern and topography

Figure 5 shows the failure pattern and topography after the landslide. As discussed in previous sections, the present FE analysis simulates a quasi-horizontal shear band 2 m below the toe of the slope. A similar quasi-horizontal failure plane was interpreted from CPTU tests (black dots) as shown in Fig. 5, which is 0.5 to 1.0 m deeper than FE simulation results. This slight difference might result from selection of soil parameters, and the geometry of slope and eroded block. Moreover, field investigation indicates that the elevation of the horizontal shear band raised about 10 m before it reached the back scarp (see lower red dotted line in Fig. 5). This observation is not reflected in the FE results. It could be because of change in soil properties or existence of another weak layer. The horizontal distance between the crest (before failure) and back scarp measured in the field after the landslide was 80 m which is consistent with the intersection of the last shear band with the ground surface. Overall, the present FE modeling can reasonably simulate the formation of failure surfaces and the distance over which the failure propagates, as observed in the field.

The topography of the debris observed after the landslide (red dash line at the top) also compares well FE simulation result. FE result shows that the soil mass dislocated into horsts and grabens and moves laterally towards the opposite side of the river. The debris blocks the river channel and forms a flat deposit. The trend shown in FE simulation has a good agreement with field investigation data. As mentioned in Section 2, Locat et al. (2011) divided the debris into four zones. The failed soil in Zones 1 and 2 covered the opposite river bank, while in Zones 3 and 4 horsts and grabens were observed. The present FE simulation shows a very similar trend.

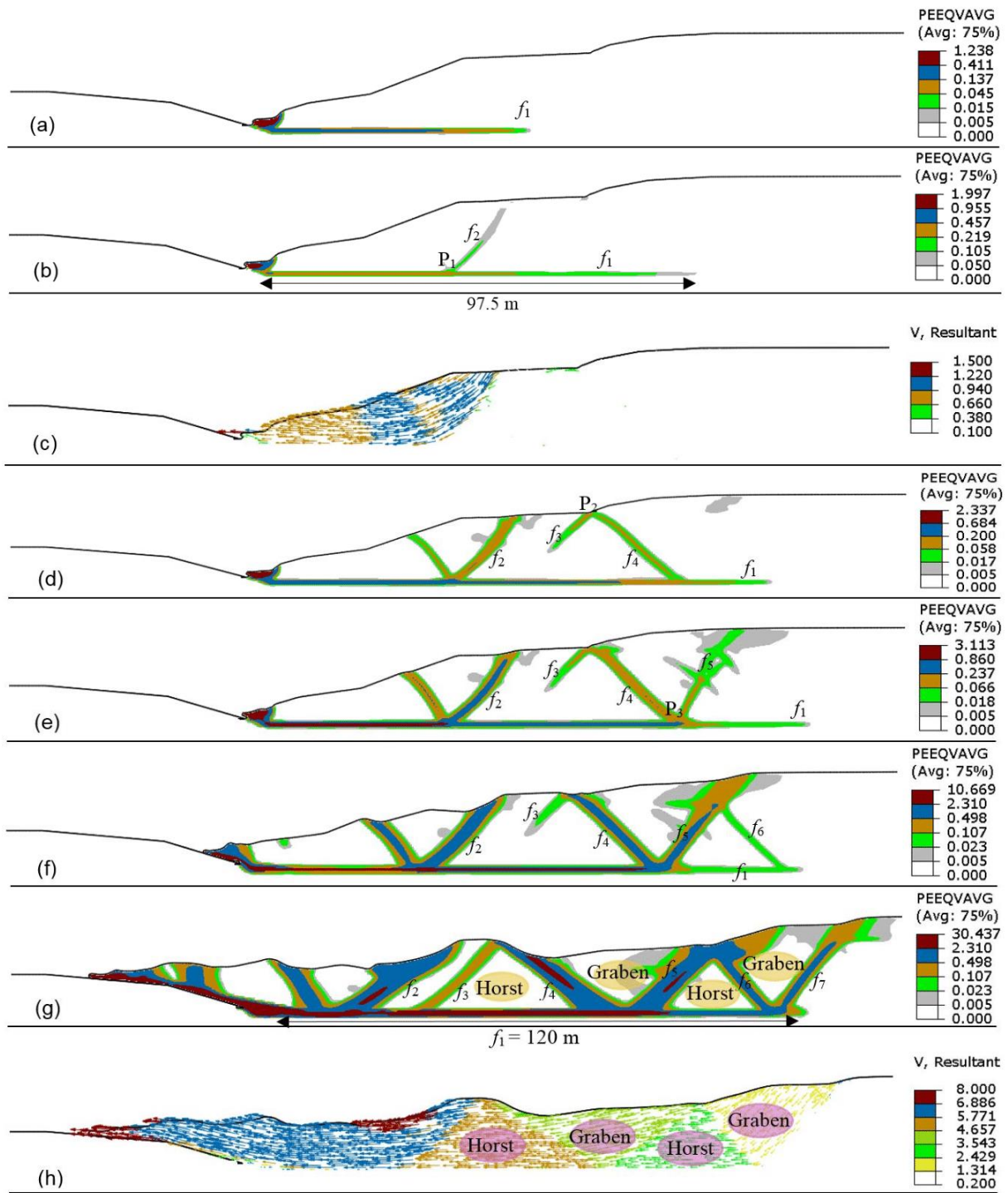


Figure 4 Formation of failure surfaces in FE simulation

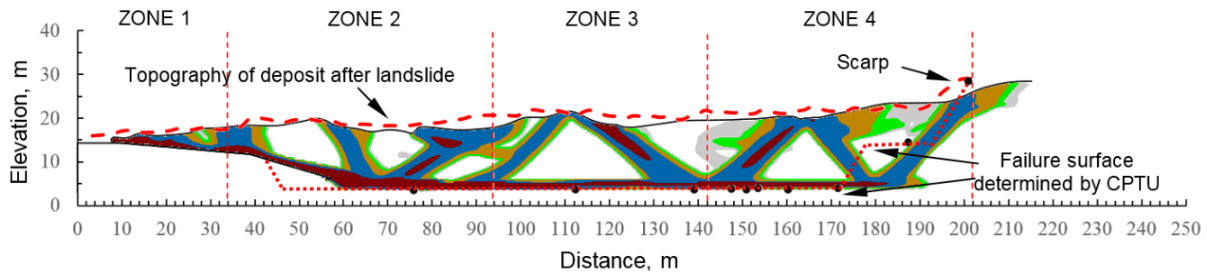


Figure 5 Comparison of the failure pattern and topography between FE modeling and field investigation

5 CONCLUSIONS

Large deformation finite element modeling technique is used to simulate the 2010 Saint-Jude landslide. Analyses are performed using the Coupled Eulerian-Lagrangian (CEL) technique available in Abaqus FE software. The FE simulation shows that a quasi-horizontal shear band forms in the sensitive clay layer, because of post-peak shear strength degradation behaviour, due to a small landslide near the toe. The soil mass above the horizontal shear band slides and dislocates into number of blocks including horsts and grabens. The present FE simulation could explain the possible failure mechanisms involved in spread. The FE results also compare well with the field investigation in terms of failure pattern, topography, and retrogressive distance, which is of critical importance in landslide hazard mapping.

ACKNOWLEDGEMENTS

The financial support from the Research and Development Corporation of Newfoundland and Labrador, NSERC and MITACS is gratefully acknowledged.

REFERENCES

- Carson, M. A. 1977. On the retrogression of landslides in sensitive muddy sediments. *Canadian Geotechnical Journal*, 14(4): 582-602.
- Demers, D., Robitaille, D., Locat, P., and Potvin, J. 2013. Inventory of large landslides in sensitive clay in the province of Quebec, Canada: preliminary analysis. *Landslides in Sensitive Clays - From Geosciences to Risk Management*, Springer, Netherland.
- Dey, R., Hawlader, B., Phillips, R. and Soga, K. 2012. Effects of shear band propagation on submarine landslide. In: *Proceedings of the 22nd International Offshore and Polar Engineering Conference*, Rhodes, Greece, 766-773.
- Dey, R., Hawlader, B., Phillips, R. and Soga, K. 2013. Progressive failure of slopes with sensitive clay layers. In: *Proceedings of the 18th International Conference on Soil Mechanics and Geotechnical Engineering*, Paris, 2177-2180.
- Dey, R., Hawlader, B., Phillips, R. and Soga, K. 2014. Stability analysis of a river bank slope with an existing shear band. *6th Canadian GeoHazards Conference*, Kingston, Ontario.
- Dey, R., Hawlader, B., Phillips, R. and Soga, K. 2015. Large deformation finite element modeling of progressive failure leading to spread in sensitive clay slopes. *Géotechnique*, 65(8): 657-668.
- Dey, R., Hawlader, B., Phillips, R. and Soga, K. 2016a. Modeling of large deformation behaviour of marine sensitive clays and its application to submarine slope stability analysis. *Canadian Geotechnical Journal*, 53:1-18.
- Dey, R., Hawlader, B., Phillips, R. and Soga, K. 2016b. Numerical modelling of submarine landslides with sensitive clay layers. *Géotechnique*, 66(6): 454-468.
- Einav, I. and Randolph, M. F. 2005. Combining upper bound and strain path methods for evaluating penetration resistance. *International Journal of Numerical Methods Engineering*, 63(14): 1991-2016.
- Griffiths, D. V. and Lane, P. A. 1999. Slope stability analysis by finite elements. *Géotechnique*, 49(3): 387-403.
- Locat, A., Leroueil, S., Bernander, S., Demers, D., Locat, J. and Ouehb, L. 2008. Study of a lateral spread failure in an eastern Canada clay deposit in relation with progressive failure: the Saint-Barnabé-Nord slide. In: *Proceedings of the 4th Canadian Conference on Geohazards: From Causes to Management*, Québec, Canada, 89-96.
- Locat, A., Leroueil, S., Bernander, S., Demers, D., Jostad, H.P. and Ouehb, L. 2011. Progressive failures in eastern Canadian and Scandinavian sensitive clays. *Canadian Geotechnical Journal*, 48(11): 1696-1712.
- Locat, A., Leroueil, S., Locat, P., Demers, D., Robitaille, D. and Lefebvre, G. 2012. In situ characterization of the Saint-Jude landslide, Quebec, Canada. In: *Proceedings of the 4th International Conference on Site Characterization*, Brazil, 507-514.
- Locat, A., Jostad, H.P. and Leroueil, S. 2013. Numerical modeling of progressive failure and its implications for spreads in sensitive clays. *Canadian Geotechnical Journal*, 50(9): 961-978.
- Locat, A., Leroueil, S., Fortin, A., Demers, D. and Jostad, H.P. 2015. The 1994 landslide at Sainte-Monique, Quebec: geotechnical investigation and application of progressive failure analysis. *Canadian Geotechnical Journal*, 52(4): 490-504.

- Locat, P., Fournier, T., Robitaille, D. and Locat, A. 2011. Glissement de terrain du 10 mai 2010, Saint-Jude, Montérégie – Rapport sur les caractéristiques et les causes. Ministère des Transports du Québec, Service Géotechnique et Géologie, Rapport MT11-01.
- Odenstad, S. 1951. The landslide at Sköttorp on the Lidan River, February 2, 1946. *Royal Swedish Institute Proceedings*, 4: 1-38.
- Quinn, P.E., Diederichs, M.S., Rowe, R.K. and Hutchinson, D.J. 2011. A new model for large landslides in sensitive clay using a fracture mechanics approach. *Canadian Geotechnical Journal*, 48(8): 1151-1162.
- Wang, C., Saha, B. and Hawlader, B. 2015. Some factors affecting retrogressive failure of sensitive clay slopes using large deformation finite element modeling. *In: Proceedings of the 68th Canadian Geotechnical Conference and 7th Canadian Permafrost Conference*, Quebec City, Quebec, Canada.

Appendix-II

Numerical Modeling of Three Types of Sensitive Clay Slope Failures

This paper has been published in the 19th International Conference on Soil Mechanics and Geotechnical Engineering, Seoul 2017. Most of the research work presented in this paper was conducted by the first author. He also prepared the draft manuscript. The other authors supervised the research and reviewed the manuscript.

Numerical Modeling of Three Types of Sensitive Clay Slope Failures

Modélisation numérique des Trois types d'argile sensible ruptures de pente

Chen Wang, Bipul Hawlader

Department of Civil Engineering, Memorial University of Newfoundland, Canada

ABSTRACT: The three major types of large-scale landslides in sensitive clay are the downhill progressive slide, flow-slide and spread. Because of strain-softening behavior of sensitive clay, the failure planes develop progressively and significant shear strain localization occurs along the failure planes (shear bands). Moreover, the failed soil mass generally displaces over a large distance. These types of landslide cannot be modeled using the commonly used limit equilibrium methods or typical finite element (FE) method developed in Lagrangian framework. In the present study, numerical simulations of these landslides—based on a large deformation FE modeling technique—is presented. The initiation of failure, formation of shear bands, global failure of the slopes, and post-failure deformation of the failed soil mass are explained. The FE simulated failure patterns compare well with the conceptual models proposed from field observation.

RÉSUMÉ: Les trois principaux types de glissements de terrain à grande échelle dans l'argile sensible sont la diapositive, le débit-slide et la propagation de descente progressive. En raison du comportement souche adoucissement d'argile sensible, les plans de rupture se développent progressivement et importante déformation de cisaillement localisation se produit le long des plans de rupture (bandes de cisaillement). En outre, la masse du sol échoué déplace généralement sur une grande distance. Ces types de glissements de terrain ne peuvent pas être modélisés en utilisant les méthodes d'équilibre limites couramment utilisés ou méthode typique éléments finis (FE) développés dans le cadre lagrangien. Dans la présente étude, les simulations numériques des thèses des glissements de terrain basés sur une grande FE modélisation de la déformation technique-est présenté. L'initiation de l'échec, la formation de bandes de cisaillement, échec global des pistes, et à la déformation post-échec de la masse du sol échoué sont expliqués. Les motifs de défaillance simulée FE se comparent bien avec les modèles conceptuels proposés par.

KEYWORDS: large-scale landslides, finite element modeling and sensitive clay.

1 INTRODUCTION

Large-scale progressive and retrogressive landslides in sensitive clays are major geohazards in eastern Canada and Scandinavia. These kind of landslides usually occur suddenly and can affect large area (>1 ha). The triggering of these landslides is attributed to natural factors (e.g. river bank erosion, earthquake and rainfall), human activities (e.g. placement of fill and pile driving) or a combination of both. Three most common types of large-scale landslides in sensitive clays are: (i) downhill progressive slides, (ii) flow-slides (sometimes called earthflows) and (iii) spreads. Figure 1 schematically shows the main features of these landslides.

Bernander and his co-workers presented a number of downhill progressive landslides in mild natural sensitive clay slopes (Bernander 2000; Bernander et al. 2016). In this type of landslide, the failure is generally initiated due to disturbance in the upslope areas and then propagates in the downslope direction over a large distance (several hundred meters in some cases, Barnander et al. (2016)). The disturbance could be resulted from construction activities such as pile driving or placement of fills. For example, Surte Landslide in Gothenburg, Sweden involved displacement of 24 ha which has been attributed to upslope pile driving. Upslope subsidence near the zone of disturbance and downslope heave are the common features of the failed soil mass (Fig. 1(a)).

The mechanisms of flow-slides are well described by Bjerrum (1955) and Tavenas (1984). In this type of landslides, multiple slides occur retrogressively (Fig. 1(b)). After the first slide, the debris gets highly remoulded and flows out leaving an unstable scarp. A second slide then occurs due to removal of the support from the soil mass in the first slide. This process continues until a final stable back scarp forms and the retrogression stops. Tavenas (1984) suggested that flow-slides might occur when: (i) an initial slide has occurred; (ii) the potential energy of the failed soil mass is high enough to remould the clay significantly; (iii) the remoulded shear strength of the clay is very low.

Finally, the spread is a type of large-scale landslide that generally triggered by erosion of soil near the toe of the slope. A quasi-horizontal failure plane forms due to toe erosion. The soil mass above this failure plane then displaces and fails successively forming a number of horsts and grabens (Cruden and Varnes 1996). The horsts are the blocks of intact clay having a sharp wedge pointing upward, while the grabens are the blocks having a flat horizontal top surface (Fig. 1(c)).

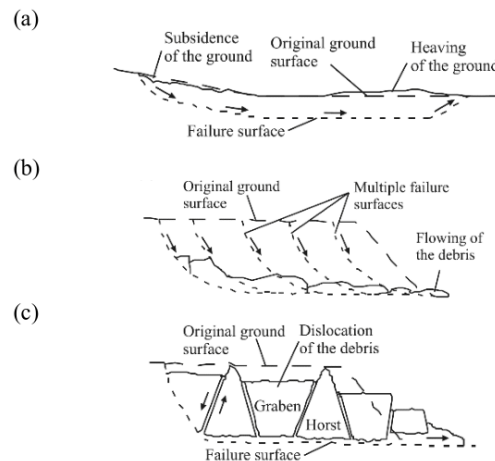


Figure 1. Three common types of large-scale landslides in sensitive clays: (a) downhill progressive slide; (b) flow-slide; (c) spread. (after Locat et al. 2011)

Because of strain-softening behavior of sensitive clays, the failure surfaces develop progressively. Moreover, a massive volume of soil mass displaces in these types of landslides. Unfortunately, the limit equilibrium methods commonly used in slope stability analysis cannot explain the progressive development of failure. Moreover, the complete failure process cannot be modeled using the typical FE methods developed in

Lagrangian framework because of significant mesh distortion and numerical issues. Therefore, conceptual or simplified models have been proposed in the past to explain such landslides (Bernander et al. 2016; Locat et al. 2011).

The objective of this study is to present large deformation FE modeling of sensitive clay slope failures. This method has been previously used by the authors and their co-workers for successful simulation of spreads (Dey et al. 2015; Wang et al. 2016). In the present study, simulations are performed for varying geometries, soil properties and triggering factors to simulate all three types of failure shown in Fig. 1.

2 PROBLEM DEFINITION

The simulation results of 3 cases are presented in this paper to explain the mechanisms involved in downhill progressive slides, flow-slides and spreads. The simulations are performed for plane strain condition. In Case-I, a mild slope ($\beta=3^\circ$) is considered to model downhill progressive failure (Fig. 2(a)). The peak undrained shear strength (s_{up}) of the top 20 m thick sensitive clay layer is 35 kPa. There is a change in slope angle at the point X in the downslope area (Fig. 2(a)). Bernander et al. (2016) showed that the downslope areas also could have a very mild slope. However, for simplicity the downslope area is assumed to be horizontal. The soil below the sensitive clay (base layer) is considered as a strong material. An embankment of 7.5 m height and 23 m crest width is placed in the upslope area at 200 m from point X. To trigger the landslide, the embankment load is gradually applied by increasing the unit weight of the fill.

In Case-II, a 30 m high riverbank slope of sensitive clay is studied. The slope angle β is 26.6° (2H:1V) and the upslope area is horizontal. The s_{up} of the sensitive clay layer increases linearly from 60 kPa at the ground surface to 110 kPa at the bottom of the sensitive clay layer. Again, a 10 m strong base layer is considered below the sensitive clay layer. The failure is triggered by toe erosion which is the most common triggering factor for the landslides in eastern Canada. In Case-III, the geometry of the slope is same as in Case-II but a 5 m crust above the sensitive clay layer is considered. The peak undrained shear strength of the sensitive clay layer increases linearly with depth from 40 to 100 kPa.

In all three cases, the mobilized shear strength of the sensitive clay layer (s_u) decreases with plastic deformation and sensitivity (S_t) as discussed in Section 3.2.

3 FINITE ELEMENT MODELING

3.1 Numerical technique

Coupled Eulerian-Lagrangian (CEL) technique available in Abaqus FE software is used. In CEL, the Eulerian material (soil) can flow through the fixed mesh. Therefore, there is no numerical issue related to mesh distortion or mesh tangling even at large strains around the failure planes. The performance of CEL technique of simulating sensitive clay slope failure has been discussed in previous studies (Dey et al. 2015, 2016a,b; Wang et al. 2016). The FE model consists of two parts: (i) soil, (ii) void space to accommodate displaced soil mass (Fig. 2). The soil is modeled as Eulerian material using the EC3D8R elements in Abaqus, which are 8-noded linear brick, multi-material, reduced integration elements. Soil and void spaces are created in Eulerian domain using Eulerian Volume Fraction (EVF) tool. For void space EVF is zero (i.e. no soil). On the other hand, EVF is unity inside the slope geometry, which means these elements are filled with Eulerian materials (i.e. soils).

Only three-dimensional model can be generated in CEL. In the present study, the model is only one element thick in the out of plane direction. The movement of soil perpendicular to the

x-y plane in Fig. 2 is restricted by applying zero velocity boundary condition in order to mimic plane strain condition. All velocity components are zero at the bottom and left vertical planes. At the right vertical plane, zero velocity boundary condition is applied from the bottom to the ground surface. However, in the void space no velocity boundary condition is applied such that the debris can flow out of the domain as shown in the following sections. This also reduces the computational cost because the model size in downslope area could be reduced. No boundary condition is applied at the soil-void interface so that the soil can move into the void space when displaced. Cubical elements of 0.3 m size are used in all the simulations.

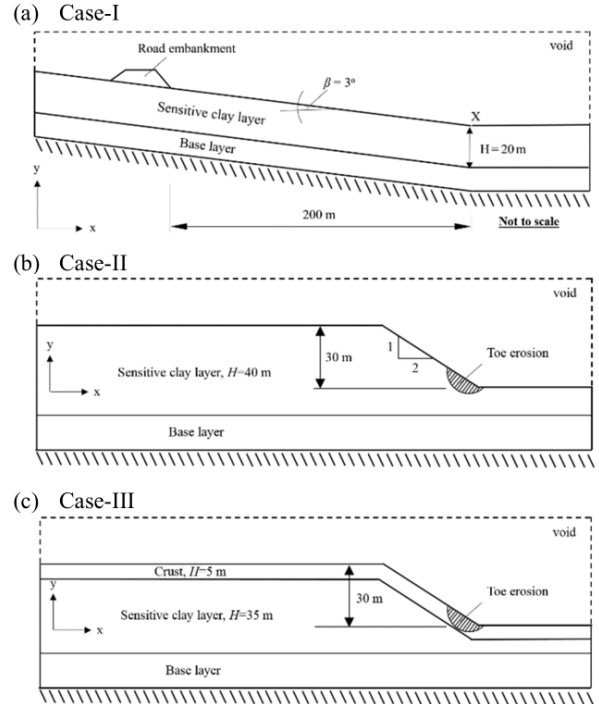


Figure 2. Geometry of the slope used in numerical analysis

The numerical analysis consists of three steps of loading. In the first step, geostatic load is applied to bring the slope in in-situ stress condition. The slopes are stable under geostatic load. In the second step, the triggering factors (e.g. upslope construction in Case-I and toe erosion in Cases II and III) are applied to initiate the landslide. In the final step, analyses continue for a period of time without any increase of external load to observe the post-slide behaviour.

3.2 Soil parameters

The analyses are performed for undrained condition because landslides in sensitive clays usually occur in a very short time period.

Sensitive clays show post-peak softening behavior in undrained loading (Tavenas et al. 1984; Quinn 2011). The mobilized undrained shear strength after the peak (s_u) can be related plastic shear strain or post-peak displacement (δ). In this study, the softening behavior of sensitive clays is defined using the following exponential relationship.

$$s_u = \left[\frac{1}{S_t} + \left(1 - \frac{1}{S_t} \right) e^{-3\delta / \delta_{95}} \right] s_{up} \quad [1]$$

where, s_u is the mobilized undrained shear strength at displacement δ ; S_t is the sensitivity of the soil; $\delta = \delta_{total} - \delta_p$; δ_p is

the displacement required to attain the peak undrained shear strength s_{up} ; and δ_{95} is the value of δ at which the undrained shear strength of the soil is reduced by 95% of $(s_{up}-s_{uR})$. Equation (1) is a modified form of strength degradation equation proposed by Einav and Randolph (2005) but in terms of displacement. The authors discussed the model parameters required in this equation and its application in modeling sensitive clay slope in previous studies (Dey et al. 2015, 2016a,b; Wang et al. 2016).

Figure 3 shows the relationship between the shear strength and shear displacement. Line oa represents a linear elastic pre-peak behavior. s_{up} is mobilized at point a and remains constant up to point b for a displacement of δ_{pc} . The curve bcd is defined by Eq. (1). After s_{uR} , the shear strength reduces slowly with shear displacement. The reduction of s_u in this zone is defined by a linear line de from s_{uR} to s_{uld} at a large displacement. After that, s_u remains constant ($s_u=s_{uld}$). The geotechnical parameters used for modeling sensitive clay are shown in Table 1.

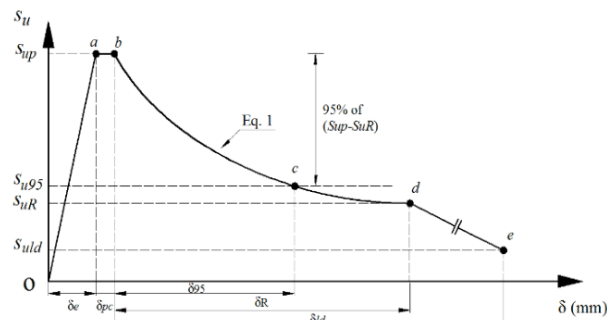


Figure 3. Stress–displacement behavior of sensitive clay

The base layer is modeled as elastic material with Young's modulus $E=200$ MPa. The crust in Case-III is modeled as elastic-plastic material without softening using the following geotechnical parameters: $s_u=50$ kPa, $E_u=10$ MPa ($=200s_u$) and $\nu_u=0.495$.

Table 1: Parameters used for modeling sensitive clay

Soil Parameters	Case-I	Case-II	Case-III
Undrained Young's modulus, E_u (MPa)	10	10	10
Poisson's ratio, ν_u	0.495	0.495	0.495
Peak undrained shear strength, s_{up} (kPa)	35	60-110	40-100
Residual undrained shear strength, s_{uR} (kPa)	$s_{up}/5$	$s_{up}/3$	$s_{up}/5$
Large displacement undrained shear strength, s_{uld} (kPa)	$s_{up}/50$	$s_{up}/50$	$s_{up}/35$
Unit weight of soil, γ (kN/m ³)	18.0	18.0	18.0
Plastic shear displacement for 95% degradation of soil strength, δ_{95} (mm)	30	30	30
Plastic shear displacement for initiation of softening, δ_{pc} (mm)	2	3	3
Plastic shear displacement for large displacement undrained shear strength, δ_{ld} (mm)	2000	500	2000

4 FINITE ELEMENT RESULTS

4.1 Case-I: Downhill progressive slide

This case demonstrates a downhill progressive slide induced by embankment construction. The equivalent plastic strain (PEEQVAVG) obtained from Abaqus is used to examine the formation of shear bands. Before placing the embankment, the shear stress in soil elements increases with depth due to self-weight of the soil. The shear stress at the bottom of the sensitive

clay layer (τ_0) can be calculated as $\tau_0=\gamma H\sin\beta$. In this case, for $\gamma=18$ kN/m³, $H=20$ m and $\beta=3^\circ$, the value of τ_0 is 18.8 kPa, which is less than s_{up} ($=35$ kPa) of the soil. Therefore, development of any plastic shear strain or failure of the slope is not expected under gravity load.

In the second step, the external load from the embankment induces additional shear stress in the sensitive clay layer and triggers the failure. Figure 4(a) shows that the failure initiates below the embankment from point A which is located at the boundary between sensitive clay and base layers. Figure 4(b) shows the failure pattern at the end of second step. The shear band then propagates mainly in downslope direction from point A. Although no additional external load is applied in the third step, the propagation of shear band continues with time because s_u reduces with accumulation of plastic shear strains in the failure planes that causes redistribution of additional loads to the surrounding soil elements. Figure 4(c) shows that the shear band propagates downhill along the bottom of the sensitive clay layer and finally reach the toe of the slope. As the failure continues, the soil around the embankment subsides and the soil near the toe of the slope heaves forming a number of inclined shear bands in the sensitive clay layer, which indicates compressive failure in this area (Fig. 4(d)).

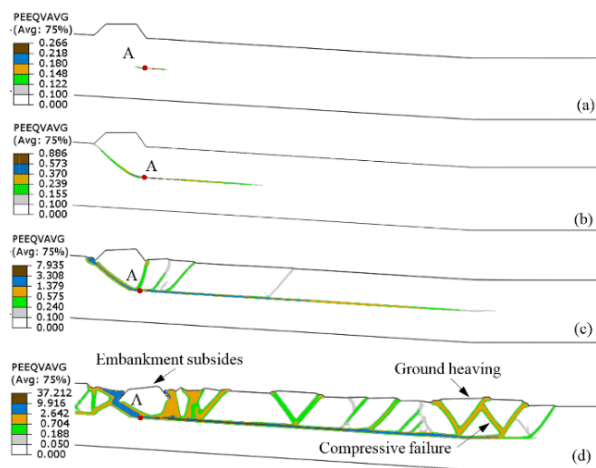


Figure 4. FE simulation of downward progressive failure (Case-I)

4.2 Case-II: Flow-slide

This case demonstrates a flow-slide near a river bank triggered by toe erosion. The slope is stable after the gravity step. In the second step, the shear strength of the soil in the eroded zone (hatched area in Fig. 2(b & c)) is reduced to 1 kPa, which causes the failure of this soil block and spreads over a large area. This phenomenon is similar to the toe erosion at river banks in the field, the failed block might be displaced a large distance in the downslope or eroded by river flow. Figure 5(a) shows that, due to removal of a small soil block near the toe, a horizontal shear band forms in the sensitive clay layer and then propagates up to the ground surface causing a global failure. The horizontal segment of the shear band is located at 10 m above the interface between sensitive clay and base layers. This implies that the location of shear band is not predefined rather it forms at critical location depending upon the kinematics of problem. Therefore, the present study could eliminate the a priori definition of the failure planes as used in previous studies for modeling sensitive clay slopes (Locat et al. 2011, Quinn et al. 2011). With displacement, the failed soil mass breaks into pieces through formation of a number of shear bands within it. When debris move sufficiently large distance, the support on the intact soil reduces that causes the second rotational slide. The depth of this slide is less than that of first slide. Similar

phenomenon has been observed in the field in flow-slides (Demers et al. 2014). The failure process continues as shown in Figs. 5(b)-5(d). Finally, the failure stopped after the fourth slide because the back scarp is shallow and is not steep enough for causing global failure of another soil mass.

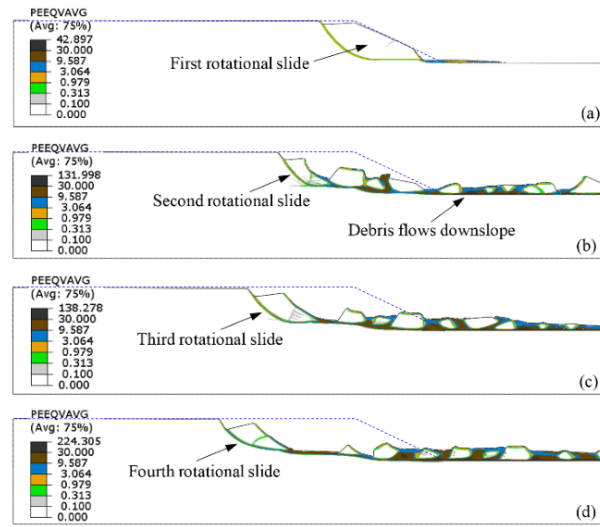


Figure 5. FE simulation of flow-slide (Case-II)

4.3 Case-III: Spread

The modeling of a spread initiated by toe erosion near the river bank is presented in this section. Similar to Case-II, the slope is stable under in-situ stress condition. Toe erosion reduces the support and trigger slope failure by formation of a horizontal shear band in the sensitive clay layer (Fig. 6(a)). As the soil above the shear band displaces to the right, s_u in the shear band reduces because of plastic deformation (see Fig. 3). At one stage curved upward shear bands form from the horizontal one and cause global failure (Fig. 6(b)). The propagation of the horizontal shear band continues and the soil mass above the horizontal shear band fails progressively. A number of horsts and grabens, similar to Fig. 1(c), are formed (Fig. 6(c)). A close examination of the simulation results show that the presence of the crust and slow movement of the failed soil blocks, as compared to Case II, are the potential causes of formation of horsts and grabens instead of flow-slide as presented in Fig. 5.

5 CONCLUSIONS

Three typical large-scale landslides in sensitive clays are simulated. Using a large deformation FE modeling technique in Abaqus, the mechanisms involved in these landslides—triggering, shear bands formation, soil mass dislocation and large displacement of debris—are examined. The simulation results are comparable to the conceptual model proposed in previous studies based on post-failure observation. It is shown that the variation of geometry of the slope, soil properties and triggering factors could change the failure pattern.

Case-I shows that an upslope loading could create a long shear band and cause a large landslide of a mild natural sensitive clay slope as observed in the field. Case-II and Case III show that a small slide/erosion near the toe of river bank could cause large landslides. Depending on mobility of the failed soil mass, the failure could be spread or flow-slide.

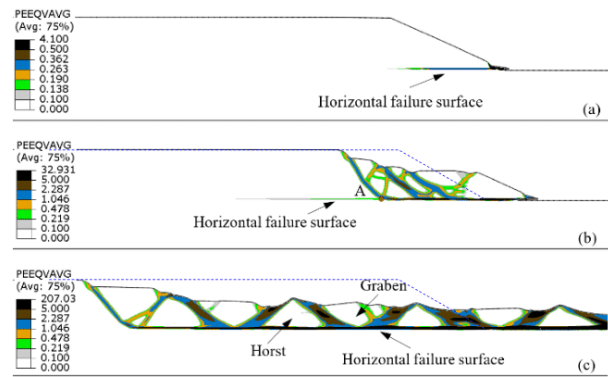


Figure 6. FE simulation of spread (Case-III)

6 ACKNOWLEDGEMENTS

The financial support from the Research and Development Corporation of Newfoundland and Labrador, NSERC and MITACS is greatly acknowledged.

7 REFERENCES

- Bernander S. 2000. Progressive landslides in long natural slopes, formation, potential extension and configuration of finished slides in strain-softening soils. Licentiate thesis, *Department of Civil and Mining Engineering, Luleå University of Technology*, Luleå, Sweden.
- Bernander S., Kullingsjo A., Gylland A.S., Bengtsson P., Knutsson S. Pusch R., Olofsson J. and Elfgrén L. 2016. Downhill progressive landslides in long natural slopes: triggering agents and landslide phases modeled with a finite difference method. *Canadian Geotechnical Journal* 53 (10), 1565-1582.
- Bjerrum L. 1955. Stability of natural slopes in quick clay. *Géotechnique* 5 (1), 101-119.
- Cruden D.M. and Varnes D.J. 1996. Landslides types and processes. In *Landslides investigation and mitigation*. Special Report 247. *Transportation Research Board, National Research Council*. Washington, D.C. 37-75.
- Demers D., Robitaille D., Locat P. and Potvin J. 2014. Inventory of large landslides in sensitive clay in the province of Quebec, Canada: preliminary analysis. *Advances in Natural and Technological Hazards Research*. 36, 77-89.
- Dey R., Hawlader B., Phillips R. and Soga, K. 2015. Large deformation finite element modeling of progressive failure leading to spread in sensitive clay slopes. *Géotechnique*, 65 (8), 657-668.
- Dey R., Hawlader B., Phillips R. and Soga K. 2016a. Modeling of large deformation behaviour of marine sensitive clays and its application to submarine slope stability analysis. *Canadian Geotechnical Journal*, 53 (7), 1-18.
- Dey, R., Hawlader, B., Phillips, R. and Soga, K. 2016b. Numerical modelling of submarine landslides with sensitive clay layers. *Géotechnique*, 66 (6), 454-468.
- Einav I. and Randolph M.F. 2005. Combining upper bound and strain path methods for evaluating penetration resistance. *International Journal of Numerical Methods Engineering*, 63 (14), 1991-2016.
- Locat A., Leroueil S., Bernander S., Demers D., Jostad H.P. and Ouehb L. 2011. Progressive failures in eastern Canadian and Scandinavian sensitive clays. *Canadian Geotechnical Journal* 48 (11), 1696-1712.
- Tavenas F. 1984. Landslides in Canadian sensitive clays - a state of the art. In *Proceedings of the 4th International Symposium on Landslides*, Toronto, Ontario, 141-153.
- Quinn P.E., Diederichs M.S., Rowe R.K. and Hutchinson D.J. 2011. A new model for large landslides in sensitive clay using a fracture mechanics approach. *Canadian Geotechnical Journal*, 48(8), 1151-1162.
- Wang C., Hawlader B. and Perret D. 2016. Finite element simulation of the 2010 Saint-Jude landslide in Quebec. In: *Proceedings of the 69th Canadian Geotechnical Conference*, Quebec City, Quebec, Canada.